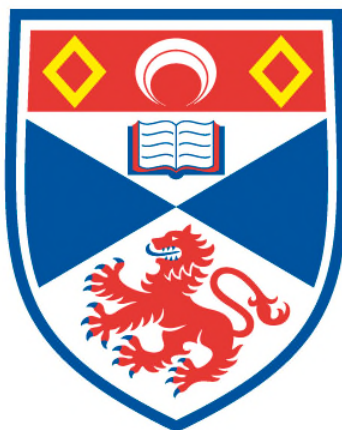


SYNTHESIS AND CHARACTERISATION OF ORDERED MESOPOROUS MATERIALS

Troy Allen Dougherty

**A Thesis Submitted for the Degree of PhD
at the
University of St Andrews**



2010

**Full metadata for this item is available in
St Andrews Research Repository
at:**

<http://research-repository.st-andrews.ac.uk/>

Please use this identifier to cite or link to this item:

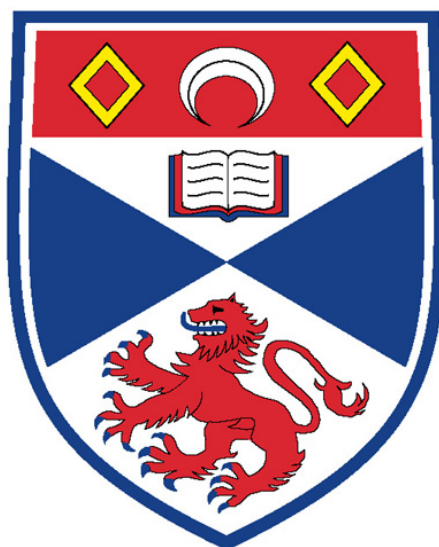
<http://hdl.handle.net/10023/1023>

This item is protected by original copyright

**This item is licensed under a
Creative Commons Licence**

Synthesis and Characterisation of Ordered Mesoporous Materials

Troy Allen Dougherty



Thesis submitted for the degree of Doctor of Philosophy
of the University of St Andrews

Abstract

Ordered mesoporous materials have attracted much attention recently for use in a wide range of applications. The oxidising materials, ceria (CeO_2) and CGO ($\text{Ce}_{0.9}\text{Gd}_{0.1}\text{O}_{2-\delta}$), have both been synthesised with ordered mesopores, but a method for the simple fabrication of these materials in high yields with crystalline pore walls has not yet been reported in the literature.

This thesis details the development of the vacuum impregnation method for the synthesis of ordered mesoporous materials with emphasis on ceria and CGO. Using the vacuum impregnation method both materials were successfully prepared. The materials exhibited the porous single crystal morphology in high yields, with unusual crystallographic features. Nitrogen physisorption, transmission electron microscopy (TEM), TEM tomography and temperature programmed studies were employed. Temperature programmed studies showed the materials to be catalytically active at lower temperatures than traditionally-prepared ceria. Photovoltaic studies showed that the materials exhibited efficient exciton quenching. The observation of nanowire extrusion during the synthetic procedure assisted in the postulation of a mechanism for product formation in the vacuum impregnation method.

The vacuum impregnation method was subsequently shown to be applicable to the synthesis of other materials, with encouraging results presented for ordered mesoporous carbon and $\text{Zr}_{0.84}\text{Y}_{0.16}\text{O}_{2-\delta}$. The syntheses of ordered mesoporous $\text{La}_{0.85}\text{Sr}_{0.15}\text{GaO}_{3-\delta}$ and $\text{La}_{0.76}\text{Sr}_{0.19}\text{CoO}_{3-\delta}$ were unsuccessful.

Declaration

I, Troy Dougherty, hereby certify that this thesis, which is approximately 50,500 words in length, has been written by me, that it is the record of work carried out by me and that it has not been submitted in any previous application for a higher degree.

I was admitted as a research student in September, 2006 and as a candidate for the degree of Ph.D in September, 2006; the higher study for which this is a record was carried out in the University of St Andrews between 2006 and 2009.

Date _____ signature of candidate _____

I hereby certify that the candidate has fulfilled the conditions of the Resolution and Regulations appropriate for the degree of Ph.D in the University of St Andrews and that the candidate is qualified to submit this thesis in application for that degree.

Date _____ signature of supervisor _____

In submitting this thesis to the University of St Andrews we understand that we are giving permission for it to be made available for use in accordance with the regulations of the University Library for the time being in force, subject to any copyright vested in the work not being affected thereby. We also understand that the title and the abstract will be published, and that a copy of the work may be made and supplied to any bona fide library or research worker, that my thesis will be electronically accessible for personal or research use unless exempt by award of an embargo as requested below, and that the library has the right to migrate my thesis into new electronic forms as required to ensure continued access to the thesis. We have obtained any third-party copyright permissions that may be required in order to allow such access and migration, or have requested the appropriate embargo below.

The following is an agreed request by candidate and supervisor regarding the electronic publication of this thesis:

Embargo on all of printed copy and electronic copy for the same fixed period of two years (maximum five) on the following ground:

publication would be commercially damaging to the researcher, or to the supervisor, or the University;
publication would preclude future publication.

Date _____ signature of candidate _____ signature of supervisor _____

Acknowledgements

Firstly, I would like to thank my supervisor, Dr. Richard T. Baker, for the opportunity to study in his research group as well as his guidance in my research.

I am grateful to EaStCHEM for their financial support throughout the length of my Ph.D, without which this work would not have been possible.

I would like to thank my research group, and especially Jonathan Kearney for helping me with temperature programmed experiments.

I would like to thank the staff of the School of Chemistry, especially Sylvia Williamson for conducting physisorption experiments for me, and Ross Blackley for assisting in powder X-ray diffraction and transmission electron microscopy.

Also, I would like to thank Dr. Nigel Neate from the Department of Mechanical, Materials & Manufacturing Engineering at the University of Nottingham for performing small-angle X-ray measurements for me, and Dr. Mike Fay from the Nottingham Nanotechnology and Nanoscience Centre for providing advanced transmission electron microscopy resources.

Finally, I would like to thank my fiancée, Helen Chapman, for her support over the last three years and for her assistance in editing this thesis.

Table of Contents

Current Research in the Synthesis of Ordered Mesoporous Materials

1.1 .. Mesoporous Silica	1
1.1.1 Introduction	1
1.1.2 SBA-15	2
1.1.3 KIT-6	2
1.1.4 FDU-12	3
1.2 .. Synthetic Methods.....	4
1.2.1 Soft Templating - Sol Gel.....	4
1.2.2 Hard Templating - Nanocasting	5
1.3 .. Materials	7
1.3.1 Ceria	7
1.3.1.1 Oxygen Storage Capacity and Oxygen Ion Conductivity	8
1.3.1.2 Electronic Conductivity	10
1.3.1.3 Previous Literature Investigations into Ordered Mesoporous Ceria...	10
1.3.2 Mesoporous Carbon.....	11
1.3.3 Yttria-stabilised Zirconia	12
1.3.4 Lanthanum-based Perovskite Materials.....	14
1.3.4.1 Strontium Doped Lanthanum Gallium Oxide	15
1.3.4.2 Strontium-doped Lanthanum Cobalt Oxide	16

An Overview of Technological Applications for Ordered Mesoporous Materials

2.1 .. Introduction.....	17
2.2 .. Nanocasting.....	17
2.2.1 Vacuum Impregnation	18
2.3 .. Heterogeneous Catalysis.....	19
2.4 .. Fuel Cells.....	20
2.5 .. Dye-Sensitised Solar Cells - Bulk Heterojunctions	22
2.6 .. Summary	23

Methods

3.1 .. Introduction	24
3.2 .. Nitrogen Physisorption	25
3.2.1 Physisorption Curves	25
3.2.2 BET Theory	27
3.2.3 BJH Theory	28
3.3 .. X-ray Diffraction.....	29
3.3.1 Powder X-ray Diffraction.....	29
3.3.2 Small Angle X-ray Scattering.....	31
3.4 .. Transmission Electron Microscopy	31
3.4.1 Electron Beam Generation	31
3.4.2 Selected Area Electron Diffraction, Fast-Fourier Transforms and Digital Diffraction Patterns.....	34
3.4.3 Energy Dispersive Spectroscopy	35
3.5 .. Temperature Programmed Experiments.....	36
3.6 .. Inductively coupled plasma mass spectrometry.....	38
3.7 .. Photoluminescence Spectroscopy	38

Experimental

4.1 .. Introduction.....	40
4.1.1 Experimental Maps.....	40
4.2 .. Sample Index	42
4.3 .. List of Chemical Reagents.....	42
4.4 .. Analytical Methods	43
4.4.1 Nitrogen Physisorption.....	43
4.4.2 TEM.....	43
4.4.3 XRD.....	44
4.4.4 TP Experiments	44
4.4.5 ICP-MS.....	47
4.4.6 Photovoltaic Studies	47

Mesoporous Silica Templates

5.1 .. Experimental Philosophy	48
5.2 .. Experimental	48
5.2.1 SBA-15	48
5.2.2 KIT-6	49

5.2.3	FDU-12	49
5.3	Results	49
5.3.1	SBA-15	49
5.3.2	KIT-6	55
5.3.3	FDU-12	59
5.4	Discussion.....	62
5.5	Summary.....	64

Mesoporous Ceria and CGO: Preliminary Experiments

6.1	Experimental Philosophy	65
6.2	Experimental	65
6.2.1	Reference Materials	65
6.2.2	Incipient Wetness Impregnation Technique	66
6.2.3	Acid Hydrolysis.....	66
6.2.4	Precipitation.....	67
6.3	Results	68
6.3.1	Reference Materials.....	68
6.3.2	Ceria Prepared Using SBA-15 and the IWIT	74
6.3.3	Ceria Prepared Using KIT-6 and the IWIT	77
6.3.4	Ceria Prepared by Acid Hydrolysis.....	81
6.3.5	Ceria Prepared by Precipitation.....	82
6.4	Discussion.....	86
6.5	Summary.....	90

Development of Vacuum Impregnation for Preparation of Mesoporous Ceria and CGO

7.1	Experimental Philosophy	91
7.2	Experimental	92
7.2.1	Additional Observations	94
7.3	Characterisation Studies	95
7.3.1	Ceria Prepared from KIT-6 Using VI.....	95
7.3.2	Ceria Prepared from SBA-15 Using VI.....	104
7.3.3	Ceria Prepared from KIT-6 Using VI (II)	109
7.3.4	CGO Prepared from SBA-15 Using VI.....	115
7.3.4.1	Tomography Study of CGO-S-V ₂	122
7.3.5	CGO Prepared from KIT-6 Using VI.....	123
7.3.5.1	Tomography Study of CGO-K-V ₂	128

7.3.6	Compositional Analysis.....	129
7.3.7	Discussion.....	133
7.4 ..	Temperature Programmed Studies.....	139
7.4.1	Ceria-K-V ₁	140
7.4.2	Ceria-S-V ₂	142
7.4.3	Ceria-K-V ₂	143
7.4.4	CGO-S-V ₂	144
7.4.5	CGO-K-V ₂	145
7.4.6	TP Cycling.....	145
7.4.7	Discussion.....	147
7.5 ..	Photovoltaic Studies.....	151
7.5.1	Discussion.....	152
7.6 ..	Thermal Resistance Studies	153
7.6.1	In-situ TEM Heating of CGO-K-V ₂	153
7.6.2	Examination of the Thermal Stability in Air	157
7.6.3	Discussion.....	162
7.7 ..	Studying the VI Method	164
7.7.1	Discussion.....	169
7.7.1.1	The Mechanism of the Vacuum Impregnation Method	169
7.8 ..	Summary.....	171

Mesoporous Carbon

8.1 ..	Experimental Philosophy	174
8.2 ..	Experimental	174
8.2.1	Mesoporous Carbon Using the IWIT	174
8.2.2	Preparation of Mesoporous Carbon Using VI.....	175
8.2.3	Molten Vacuum Impregnation	175
8.3 ..	Results	176
8.3.1	Mesoporous Carbon Using the IWIT	176
8.3.2	Mesoporous Carbon Using VI.....	178
8.3.2.1	Mesoporous Carbon Using Concentrated Precursor Solution	178
8.3.2.2	Mesoporous Carbon Using Dilute Precursor Solution.....	180
8.4 ..	Discussion.....	182
8.4.1	Product Characterisation.....	182
8.4.2	Implications for the Vacuum Impregnation Method	185
8.4.3	Modifications to the Vacuum Impregnation Method	185
8.5 ..	Summary.....	185

Other Mesoporous Materials

9.1 .. Experimental Philosophy	187
9.2 .. Experimental	187
9.2.1 Lanthanum Strontium Gallate	187
9.2.2 Lanthanum Strontium Cobaltite	189
9.2.3 Yttria Stabilised Zirconia	190
9.3 .. Results	191
9.3.1 Lanthanum Strontium Gallate (LSG)	191
9.3.2 Lanthanum Strontium Cobaltite	194
9.3.3 Yttria-Stabilised Zirconia	196
9.3.3.1 Partially Stabilised Zirconia	196
9.3.3.2 Cubic YSZ	200
9.4 .. Discussion	202
9.4.1 Ordered Mesoporous Perovskites	202
9.4.2 Ordered Mesoporous YSZ	203
9.5 .. Summary	204

Conclusions 205

Future Work 212

Appendices 214

References 216

Abbreviations

BET	Brunauer-Emmett-Teller (surface area calculation)
BJH	Barret-Joyner-Halenda (pore size calculation)
CCD	Charge-coupled device
CGO	Cerium-gadolinium oxide
DDP	Digital diffraction pattern
EDS	Energy dispersive X-Ray spectroscopy
FFT	Fast-Fourier transform
HRTEM	High-resolution TEM
ICDD	International Centre for Diffraction Data
ICP-MS	Inductively coupled plasma mass spectrometry
ITO	Indium tin oxide
IWIT	Incipient wetness impregnation technique
LSC	Lanthanum strontium cobaltite
LSG	Lanthanum strontium gallate
LSGM	Lanthanum strontium gallium magnesite
LSM	Lanthanum strontium manganite
MFC	Mass flow controller
MS	Mass spectrometer
PV	Photovoltaic
PL	Photoluminescence
PTFE	Polytetrafluoroethylene
SAXS	Small-angle X-ray scattering
SAED	Selected area electron diffraction
SOFC	Solid oxide fuel cell
TEM	Transmission electron microscope/microscopy
TEOS	Tetraethyl orthosilicate
TP	Temperature programmed
TPD	Temperature programmed desorption
TPO	Temperature programmed oxidation
TPR	Temperature programmed reduction
TSE	Tensile strength effect
VI	Vacuum impregnation
XRD	X-ray diffraction
YSZ	Ytria stabilised zirconia

Chapter 1

Current Research in the Synthesis of Ordered Mesoporous Materials

1.1 Mesoporous Silica

1.1.1 Introduction

The first well-studied ordered mesoporous material, a material with 2-50 nm pores in an ordered array,¹ was kanemite ($\text{NaHSi}_2\text{O}_5 \cdot 3\text{H}_2\text{O}$) prepared using ionic surfactants by Yanagisawa *et al.* in 1990.² In 1992, the first ordered mesoporous aluminosilicates were synthesised by Mobil scientists. These were MCM-41 (Mobil Composition of Matter, No. 41), which had a 1D cylindrical pore network in a hexagonal array (space group $p6mm$), and MCM-48 which had a 3D bi-continuous pore structure in a cubic array (space group $Ia3d$).³ These materials had a very high specific surface area ($>1,000 \text{ m}^2\text{g}^{-1}$), as with some nanoparticulate systems, but the regular pore network produced a very high pore volume as well ($0.79 \text{ cm}^3\text{g}^{-1}$ for MCM-41). While ordered mesoporous kanemite involved a complicated synthesis, the relatively simple method used by Kresge *et al.* in the synthesis of the MCM-*n* family of materials allowed for the rapid development of similar materials. The initial mesoporous silicas had pore sizes near the micropore ($<2 \text{ nm}$) range but the development of new mesoporous silicas, as well as manipulation of the reaction conditions (for example, temperature, swelling agents), allowed mesoporous silicas with a wide range of pore-sizes, wall-thicknesses, and pore morphologies to be produced. This allowed for increased applications in the fields of catalyst supports, where catalytic particles were dispersed upon the mesoporous material greatly increasing the surface area available for the reaction in heterogeneous catalysis,⁴ nanocasting, where the porous material was infiltrated by another material and subsequently removed producing a negative replica of the original structure,⁵⁻⁶ drug delivery, for the controlled release of bioactive agents at targeted sites at a specific rate,⁷

adsorbents, optical materials and electrodes for solar cell and fuel cell applications.⁸ One of the most studied ordered mesoporous silicas has been SBA-15.

1.1.2 SBA-15

SBA-15 (University of Santa Barbara Amorphous, No. 15) has 1D cylindrical pores arranged in a hexagonal array ($p6mm$) similar to MCM-41.⁹ These are schematically represented in Figure 1.1.1. An important difference between SBA-15 and MCM-41 is that the cylindrical pores in SBA-15 are interconnected by disordered micropores (≈ 2 nm)¹⁰ that allow for the movement of material between the mesopores. The particles form large hexagonal prisms that can curve along the longitudinal axis. The cylindrical mesopores are typically 5-30 nm in diameter. Large pores are created by increasing the reaction temperature or by incorporating swelling agents, for example, mesitylene.

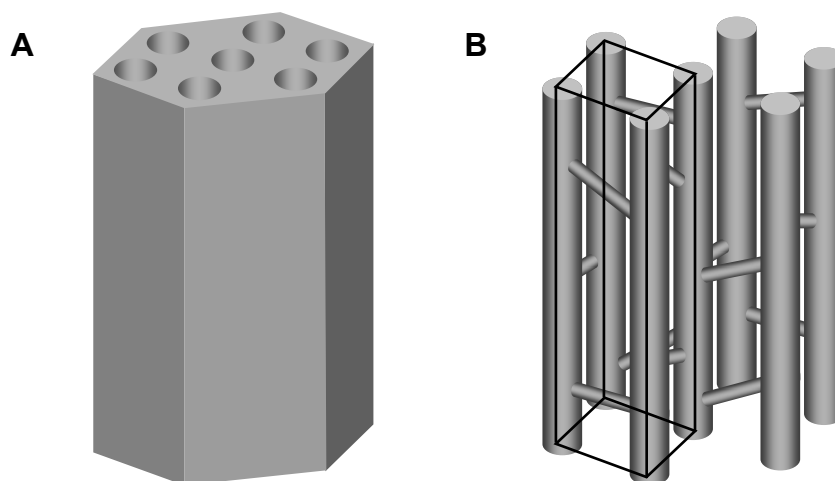


Figure 1.1.1: [A] Schematic model of a hexagonal unit cell of SBA-15; [B] schematic model of the pore network from schematic [A], with reduced unit cell shown.

1.1.3 KIT-6

A well studied 3D ordered mesoporous silica is KIT-6 (Korea Institute of Technology, No. 6).¹¹ KIT-6 has a 3D bi-continuous wormhole pore system arranged in a cubic array similar to MCM-48. The pore network of KIT-6 is schematically represented in Figure 1.1.2. The particles form large masses that are not faceted in any particular fashion. The pores typically have a 4-12 nm diameter. KIT-6 has been used extensively to template other mesoporous materials.

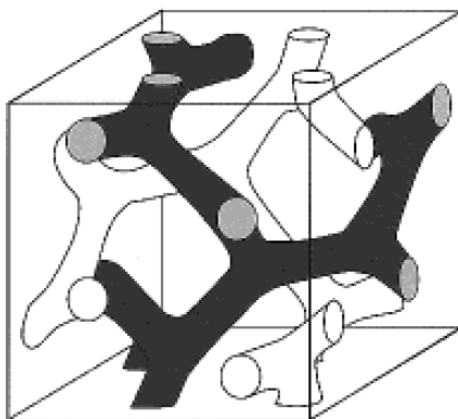


Figure 1.1.2: Schematic model of KIT-6 showing the bi-continuous pore network. The structure is based on various reports but this image was taken from the report by Shin *et al.*¹²

1.1.4 FDU-12

A more regular 3D pore network can be seen in the ordered mesoporous silica FDU-12 (Fudan University, No. 12).¹³ FDU-12 has a face-centred cubic (FCC) 3D cage pore system (space group $Fm-3m$), which is a more regular array of pores than the $Ia3d$ materials. The pore network of FDU-12 is schematically represented in Figure 1.1.3. The particles, as with KIT-6, form large unfaçeted porous masses. The pores are typically 10-12 nm with a narrower pore entrance of 4-9 nm. Large pores are formed by swelling agents, for example, mesitylene. Increasing the temperature of the hydrothermal treatment increases the size of the pore entrances. FDU-12 has been used recently for templating various metal oxide materials.

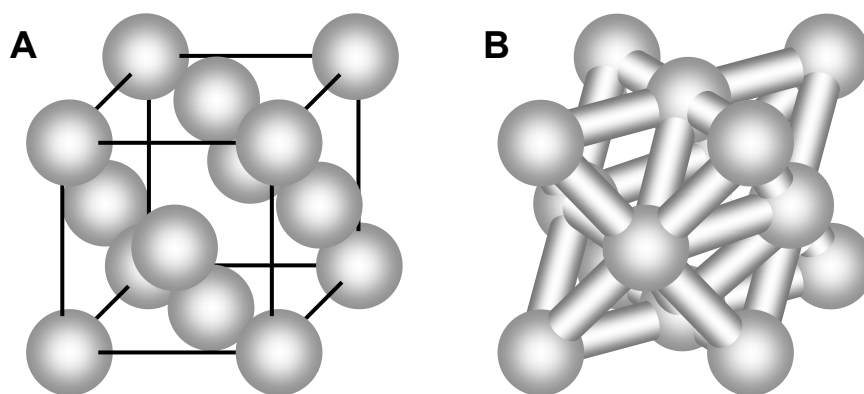


Figure 1.1.3: [A] Schematic model of the FCC arrangement of the pores of FDU-12; [B] FDU-12 with the channels modelled (based on the structure reported by Yue and Zhou⁵).

1.2 Synthetic Methods

There have been various approaches to the synthesis of ordered mesoporous materials. The synthesis of mesoporous kanemite involved a lengthy ion exchange process (stirring of kanemite in alkyltrimethylammonium chloride at 65 °C for 168 h twice). MCM-41 was synthesised by the hydrothermal treatment of hexadecyl-trimethylammonium chloride, tetramethylammonium silicate and alumina in a static autoclave at 150 °C over 48 h. The synthesis of SBA-15, KIT-6 and FDU-12 all involve the hydrolysis of silicate precursors in an acidic solution containing non-ionic polyether surfactants, typically over 48 h at 35-140 °C. While sol-gel remains the most common technique for synthesising mesoporous silica and other materials, hard templating, or nanocasting, is becoming frequently used for synthesising mesoporous materials.

In this investigation, both sol-gel and hard templating (namely the incipient wetness impregnation technique and vacuum impregnation) were investigated for the synthesis of mesoporous materials.

1.2.1 Soft Templating - Sol Gel

The synthesis of mesoporous materials using sol-gel techniques involves the use of structure directing agents (surfactants) in solution, around which a solid is formed. There are two proposed mechanisms in soft templating. First, in the co-operative self assembly pathway the anion (the silicate in the production of mesoporous silica) interacts with the surfactant to form micelles that, in turn, form a liquid crystal upon which the structure of the mesoporous material is based. Second, the true liquid crystal templating pathway in which the surfactant forms a liquid crystal independently of the anion around which the structure of the mesoporous material is based.¹⁴ The micelles can be manipulated to expand the mesopore size by changing the length of the alkyl chain of the surfactant, by introducing auxiliary organic molecules such as aromatics, n-alkanes or fatty acids,⁴ or by combining different surfactants.¹⁵ Altering the synthesis temperature also has an effect on the size of the surfactant micelles.

The surfactants are typically one of two types - ionic or non-ionic. Ionic surfactants are usually tetralkyl ammonium salts or aryl sulfates while non ionic salts are typically from the polyether family, for example, the block co-polymer $\text{EO}_n\text{PO}_n\text{EO}_n$, where EO is $(\text{CH}_2\text{CH}_2\text{O})$ and PO is $(\text{CH}_2\text{CH}_2\text{CH}_2\text{O})$. These are known by the trade name, Pluronics[®]. When ionic surfactants are used, the interactions between the surfactant and the precursor molecules are ionic, whereas when using non-ionic surfactants the interactions primarily involve hydrogen bonding. Their weaker interactions mean that non-ionic surfactants can be removed by

solvent-extraction (using ethanol or acid) in high yields (>90%) which has economic and environmental benefits over ionic surfactants.¹⁶ The alternative to solvent extraction is for the organic surfactant to be removed by calcining in air at moderate temperatures (at least 300 °C depending on the material stability).

Sol-gel syntheses can produce ordered mesoporous materials in very high yields, but they are dependant on the availability of suitable precursor reactants to undergo reaction, for example, hydrolysis, precipitation or agglomeration, to form the desired structure around the surfactant matrix. For the synthesis of ordered mesoporous silica, tetraethyl orthosilicate or sodium silicate both hydrolyse well in acidic media to produce high yields of well ordered product. Not all elements have such well studied sol-gel chemistry, however, and the solubility in the pH of the reactive media must also be taken into consideration. Despite this, sol-gel techniques have been utilised to produce well ordered SiO₂, WO₃, SnO₂, HfO₂, SiTiO₄, Al₂TiO₅, ZrTiO₄, ZrW₂O₅,¹⁷ ZrO₂, Al₂O₃, Nb₂O₅, Ta₂O₅, Al₂O₃-SiO₂,¹⁷⁻¹⁸ 4ZrO₂-P₂O₅, Li₂O-2TiO₂, CaO-TiO₂, NiO-TiO₂, YbO-2TiO₂ and Li₂O-2ZrO₂,¹⁸ TiO₂,¹⁷⁻¹⁹ TiO₂-SiO₂,¹⁹ Zr_xCe_{1-x}O_{2-δ},²⁰ and Zr_{0.84}Y_{0.16}O_{2-δ}.²¹ These materials typically had thin (4-6 nm) amorphous or nanocrystalline pore walls with small (5-8 nm) mesopores. The specific surface areas and pore volumes were high (120-200 m²g⁻¹ and 0.43-0.55 cm³g⁻¹, respectively) for dense materials, indicating good product yields. Mesoporous carbon has also been produced using sol-gel methods recently, but the pores are typically small (2-7.4 nm).²²⁻²⁴

1.2.2 Hard Templating - Nanocasting

Nanocasting involves taking an already formed ordered mesoporous material, typically silica or carbon due to the high quality of these materials (polymer beads have also been used), and then using this as a mould for a new material. Nanocasting employs a new range of synthetic conditions that has allowed for a new range of materials to be synthesised. The product must be resistant to the conditions under which the template is removed. This is typically digestion by either hot NaOH or HF for mesoporous silica and oxidation in air for mesoporous carbon. While this still limits the scope of potential products, the range of potential products has increased beyond those materials that can be synthesised by sol-gel methods alone. Additionally, increased calcination temperatures can be achieved without significant loss of structural ordering allowing for crystalline ordering of the pore walls rather than the amorphous or nanocrystalline pore walls that are often produced using sol-gel methods. This produces porous single crystals.⁵ This also allows for the possibility of different crystal phases of the same composition. For example, yttria-stabilised zirconia (YSZ) changes phases from tetragonal to cubic at elevated temperatures. The limiting

temperature is the temperature at which the reactant or product begins to react with the template, the product melting, boiling, sublimation or decomposition temperature or sintering of the materials causes loss of the porous structure.

There have been five principal methods reported in the literature for nanocasting mesoporous materials (here the nomenclature adopted in the review by Yue and Zhou is used for continuity as the nomenclature varies between articles):⁵ the evaporation method, the surface modification method, the dual solvent method, the one-step nanocasting method and the solid-liquid method. The evaporation method is a simple method used widely involving the addition of a metal nitrate precursor in ethanol to the mesoporous template. The precursor moves into the template through capillary action and then the solvent evaporates leaving the solute inside the template. This method is also commonly called the incipient wetness impregnation technique (IWIT). The surface modification method involves modification of the pore walls of the silica, for example, aminosilylation, to form a functionalised surface on the template. The precursor is specifically selected to bond to the functionalised template to anchor to the modified pore wall for increased template-precursor bonding. The dual solvent method involves the mixture of two solutions, one containing the template, the other the precursor. The impregnating material is expected to move into the pores during stirring. The one-step nanocasting method involves the addition of metal precursors to the synthesis of mesoporous silica. During calcination it is proposed that the metal atoms form nanoparticles, and ultimately agglomerate to form mesoporous particles that can exist independently upon removal of the silica template.²⁵ The solid-liquid method involves the careful selection of a precursor material with a melting point below the temperature at which it decomposes to its oxide. This is ground with the mesoporous template and then calcined. In its liquid phase or phases if there are liquid phases involving the water of hydration, the precursor moves into the template via capillary action.²⁶ A non-exhaustive search of the literature can find numerous reports in which nanocasting has been used to produce a variety of ordered mesoporous materials using mesoporous silica as the template. These include mesoporous carbon (see Section 1.3.2 where mesoporous carbons are discussed in more detail), Cr_2O_3 ,²⁶⁻³¹ Co_3O_4 ,^{26, 29-34} In_2O_3 ,^{25, 30-31, 34} MnO_x ,^{30-31, 35-37} NiO ,^{26, 30-31, 38} Fe_2O_3 ,^{30-31, 39} CeO_2 ,^{26, 30-31, 40-41} WO_3 ⁴¹⁻⁴² and ZrO_2 .⁴³ Mesoporous carbon has also been used as a template to produce mesoporous SiO_2 ,⁴⁴⁻⁴⁵ CeO_2 ,⁴⁶ ZnO ⁴⁷ and MgO .⁴⁸⁻⁴⁹ This is known as double replication which results in the same pore structure as the original silica template, rather than the inverted pore structure (in the case of the experiment with SiO_2 this seemed to be redundant, but it proved the concept of double replication).

The materials that were investigated as candidates for ordered mesoporous materials in this investigation were CeO_2 , $\text{Ce}_{0.9}\text{Gd}_{0.1}\text{O}_{2-\delta}$ (CGO), carbon, $\text{Zr}_{1-x}\text{Y}_x\text{O}_{2-\delta}$ (yttria-stabilised zirconia; YSZ), $\text{La}_{0.85}\text{Sr}_{0.15}\text{GaO}_{3-\delta}$ (lanthanum strontium gallate; LSG), and $\text{La}_{0.85}\text{Sr}_{0.15}\text{CoO}_{3-\delta}$ (lanthanum strontium cobaltite; LSC). These materials will be discussed further in the remainder of this chapter.

1.3 Materials

1.3.1 Ceria

Ceria is the oxide of the rare earth metal cerium, the most abundant of the rare earth metals. Ceria is used widely industrially to decolourise glass (as well as for ultra-violet radiation absorption), for increasing the photostability of polymers and pigments, as an opacifier in ceramics (due to its high refractive index), as a protective coating for metals, for polishing glass, as an additive for self-cleaning applications such as oven linings, as a key component in automotive three-way catalysts, as well as in many other industrial catalysts, and is receiving increasing attention for applications in new technologies such as intermediate temperature solid oxide fuel cells (SOFCs) and photovoltaics.⁵⁰ These applications spawn from the stability and conductivity, both electronic and ionic, of ceria as well as the ease by which ceria can be blended with other compounds to form complex oxides that combine the properties of the materials, for example, $\text{Ce}_x\text{Gd}_{1-x}\text{O}_{2-\delta}$, $\text{Ce}_x\text{Sm}_{1-x}\text{O}_{2-\delta}$ and $\text{Zr}_x\text{Ce}_{1-x}\text{O}_{2-\delta}$. Ceria is also of low toxicity, and its low solubility means that it cannot be absorbed into the body easily. It is only toxic when administered intravenously.

Ceria forms cubic crystals with the fluorite ($Fm\bar{3}m$) structure in which each Ce atom is coordinated to 8 oxygen atoms (Figure 1.3.1).

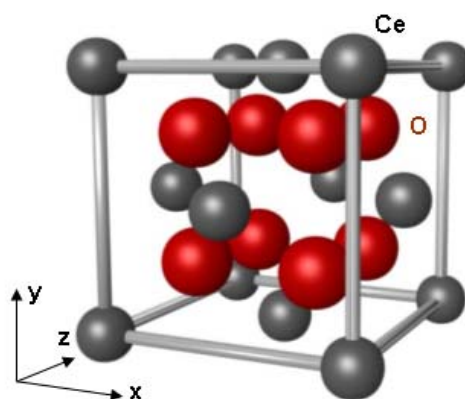
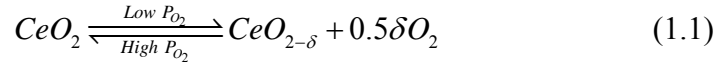


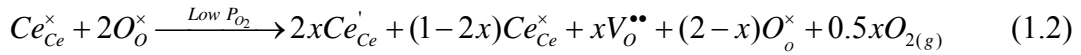
Figure 1.3.1: Schematic unit cell of ceria showing the fluorite structure.

1.3.1.1 Oxygen Storage Capacity and Oxygen Ion Conductivity

Cerium commonly exists as cerium metal (which spontaneously oxidises), cerium (III) and cerium (IV). Ce_2O_3 also spontaneously oxidises in air to form CeO_2 at room temperature ($\Delta H^\circ = -191 \text{ kJmol}^{-1}$ and $\Delta G^\circ = -172 \text{ kJmol}^{-1}$).⁵¹ This variable oxidation state allows for ceria to form an equilibrium with the gas phase dependant on the oxygen partial pressure as shown in equation 1.1:



When considering unit cells the expression is better expressed in Kröger Vink notation as in equation 1.2:



This shows that at low P_{O_2} oxygen ion vacancies are formed. This is a separate mechanism than the formation of intrinsic defects (interstitial ions), which increase in concentration with temperature. The variable oxygen state of ceria is the basis of its oxygen storage capacity, and three-way catalysis, where ceria absorbs oxygen in high P_{O_2} conditions and oxidises reactants under reducing conditions. Oxygen vacancies can also be introduced into the ceria matrix by aliovalent doping as shown in Equation 1.3 and Figure 1.3.2.

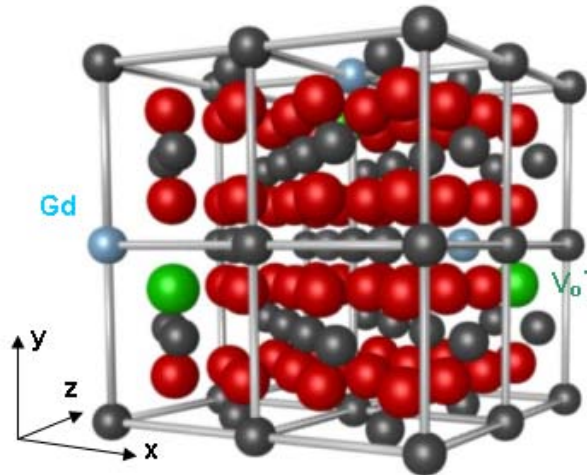
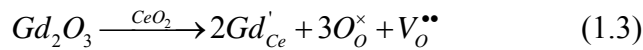


Figure 1.3.2: Schematic unit cell of $Ce_{0.9}Gd_{0.1}O_{2-\delta}$ showing oxygen vacancies in the fluorite structure.

When oxygen vacancies are present, generated either intrinsically or extrinsically by reducing the sample or doping, neighbouring oxygen ions are able to migrate to vacant sites. This is the basis of oxygen ion conduction. This has two principal effects. Firstly, oxygen ions from the centre of the material can be conducted to the surface to oxidise reactants in an oxidation experiment allowing for the entire material, rather than just the surface, to become reduced. Secondly, if there is an oxygen partial pressure differential between two sides of the material then the system will attempt to reach equilibrium (Figure 1.3.3) via the net flux of O^{2-} ions through the material.

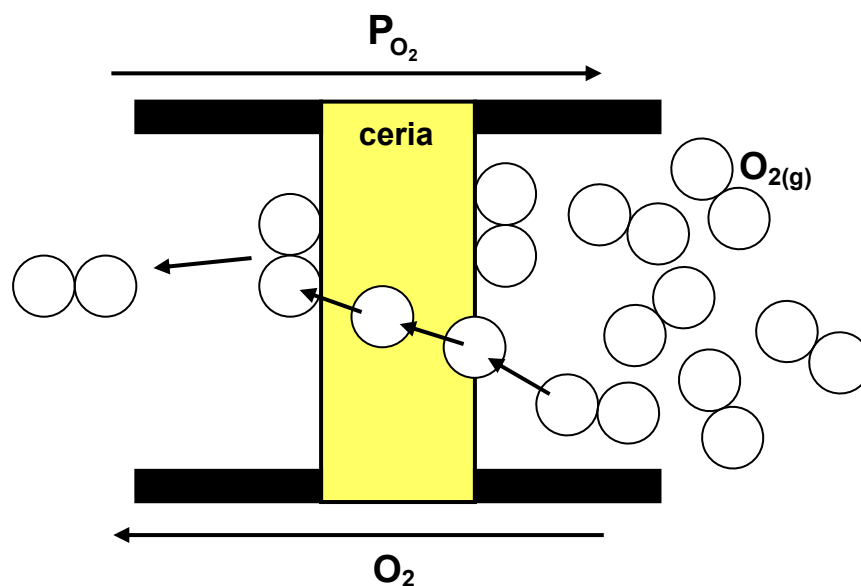


Figure 1.3.3: Schematic diagram showing how oxide ions are transported across a ceria membrane to equilibrate P_{O_2} .

At the high P_{O_2} interface dioxygen would tend to be reduced to form oxide ions, and at the low P_{O_2} interface the oxide ions would tend to be oxidised to form oxygen producing a cathode and an anode, respectively. If a porous electrical conductor is attached to each interface and a circuit is made then an oxygen sensor results (as used in automotive exhausts). By applying a potential an oxygen pump is formed. At high enough temperature the conductivity is sufficient that doped ceria is a potential candidate for the electrolyte material in an intermediate temperature SOFC. At the anode the oxide ions react with the fuel gas (e.g. hydrogen, methanol, methane), while at the cathode the dioxygen is reduced to equilibrate the low P_{O_2} at the anode (see Section 2.4). CGO has a relatively high ionic conductivity as shown in Figure 1.3.4.

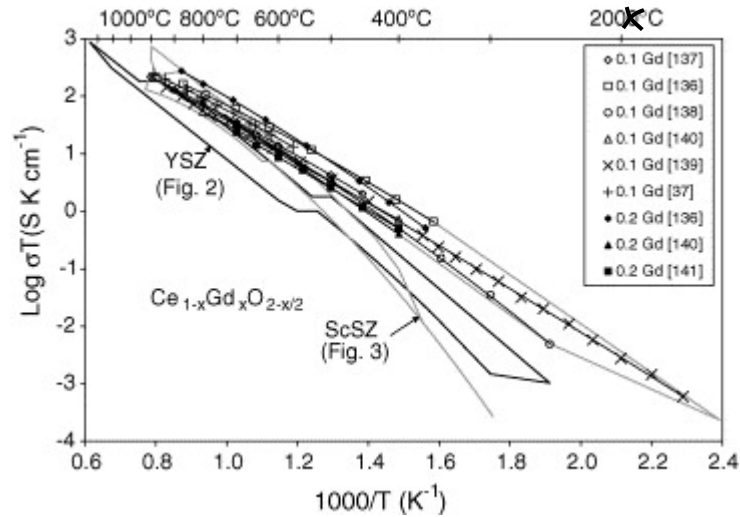
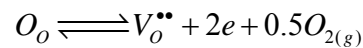


Figure 1.3.4: Graph showing the oxygen ion conductivity of CGO, compiled by Fergus⁵² based on reported conductivities.⁵³⁻⁵⁹ Note: the YSZ conductivities are expanded in Figure 1.3.5A. ScSZ is Sc₂O₃ stabilised zirconia.

The oxygen storage capacity and oxygen transport properties also make ceria a very attractive catalyst for oxidation reactions.

1.3.1.2 Electronic Conductivity

Ceria exhibits mixed conductivity meaning that, in addition to its ionic conductivity, it also conducts electrons through a semiconducting mechanism. The electronic conductivity of ceria is dependant on temperature, P_{O_2} , purity and/or dopant concentrations. At high temperatures and low P_{O_2} ceria is an n -type semiconductor where electrons are liberated following the reduction of the primary charge carrier:



The electrons themselves travel through the material through a small-polaron mechanism (electrons hop between cerium atoms, $Ce^{3+} \longrightarrow Ce^{4+} + e$, rather than by a band model), severely limiting the mobility of the electrons.⁶⁰⁻⁶¹ The mixed conductivity of ceria, while useful for some applications, for example, SOFC anode materials, is detrimental for others, such as SOFC electrolytes, as it could cause the system to short circuit.

1.3.1.3 Previous Literature Investigations into Ordered Mesoporous Ceria

Mesoporous ceria has been reported using both cooperative self-assembly and nanocasting. The earliest investigations showed that using cooperative self-assembly dramatically

increased the specific surface area (up to $200 \text{ m}^2\text{g}^{-1}$) relative to pyrolysis or precipitation methods, yet the products were nanoparticulate without long-range order.⁶²⁻⁶⁴ The products were thermally unstable which was attributed to the lack of grain growth at the low synthesis temperatures. Further investigations using the cooperative self-assembly method have been conducted with similar results.⁶⁵⁻⁸⁰ Generally high specific surface areas and pore volumes were reported ($100\text{-}300 \text{ m}^2\text{g}^{-1}$ and $0.12\text{-}0.42$, respectively). The general conclusion that can be drawn from these reports is that when using ionic surfactants order could not be achieved, but using block co-polymers ordered mesoporous ceria could be produced. Various investigations did, however, show that high specific surface area ceria had improved properties compared to traditionally prepared ceria as oxidation catalysts,^{62, 65-67, 80} photovoltaics,⁷⁴ and that they had an improved oxygen storage capacity.⁶² The results of nanocasting ceria on silica,^{30, 40-41, 81-82} carbon,⁴⁶ and polymethylmethacrylate bead templates⁸³ have been more successful. While the specific surface areas and pore volumes were typically lower ($110\text{-}200 \text{ m}^2\text{g}^{-1}$ and $0.18\text{-}0.42 \text{ cm}^3\text{g}^{-1}$, respectively) electron microscope images showed that the material is truly ordered over a wide range. The physisorption results, electron micrographs, small angle X-ray patterns (and private correspondence)⁸⁴⁻⁸⁵ suggest that the overall yields were low compared to some of the materials listed in Section 1.2.2 (for example, TiO_2 , Nb_2O_5 , Ta_2O_5 , SnO_2). Nanocast ceria was shown to be a more active oxidation catalyst than disordered ceria (prepared, for example, by the thermal decomposition of cerium nitrate).^{46, 81}

CGO was also prepared very recently (2008) by nanocasting mesoporous silica.⁸⁶

1.3.2 Mesoporous Carbon

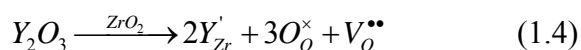
Since the discovery of buckminsterfullerene and carbon nanotubes,⁸⁷⁻⁸⁸ nanostructured carbon has received much attention. Mesoporous carbon has a wide range of potential applications as catalyst supports, separation media, in advanced electronic media in supercapacitors and in battery and low-temperature fuel cell electrodes. Mesoporous carbon has high electrical and thermal conductivity, chemical stability (corrosion resistance and thermal stability though not in humid, oxidising conditions above 100°C), a low density, high specific surface area and high pore volume. It has been shown that by moving from carbon black to materials with larger, more ordered pores, with increasing crystallinity, the conductivity of carbon nanomaterials is increased, for example, in nanotubes, nanohorns, nanocoils, nanofibres and ordered mesoporous carbon.⁸⁹

Ordered mesoporous carbon has been synthesised by both nanocasting, based on silica, and soft-templating using surfactants.²²⁻²⁴ The first reports of nanocasting to produce a direct

replica of the silica, was using SBA-15 to produce CMK-3.⁹⁰ CMK-1 had been synthesised previously, based on MCM-48, but a structural transformation occurred upon removal of the silica template meaning the ordered mesoporous carbon was not a replica of the original template.⁶ The general method is simple and involves impregnating the silica template with a carbonaceous precursor (e.g. sucrose, furfuryl alcohol, polymer resin) which is then catalytically carbonised using sulphuric acid, followed by annealing under an inert atmosphere. After digesting the silica using NaOH an ordered mesoporous carbon is produced having the negative structure of the original silica template. Since 1999 this method has been applied to various silica templates to produce many CMK-*n* materials. These materials have been applied to some technological applications to date and have shown that ordered mesoporous carbons increased the mass transport of reactants and products in low-temperature fuel cells⁹¹⁻⁹² and are effective templating agents (noted in Section 1.2.2). It has been shown that it is possible to produce ordered mesoporous carbon with crystalline (graphite) pore walls by using a physical vapour deposition synthesis⁹¹ or by annealing the as-prepared mesoporous carbon at temperatures above 2300 °C in Ar for 0.5 h, though the latter resulted in approximately a 70 % loss of specific surface area, 60 % loss in pore volume and extensive broadening of the small-angle X-ray peak indicating that long-range order had been significantly degraded.⁹³ An ordered mesoporous carbon is attractive for its favourable electronic properties with respect to amorphous carbon.

1.3.3 Yttria-stabilised Zirconia

YSZ ceramics are prepared by the addition of yttria (Y₂O₃) to zirconia (ZrO₂) in order to stabilise unstable crystal phases at room temperature. At room temperature pure zirconia exists as monoclinic crystals that go through phase transformations to tetragonal and cubic phases with increasing temperature. On addition of 8 mol% yttria it can be stabilised in the cubic fluorite structure (discussed in Section 1.3.1), even when subsequently lowered to room temperature. Below a concentration of 8 mol% yttria, different combinations of cubic, tetragonal and monoclinic ZrO₂-Y₂O₃ solid solutions exist depending on the molar ratio of zirconia and yttria. This aliovalent doping of Y³⁺ to ZrO₂ creates oxygen ion vacancies similar to Gd₂O₃ in CGO (Equation 1.4).



The creation of these oxygen vacancies allows for oxygen ion conductivity. YSZ has been well studied as a SOFC electrolyte material, as well as for porous SOFC anodes. The

oxygen ion conductivity peaks at 8 mol% yttria as studied in various investigations and collated in Figure 1.3.5.

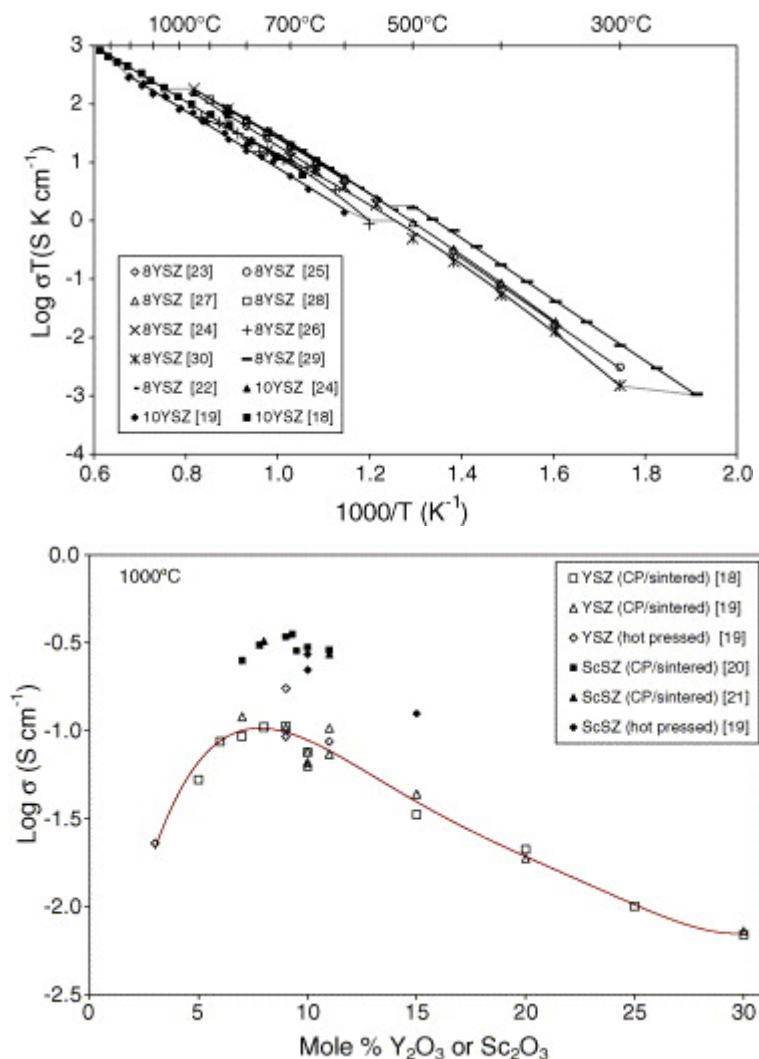


Figure 1.3.5: Graphs showing [A] the oxygen ion conductivity of YSZ and [B] the effect of dopant concentration on conductivity at 1000 °C complied by Fergus⁵² based on reported conductivities.⁹⁴⁻¹⁰⁴

There are limited reports in the literature for the synthesis of ordered mesoporous YSZ.^{21, 105-107} All reports have used soft-templating to produce YSZ with the fluorite structure using temperatures as low as 500 °C. The pore walls were composed of 4-5 nm nanoparticles. To the author's knowledge, there have been no reports of ordered mesoporous YSZ using nanocasting. ZrO_2 has been produced by this method, but significant levels of silica were detected after the removal of the SBA-15 template.⁴³ The zirconia-silica phase diagram (Figure 1.3.6) shows how zirconia may react with a silica template at these calcination temperatures, and therefore using mesoporous carbon to template YSZ may be required to circumvent this problem.

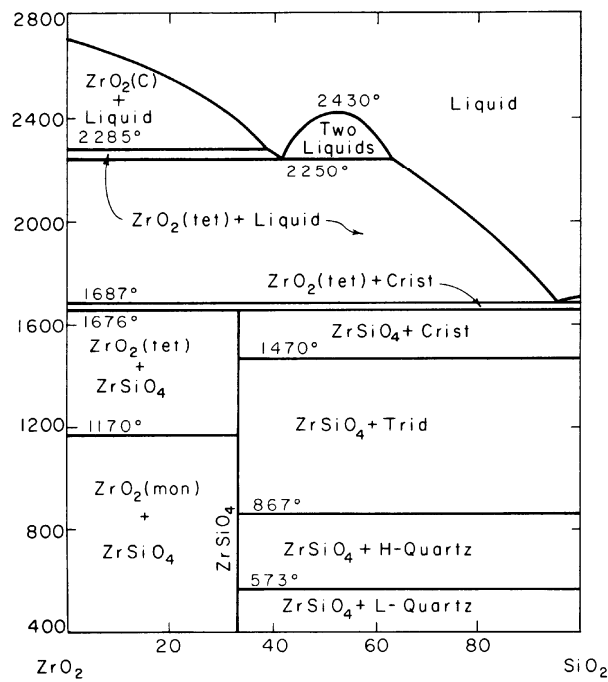


Figure 1.3.6: Phase diagram for the ZrO_2 - SiO_2 system.¹⁰⁸

1.3.4 Lanthanum-based Perovskite Materials

The other commonly investigated materials for SOFC applications are based on the perovskite ($Pm3m$) system, LaGaO_3 . Perovskite materials are based on the ABO_3 system where A^{2+} is typically a large cation coordinated to 12 oxygen ions and B^{2+} is a smaller cation coordinated to 6 oxygen ions as shown in Figure 1.3.7.¹⁰⁹ Altering the sizes of the cations can cause tetragonal or orthorhombic phases. In Figure 1.3.7 the relative sizes of the ions are represented for La in the A site, and Ga in the B site.

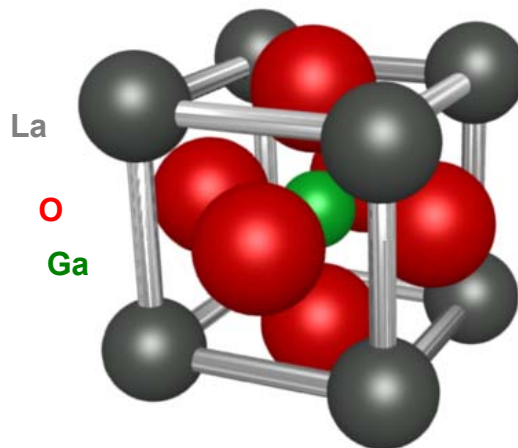
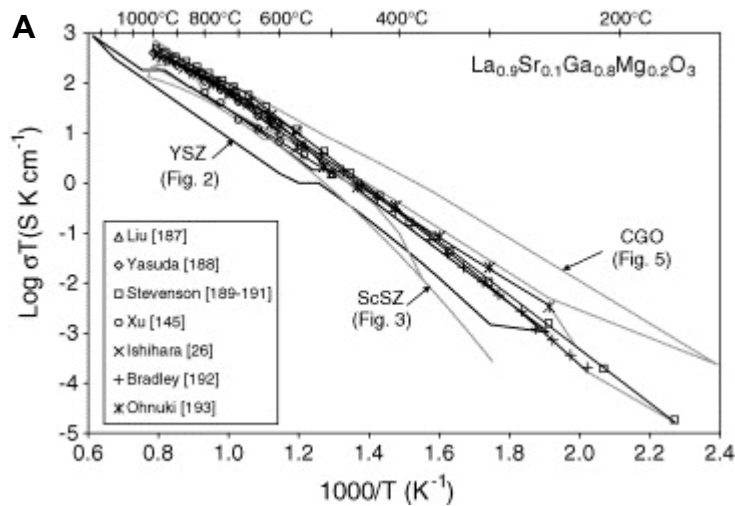


Figure 1.3.7: Schematic unit cell of LaGaO_3 showing the perovskite structure.

1.3.4.1 Strontium Doped Lanthanum Gallium Oxide

LaGaO_3 is typically doped with Sr and Mg to increase its conductivity. This produces lanthanum strontium gallate (LSG) and lanthanum strontium gallium magnesite ($\text{La}_{1-x}\text{Sr}_x\text{Ga}_y\text{Mg}_{1-y}\text{O}_{2-\delta}$, LSGM). Other potential dopants are the subject of ongoing investigations. The conductivities from literature results are presented in Figure 1.3.8 where it was shown that LSGM materials have a higher conductivity than YSZ and an equivalent conductivity to CGO. The conductivity of LSGM and CGO at 800 °C can be seen to be equivalent to YSZ at 1000 °C. LSG has no easily reducible elements and therefore it does not become electronically conducting in a reducing atmosphere, for example, at the anode of a SOFC.⁵² Nickel can be added to porous LSG to create a cermet which is a mixed conductor for SOFC anode applications,¹¹⁰⁻¹¹¹ though other metals would be preferable. An M-LSG electrode attached to a LSG electrolyte would be preferable, to maintain chemical and thermal stability between the electrode and the electrolyte. It has been reported that using Ni-containing cermet anodes on LSGM electrolytes causes a new boundary phase to form (LaNiO_3 or La_2NiO_4) which has a lower conductivity than either the electrolyte or electrode, decreasing the overall conductivity of the SOFC.¹¹²



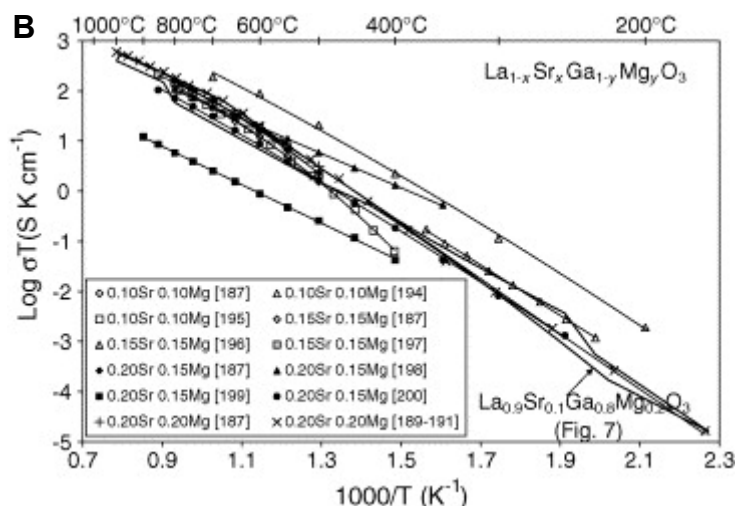


Figure 1.3.8: Graphs showing the oxygen ion conductivity of LSG-based materials: [A] compared to other SOFC materials including CGO and YSZ; [B] effect of dopant concentration on the conductivity of LSGM. Compiled by Fergus⁵² based on reported conductivities.^{100, 113-126}

To date, to the author's knowledge, there have been no reports of ordered porous LSG or LSGM materials.

1.3.4.2 Strontium-doped Lanthanum Cobalt Oxide

The other commonly studied perovskite materials for SOFC applications are based on doped lanthanum manganite, chromite and cobaltite. Lanthanum strontium cobaltite ($\text{La}_{1-x}\text{Sr}_x\text{CoO}_{3-\delta}$) was elected for investigation as, in the first instance, lanthanum strontium cobaltite appeared to have soluble, non-volatile, readily available and relatively cheap precursors to experiment with.

Lanthanum strontium cobaltite (termed LSC in this thesis), has been shown to have high oxygen ion conductivity and high chemical resistance making it a potential electrode material for SOFCs.¹²⁷⁻¹²⁸ Other dopants have been investigated to enhance conductivity of LSC,¹²⁹ but as yet LSC has not attracted as much attention as the aforementioned materials. It should be noted that cobalt is widely considered toxic and can have health implications, although case studies have shown that cobalt is removed from the body after the source is identified (unlike, for example, lead), as cobalt is an essential element for the production of vitamin B₁₂.¹³⁰

To date, to the author's knowledge, there have been no reports of ordered porous LSC or doped LSC materials.

Chapter 2

An Overview of Technological Applications for Ordered Mesoporous Materials

2.1 Introduction

In this chapter the key technologies that are mentioned throughout this thesis are discussed with emphasis on the components to which ordered mesoporous materials could be applied. This cannot be an exhaustive commentary on the development of these technologies as, while in this investigation the properties of materials were investigated with these applications in mind, not all parameters have been investigated sufficiently to determine the suitability of the prepared ordered mesoporous materials for their implementation in these technologies.

2.2 Nanocasting

As mentioned in Section 1.2.2, nanocasting has the potential for producing ordered mesoporous materials with crystalline pore walls. The adaptation of this process in order to produce ordered mesoporous materials would be of great technological interest. It has been stated that ‘the present synthesis technique is suitable for the production of carbon molecular sieves in a large industrial scale’,⁶ and therefore any improvements to this method for increasing the yield, manipulating the morphology, simplifying the process and decreasing the production with a view to decreasing the cost, would only improve the economic viability for the large-scale application of ordered mesoporous materials in existing or new devices. The method discussed most in this thesis is based on the industrial process of vacuum impregnation (VI).

2.2.1 Vacuum Impregnation

VI is an industrial technique, widely used since the 1950s, by which porosity in materials is replaced by a second material. In metallurgy, VI has the effect of restoring pressure tightness to leaking parts, preventing corrosion by trapped material in pores and between joints in joined materials, sealing brazed assemblies that cannot be brazed again (brazing is a process where two components are joined by having the space between them filled by a molten alloy via capillary action), improving the bonding between materials and sealing the surface of materials prior to finishing.¹³¹ VI is widely used in automotive, aerospace, naval, military, pneumatic, hydraulic, filtration and fuel supply systems.¹³¹⁻¹³² VI is also used in fruit and vegetable processing to exchange inherent gases with external fluids.¹³³ In both situations, the solid is immersed in a liquid and then the pressure above the liquid is reduced to 'vacuum'. This causes the inherent gasses to diffuse into the liquid before being pumped away. Once the system is returned to atmospheric pressure the liquid enters the vacated pores. When the material is removed from the liquid, excess liquid can be removed, and, if desired, the liquid is cured by ageing or thermal processes. A schematic for VI is shown in Figure 2.2.1.

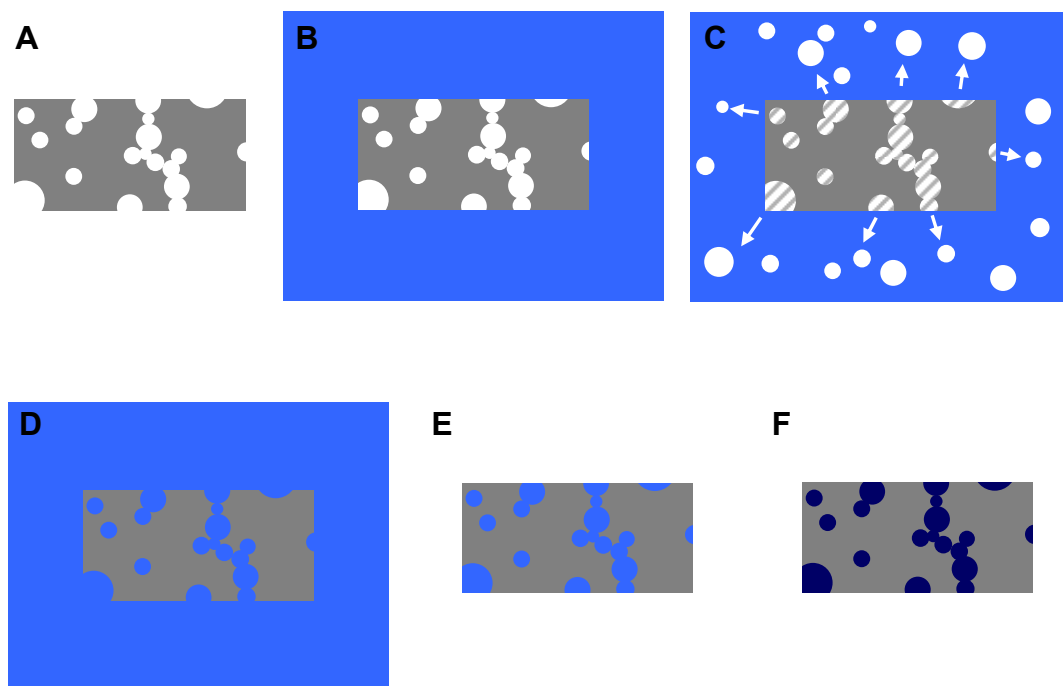


Figure 2.2.1: Schematic for VI processing of [A] a porous particle; [B] the particle is immersed in the impregnating liquid; [C] the pressure is lowered causing the gases in the pores to migrate out of the pores; [D] Once the system is returned to atmospheric pressure, or even increased beyond atmospheric pressure, the liquid moves into the pores; [E] the material, with impregnated pores, is removed from the liquid; [F] a final curing process causes the liquid to solidify, if required, to enhance the material properties.

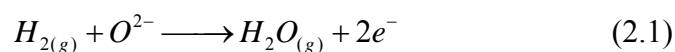
2.3 Heterogeneous Catalysis

Heterogeneous catalysts employ a catalyst that is in a different phase to the reactant (solid, gas, liquid, immiscible liquids). The reaction occurs on the surface of the catalyst. There are five primary processes which control the reaction: diffusion of reactants to the catalytic reaction site, adsorption onto the surface, the reaction, desorption of the products and diffusion of the products away from the reaction site. The reactants must diffuse towards the catalytic site and the products away from the site where the reaction took place. This is often the rate limiting step. If the catalytic site has a narrow entrance with fast reaction kinetics then the reaction can only occur when reactants diffuse past the products. The attractive force of both the reactant and product to the catalyst are pivotal. Products that bind too strongly would deactivate the catalyst. The adsorbed species themselves are highly mobile activated species. Finally, the concentration of active catalytic sites will affect the rate of the reaction.

Ordered porous materials have received much attention for their application in heterogeneous catalysis. They represent an opportunity to move towards environmentally friendly catalysis (compared to, for example, liquid acid catalysts). Most research to date has been on microporous solids (e.g. zeolites) in chemical processing, though there has been some work on increasing the pore sizes. When heterogeneous reactions involve larger molecules, or are diffusion-limited, mesoporous materials could assist in increasing the rate of the diffusion of reactants and products in the reaction.¹³⁴ Often mesoporous silica is used as a catalyst support for the impregnation of catalytic sites. For example, oxidation using Pt¹³⁵ or Au,¹³⁶ hydrogenation using Pt,¹³⁷ Ni,¹³⁸ Ru/Cu,¹³⁹ Ru/Pt, Pd/Ru, Ru/Sn or Cu/Ru,¹⁴⁰ carbon-carbon bond formation using Pd (Heck reaction),¹⁴¹⁻¹⁴² water-gas shift using Pt,¹⁴³ and Fischer-Tropsch reactions with Co¹⁴⁴ or Co/Ru.¹⁴⁵ In these materials metal nanoparticles act as the catalysts and are finely dispersed in the mesoporous silica creating a material which has easily accessible sites for gaseous reactants. The silica template itself does not offer functionality unless it is doped, for example, to add stability to the catalyst. Adding functionality to the template could improve the heterogeneous catalyst further, for example, by synthesising a mesoporous template from a catalytically active material (e.g. ceria, CGO, YSZ). Metal nanoparticles could still be impregnated as above to increase the reaction rate, except as the catalyst support could contribute to the reaction the surface area for the reaction would be increased. An ideal application for a heterogeneous ordered mesoporous catalyst would be in SOFC electrodes.

2.4 Fuel Cells

Fuel cells are electrochemical reactors, similar to batteries, except the fuel and oxidant are continuously supplied. Fuel cells have several advantages for energy conversion over competing technologies in that they have a high efficiency, have low emissions, are relatively simple and do not have moving parts. In this thesis, oxide materials with the potential for applications as solid oxide fuel cell (SOFC) electrode materials were investigated, and therefore only the SOFC will be discussed in detail here (though as mentioned in Section 1.3.2 mesoporous carbon is under development for use as an electrode material in low-temperature fuel cells). As mentioned in Section 1.3.1.1, fuel cells oxidise a fuel at the anode where electrons are also produced (Equation 2.1).



The electrons travel through an external circuit to the cathode where they reduce oxygen to form oxide ions (Equation 2.2).



The oxide ions travel through the electrolyte (typically YSZ, CGO or LSG based), which itself must be electronically insulating in order for a current to be generated in the external circuit. The anode material is typically the same as the electrolyte with dispersed metal species that act as both a catalyst for the oxidation reaction and as an electrical conductor. This creates a ‘three-phase boundary’ where the reaction occurs only at sites where the reaction gas, metal catalyst and oxide ion conductor are in contact. Porous anode materials are used to increase the total surface area of the three phase boundary. A SOFC system is schematically represented in Figure 2.4.1.

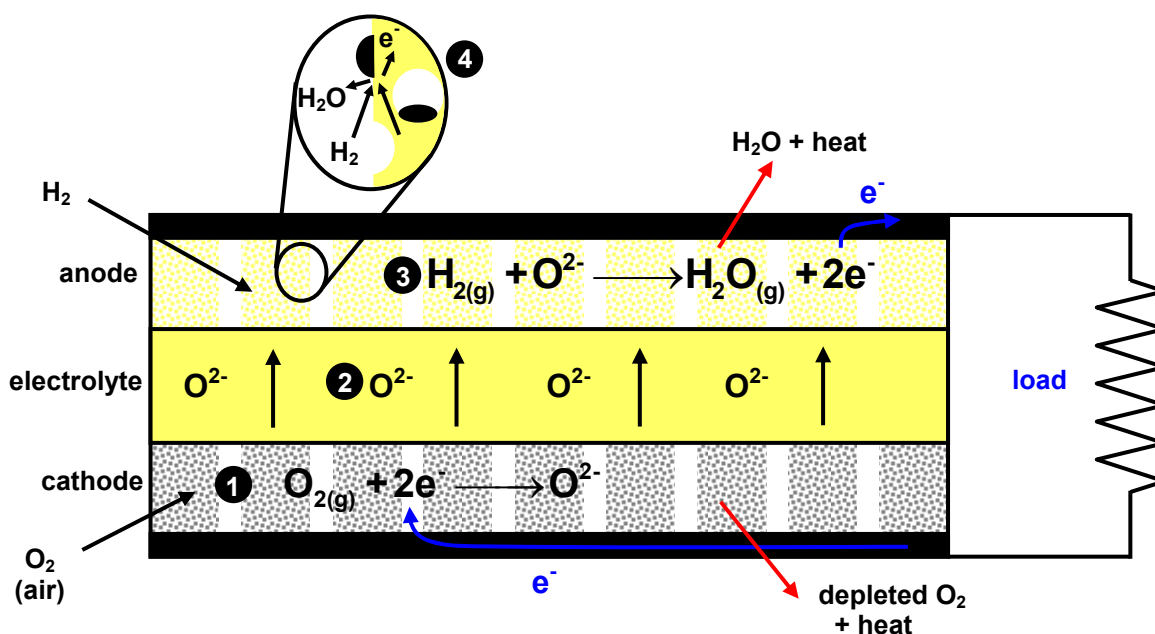


Figure 2.4.1: Schematic diagram for a SOFC: [1] oxygen is reduced at the three phase boundary at the porous cathode; [2] oxide ions are conducted through the electrolyte into the porous anode; [3] the oxide ions reduce the fuel gas at the three phase boundary (enlarged at [4]), producing electrons. The electrons are conducted through the external circuit back to the cathode generating a current.

The requirements of a SOFC electrode are a high electrical conductivity, fast charge transfer kinetics, stability in the respective environment (oxidising at the cathode and reducing at the anode) and chemical, mechanical and structural stability with the electrolyte and interconnect materials.⁵² For these reasons it is of interest to prepare electrode materials from a similar composition to the electrolyte where possible. In SOFCs with YSZ electrolytes, Ni-YSZ cermets are often used as the anode, and $La_xSr_{1-x}MnO_{3-\delta}$ (LSM) as the cathode (though LSM and YSZ do react under operating conditions). SOFCs with CGO electrolytes could use Ni-CGO as the anode (the electronic conductivity of pure CGO under reducing conditions and at intermediate temperatures is still low).¹⁴⁶ CGO also oxidises deposited carbon at moderate temperatures. Deposited carbon is a significant contributor to anode deactivation when using hydrocarbon fuels. By preparing electrode materials from the same material as the electrolyte the issues relating to the chemical and mechanical stability (differences in thermal expansion of materials) can be avoided. Developing anode materials with ordered mesopores would allow for a massive increase in the surface area of the three phase boundary increasing the reaction rate, while the increased pore volume would increase the diffusion of reactants to, and products away from, active catalytic sites.

2.5 Dye-Sensitised Solar Cells - Bulk Heterojunctions

Photovoltaic (PV) systems convert energy from light to electricity and systems based on silicon have been commercially available since the 1970s. In this thesis, only applications for organic dye-sensitised solar cells were investigated and therefore the other types of photovoltaic systems will not be discussed. Dye-sensitised solar cells are one type of thin-film PV technology, termed ‘second generation’, that has been developed in an attempt to decrease production costs associated with first generation solar cells which were based on single junction silicon cells (Figure 2.5.1).

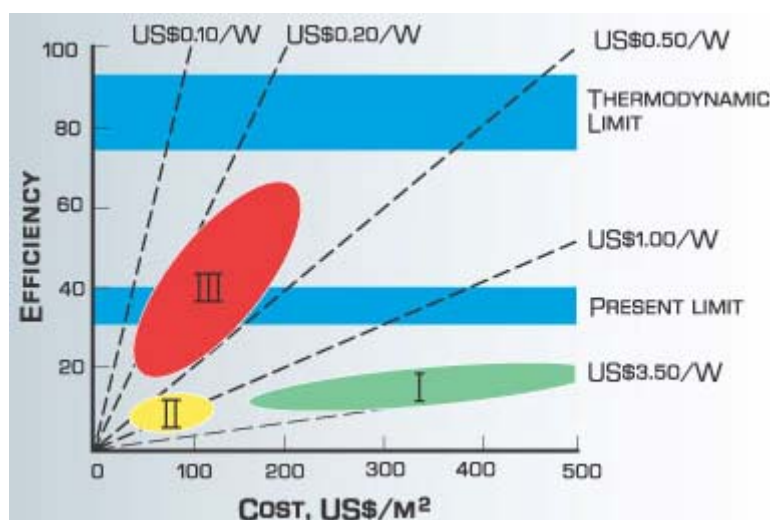


Figure 2.5.1: Chart showing the potential efficiencies for generation I, II and III photovoltaics.¹⁴⁷

Dye-sensitised solar cells are based on an organic semiconductor dye that is sandwiched between two conducting electrodes, at least one of which is transparent to light (typically indium tin oxide; ITO). The dye absorbs photons which results in the formation of excitons. Excitons are bound states of energy - an electron and an electron hole - that are a means of transporting energy without transporting charge. To create a current the exciton binding energy must be overcome to separate the exciton into its constituent charges. The electron and the electron hole must then be captured in a process called exciton quenching within the exciton lifetime before recombination occurs. If recombination occurs then the charge will be lost and the energy cannot contribute to the cell potential, decreasing the efficiency of the solar cell.¹⁴⁸ The excitons travel through the polymer by a random walk process, and in a typical lifetime they will recombine within 20 nm.¹⁴⁹⁻¹⁵¹ As it is difficult to synthesise a cell with a 20 nm thick dye layer that can absorb all of the incident solar radiation, a porous inorganic semiconductor (commonly TiO_2) is often placed in the cell which, when blended with the dye, is called a bulk heterojunction. The purpose of the bulk heterojunction is to accept the electrons from the dye and transport them to the cathode. A schematic for a dye-sensitised solar cell is shown in Figure 2.5.2.

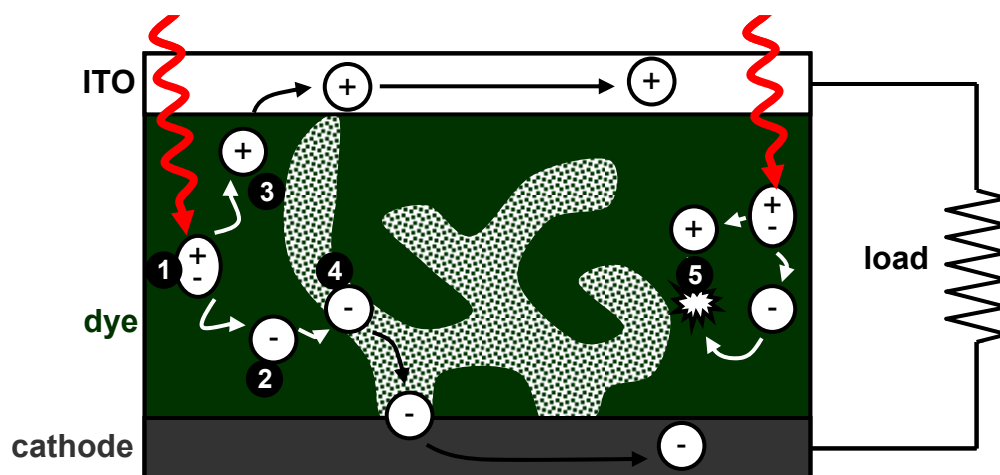


Figure 2.5.2: Schematic diagram of a dye-sensitised solar cell: [1] exciton generation and separation into the free charges; [2] electrons and [3] electron holes; [4] capture of electrons by the bulk heterojunction; [5] annihilation of electron and electron hole pairs formed away from the heterojunction.

Due to the distance in which an exciton must be captured, an ordered mesoporous material could be used as a bulk heterojunction rather than the macroporous (>50 nm pores) materials that are commonly examined. The primary difficulty with mesoporous materials is impregnating the smaller pores with the viscous organic dye.

2.6 Summary

Ordered mesoporous materials have a wide range of applications which have many different chemical, temperature and mechanical requirements. The most important factors for wide-scale development would be cost, product quality and being able to tailor products to the application (for example, SOFC electrodes with thicker pore walls for mechanical stability or bulk heterojunctions for dye-sensitised solar cells with small pore diameters for efficient exciton quenching while ensuring total dye penetration). Ordered mesoporous materials show many improved functional properties with respect to not only bulk materials, but disordered nanomaterials, thereby making them attractive for commercial applications.

Chapter 3

Methods

3.1 Introduction

Analysing the mesoporous materials that were synthesised was integral for determining the success of specific synthesis routes and for improving subsequent procedures. Different properties of the synthesised mesoporous materials needed to be analysed, using various analytical techniques in order to produce a comprehensive overview of the properties of the materials. These analytical procedures included:

- Analysis of the chemical composition of the material to confirm it was the desired product.
- Analysis of the short range structural order at high resolution, including the crystal and pore structures, to understand the crystalline nature of the material and the nature of individual pores.
- Understanding how the pores were arranged with respect to each other to aid in understanding the synthesis procedures and potential ultimate applications of the material.
- Analysing the surface of the material to aid in understanding the synthesis procedures and applications for the material.

The results of these analyses were studied in order to suggest potential applications. Suitable experiments were then designed to test the material properties to determine if the materials had real world applications.

The main analytical methods employed in this work were nitrogen physisorption, transmission electron microscopy, X-ray diffraction, temperature programmed studies and photoluminescence spectroscopy. These are discussed in this chapter.

3.2 Nitrogen Physisorption

Physisorption allows the determination of pore characteristics by the adsorption of an adsorbate (in these experiments, nitrogen) onto the surface of a porous material at increasing and decreasing pressures. By monitoring the uptake of the adsorbate relative to the pressure, a physisorption isotherm is produced. Using specific parts of this isotherm the specific surface area and pore-size distribution can be calculated by applying the Brunauer-Emmett-Teller (BET)¹⁵² and Barrett-Joyner-Halenda (BJH)¹⁵³ methods, respectively.

3.2.1 Physisorption Curves

The shapes of the physisorption isotherms are related to the type of material and the structure of the pores, and therefore can assist in the identification of the porous matrix being studied. Figures 3.2.1A and B shows the various IUPAC classifications for physisorption isotherms and hysteresis curves, respectively. These characterise different adsorption and desorption behaviours which are determined by how the adsorbent and adsorbate interact with each other.

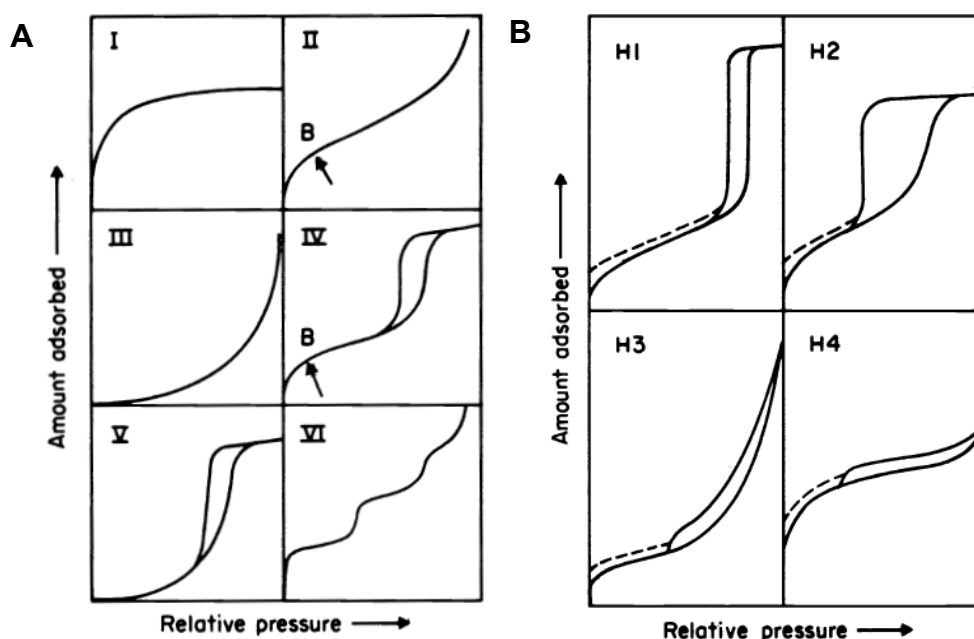


Figure 3.2.1: [A] The IUPAC defined classifications for physisorption isotherms and [B] hysteresis curves.¹ Individual curve shapes are described in the text.

Figure 3.2.1A shows the isotherms that can identify the porous properties of a material. Typically there are four components to an isotherm, not all of which may be present. At low pressures, an adsorbent monolayer is formed creating a steep curve in the isotherm as the gas is adsorbed. The uptake of adsorbate into micropores is also observed at low pressures. At intermediate pressures, there is low uptake of adsorbate where the monolayer formation has occurred, but multilayer formation has not yet been initiated. This can be followed by pore

filling (capillary condensation) which occurs with hysteresis if the pores are in the mesopore range. At higher pressures, multilayer formation and macropore filling (interparticle porosity) may be observed in the form of further adsorbate uptake. The IUPAC classifications are as follows:

- Type I isotherms are characteristic of microporous (<2 nm pore diameter) solids. Small pores lead to high adsorption at low pressure and there is no hysteresis observed.
- Type II isotherms are typical of non-porous and macroporous (>50 nm diameter) materials and also carbons with both micro- and mesopores. Monolayer formation at low pressure is followed by a linear B section (indicated in Figure 3.2.1A:II). Thereafter, unlimited multilayer formation occurs.
- Type III isotherms are characteristic of materials that have weak adsorbate-adsorbent interactions and therefore do not adsorb at low pressures. Once nucleated at higher pressures, the stronger adsorbate-adsorbate interactions become the driving force for adsorption. There is no linear B section. Materials that give a Type III hysteresis are not common (e.g. nitrogen adsorbing on polyethylene).
- Type IV isotherms are typical of mesoporous solids. Monolayers are formed at low pressures followed by a linear B section. Pore filling occurs at higher pressures with hysteresis observed during desorption. At higher pressures multilayer formation may be observed.
- Type V isotherms are related to Type III but the materials have some pores which give rise to a blend of the Type III and Type IV curves.
- Type VI isotherms have stepwise multilayer adsorption where each step represents the volume of adsorbate required to cover a single layer of the sample. An example of a Type VI isotherm is argon or krypton adsorbing on graphitised carbon black.

The classification of the hysteresis curves is less well defined than the physisorption isotherms. H1 and H4 are the extreme cases of mesoporous capillary condensation. As the pressure increases the pressure required for condensation in pores is achieved and the pores begin to fill. Pore filling occurs via a cylindrical meniscus throughout the matrix giving rise to a gradient as pressure increases. As the pressure decreases desorption can occur by a different mechanism (e.g. hemispherical meniscus), giving rise to hysteresis. The range of hysteresis curves possible in mesoporous materials is shown in Figure 3.2.1B.

The classical descriptions for the types of materials that lead to the four types of hysteresis are:

- Uniform spheres in a regular array leading to a narrow pore size distribution (Type H1).

- Some corpuscular systems, such as silica aerogels, with a large distribution of pore-size and shape (Type H2). There are conflicting literature reports regarding the types of pore systems the H2 hysteresis may refer. One interpretation is a system with bottlenecked pores in which gas condenses in the pores at high pressure while desorption is limited by reliquefaction in the smaller channels.^{1, 154}
- Plate-like particles giving rise to slit-shaped pores with unlimited adsorption at high P/P_0 (Type H3).
- Narrow slit-shaped pores with a Type I isotherm and limited adsorption at high P/P_0 indicating microporosity (Type H4).

3.2.2 BET Theory

While the BET method is widely used for the calculation of the specific surface area from the physisorption isotherm, it has limitations. The BET equation (3.1) is based on the Langmuir isotherm,¹⁵⁵ and is applied to the linear section B of the isotherm (shown in Figures 3.2.1A:II and IV). It is therefore often limited to $P/P_0 \approx 0.05-0.30$.

$$\frac{P}{n^a(P_0 - P)} = \frac{1}{n_m^a C} + \frac{(C-1)P}{n_m^a C P_0} \quad (3.1)$$

$$C = e^{\left(\frac{\Delta E_1 - \Delta E_L}{RT} \right)}$$

n^a amount adsorbed, mmol g⁻¹; n_m^a is monolayer capacity; mmol g⁻¹; P/P_0 is relative pressure; C is the BET constant; E_1 is heat of adsorption for the first layer, J mol⁻¹; E_L is heat of adsorption for the second and subsequent layers, J mol⁻¹; R is the gas constant, 8.314 J K⁻¹ mol⁻¹; T is temperature, K.¹⁵²

A plot of $\frac{P}{n^a(P_0 - P)}$ versus $\frac{P}{P_0}$ over the linear B range produces a straight line plot from

which C and n_m^a can be derived. The fit of the data to this straight line can be used to test the validity of applying the BET equation to the set of physisorption data points being used to calculate the specific surface area. This test was conducted for all BET calculations in this report. The BET equation is based on several assumptions: that an adsorbate of a known, fixed size will adsorb onto one surface site, unaffected by adjacent and other local sites; that surface sites will accommodate only one adsorbate molecule (this assumption allows for surface tension to be neglected from the derivation of the BET equation); that the adsorption sites are in a regular array across the surface, creating the maximum number of adsorption sites on the surface; that adsorption and desorption can only occur from exposed sites; that

multilayer formation is unlimited; and that the energy of formation of the first monolayer is unique, but the energy of subsequent layers is equal to the energy of liquefaction. Literature investigations report that this combination of factors may mean that specific surface areas may only be accurate to within 20%.¹ This IUPAC report does, however, still recommend the use of the BET equation for the calculation of the specific surface area of mesoporous materials.

3.2.3 BJH Theory

The BJH method is widely used for analysis of the pore size distribution of a porous material and can be calculated from both the adsorption and desorption physisorption traces with the latter generally giving smaller pore sizes. Typically, the desorption values are reported in the literature, but a critical analysis of the application of the BJH equation suggests that both traces should be used in analysing porous materials to prevent valuable information from being discarded.¹⁵⁴ The BJH equation (3.2) is modified from the Kelvin equation,¹⁵⁶ but it also accounts for multilayer adsorption (t).

$$\ln \frac{P}{P_0} = \frac{2\gamma V_m}{rRT} + t \quad (3.2)$$

γ is surface tension, dyne cm⁻¹; V_m is molar volume, cm³ mol⁻¹; r is radius of the liquid-vapour interface, cm; t is thickness of a monolayer.¹⁵³

Multilayer adsorption effectively decreases the pore size available for condensation, as after the initial monolayer is formed the pore volume for multilayer adsorption is reduced by the volume of this monolayer which coats the surface of the material, and therefore t must be taken into consideration when the area of the curve after monolayer formation is used in the calculation of the pore size distribution. The Kelvin equation, and inherently the BJH method, makes three principle assumptions: the gas is an ideal gas; the liquid is incompressible at P_1 , the number density; the density well inside the liquid, and $\frac{2\gamma}{R} \gg P_K - P_V$, where P_K is the usual vapour pressure and P_V is the vapour pressure at $r \rightarrow \infty$. This is the approximation used to obtain the Kelvin pressure in the derivation of the Kelvin equation. All of these assumptions have been found to be valid, or at least innocuous if used consistently,¹⁵⁷ except at the critical temperature for the adsorbate. This is 126 K for nitrogen. Nitrogen physisorption experiments are typically conducted at 77 K.

Different models for specific types of mesoporous materials have shown that the BJH method can underestimate pore size and care must be taken to ensure that the correct parts of

the isotherm are analysed, while important aspects are not disregarded.¹⁵⁴ This review also highlights commonly misreported and erroneous peaks that can arise from this method but, as with the BET method, advises that with careful application useful information can be obtained by using the BJH equation.

3.3 X-ray Diffraction

3.3.1 Powder X-ray Diffraction

Powder X-ray diffraction (XRD) is a useful non-destructive diagnostic method for phase identification of crystalline materials. Incoming X-rays of a known wavelength (λ) are reflected by the ordered lattices of the sample and interfere constructively at specific angles according to the Bragg equation (3.3) and so create peaks in the XRD pattern (Figure 3.3.1).

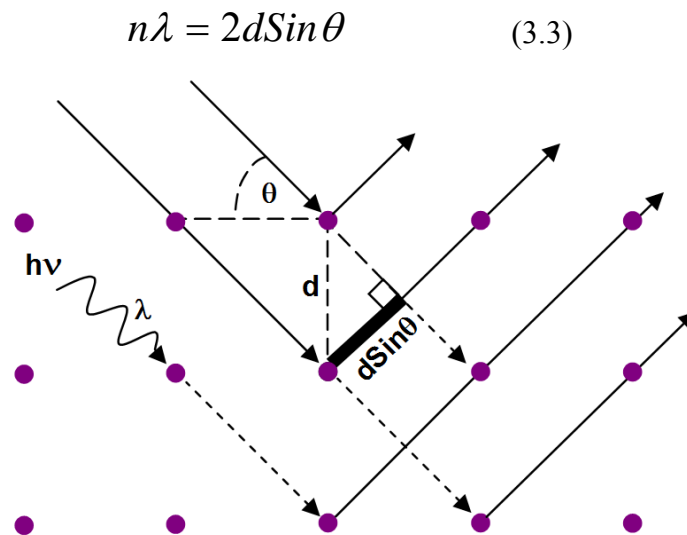


Figure 3.3.1: X-ray scattering; n is an integer; d is the lattice spacing, m; θ is angle of incident radiation, rad.

By analysing powders in which every three-dimensional crystallographic orientation is represented equally, three-dimensional crystallographic information is obtained in a one-dimensional experiment. This is done by taking many measurements over a large range of angles (Figure 3.3.2).

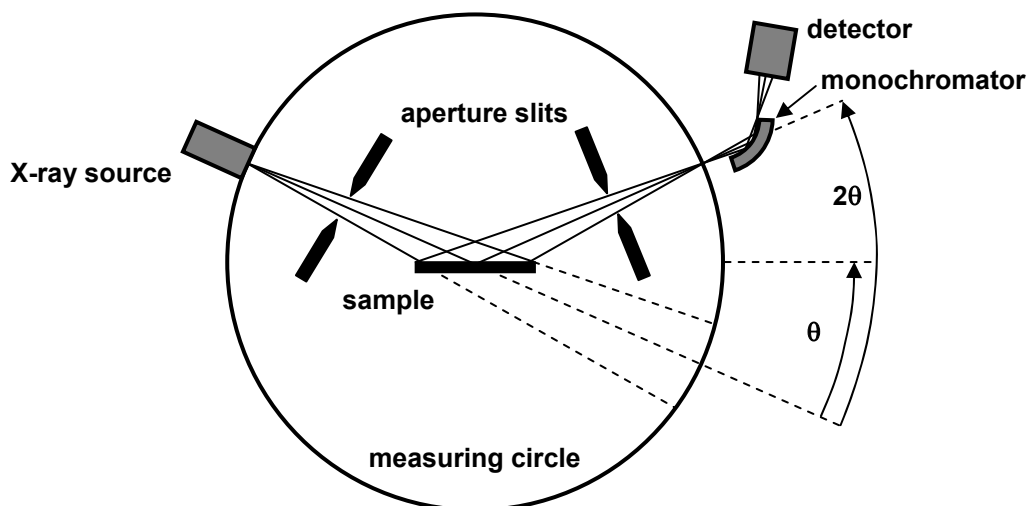


Figure 3.3.2: Schematic diagram of a powder XRD experiment (adapted from KS Analytical Systems).¹⁵⁸

Using the Bragg equation the 2θ values can be converted to d-spacings. The d-spacing, as was shown in Figure 3.3.1, is the distance between the reflecting crystallographic planes. This is shown in the 3D models of Figure 3.3.3.

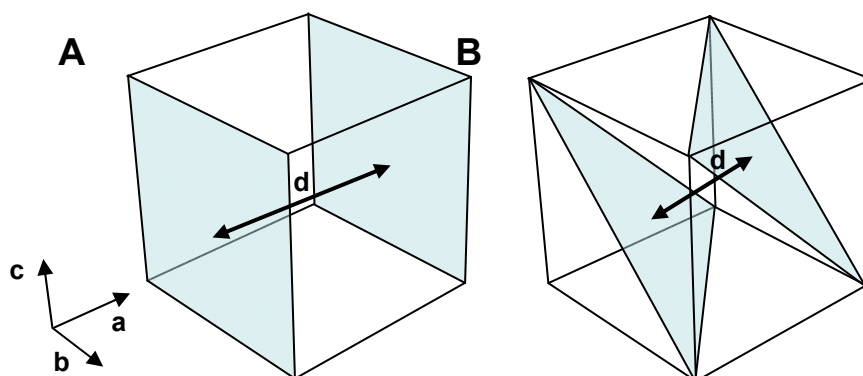


Figure 3.3.3: Planes with [A] the (100) and [B] (111) Miller indices for cubic structures.

A family of crystallographic planes is identified with respect to the real space unit cell vectors $[abc]$ using the reciprocal space lattice vectors (hkl) . These are Miller indices. This results in a diffraction pattern in reciprocal space which is normal to the lattice planes. $[abc]$ vectors that are identical due to the symmetry of the lattice can be collectively identified $\langle abc \rangle$ while (hkl) vectors that are identical due to the symmetry of the lattice can be collectively identified as $\{hkl\}$. From the characteristic X-ray pattern lattice parameters can be determined by referencing to the database of the International Centre for Diffraction Data (ICDD).

Particle size information can be obtained by analysing peak-broadening by application of the Scherrer equation (3.4).

$$p = \frac{K_w \lambda}{b \cos \theta} \quad (3.4)$$

p is 'true' size or $\sqrt[3]{V}$ of the crystallites, m ; K_w is the Scherrer constant for half-width method (0.855 for spherically shaped cubic crystals using the $\{111\}$ peak); b is 'additional broadening' - the width of the diffraction maximum measured at half of the diffraction peak at angle θ ; rad.¹⁵⁹

The peak broadening must be standardised to the XRD instrument being used. The peak height is subtracted from the background. The peak width for the Scherrer equation (b) is calculated by subtracting the instrument broadening. The instrument broadening is measured from a reference silicon pattern (b_s). This is subtracted from the experimental XRD pattern (b_m) as shown in Equation (3.5).

$$b = \sqrt{b_m^2 - b_s^2} \quad (3.5)$$

3.3.2 Small Angle X-ray Scattering

Small-angle X-ray scattering (SAXS) works on similar principles, except that the detector is placed closer to the primary beam and can collect scattered X-rays at smaller angles. As θ and d are inversely proportional, SAXS can be used to detect long-range order in the mesopore range. Measured 2θ values of 0.5 - 5.0° correspond to $d = 17.6$ - 1.8 nm (at lower angles the zero peak becomes problematic), compared to a typical range of $2\theta = 5$ - 100° ($d = 1.8$ - 0.1 nm) for standard powder XRD.

3.4 Transmission Electron Microscopy

In transmission electron microscopy (TEM) a beam of electrons interacts with electrons in the material under study and this process is exploited to give rise to high-resolution imaging and spectroscopy.

3.4.1 Electron Beam Generation

Figure 3.4.1 shows a schematic diagram of the electron beam generation for a JEOL 2010 Transmission Electron Microscope (TEM). The cathodic LaB_6 crystal emits electrons via thermionic emission. The electrons are caused to converge by the Wehnelt cylinder (which

has a higher negative potential than the electrons) to form a more focused beam and the electrons are accelerated towards the anode to give electrons of a known kinetic energy (E) and wavelength (λ ; Equation 3.6).

$$\lambda = \frac{h}{\sqrt{2mE}} \quad (3.6)$$

λ , m; h is the Planck constant, 6.626×10^{-34} J s; m is the rest mass of an electron, E, J.

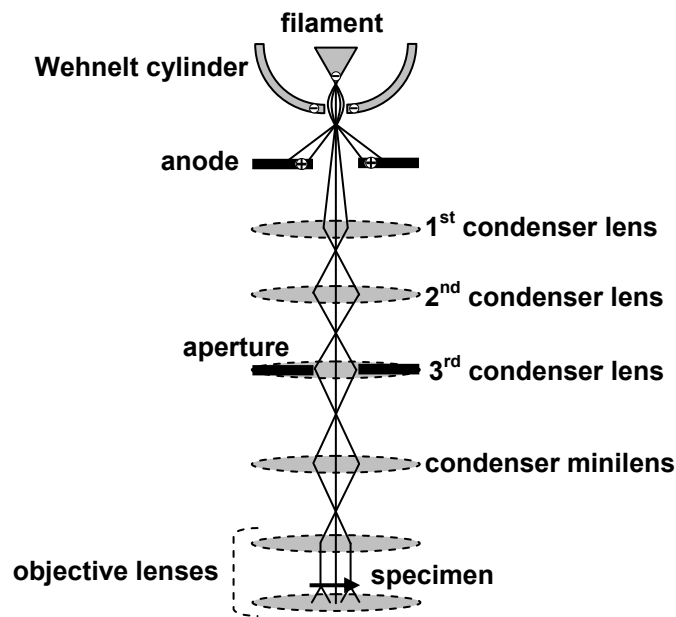


Figure 3.4.1: Schematic diagram for the generation of a focused electron beam in a TEM and the lens configuration above the specimen.¹⁶⁰

A high accelerating voltage means that electrons with wavelengths much smaller than that of light can be produced and used for imaging. This gives increased resolution (the ability to distinguish two adjacent particles; d) compared to light microscopy (Equation 3.7). To minimise the interaction of the electron beam with gas molecules the entire microscope column is maintained under vacuum.

$$d = \frac{\lambda}{2n \sin \theta} \quad (3.7)$$

d is resolution, m; λ is wavelength, m; n is refractive index (1 for microscope vacuum); θ is angular resolution equal to half the angle of the cone of the electron beam ($\approx 10^{-2}$ rad).

The lenses are magnetic or electrostatic rather than glass, as in optical microscopes. The lenses must be symmetrical and aligned correctly to provide a focused beam. Common aberrations are spherical aberration where the lens is not symmetrical, chromic aberration where a range of wavelengths are refracted differently, and astigmatism where different perpendicular planes have different foci. The condenser lenses form the beam while the objective lens focuses the beam onto the sample. As the electron beam reaches the sample the transmissibility depends on the accelerating voltage, sample thickness and composition. The elastically scattered electrons, those that change direction upon interaction with the sample without changing energy, pass through the specimen. The beam exiting the sample is then expanded by the intermediate and projector lenses onto the phosphorescent screen, charge-coupled device (CCD) or photographic film producing a phase contrast image (Figures 3.4.2A and B).

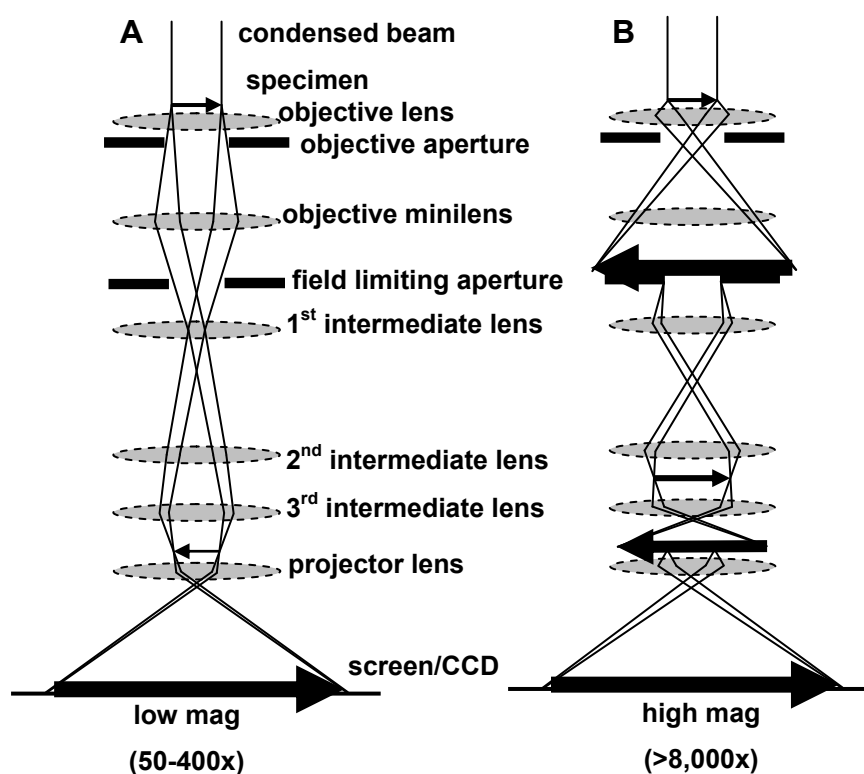


Figure 3.4.2: Schematic diagram for the operation of TEM: [A] lens configuration for the electron beam below the specimen for low magnification and [B] high magnification imaging.¹⁶⁰

Auxiliary TEM equipment that is discussed in this project includes tomography, the use of in-situ heating stages, and environmental TEM. Tomography uses a series of images that are taken of an area of the sample as it is tilted over a wide range of angles (in one direction by rotating the entire specimen holder), inside the microscope. Once these images have been aligned to each other they can be viewed as a video, or analysed using modelling software to create a 3D model. This allows information about the 3D structure of a material to be obtained from a series of 2D images. In-situ heating utilises a specialised sample stage with a

heating element in which the sample grid can be heated to high temperatures inside the microscope column. The real time effect of temperature can be observed on the micro- or nanostructure of the sample. Environmental electron microscopy allows reactions to be conducted inside the microscope column under direct observation. Gases can be passed over the sample and are then pumped away by vacuum systems to maintain the vacuum in the rest of the electron microscope column. Coupled with a heating stage this allows the study of reaction mechanisms at high magnification that might not take place under vacuum.

3.4.2 Selected Area Electron Diffraction, Fast-Fourier Transforms and Digital Diffraction Patterns

Selected area electron diffraction (SAED) uses the same principles as XRD (Section 3.3). When the electron beam interacts with the sample diffracted electrons are refracted according to Bragg's law. This produces a 2D diffraction pattern that is represented in reciprocal space. SAED is most commonly used for the analysis of crystalline solids in an electron microscope. From the SAED pattern the crystal structure of the material can be studied. The d-spacings and angles between spots can be measured using analytical software and indexed by referencing the data to the database of the ICDD. From the lattice reflections the zone axis of the crystal or material can also be determined. Amorphous materials give rise to diffuse rings in the SAED pattern.

In this report, in order to analyse sample mesostructure, Fast-Fourier transforms (FFT) were used to produce digital diffraction patterns (DDPs) from the TEM CCD image. A Fourier transform converts a frequency into a function which means that a repetitive pattern can be represented as a discrete data point. A FFT is a mathematical algorithm that computes discrete Fourier transforms. The DDP is a 2D image representing the repeat units of the TEM image calculated using the FFT. Images of a sample with uniform repeating units give rise to DDPs containing sharp spots at distances inversely proportional to the lattice spacing, in essence a simulated SAED pattern. Using FFTs of low magnification images, mesopore spacings can be determined using the same method since the FFT is performed on the TEM image regardless of the magnification. The mesopore d-spacings are very close to, and sometimes within, the undiffracted electron beam when using SAED. SAED is a good method for obtaining the lattice spacings for crystals, but due to the central spot overwhelming the spots relating to mesopore d-spacings, it is not a feasible technique for obtaining these larger d-spacings. As a DDP is a calculated pattern, the undiffracted beam (strictly, the (000) spot) is not as intense, and so using a DDP, the mesopore d-spacings can be resolved.

3.4.3 Energy Dispersive Spectroscopy

The electrons that are scattered inelastically, that is those that change direction and energy, interact with the atoms in the sample to generate various forms of radiation (Figure 3.4.3A). These various forms of radiation can be analysed by auxiliary attachments to the microscope, giving rise to a wide range of spectroscopic techniques at high resolution. Energy Dispersive Spectrometry (EDS) allows the elements present in the sample to be characterised by recording the characteristic X-rays that are emitted. When the electron beam ejects electrons from inner shells, electrons of higher energies fill the electron holes (Figure 3.4.3B). As each element has a different electronic configuration the energies of the radiation emitted are characteristic and quantitative. Therefore, the relative intensities observed for a sample are proportional to the elemental composition of that sample.

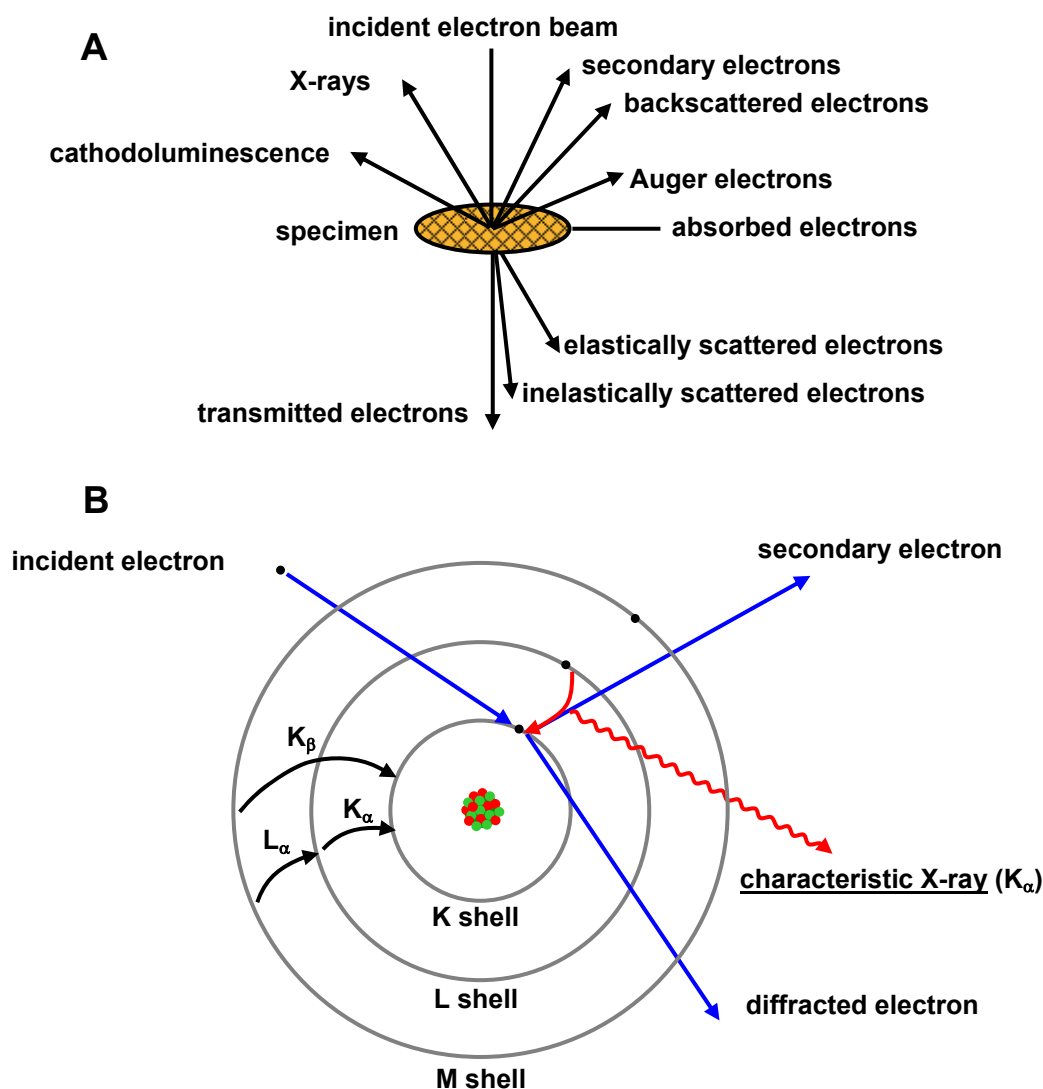


Figure 3.4.3: [A] schematic representation of the interaction of the electron beam and the sample and the different types of radiation which are generated that can be used in high resolution spectroscopy; [B] Schematic representation of the interactions between the incident electrons and sample electrons for characteristic X-ray generation showing that the X-ray energy is proportional to the difference in the electron band energy levels.

3.5 Temperature Programmed Experiments

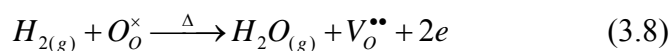
Temperature programmed (TP) experiments employ a convenient method to analyse the adsorption, desorption, redox, or catalytic properties of a powdered material. By passing a gas stream over the powder and increasing the temperature, while analysing changes in the gas composition, the reaction occurring in the reactor can be studied as a function of temperature. The reactivity of a material will be related to this function since a more reactive species will react at a lower temperature. This can then be compared to reference materials to guide the development of new materials.

This method was first used for analysing catalysts by Amenomiya and Cvetonovic.¹⁶¹ In a temperature programmed desorption (TPD) experiment, they measured at which temperatures ethylene desorbed into an inert carrier gas, helium, from an alumina catalyst. Two separate active sites were identified. TP experiments can be used to analyse materials using different gas mixtures giving rise to a range of different TP experiments, namely: temperature programmed reduction (TPR), using a reducing gas (e.g. hydrogen, carbon monoxide) to examine the redox properties of the sample; temperature programmed oxidation (TPO), using an oxidising gas (e.g. oxygen, air), for example, to quantify carbon deposition on a catalyst by measuring the subsequent carbon dioxide and monoxide peaks in a TPO following catalysis reactions, or to study the reoxidation of reduced samples; temperature programmed reaction, using a reactive gas (e.g. methane, methanol), to examine a catalytic reaction and the products of reaction; and temperature programmed surface reaction, where adsorbed surface species are reacted with a gas (e.g. adsorbed ammonia with nitrous oxide). In this report only TPD, TPR and TPO were used, and therefore the other types of TP experiments will not be discussed in detail. All experiments use the same apparatus and experiments can be changed by altering the composition of the gas stream (discussed in detail in Section 4.4.4).

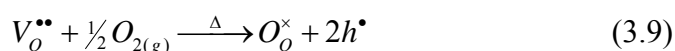
TPD provides information about species that are adsorbed on the surface of the sample without any reactions taking place to investigate the innate properties of the material. As the temperature is increased, more tightly bound species are desorbed from the sample into the inert carrier gas. The desorbed species are transported downstream for analysis by either a mass spectrometer (MS), gas chromatograph, or by thermal conductivity detector. The detection of the desorbed species is affected by the rate of the desorption process, the rate at which reactants diffuse to the phase boundary (which will be also be affected by the relative amount of sample surface which is accessible to the gas), readsorption of the products onto the sample, and the time taken for the products to travel from the sample to the detector.

TPR experiments are similar to TPD experiments, except that rather than using an inert

carrier gas, a reducing gas is used. This has the effect that any species that are active to the reducing gas (i.e. oxidising materials), will contribute to the TPD spectrum, for example the reaction of hydrogen gas with oxide species in a catalyst material (Equation 3.8).



TPO experiments have been traditionally used to quantitatively determine the amount of carbon that has been deposited during previous catalysis experiments. By analysing the amount of the carbon dioxide and carbon monoxide produced as the temperature increases, the amount of deposited carbon can be determined. In this investigation TPO was used as part of a cycling experiment to measure at which temperatures samples absorbed oxygen as shown by the Kröger Vink expression in Equation 3.9.



In this investigation a MS was used for analysing the gas stream. In mass spectrometry, gas molecules are passed through an ion source (e.g. an electron beam) that ionises the gas stream, $M + e^- \longrightarrow M^+ + 2e^-$. This has two effects: the gas molecules are charged (e.g. $O_2 \longrightarrow O_2^+$) and can therefore be manipulated using an electric field; and molecules become fragmented. For example, water will give MS signals at a mass to charge ratio (m/z) of 18 ($H_2O_{(g)}^+$), 17 (OH^+), 16 (O^+), and 1 (H^+). The instrument used was a quadrupole MS. By applying a voltage to a system of four electromagnets only one m/z ratio is admitted to the detector at a time. All other m/z values are deflected either too weakly or too strongly by the electric field to reach the detector. By scanning the voltage, molecular fragments over a range of m/z ratios can be detected in turn. It must be noted that a molecule with the molecular weight, M, that carries a double charge will have a peak at m/z = M/2, so care must be taken in identifying and interpreting these peaks. Peaks at m/z = M/2, and peaks due to minor molecular fragments, can assist in identifying the species giving rise to the M peak if there are multiple possible species at that m/z ratio. For example carbon monoxide and molecular nitrogen both have M = 28. Therefore, coinciding peaks at m/z = 12 (carbon), 14 (nitrogen), and 16 (oxygen), will assist in the correct identification of the m/z = 28 peak.

3.6 Inductively coupled plasma mass spectrometry

Inductively coupled plasma mass spectrometry (ICP-MS) is an analytical technique for quantitatively determining the concentration of the constituent elements that comprise a sample. The instrument used here contained three main components: a laser, ICP and a MS. Laser ablation was used to volatilise a section of solid material which was subsequently swept into the ICP stream. In the ICP, argon atoms are separated into ions and electrons using electrons that were first accelerated by a magnetic field. This produces a high-temperature ($\sim 10,000$ °C) plasma. The ablated material was introduced into the ICP stream using an argon carrier stream which caused the sample atoms to become ionised. The ionised sample atoms were extracted from the plasma and analysed by a MS, typically a quadrupole (as described in Section 3.5) or octopole MS. This allows for the determination of a wide-range of elements at concentrations as low as ppb.

3.7 Photoluminescence Spectroscopy

Photoluminescence (PL) spectroscopy is an effective technique for determining the quenching efficiency of excitons in a dye-sensitised solar cell. PL involves exciting a sample with a laser pulse, at a known wavelength, and then recording the spectrum that is emitted from the sample. This method uses a spectrograph coupled to a streak camera that records the spectrum using a CCD (a schematic diagram is shown in Figure 3.7.1). The spectrograph horizontally splits the light emitted from the sample according to wavelength by the phenomenon of dispersion, prior to entering the streak camera. Streak cameras are used in time-resolved spectroscopy and typically have a temporal resolution of ~ 1 ps, allowing for the direct detection of photons. The photons are used to generate free electrons in a photocathode. The number of electrons emitted is proportional to the intensity of the light. The beam of electrons is deflected using a sweep electrode to deflect the point of impact across the CCD increasing the temporal resolution. This means that every image the CCD takes has multiple data points sorted temporally. Analysis software can then manipulate the data to relate the CCD image to when the photons arrived at the photocathode.

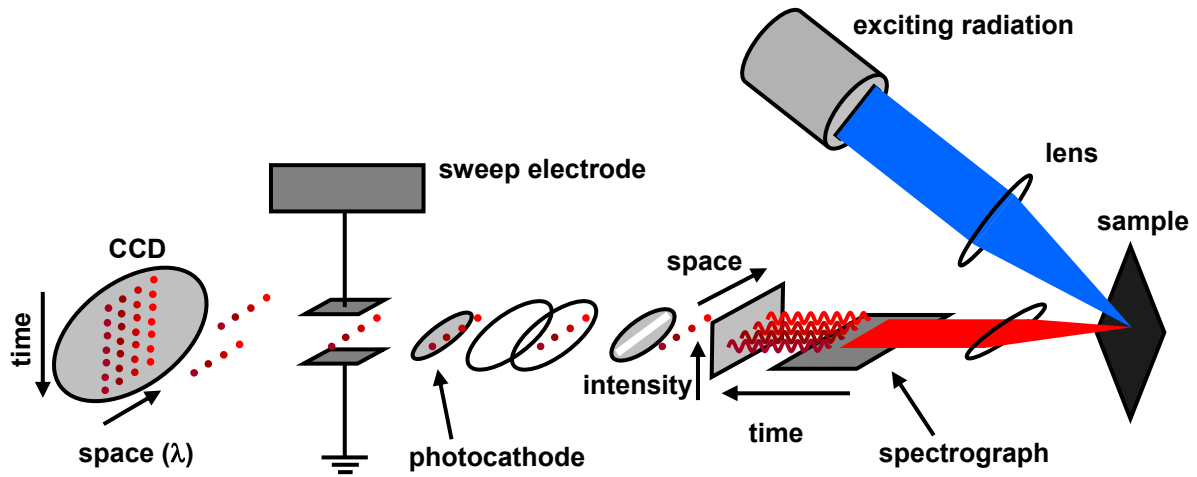


Figure 3.7.1: Schematic diagram of a PL spectrometer
(located at the School of Physics & Astronomy, University of St Andrews).¹⁶²

This means that the PL spectrometer can be used to select the wavelength of emitted light and plot the intensity of emitted light of this frequency against time. The light emitted from the sample produces a decay curve as shown in the schematic diagram, Figure 3.7.2.

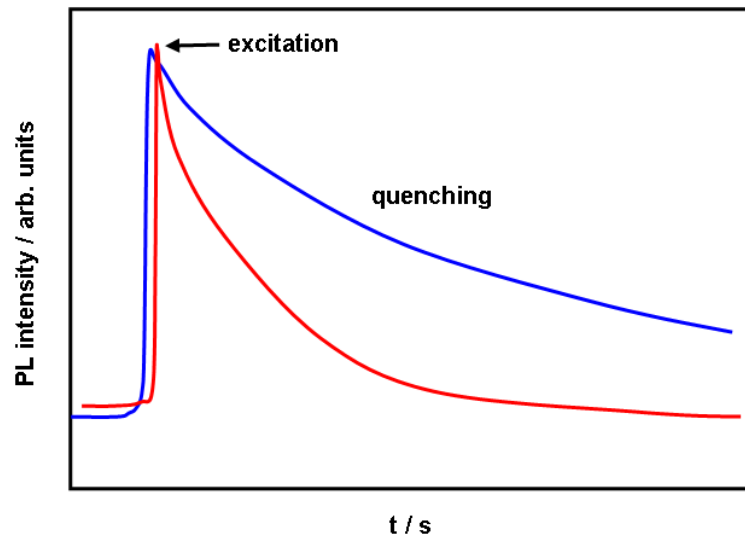


Figure 3.7.2: Example of a PL decay curve showing the excitation and decay of materials with a relatively short (■) and long (■) τ (decay time).

From the decay curve the decay half-life of the photoluminescence of the material can be calculated and compared with reference materials using Equation 3.10.

$$I(t) = I_0 e^{-\frac{t}{\tau}} \quad (3.10)$$

$I(t)$ is PL intensity, arbitrary units, at time t , s; I_0 is initial PL intensity; τ , s.

Chapter 4

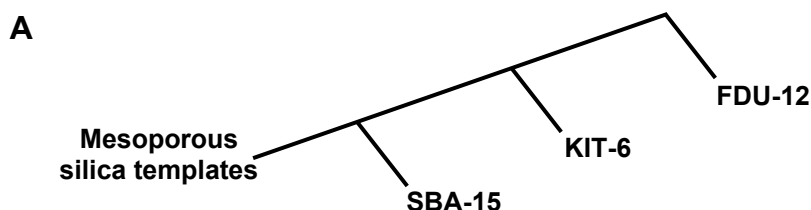
Experimental

4.1 Introduction

Various methods were employed to synthesise the mesoporous materials described in this work as the investigation evolved. The principle techniques used were hydrolysis (Sections 5.2.1-3, and 6.2.3), precipitation (Sections 6.2.1 and 6.2.4), sol-gel (Section 6.2.1), incipient wetness impregnation (Sections 6.2.2, 8.2.1), and vacuum impregnation (Sections 7.2, 8.2.2, and 9.2). Further specific details about the experimental synthesis procedures can be found in these sections.

An experimental map outlining the progression through these methods is shown in this chapter, along with the sample index used to define the products synthesised. Technical details of the analysis techniques described in Chapter 3 are also presented in this chapter.

4.1.1 *Experimental Maps*



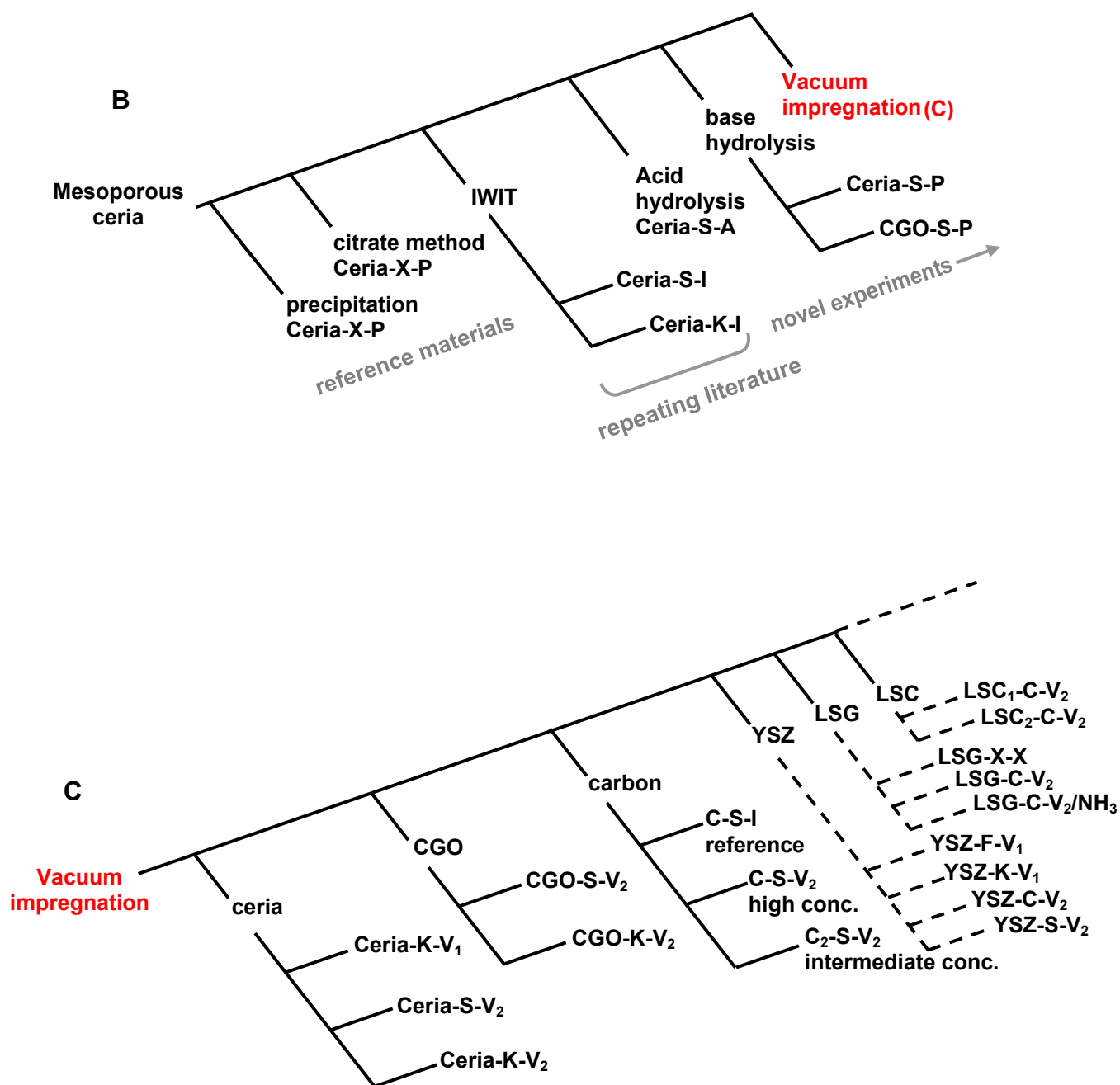


Figure 4.1.1: Experimental maps outlining the progression of experiments in [A] Chapter 5, [B] Chapter 6, and [C] Chapters 7-9.

4.2 Sample Index

Table 4.1: Table demonstrating the sample index used throughout this report to describe different materials. The different material compositions, templates and methods are presented.

Ceria	-	K	-	V ₁
composition	template		method	
C (carbon)	C (carbon)		A (acid hydrolysis)	
Ceria	F (FDU-12)		Cit (Citric acid)	
CGO	K (KIT-6)		I (IWIT)	
LSC	S (SBA-15)		P (precipitation)	
LSG			V ₁ (VI generation 1)	
YSZ			V ₂ (VI generation 2)	

4.3 List of Chemical Reagents

n-butanol..... Sigma (99% purity)
 Ce(NO₃)₃.6H₂O Acros (99.5%)
 citric acid Alfa Aesar (99.5%)
 Ga(NO₃)₃.xH₂O..... Alfa Aesar (99.9%)
 Gd(NO₃)₃.6H₂O Alfa Aesar (99.9%)
 30 % H₂O₂ Sigma Aldrich (reagent grade)
 KCl Fisher (reagent grade)
 La(NO₃)₃.6H₂O Acros (99.999%)
 Mg(NO₃)₂.xH₂O..... Alfa Aesar (99.999%)
 mesitylene..... Alfa Aesar (>98%)
 Pluronic P123 Aldrich
 Pluronic F127 Sigma
 Sr(NO₃)₂ Aldrich (>99%)
 d-sucrose..... Fluka (99.5%)
 tetraethyl orthosilicate Acros (98%)
 Y(NO₃)₃.6H₂O Aldrich (99.9%)
 ZrOCl₂.8H₂O Alfa Aesar (99.9%)
 Milli-Q grade H₂O was used in all syntheses
 Standard stock chemicals not listed.

4.4 Analytical Methods

4.4.1 Nitrogen Physisorption

Nitrogen adsorption-desorption isotherms were measured using Micrometrics ASAP 2020 and Micrometrics Tristar III instruments at 77 K. Samples were degassed at 120 °C for 4 h (ramp rate 10 °C min⁻¹ with a 30 min dwell at 90 °C) under vacuum (2.63×10^{-5} atm) prior to analysis. The sample was then exposed to increasing nitrogen pressures up to 0.9999 atm. Measurements continued to be taken as the sample was then taken down to 0.2 atm for the desorption experiment. At this pressure all data required for calculations from the desorption experiment had been collected. The length of the analysis depended on the amount of nitrogen the sample adsorbed and ranged from 12 to 48 h. The Micrometrics ASAP 2020 V3.00 software package was used to calculate the BET specific surface area, BJH pore size distribution and pore volume from the physisorption results.

4.4.2 TEM

TEM samples were prepared by first suspending a small amount of the sample in hexane or ethanol using an ultrasonic bath (for 15 min). The suspension was allowed to stand for 10 min so that large particles would sink. Liquid from the top of the suspension was dispersed onto a copper 300-mesh holey carbon grid (a nickel grid was used for the high-temperature experiment in Section 7.6.1). The grid was dried under a 60 W light bulb for at least 8 h. TEM preparation was carried out in a room not used for general experimental synthesis to prevent sample contamination.

TEM images were collected using a JEOL JEM 2011 electron microscope fitted with a LaB₆ filament and operated at 200 kV. Semi-quantitative elemental analysis was performed with an Oxford Instruments X-Ray analysis ISIS 300 EDS detector. Analysis of images, lattice spacings and FFTs was performed using Gatan's Digital Micrograph 3.3.4 graphics suite and the software package ImageJ 1.42q.

High temperature TEM and 3D tomography was performed on a JEOL 2100F TEM/STEM electron microscope with a field emission gun operated at 200 kV (Nottingham Nanotechnology and Nanoscience Centre, NNNC). The Serial EM software package, developed by Mastronarde, was used for the 3D tomography analysis.¹⁶³

High-resolution EDS was performed using an Oxford Instruments EDS probe on the 2100F microscope operating in STEM mode. Some samples were also plasma cleaned first to remove organic impurities so preventing carbon deposition under the electron beam.

4.4.3 XRD

XRD samples were placed on a glass microscope slide and spread to form a layer of uniform thickness. The amount of sample used was sufficient to cover an area exceeding the size of the incident X-ray beam to a sufficient depth that no glass-phase peaks were observed. This avoided Al, plastic and glass peaks in the resulting XRD patterns which might have resulted from using traditional XRD plates.

Powder XRD data were collected using a Philips PW 1710 diffractometer with Cu K α radiation ($\lambda = 0.154$ nm). Scan rates in a typical experiment involved a step size of 0.02° (2θ) with a dwell time of 1.2 s, over a range of $2\theta = 10$ - 80° .

SAXS samples were suspended in solvents (silica in acetone, ceria and CGO in water) and were deposited on single-crystal wafers of silicon. Diffraction measurements were carried out on a Bruker-AXS D8 Advance with a Cu X-ray source, parallel beam geometry, a 0.1 mm incident beam slit, sample rotation, and a Sol-X X-ray detector set to Cu K α X-ray energy.

4.4.4 TP Experiments

A schematic setup for the TP equipment is shown in Figure 4.4.1. The equipment was designed and built in-house and based on that used by Baker and Metcalfe.¹⁶⁴

Five gas cylinders were connected to the TP equipment: argon; 5 % hydrogen in argon (5% H₂/Ar); 5 % oxygen in argon (5 % O₂/Ar); a calibration gas with known ratios of ethane, ethylene, carbon dioxide, hydrogen, carbon monoxide, oxygen and argon; and a fifth gas line for conducting alternative experiments (e.g. CO, methane). The cylinders are regulated at 1 bar and connected to the equipment using PTFE tubing.

The valves, V1-V3, were quarter-turn plug valves and were used to isolate the gas supply and the traps. From V1 to V5, 1/8" stainless steel tubing was used. The schematic diagram shows the combination of oxygen traps and water traps that were used to coincide with the incident gas stream to remove any trace of moisture or oxygen during TPD and TPR experiments, and moisture during TPO experiments. The argon gas stream fed directly into a mass flow controller (MFC) while the other four gas streams fed through a four-way switching valve, V4, to another MFC. The MFCs were set to deliver a flow rate of 50 mLmin⁻¹. The two gas streams fed to a switching valve, V5, which simultaneously switched between the two incoming gas streams and either the exhaust gas stream, or the gas stream that continued on to the rest of the apparatus. This meant that two gases could simultaneously be flowing and be switched from the exhaust to the apparatus without delay, preventing air and moisture entering either gas line. From V5 onwards the gas line was 1/16" glass-lined steel tubing (1/32" I.D.) that was trace-heated. This had the effect that reacted

species would be less likely to adsorb on the inner surface of the tube (the trace heating would be sufficient to desorb moisture and other volatile species) and by reducing the volume of the system the time-lag in the analysis of species (from the reactor to the MS) would be decreased. Valves, V6 and V7, were 6-way switching valves to control the flow of gasses between the reactor line and the bypass. The two valves were operated in unison and were used for two principal reasons: when the reactor was being changed the bypass was used to maintain system integrity, and when the type of gas was being changed using the switching valve, V5, the bypass could be used to ensure that an undesired mixture of gases was not passed to the reactor.

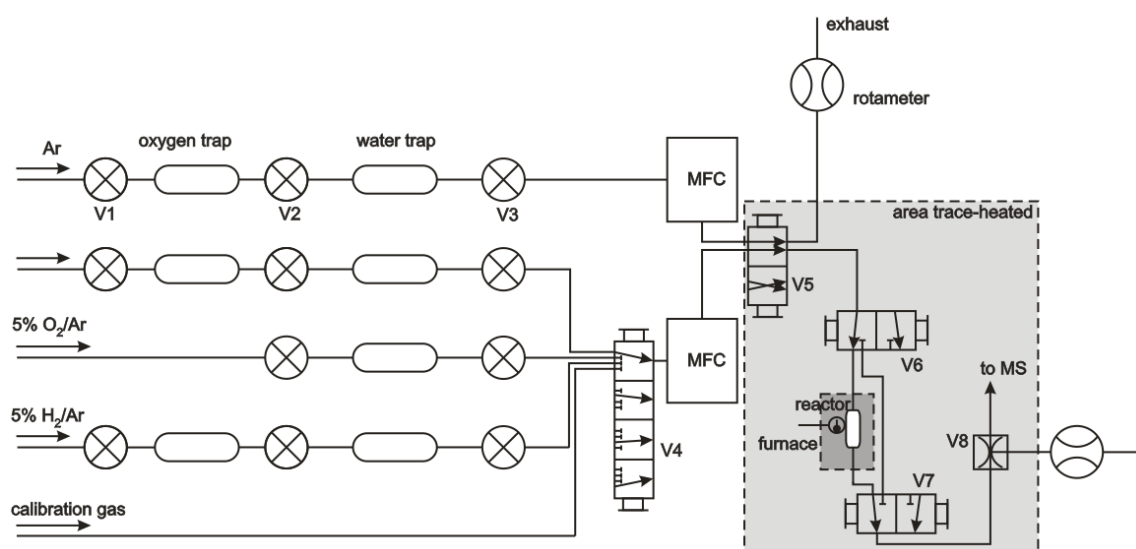


Figure 4.4.1: Schematic setup of the TP equipment. Components are described in the text.

Next in line was the quartz micro-reactor. This was built in-house and consisted of a 1/4" O.D. tube that broadened to a 1/2" O.D. tube in the middle as shown in Figure 4.4.2. The central bubble contained a sintered glass frit on which the powdered sample was placed. A K-type thermocouple was held in place against the bubble at the height of the glass frit inside the furnace, and fed into the MS operating software to record the temperature of the furnace near to the sample. The reactor fitted into the vertically mounted tube furnace that was also designed and built in-house. The furnace consisted of a 300×25 mm I.D. quartz tube encased in a 115 mm steel shell containing insulation. A K-type thermocouple fed from inside the furnace into the furnace controller.

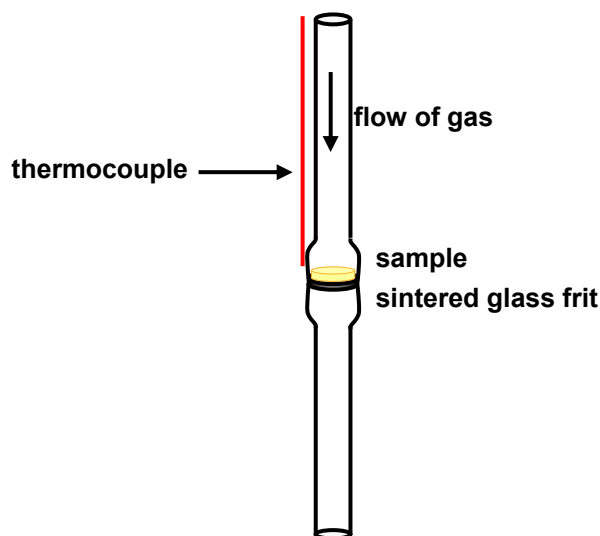


Figure 4.4.2: Quartz reactor used for TP experiments.

After the gas stream had passed through the reactor and switching valve, V7, a sample was drawn off using a needle valve, V8, along a trace-heated capillary to the MS.

The MS was a VG Sensorlab 300 AMU quadrupole Mass Spectrometer set to detect m/z values of 1 (H), 2 (H_2), 12 (C), 14 (N), 16 (O), 17 (OH), 18 (H_2O), 28 (CO or N_2), 32 (O_2), 40 (Ar), and 44 (CO_2). Analogue scans had been performed on various gas mixtures to confirm that the MS recorded these m/z values correctly.

Moisture traps containing silica gel and zeolite had been fitted in-line to the MS vacuum lines to reduce moisture and other MS peaks associated with desorption of volatile substances from the vacuum pump oil (known as backflow) and the MS environment was controlled to keep a stable working temperature, in order to decrease instrument drift which could affect the baseline of the MS traces.

In a typical TPD experiment, 50 mg of powder sample (without any further processing, for example, grinding) was placed into the reactor, ensuring it completely covered the glass frit, and this was placed into the furnace. The sample was then purged under Ar until all traces of air and moisture (identified using the MS) had been removed (usually 10 min). After this time the furnace was turned on and typically heated to 800 °C at a rate of 5 °C min⁻¹.

In a typical TPR experiment, 50 mg of powder sample was placed into the reactor, ensuring it completely covered the glass frit, and this was placed into the furnace. The sample was then purged under Ar until all traces of air and moisture (identified using the MS) had been removed (usually 10 min). After this time the gas flow was switched over to 5 % H_2 /Ar using V5 and the furnace was turned on immediately. Again, heating was typically up to 800 °C at a rate of 5 °C min⁻¹.

In concurrent experiments (i.e. cycling experiments), following one of the above

experiments the reactor was cooled down to room temperature under either Ar or 5 % H₂/Ar. Before another experiment was run (if the previous experiment was not a TPD), the gas flow was switched to Ar and the reactor was purged until traces of all other gases had been removed (followed using the MS). At this time the appropriate gas was selected, using V4, and purged for 20 min through the bypass, followed using the MS, before switching the gas flow to the reactor using V5. At this time the furnace was turned on. If the desired maximum temperature was lower than 800 °C the ramp rate of 5 °C min⁻¹ was maintained to ensure the results were comparable.

4.4.5 ICP-MS

ICP-MS analyses were performed using an Agilent 7500 system with a New Wave Nd:YAG laser system (spot size 80 µm). The samples were blended with Teflon (1:4 sample:Teflon) to form a pellet prior to laser ablation.

4.4.6 Photovoltaic Studies

Photovoltaic studies were conducted by Suzanne Patterson in the School of Physics & Astronomy, University of St Andrews, using Ceria-K-V₁ synthesised in Section 7.2.

A Ceria-K-V₁ suspension (10 mgmL⁻¹) was spin coated onto indium-tin (ITO) oxide glass. Once dry this was heated to 400 °C. A polymer solution was then spin coated onto the ceria-coated ITO glass. This was repeated with a reduced Ceria-K-V₁ sample that was thermally treated at 450 °C in a tube furnace for 1 h in 5% H₂/Ar. This was tested against reference silica and titania materials using photoluminescence spectroscopy.

Time resolved photoluminescence experiments were carried out by exciting the sample (held under vacuum at 4.93×10⁻⁵ atm), with the polymer film facing the incident radiation at $\lambda = 800$ nm, frequency doubled to 400 nm, in 100 fs pulses at a repetition rate of 80 MHz, using a Spectra-Physics Mai-Tai Ti:sapphire oscillator. A blue filter was used to block any residual 800 nm excitation from reaching the sample and the intensity of the excitation was set below the onset of exciton-exciton annihilation in order to prevent additional quenching.

Emission from the sample was collected with a lens and focused into a Chromex 250is imaging spectrograph. The selected emission range was then reflected into a Hamamatsu C6860 streak camera.

Chapter 5

Mesoporous Silica Templates

5.1 Experimental Philosophy

The initial method chosen for the synthesis of mesoporous materials was the IWIT. This was for several reasons:

- It had already been successfully used to produce mesoporous ceria and other materials.
- There was scope for modifying the template morphology with less impact on the experimental design to produce a wide range of products.
- There was less reliance on an individual chemical's properties so once a method had been developed and refined its application to other materials was expected to be simpler than a more complex synthetic route.

For this method a variety of mesoporous templates needed to be synthesised. Those initially chosen were SBA-15, KIT-6 and FDU-12. These, having been used in previous investigations, allowed comparison of results with previously published work. These three templates also represented a range of silica template morphologies.

5.2 Experimental

All mesoporous silica templates were synthesised as per previous literature procedures.^{9, 11, 13}

5.2.1 SBA-15

In a typical synthesis of SBA-15, 2 g of non-ionic surfactant, Pluronic P123, was added to 15 cm³ water and 60 cm³ 2 M HCl and stirred at 40 °C for 8 h. After this time, 4.25 g TEOS was added and stirred for 24 h at the same temperature. The mixture was then placed in a sealed PTFE container in an oven at 100 °C for 24 h for hydrothermal treatment. Before it had cooled down, the resulting white solid was filtered using a Buchner funnel, washed with water and dried in an oven at 105 °C.

5.2.2 KIT-6

In a typical synthesis of KIT-6, 6 g of Pluronic P123 was added to 180 cm³ water and 50 cm³ 2 M HCl and stirred at 35 °C for 6 h. 6 g of n-butanol was added and stirred for a further 1 h. 12.48 g TEOS was added and the mixture was stirred at the same temperature for 24 h. The mixture was then placed in a sealed PTFE container in an oven at 100 °C for 24 h for hydrothermal treatment. Before it had cooled down, the resulting white solid was filtered using a Buchner funnel, washed with water and dried in an oven at 105 °C.

5.2.3 FDU-12

In a typical synthesis of FDU-12, 2 g of Pluronic F127, 2 g of mesitylene, and 5 g KCl were added to 120 cm³ 2 M HCl and stirred at 40 °C for 2 h. 8.3 g TEOS was then added followed by vigorous stirring for an additional 24 h. The mixture was then placed in a sealed PTFE container in an oven at 100 °C for 24 h for hydrothermal treatment. Before it had cooled down, the resulting white solid was filtered using a Buchner funnel, washed with water and dried in an oven at 105 °C.

In all cases the surfactant was removed by calcining in alumina furnace boats at 500 °C in air for 5 h in a tube furnace with a PID controller with a ramp rate of 5 °C min⁻¹. Refluxing using 100 cm³ EtOH for 10 h followed by vigorous stirring with 100 cm³ of 15% H₂O_{2(aq)} at 35 °C was also examined as an alternative to calcination.

5.3 Results

The silica templates were characterised by TEM, nitrogen physisorption and SAXS, these being the most common and informative techniques for non-crystalline mesoporous materials.

5.3.1 SBA-15

From physisorption results, the specific surface area and pore volume of SBA-15, prepared in a number of batches, were determined to be 800-890 m²g⁻¹ and 1.0-1.1 cm³g⁻¹, respectively. The adsorption-desorption isotherm was Type IV with Type H3 hysteresis (Figure 5.3.1). This adsorption behaviour is typical of mesoporous materials with capillary condensation in mesopores. At higher P/P₀ values SBA-15 showed further adsorption attributed to interparticle porosity. The pore-size distribution showed narrow peaks at 5.9-7.3 nm (determined from the adsorption and desorption branches). The micropore volume was calculated to be 0.075 cm³g⁻¹ by t-plot analysis.

Using ethanol and H₂O_{2(aq)} to remove the surfactant did not appreciably enhance the physisorption results - the specific surface area and pore volumes were calculated to be 707 m²g⁻¹ and 0.98 cm³g⁻¹, respectively.

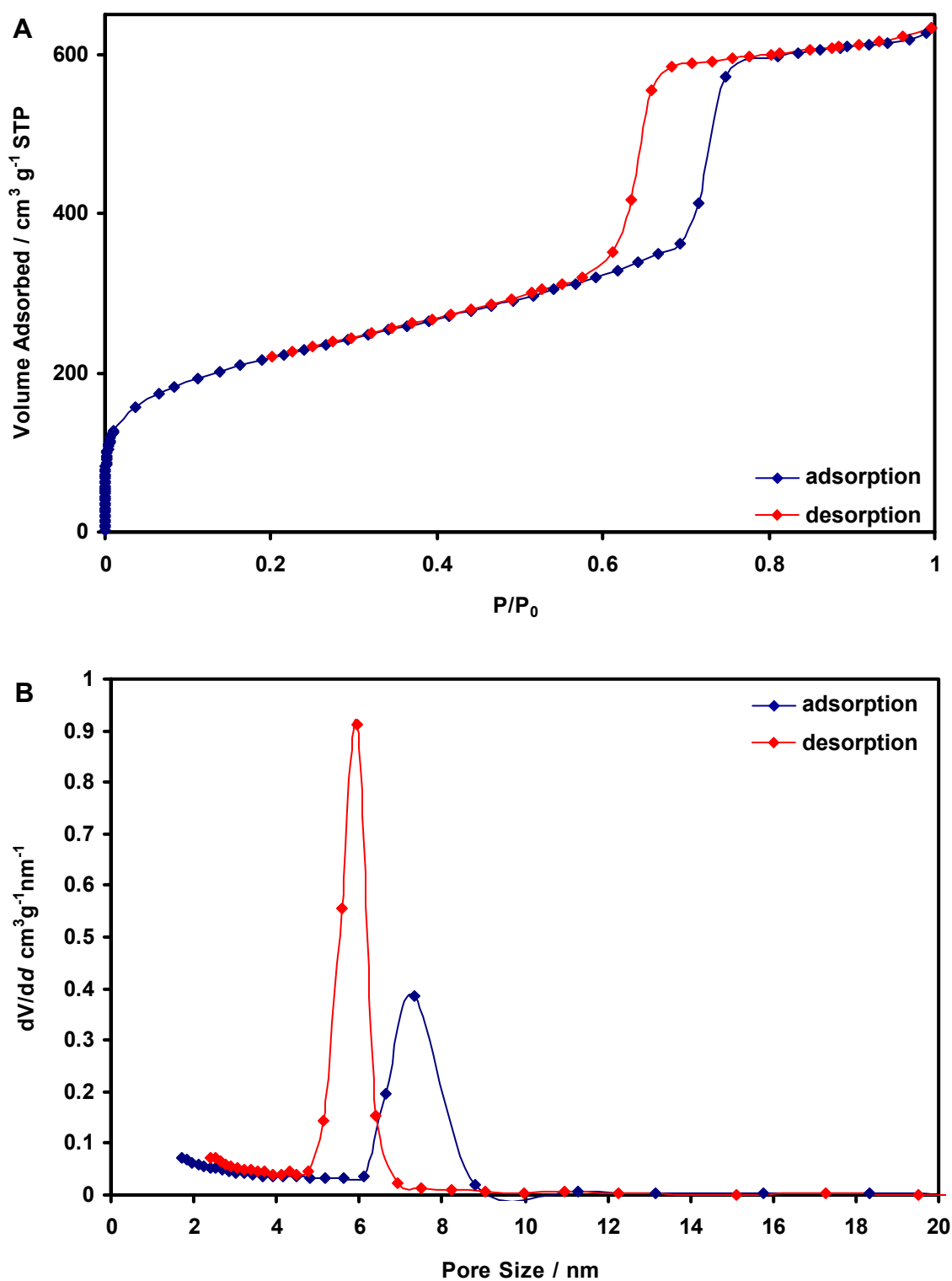
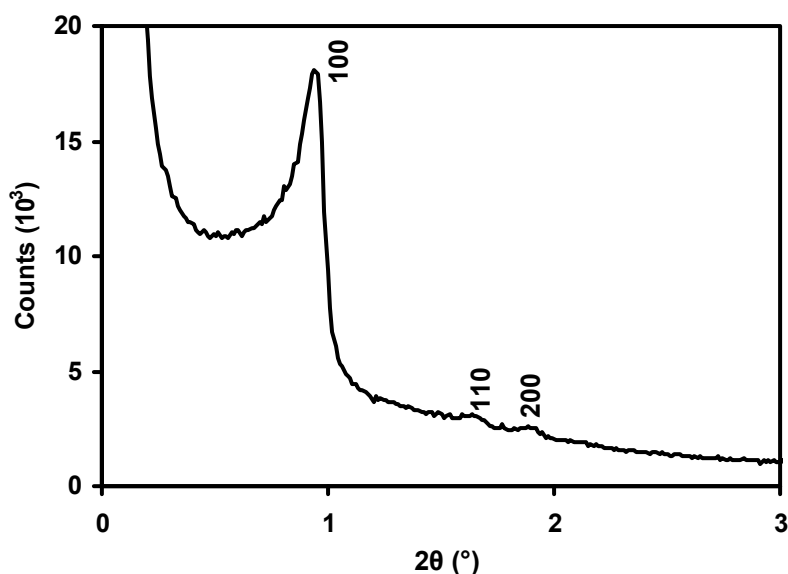


Figure 5.3.1: [A] Physisorption isotherm and [B] pore size distribution for SBA-15.

The diffraction pattern obtained by SAXS (Figure 5.3.2) revealed one strong peak and two less intense peaks corresponding to the $\{100\}$, $\{110\}$ and $\{220\}$ pore spacings, as shown in the schematic diagram in Figure 1.1.1.



Peak 2θ (°)	Indices	d-spacing (nm)
0.95	100	9.3
1.67	110	5.3
1.90	200	4.6

Figure 5.3.2: SAXS pattern for SBA-15.

TEM analysis of SBA-15 showed the material to consist of relatively large, completely porous particles, of approximately 100-150 nm in width by 300-500 nm in length. The porous structure was similar to that described in the literature. That is, the structure contained one-dimensional cylindrical pores of high aspect ratio arranged in a hexagonal array. Figures 5.3.3A and B confirmed that the particles were completely porous and that the yields were high, as was evident from the quantity of material with ordered pore structure present. Also clearly visible was how particles of small diameter bend along their length while maintaining parallel curved pores. While most of the pores in these images were visible along the [100] axis, Figure 5.3.3B showed some particles curving to present the [001] axis which showed that the pores were cylindrical and hexagonally arranged within individual particles. The particles themselves were also faceted along the [100] plane when viewed in cross-section. This led to the commonly observed hexagonal prisms observed in Figure 5.3.3B, but also to the polymorph observed in Figure 5.3.3C.

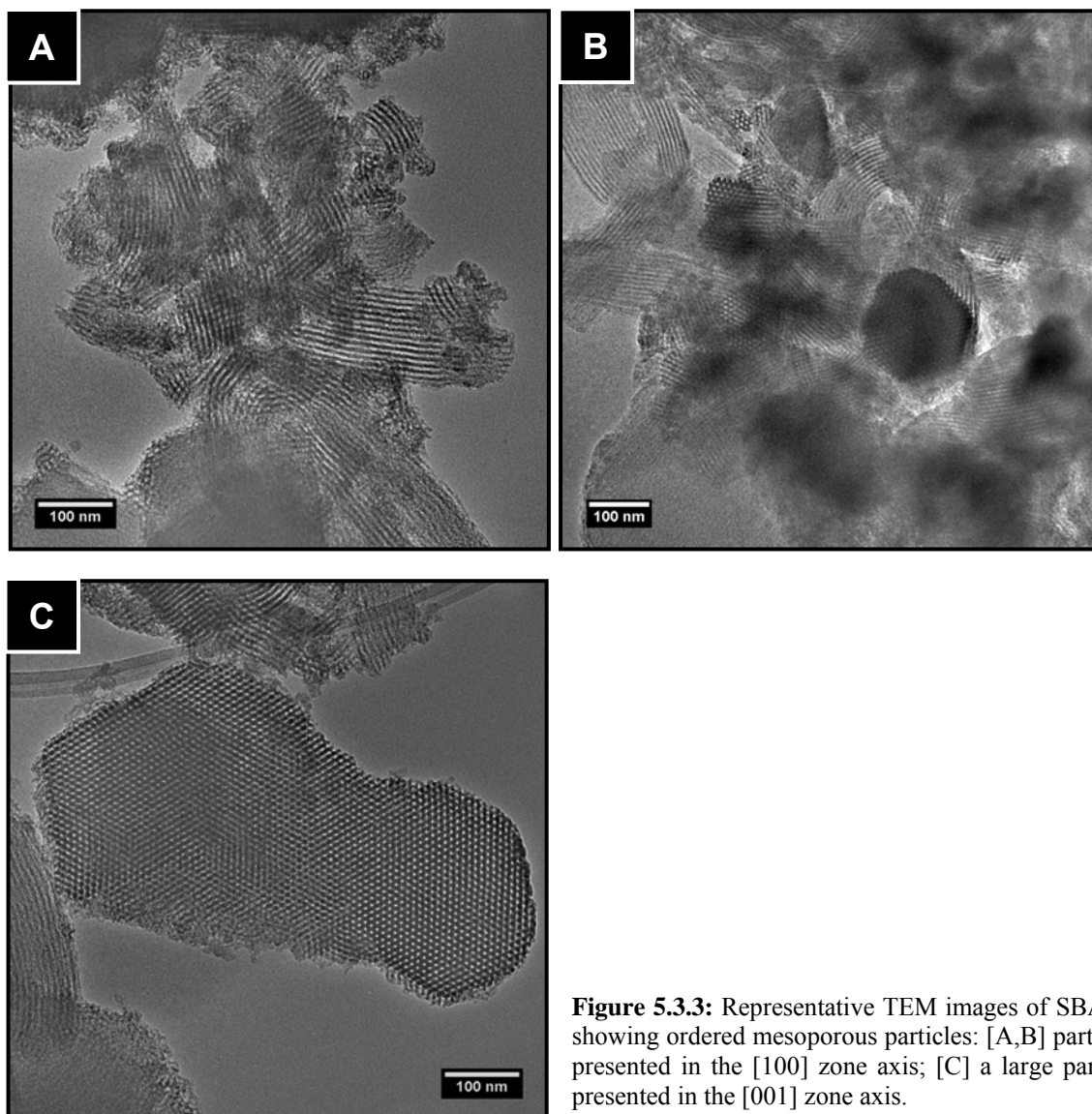


Figure 5.3.3: Representative TEM images of SBA-15 showing ordered mesoporous particles: [A,B] particles presented in the [100] zone axis; [C] a large particle presented in the [001] zone axis.

Figure 5.3.4A shows an image of the [0001] zone axis of a particle. The DDP pattern for this image shows that the pores were regularly arranged. Figure 5.3.4B shows a HRTEM image of the nanorods that comprise the mesoporous particles. The nanorods were smooth, amorphous, and the DDP showed that the pores were regularly arranged as there was no variation in the diffraction pattern which could be attributed to pore irregularities. The small variation in the position of the spots was attributed to the curvature of the pores which could be seen in the TEM image. The d-spacings were measured to be 7.5-8.6 nm based on the ($\bar{1}010$) and (100) DDP reflections.

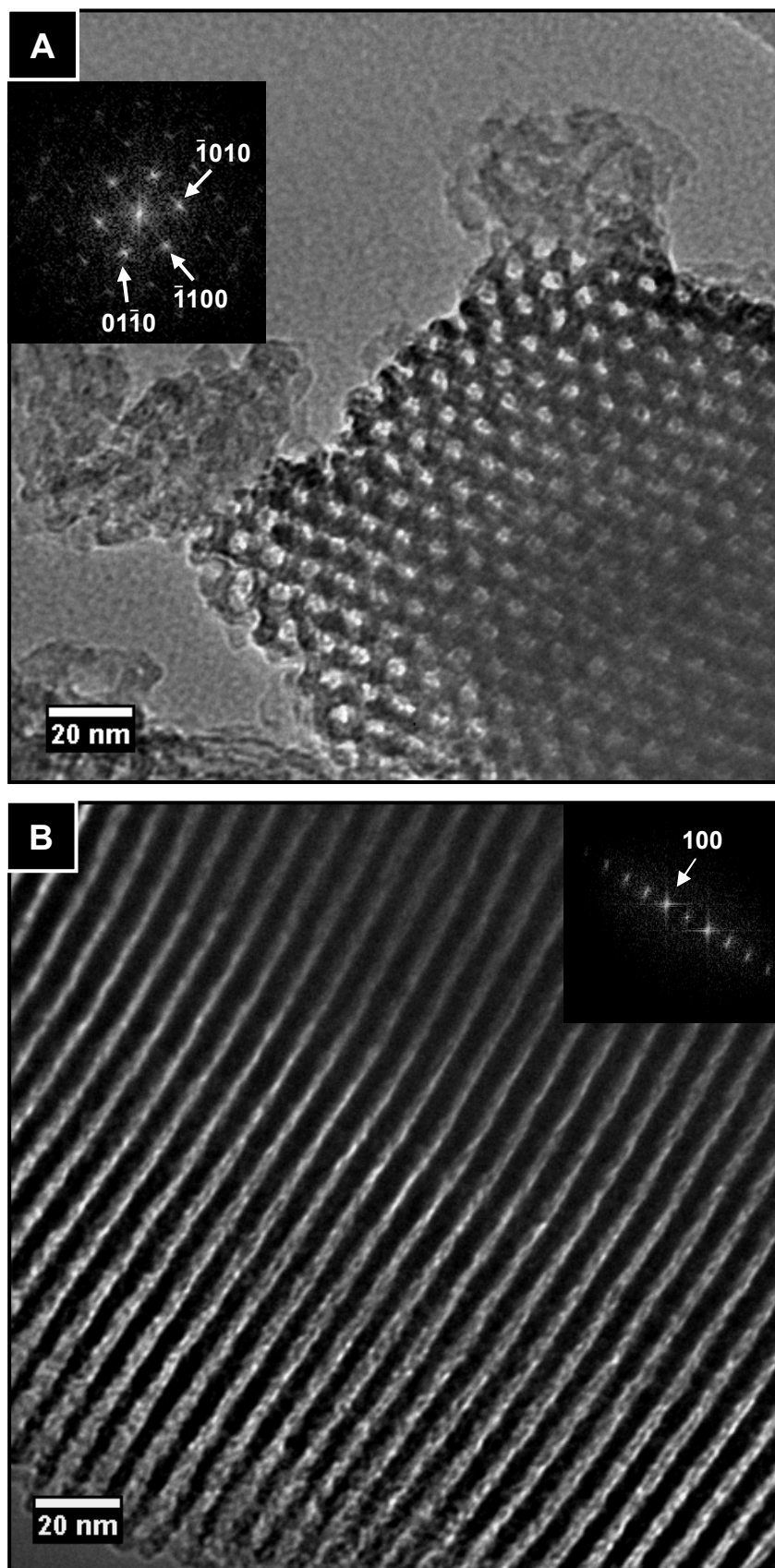
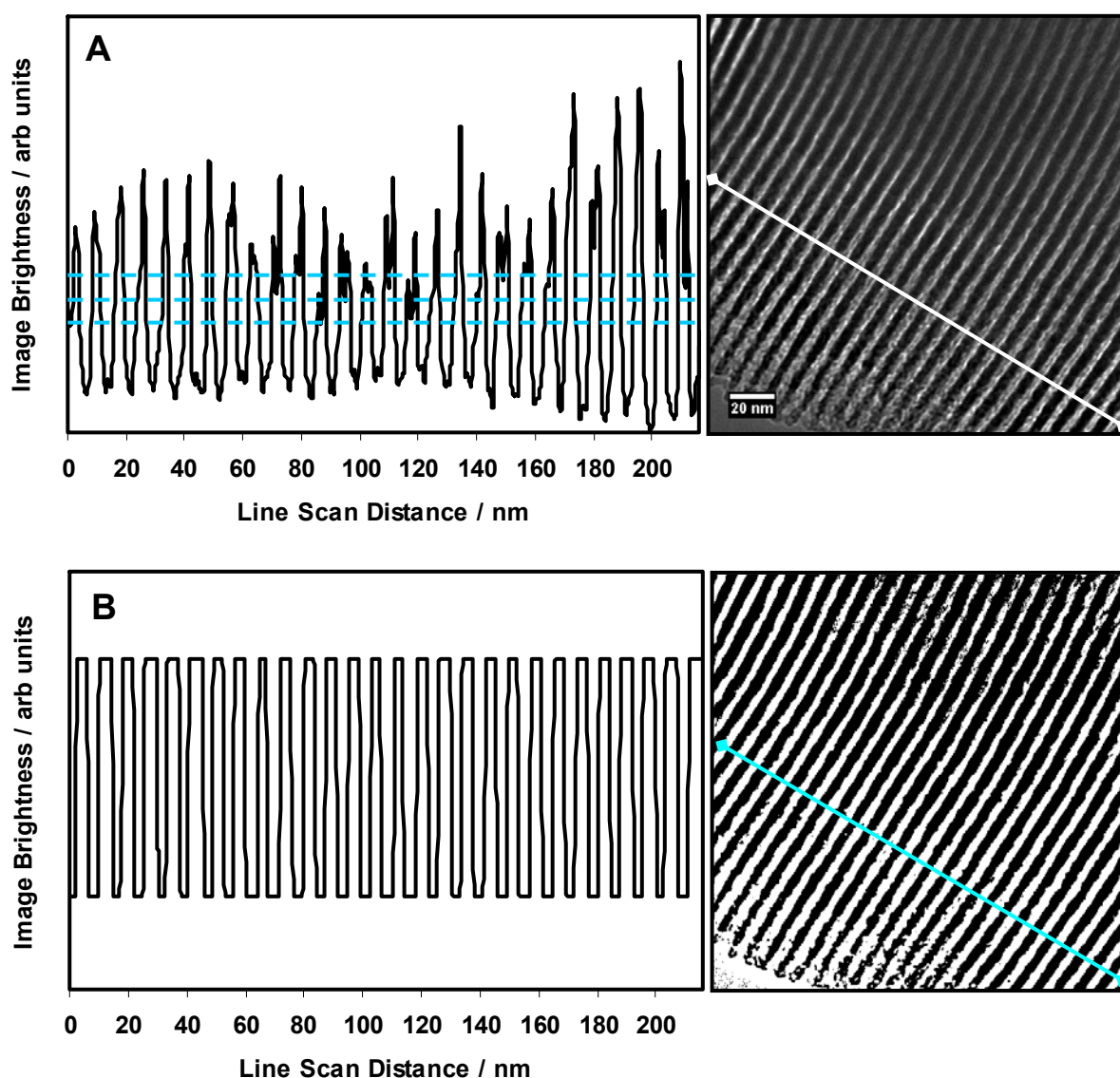


Figure 5.3.4: TEM images of SBA-15: [A] HRTEM image viewed down the [0001] zone axis with inset DDP of the entire image; [B] HRTEM image viewed down the [100] zone axis with inset DDP of the entire image.

Investigations into pore and wall-width analysis using contrast-line scanning orthogonal to the pores are shown in Figure 5.3.5. The example presented was based on Figure 5.3.4B. Without modifying the image, sharp peaks were observed (Figure 5.3.5A) as the contrast increased steadily from the centre of the pores to the centre of the walls. In this analysis the pore and wall sizes could not be accurately determined as taking measurements at various peak heights would present different results. Attempts at adjusting the image threshold using analysis software (Figure 5.3.5B) produced a more distinct boundary between the pores and the walls, but the threshold limit was set arbitrarily. This is illustrated in Figure 5.3.5C where a higher threshold leads to exaggeration of the pore wall size. This meant that pore and wall sizes could not be obtained accurately using this method. This method could be used to measure d-spacings from the image, for example, along a distance of 200.5 nm there are 26 peak maxima giving a pore spacing of 7.71 nm. To ensure this technique is accurate the line scan must be perpendicular to the pores, and in SBA-15 the pores are curved in the [100] direction. This data can be generated mathematically, with less human error, by FFT (DDPs).



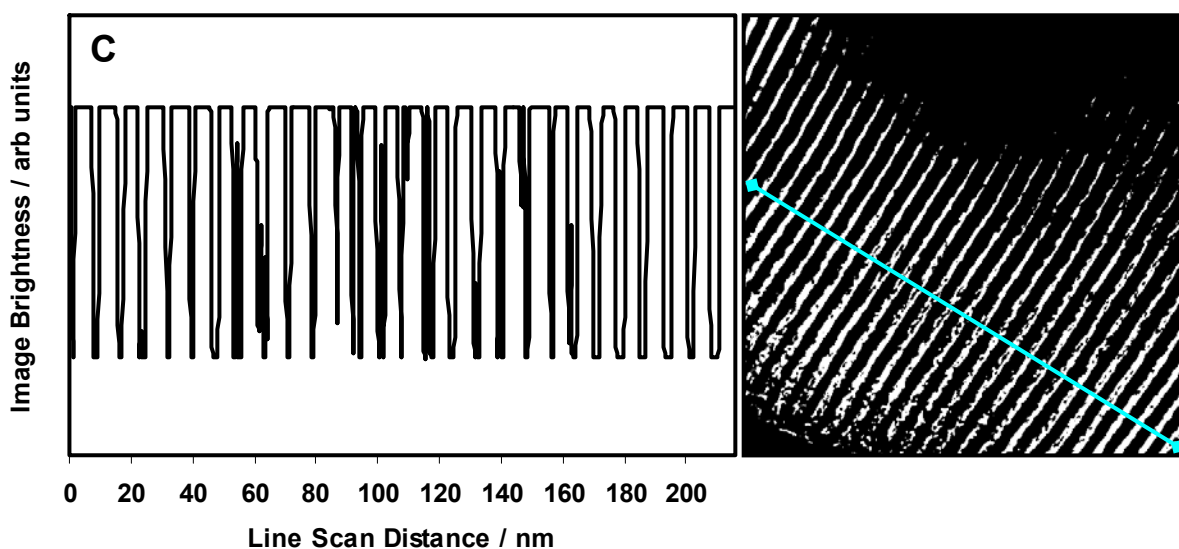
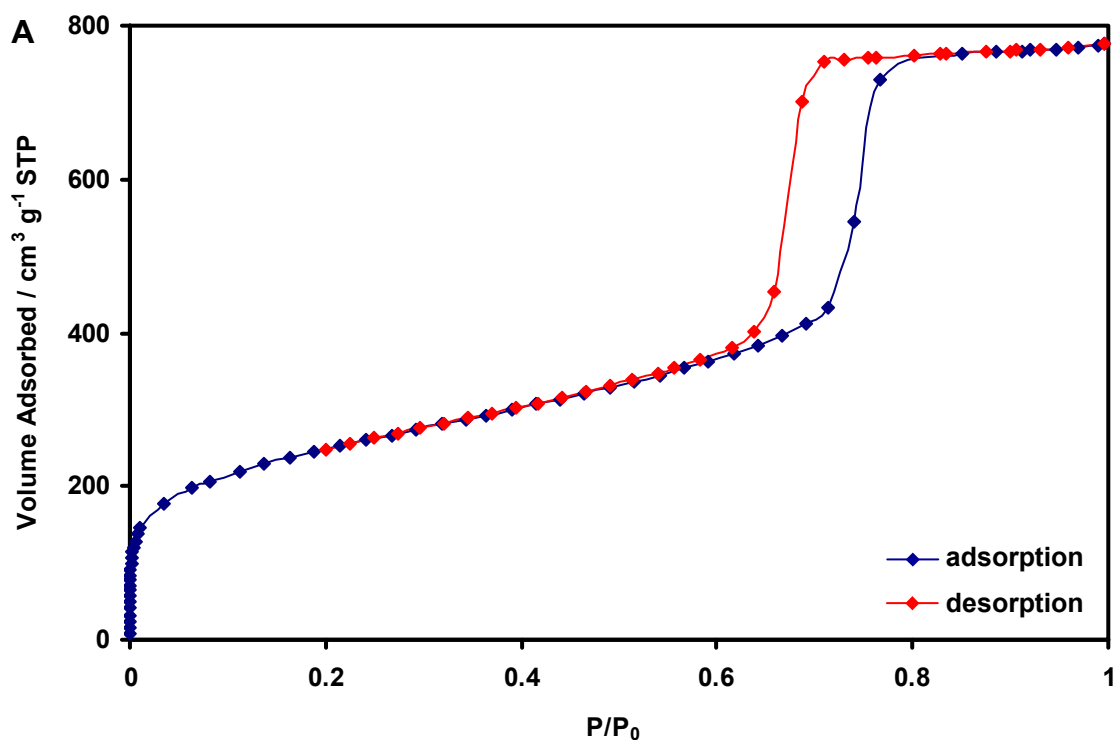


Figure 5.3.5: Line scans of Figure 5.3.4: [A] no image adjustment; [B] with image threshold adjustment; [C] with increased image threshold adjustment. TEM images appended showing line-scans and the effects of the image adjustments.

5.3.2 KIT-6

From physisorption results, the specific surface area and pore volume for KIT-6, prepared in a number of batches, were determined to be 840-990 m^2g^{-1} and 1.2-1.4 cm^3g^{-1} , respectively. The adsorption-desorption isotherm was Type IV with Type H3 hysteresis (Figure 5.3.6). This adsorption behaviour is typical of mesoporous materials with capillary condensation in mesopores. The pore-size distribution showed peaks at 6.4-7.2 nm. The micropore volume was calculated to be 0.069 cm^3g^{-1} by t-plot analysis.



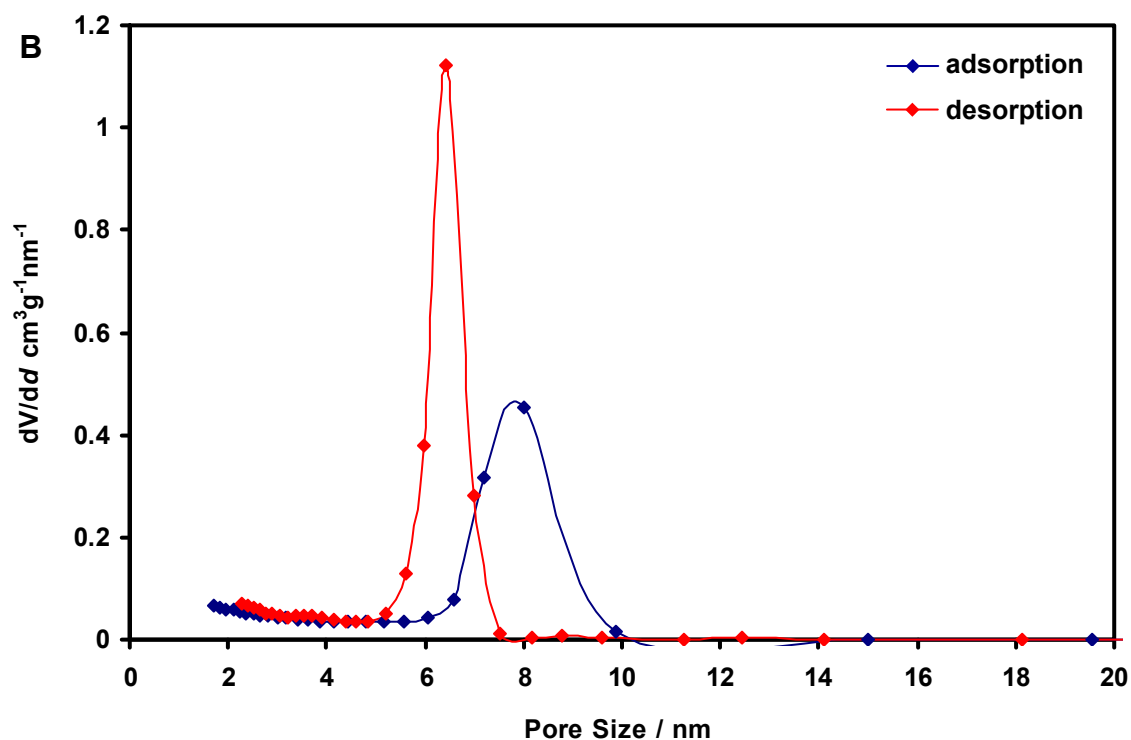
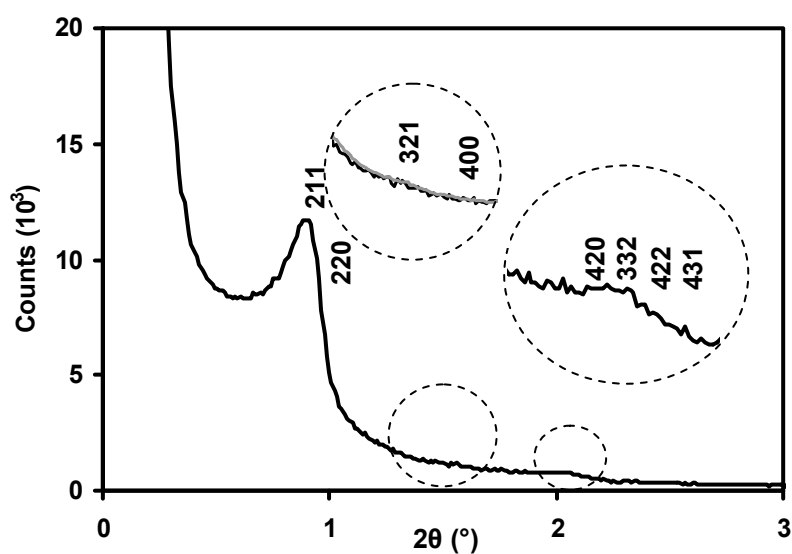


Figure 5.3.6: [A] Physisorption isotherm and [B] pore size distribution for KIT-6.

The diffraction pattern obtained by SAXS had only one clear peak at $2\theta = 0.92^\circ$ which was indexed to the {211} reflection, and two sets of overlapping shoulder peaks that correlated to a multitude of peaks seen in the literature (Figure 5.3.7).¹¹



Peak 2θ (°)	index	d-spacing (nm)
0.92	211	9.6
1.59	321, 400	5.6
2.06	420, 332, 422, 431	4.3
Other		minor/overlapping peaks

Figure 5.3.7: SAXS of KIT-6 with expected peaks indexed. 5 point moving trend line added for {321} and {400} peak insert.

TEM images showed large particles, some larger than 1 μm across, that contained arrays of ordered mesopores across their entirety. Figure 5.3.8A shows an agglomeration that may be due to overlapping particles. Three areas have had DDPs taken and all spots index to the (211) pore orientation with a pore spacing of 7.2 nm, although the pores in the upper left were in a different zone axis. The two lower DDPs both index to the same [210] zone axis pattern. The pores were highly uniform along their length. This TEM image came from the KIT-6 batch that was subsequently used for synthesising Ceria-K-I and Ceria-K-V₁ in this thesis.

Figure 5.3.8B shows a TEM image of KIT-6 down the [111] zone axis where it appears that the pores were arranged hexagonally with a pore spacing of 9.2 nm equivalent to the [220]. This is within 7.6 % of the [211] spacing, calculated using the lattice constant. Figure 5.3.8C shows a different particle where the pores are arranged in a rhombus, similar to the DDP in Figure 5.3.8A. This is a [210] zone axis with pore spacings of 9.7 nm for the [211] pores. The variation in the DDPs was noticeable when measuring spacings and angles. For example, in Figure 5.3.8C, the calculated angle between (211) spots was 80.40°. The two measured angles, on opposite sides of the (000) spot were 80.48 and 86.2°. The four d-spacings were 9.7 ± 0.8 nm, but the variation could be as high as ± 1.2 nm by collecting more extreme results. These TEM images for Figures 5.3.8B and C came from the KIT-6 batch that was subsequently used for synthesising Ceria-K-V₂ and CGO-V₂.

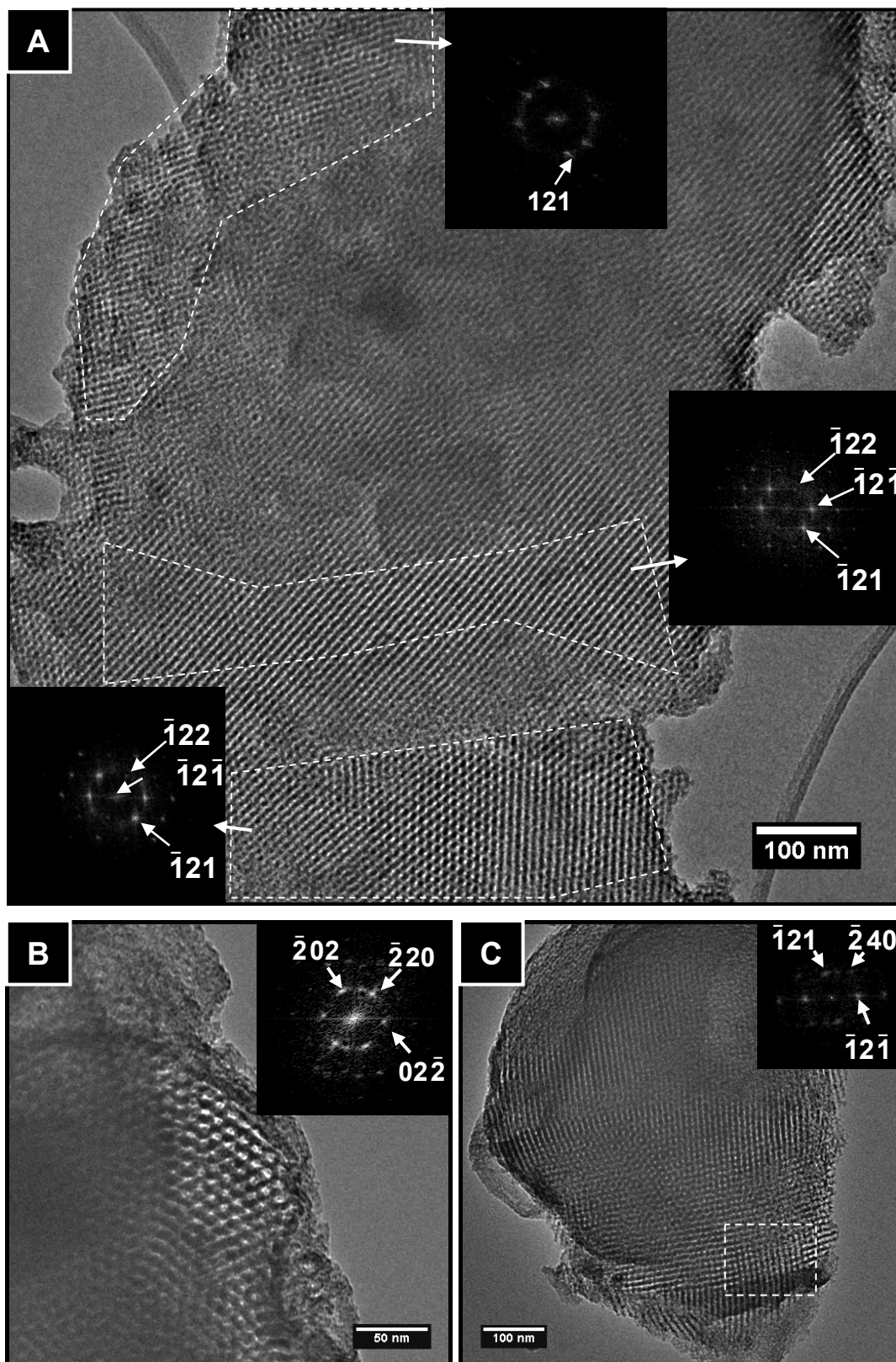


Figure 5.3.8: TEM images of KIT-6: [A] large particle with inset DDPs of indicated regions confirming the [210] zone axis; [B] image of KIT-6 viewed down the [111] zone axis with inset DDP of the entire image; [C] image of KIT-6 viewed down the [210] zone axis with inset DDP of the indicated region.

5.3.3 FDU-12

From physisorption results, the specific surface area and pore volume for FDU-12 were determined to be $616.6 \text{ m}^2\text{g}^{-1}$ and $0.50 \text{ cm}^3\text{g}^{-1}$, respectively. The adsorption-desorption isotherm was Type IV with Type H2 hysteresis (Figure 5.3.9) typical of a mesoporous material with bottlenecked pores. The pore-size distribution showed a narrow peak at 8.4 nm on the adsorption trace and a very sharp peak at approximately 4 nm on the desorption trace. The micropore volume was calculated to be $0.055 \text{ cm}^3\text{g}^{-1}$ by t-plot analysis.

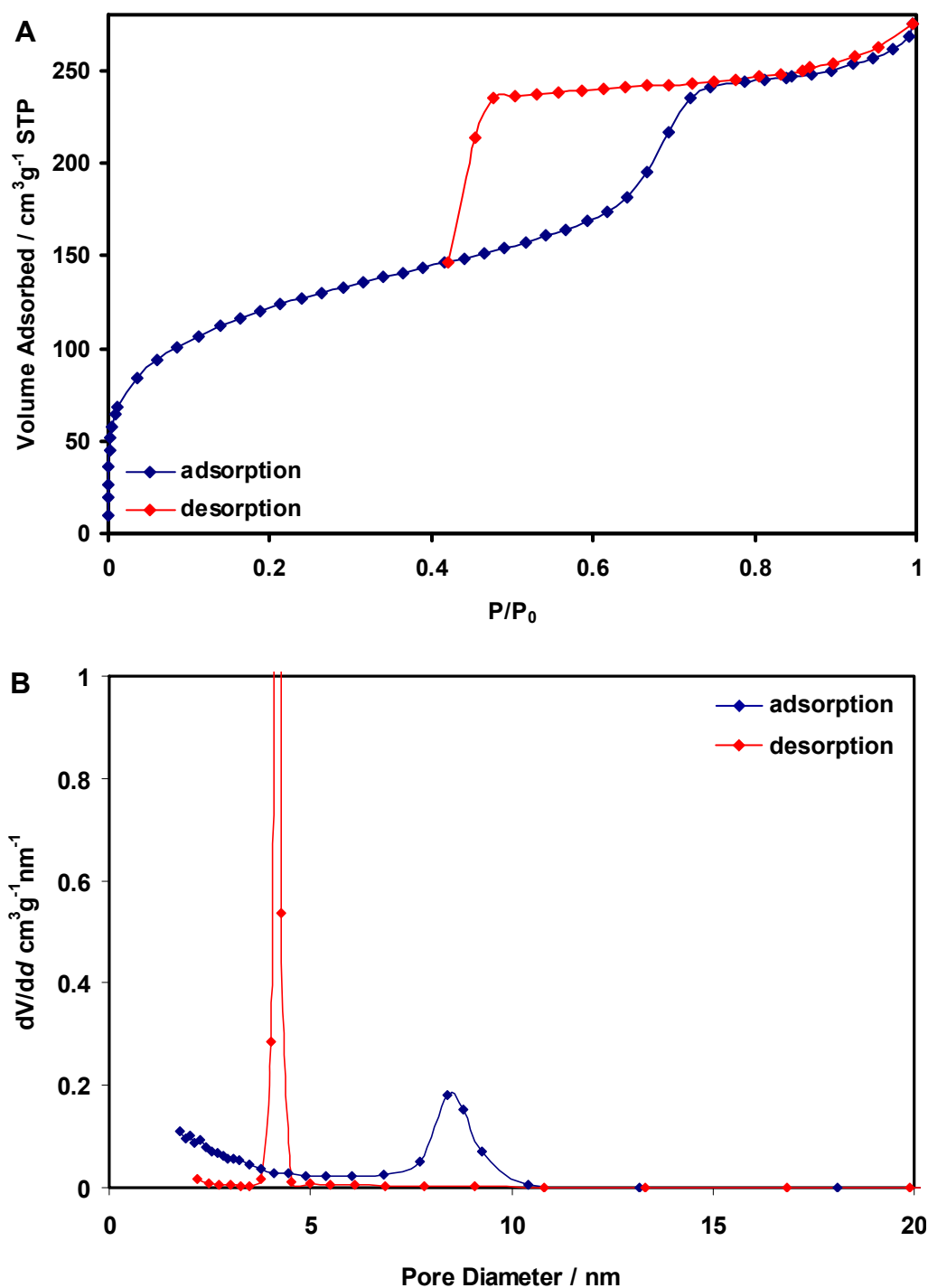


Figure 5.3.9: [A] Physisorption isotherm and [B] pore size distribution for FDU-12.

FDU-12 was not subjected to SAXS study as it was not used as extensively throughout this investigation as SBA-15 and KIT-6.

TEM images showed the material to be made up of large particles, some larger than 1 μm across, with pores in a cubic arrangement spanning their entirety. Most often, the pores were in a single orientation in each individual particle as shown in Figure 5.3.10A which clearly showed the same pore arrangement across the entire particle as viewed down the [100] zone axis. As with KIT-6, the particles did not form into regular shapes and any outgrowths appeared to be porous without conforming to the ordered-porous network of the bulk (circled in Figure 5.3.10A). The DDP of this image showed the material to have very uniform pores across the material. The halo around the (000) spots at a radius of approximately 11.8 nm corresponded to a region at the top-right of the image (deduced by taking selected-area DDPs), whilst in DDPs of the pores in the lower left of the image this halo feature was negligible. The origins of this halo were unidentified.

Figure 5.3.10B shows the pores viewed down the [110] zone axis. The pores appeared in a diamond arrangement when viewed down this axis. The less focused pores in the left of the image show that the pores continue into the thicker part of the particle. This was the imaging limit due to the particle being opaque to electrons in this region because of its thickness. The DDP confirmed that this is the [110] zone axis with the (111) and (220) pores giving d-spacings of 9.6-13.4 and 8.0-8.9 nm, respectively. The large variation in the (111) spacing was attributed to small variations in the porous structure (visible in the DDP), and the particle being slightly misaligned - the angle between $d_{\bar{1}11}$ and $d_{1\bar{1}1}$ was measured to be 81.2° rather than 70.5° as expected. The ratios for the (111) and (220) d-spacings were within the range reported in the literature.¹³

The (100) reflections in both DDPs (taken on the major axis only for Figure 5.3.10D) corresponded to a d-spacing of 10.5 nm.

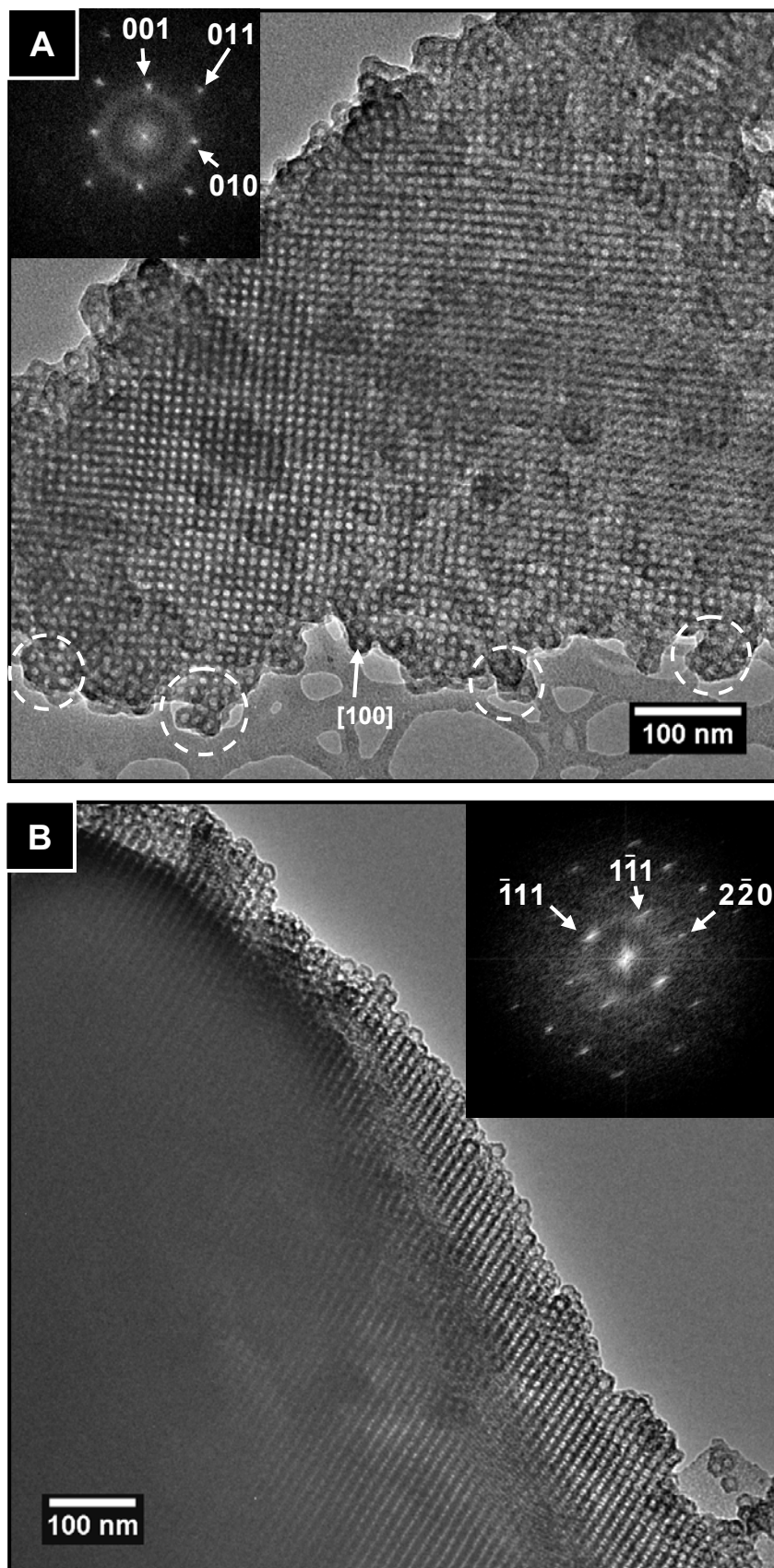


Figure 5.3.10: TEM images of FDU-12: [A] particle viewed down the [100] zone axis with inset DDP of the entire image (regions indicated do not conform to the pore matrix of the rest of the particle); [B] particle viewed down the [110] zone axis with inset DDP of the entire image.

5.4 Discussion

The results presented in Section 5.3 were consistent with those reported in the literature for SBA-15, KIT-6 and FDU-12. Physisorption results showed all materials to have very high specific surface area and large pore volumes. The variation in specific surface area between batches was large and likely attributed to temperature fluctuations (the surfactant micelles change radius with temperature). As the project progressed temperature effects were reduced by improving the environmental insulation around the equipment to reduce these fluctuations. This resulted in a specific surface area consistently at the higher end of the reported ranges. The physisorption isotherms were consistent with mesoporous materials (Type IV). All three mesoporous silicas also showed hysteresis typical of mesoporous materials with FDU-12 showing Type H2 hysteresis expected for bottlenecked pores (adsorption into large cages but desorption limited by the pore entrances). The pore shape could not be conclusively determined for the other materials from the hysteresis curves. Attempts at SAED could not resolve the diffracted spots from the central undiffracted spot, but FFT allowed useful numerical data to be elicited from the TEM images without having to measure pore spacings from the images themselves. It is worth noting that the method of preparation of the TEM grids meant that only the finest particles were present on the grids. Large aggregates were allowed to settle out of suspension during preparation so that only the smallest stayed in suspension, and the images taken were generally of selected areas which represent a very small fraction of the sample. This meant that while quantitative data such as d-spacings could be derived, it was difficult to measure bulk properties using TEM.

There were some discrepancies within the results, and between the experimental data and the literature:

- The pore sizes observed in TEM were smaller than those observed in the pore size distribution curves.
- The SAXS data was not as well defined as some of the literature results (the signal to noise ratio was lower and the peaks were broader).
- In the pore size distribution curves, a peak at 3.8 nm was seen on the desorption branch in some batches of mesoporous silica where there was no corresponding peak in the adsorption branch (shown to be particularly strong for FDU-12 but also present in some batches of SBA-15 and KIT-6).

With regards to investigating porosity by TEM, it was determined that TEM allowed better examination of the nanorods than of the pores themselves due to the three-dimensional nature of the materials. For example in Figure 5.3.10A, despite being a well-aligned image, the 'holes' in the material were not the pores, but the smallest gap in the silica that the electron

beam could focus on. Figure 5.4.1 shows that the ‘holes’ observed in the images could, in fact, correspond to the pore entrances, which were significantly smaller than the pores themselves. Whether the pores themselves or the pore entrances were imaged would depend to some extent on the position of the focal plane of the microscope. Where the depth of field of the TEM is larger than the pore diameter, the pore entrances would be expected to be visible in the image. This would be expected to be the case for FDU-12 and KIT-6. Despite this, TEM remained the best technique for examining the quality of these materials as long as it was used in conjunction with knowledge of the expected three-dimensional matrix.

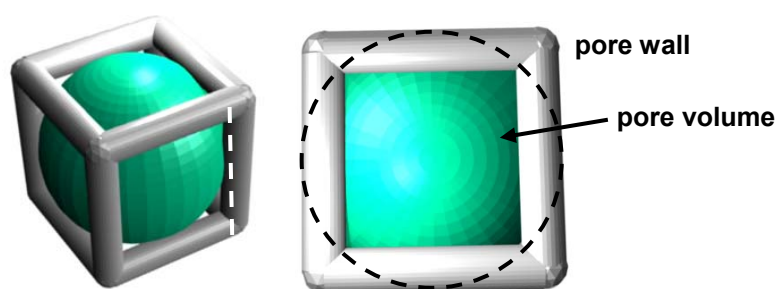


Figure 5.4.1: Model showing pore size relative to pore walls.

The SAXS patterns could not be refined as well as in some literature reports for these materials despite repeated attempts to improve resolution. The best results, that is, those with the highest signal to noise ratio, were achieved by increasing the sample thickness and scan time. It is possible that further extending the scan times would further enhance results by increasing resolution. However, it was decided, since the equipment was not on-site and other analytical techniques showed results consistent with the literature, that a prolonged SAXS investigation of the silica materials would not yield significantly new data. The d-spacings obtained from the DDP data fell under the SAXS curves, but the d-spacings showed some variation between particles in TEM. This highlights the difference between the accuracy of TEM and the derived DDPs and the advantage of bulk analysis techniques, such as SAXS, which obtain average values.

The anomalous peak in the pore size distribution curves (Figures 5.3.1 and 5.3.6) was attributed to the tensile strength effect (TSE), characteristic in that the peak is missing in the adsorption branch. The nature of the TSE is discussed in-depth by Groen et al.¹⁵⁴ Essentially, pores smaller than approximately 4 nm are filled and emptied at similar pressures leading to no hysteresis in the physisorption isotherm. In mesopores, condensation is preceded by a metastable cylindrical meniscus and evaporation by a hemispherical meniscus, which produces hysteresis. During desorption, at a sufficiently low pressure for the condensate in

the smaller pores to evaporate ($P/P_0 \approx 0.45$ for N_2 at 77 K), there is a sudden decrease in the volume of adsorbate adsorbed (observed in Figure 5.3.9A as a forced closure of the hysteresis loop). When this data is fed into the BJH equation it translates into an artificial peak on the desorption branch at 3.8 nm, which is a property of the adsorbate, rather than the material being measured.

The TSE can also be exacerbated in pore networks when the adsorbate condenses in a pore but is then bottlenecked. If the pore entrance is sufficiently small any condensate evaporating in the pores will then condense again in the channel giving only information on the channels in the desorption branch. This will produce a Type H2 hysteresis curve as was observed in Figure 5.3.9A.

5.5 Summary

Table 5.1: A summary of the properties of SBA-15, KIT-6 and FDU-12 synthesised in Chapter 5. Ranges are given if multiple measurements were taken and variability could affect subsequent experiments.

	BET specific surface area (m^2g^{-1})	Pore volume (cm^3g^{-1})	t-plot micropore volume (cm^3g^{-1})	BJH pore size(nm)	d-spacing (nm) TEM	d-spacing (nm) SAXS
SBA-15	800-890	1.0-1.1	0.075	5.9-7.3	7.5-8.6 [100]	9.3 [100]
KIT-6	840-990	1.2-1.4	0.069	6.4-7.2	7.7-9.7 [211]	9.6 [211]
FDU-12	616	0.5	0.055	8.4, <4*	10.5 [100]	

* the channel size of FDU-12 was unable to be determined due to the TSE as discussed in Section 5.4.

All three silica templates were successfully synthesised and analysis showed them to be consistent with literature reports (Table 5.1). Yields were high and sample quality appeared to be good. The best analytical techniques for analysing these materials were TEM, and the DDPs of TEM images for analysis of sample quality, and data derived from physisorption experiments for quantitative analysis. SAXS was a good technique for bulk analysis but lacked the resolution of the other methods for the mesoporous materials examined here to allow it to be used as a surveying technique.

Chapter 6

Mesoporous Ceria and CGO: Preliminary Experiments

6.1 Experimental Philosophy

The initial materials chosen to be synthesised were based on ceria. Ceria was chosen for the properties it might have when made as an ordered mesoporous material. Mesoporous ceria had been historically investigated the most of the mesoporous materials that would be attempted in this project. The literature investigation indicated that the most successful and flexible method would likely be nanocasting. Increasing the product quality and yields would be the primary goals. The literature investigation had suggested that using nanocasting may lead to a material with an increased thermal stability compared to those prepared by soft templating. Therefore, this method was attempted first. The thermal stability of materials prepared by nanocasting had been attributed to thermal treatment inside the silica template, such as more extensive sintering, that was not possible when using organic templates.^{5, 165} Two new techniques for synthesising mesoporous ceria were also attempted and are described in this chapter. These were acid hydrolysis and precipitation. The syntheses of nanoparticulate and bulk reference materials are also described in this chapter.

6.2 Experimental

6.2.1 Reference Materials

Reference materials were synthesised to compare the morphology, surface texture and properties of ceria synthesised without ordered mesopores.

Bulk ceria (Ceria-X-P) was synthesised by adding 2 M NaOH drop-wise to a saturated solution of $\text{Ce}(\text{NO}_3)_3 \cdot 6\text{H}_2\text{O}$ in water while stirring. Once sufficient NaOH had been added to gel the mixture, the gel was dried overnight in an oven at 95-105 °C. The resulting solid was then calcined at 300 °C for 5 h in air (ramp rate 5 °C min⁻¹ using a tube furnace) to form ceria.

Nanoparticulate ceria (Ceria-X-Cit) was synthesised using a modified citrate method based on that reported by Muccillo *et al.*¹⁶⁶ 10 g of $\text{Ce}(\text{NO}_3)_3 \cdot 6\text{H}_2\text{O}$ was dissolved in 250 cm³ water and stirred at room temperature until dissolved. To this was added 8.85 g citric acid and the solution was stirred for 10 h. The temperature was raised to 80 °C and maintained until a dry foam had formed indicating the loss of water and $\text{NO}_{2(g)}$. The resulting solid was calcined at 300 °C for 5 h in air (ramp rate 5 °C min⁻¹) to form ceria.

Both materials were ground lightly for less than one minute with a pestle and mortar prior to investigation to break up large aggregates.

6.2.2 Incipient Wetness Impregnation Technique

The IWIT is a common synthetic method for the synthesis of mesoporous materials (as discussed in Section 1.2.2). It has been used in previous reports for the synthesis of mesoporous ceria and CGO using SBA-15, KIT-6 and FDU-12 silica templates (Sections 1.1.2-4). The purpose of this experiment was to reproduce literature results and, if successful in synthesising a well ordered mesoporous ceria in high yields, to examine the catalytic properties of the material.

IWIT syntheses were conducted as per a literature procedure.⁸¹ In a typical experiment, 4.7 g of $\text{Ce}(\text{NO}_3)_3 \cdot 6\text{H}_2\text{O}$ was dissolved in 20 cm³ ethanol and added drop-wise to 1 g of mesoporous silica template (SBA-15 and KIT-6; synthesised as in Section 5.2). This was dried in an oven at 60 °C overnight and then calcined at 400 °C for 6 h in air (ramp rate 1 °C min⁻¹). A further 3.3 g of $\text{Ce}(\text{NO}_3)_3 \cdot 6\text{H}_2\text{O}$ in 20 cm³ ethanol was allowed to absorb into the mesoporous silica as above. The resulting solid was dried in an oven at 60 °C overnight and then calcined at both 400 and 600 °C for 6 h in air (ramp rate 1 °C min⁻¹). The silica template was digested by stirring with approximately 20 cm³ 1-2 M NaOH. Buchner filtration was used to recover the sample material from the solution. The sample was sucked dry and the digestion step was repeated three times. The resulting solid was washed with water and dried overnight in an oven at 105 °C.

Cerium acetylacacetate ($\text{Ce}(\text{AcAc})_3 \cdot x\text{H}_2\text{O}$) dissolved in acetone was also used as a precursor solution in the IWIT of SBA-15. All other aspects of the experimental procedure were unchanged.

6.2.3 Acid Hydrolysis

The acid hydrolysis synthesis was analogous to the syntheses of the silica templates detailed in Section 5.2. Literature reports using the co-operative self-assembly pathway for ceria to date had used neutral conditions, but it has been established that the effect of the hydrochloric acid is twofold: the low pH causes protonation of the polyether chain and the

chloride ions complex to the surfactant micelle regulating the rate of hydrolysis.¹⁶⁷ The challenge was that ceria is soluble at low pH and therefore product yields were likely to be low.

Three cerium salts were examined as sol-gel precursor candidates. These were cerium acetylacetonate hydrate ($\text{Ce}(\text{AcAc})_3 \cdot x\text{H}_2\text{O}$), cerium citrate ($\text{Ce}(\text{Cit})_3$, as synthesised in Section 6.2.1 but not calcined), and cerium acetate ($\text{Ce}(\text{OAc})_3$, synthesised from $\text{Ce}(\text{OH})_3(s)$ and acetic acid). Preliminary tests showed that, of these three candidates, only $\text{Ce}(\text{Cit})_3$ formed a solid product in acidic media. These tests involved three 25 cm³ beakers containing 20 cm³ of 2 M HCl. Into a beaker was placed 1 g of precursor powder and it was given time to dissolve. $\text{Ce}(\text{Cit})_3$ (cream solid) formed a white solid in the bottom of the beaker and the other two precursor solutions dissolved. After 24 h there was also a white solid in the bottom of the $\text{Ce}(\text{OAc})_3$ beaker. Upon agitation this solid dissolved.

In a typical acid hydrolysis experiment, 2 g of Pluronic P123 was added to 15 cm³ water and 60 cm³ of 2 M HCl while stirring at 35 °C. To this mixture was added sufficient (>10 g) $\text{Ce}(\text{Cit})_3(s)$ powder to form a solid product. The solid formed instantly once sufficient $\text{Ce}(\text{Cit})_3(s)$ powder had been added. The product was then filtered, dried overnight in an oven at 105 °C in air and calcined at 300 °C for 5 h in air (ramp rate 5 °C min⁻¹) to form ceria. The solution was not treated hydrothermally because in the silica template syntheses it had been observed that the elevated temperature increased the solubility of the silica in the acidic solution. Hot filtration had been used before additional silica formed. Ceria is more soluble than silica in acid.¹⁶⁸

6.2.4 Precipitation

A precipitation synthesis was attempted as an alternative to acid hydrolysis. As cerium salts form insoluble hydroxides in alkaline solutions the product yields should be high. The challenge with this synthesis was whether the structure-directing agents would form the cerium hydroxide into mesoporous structures during the precipitation phase.

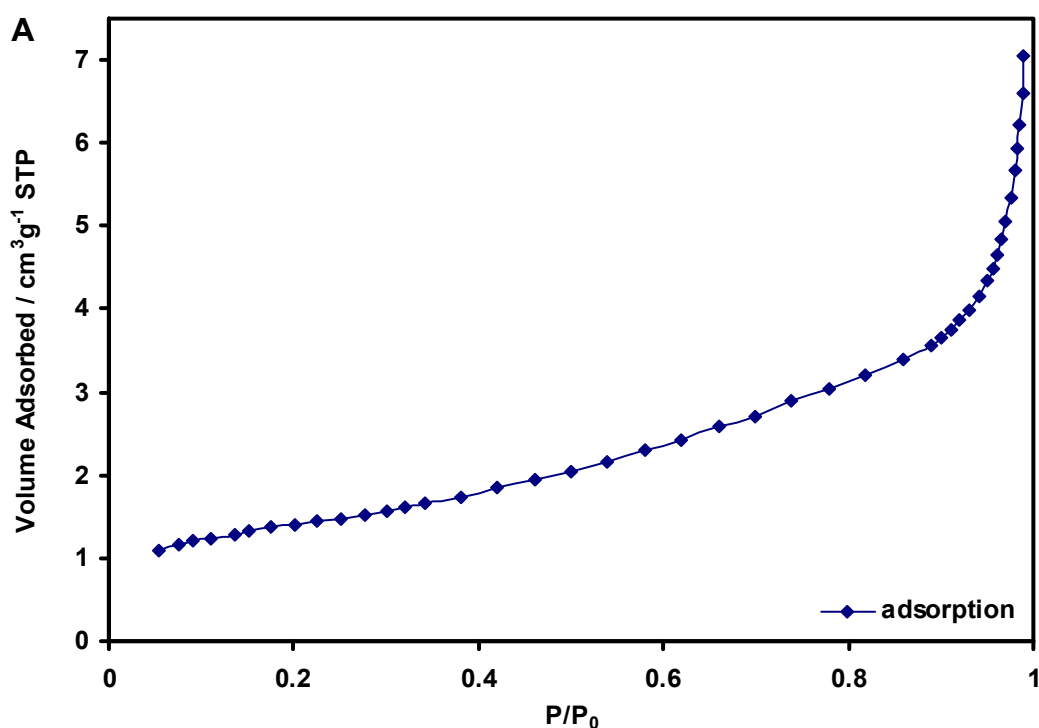
In a typical precipitation experiment, 2 g of Pluronic P123 and 3 g of $\text{Ce}(\text{NO}_3)_3 \cdot 6\text{H}_2\text{O}$ were added to 73 cm³ water and this was stirred for 4-6 h to homogenise the mixture. While stirring vigorously, alkaline solution, either 2 M NaOH or conc. $\text{NH}_3(aq)$, was added drop wise causing a precipitate to form immediately. The resulting precipitate was filtered using Buchner filtration, dried overnight in an oven at 105 °C in air and then calcined at 300 °C for 5 h in air (ramp rate 5 °C min⁻¹) to form ceria.

6.3 Results

The ceria and CGO materials were characterised by TEM, nitrogen physisorption, XRD and SAXS where appropriate.

6.3.1 Reference Materials

From physisorption results, the specific surface area and pore volume of Ceria-X-P were determined to be $4.8 \text{ m}^2\text{g}^{-1}$ and $0.011 \text{ cm}^3\text{g}^{-1}$, respectively. The adsorption isotherm was Type II with very low adsorption values. The desorption isotherm was not reported due to the low adsorption value. This is consistent with a non-porous material and is in agreement with the very low pore volume (Figure 6.3.1). The pore-size distribution showed that there were no well defined pores.



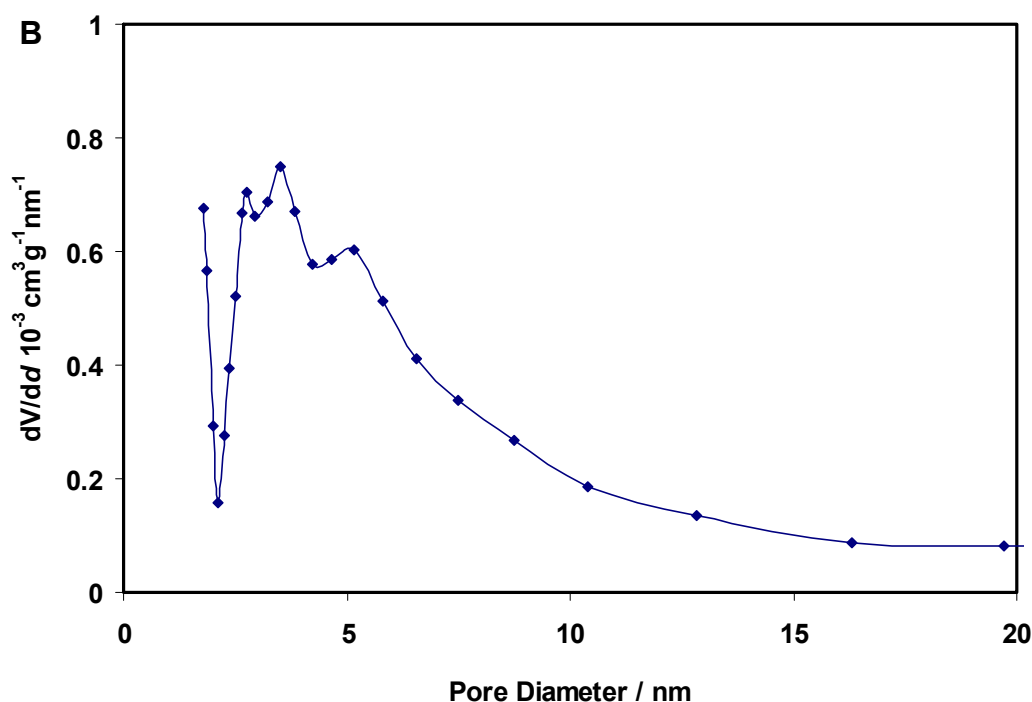


Figure 6.3.1: [A] Physisorption isotherm and [B] pore size distribution for Ceria-X-P.

TEM images of Ceria-X-P showed a large number of single-crystalline nanoparticles with a small particle size range (5-15 nm). The particles were approximately spherical in shape or had formed truncated polyhedra. There were no large agglomerations (dense masses of particles larger than 1 μm) observed using this synthesis temperature as can be seen in Figures 6.3.2A and B. The electron transparency of the groups of particles imaged showed that the agglomerations that were present were not thick. It should be noted that the preparation of TEM specimens was not representative in this respect (as described in Section 4.4.2): only particles that were suspended in the solvent - that is, for which the forces involved in surface tension and Brownian motion exceeded those causing gravitational separation - were transferred onto the TEM holey carbon grid. DDPs of the nanoparticles were consistent with ceria with the fluorite crystal structure and confirmed the expected (111) diffraction spots. Figure 6.3.2C shows that although there were many nanoparticles present and the calcination temperature used appeared to be sufficiently low that significant particle sintering had not occurred, in certain locations the lattice planes of adjacent nanoparticles had aligned across significant distances. This alignment of the crystallographic planes indicated that the ceria nanoparticles had interacted sufficiently with each other, either through interparticle contacts or through local electrostatic effects, to cause localised alignments. It is possible that these could propagate throughout the material prior to grain growth over longer annealing times, or at higher temperatures.

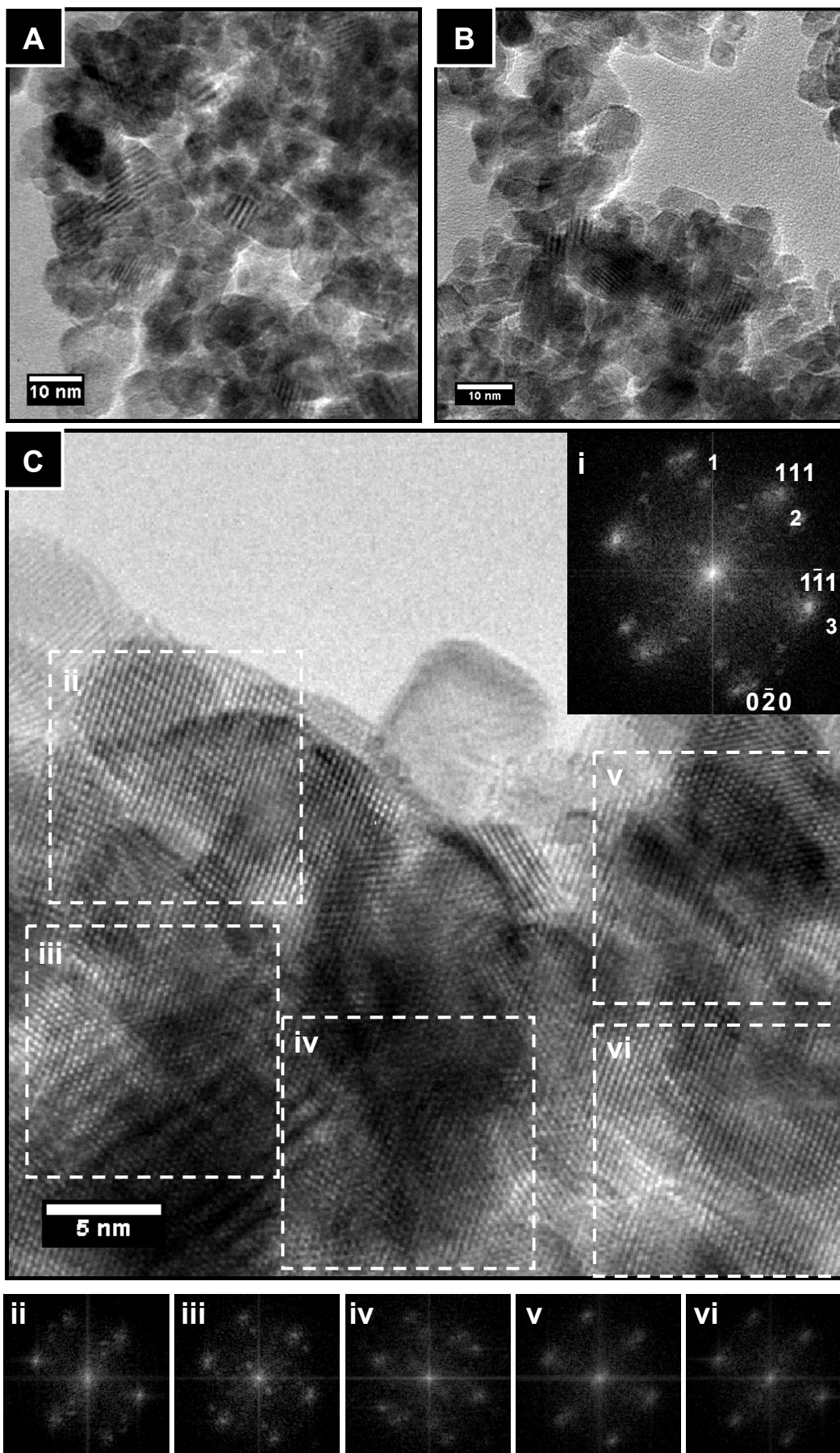


Figure 6.3.2: TEM images of Ceria-X-P: [A,B] TEM images of ceria nanoparticles; [C] HRTEM image of ceria nanoparticles showing aligned lattice planes; [i] DDP of entire image [C]; [ii-vi] DDPs of selected areas indicated in [C].

Table 6.1: Tabulated data from DDPs (i-vi) from Figure 6.3.2: Spots are indexed in the DDP in (i). Data sets are given in d-spacing (nm) and angle (referenced to a common normal for all DDPs, in degrees). When there are two diffraction patterns in a DDP two data sets are given and common data sets in the table are referenced to 'α' and 'β' patterns to show common diffractions.

DDP/Spot	1	2	3
i (pattern α)	0.27 nm	0.31	0.31
	100.3°	48.3	341.0
i (pattern β)	0.35*	0.31	0.31
	100.3	31.3	312.6
ii (pattern α)	0.27	0.33	0.31
	110.3	51.0	340.7
iii (pattern α)	0.28	0.31	0.31
	103.0	49.1	341.6
iv (pattern α)	0.27	0.33	0.32
	106.9	54.6	340.0
iv (pattern β)	0.38*	0.31	-
	94.9	32.6	-
v (pattern α)	0.27	0.31	0.31
	101.9	49.7	339.4
vi (pattern α)	0.27	0.31	0.31
	101.6	45.7	337.7

* inverse-DDPs showed these reflections to be caused by moiré double diffractions.

From physisorption results, the specific surface area and pore volume of Ceria-X-Cit were determined to be $19.3 \text{ m}^2\text{g}^{-1}$ and $0.026 \text{ cm}^3\text{g}^{-1}$, respectively. The adsorption-desorption isotherm was Type II with very low adsorption values. There was no hysteresis observed. The sharp increase at higher P/P_0 values was likely to have been caused by interparticle porosity. This is consistent with a non-porous material and is in agreement with the very low pore volume (Figure 6.3.3). The pore-size distribution showed no well defined peaks except for a single peak at approximately 3.5 nm in the desorption branch (likely to be caused by the TSE described in Section 5.4).¹⁵⁴

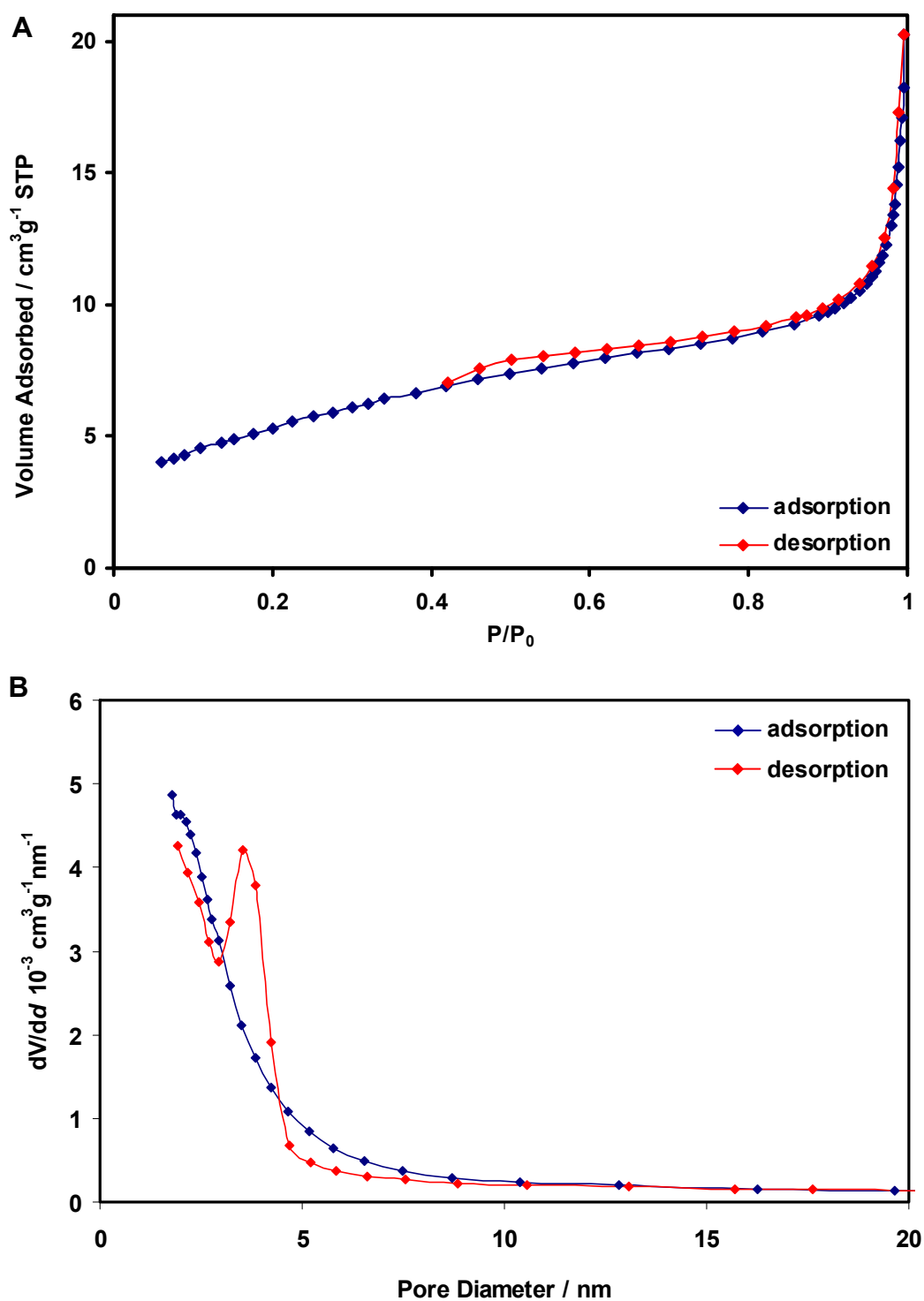


Figure 6.3.3: [A] Physisorption isotherm and [B] pore size distribution for Ceria-X-Cit.

The diffraction pattern obtained by SAXS showed no peaks for Ceria-X-Cit indicating that no ordered pores were detected by this method (Figure 6.3.4). High angle powder XRD showed that the material was consistent with single phase cerium oxide with the fluorite structure ($Fm3m$, ICDD 43-1002; Figure 6.3.5). By applying the Scherrer equation to the peak broadening an average particle size of 32.9 nm was calculated.

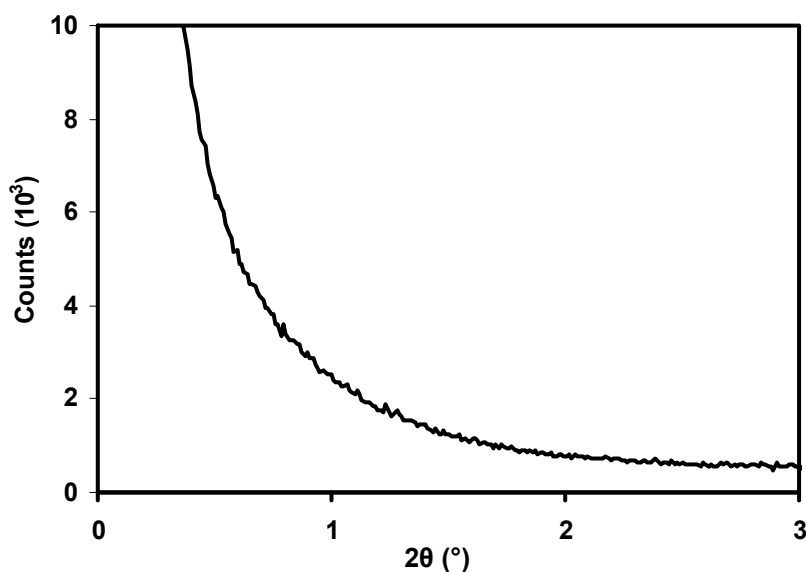


Figure 6.3.4: SAXS pattern of Ceria-X-Cit.

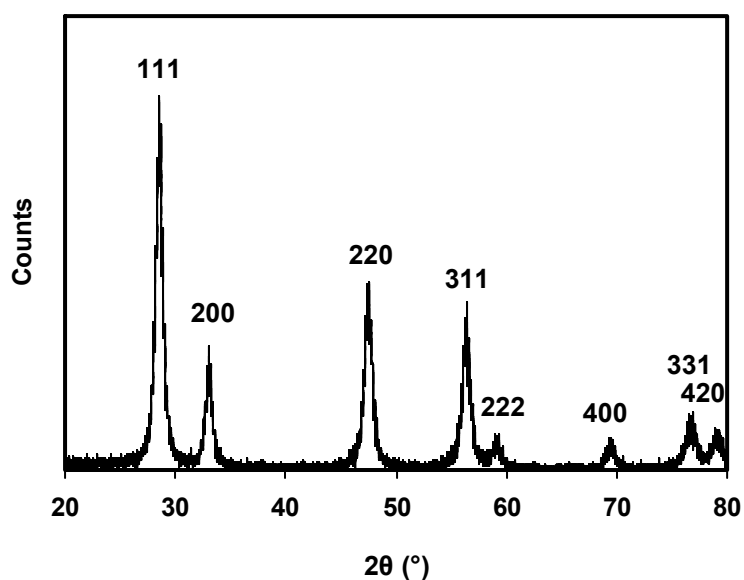


Figure 6.3.5: Powder XRD pattern of Ceria-X-Cit (indexed to ICCD 43-1002).

TEM of Ceria-X-Cit showed nanoparticles with a 15-20 nm diameter that formed agglomerates at least 500 nm across (Figure 6.3.6). TEM indicated that the ceria particles were polyhedral in shape, as observed in Ceria-X-P, and were monocrystalline. DDPs of the images confirmed reflections corresponding to crystalline ceria. Using this synthesis temperature no large monocrystalline particles were observed.

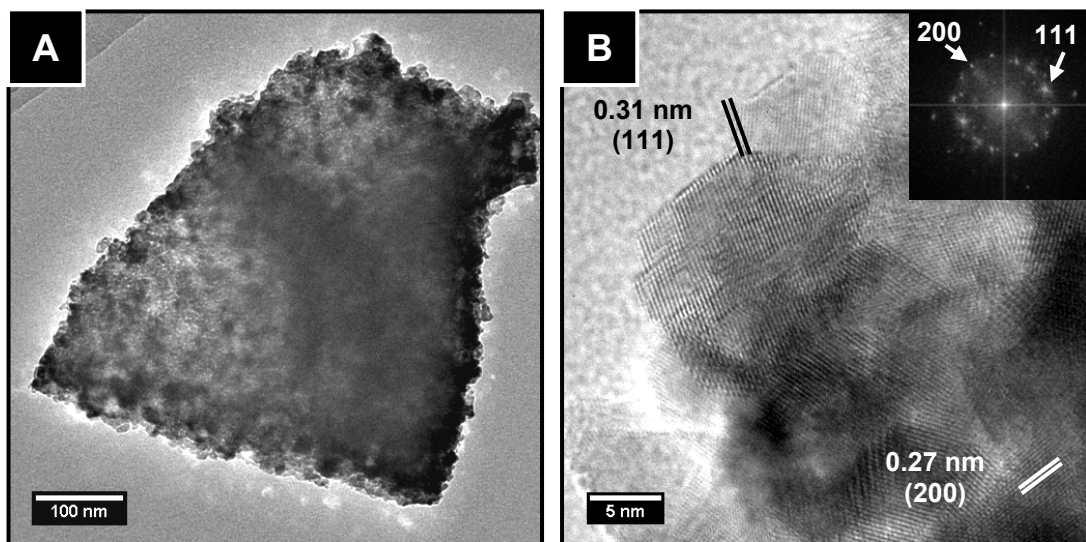


Figure 6.3.6: [A] TEM image showing the bulk structure of Ce-X-Cit; [B] HRTEM image of Ceria-X-Cit with inset DDP showing the crystalline structure of the nanoparticles.

6.3.2 Ceria Prepared Using SBA-15 and the IWIT

TEM analysis of Ceria-S-I confirmed the sample to have domains of ordered mesoporous material. Figure 6.3.7A shows a particle viewed down the [100] mesopore zone axis. The shape of the pores can be seen to be similar to the 1D parallel pore structure seen previously in SBA-15 (Figure 5.3.4E). The pores are also curved along their length while retaining the parallel pore structure, as in the silica template. It can also be seen that there is a significant amount of disordered nanoparticulate material around the porous particle. The low occurrence of the ordered mesoporous material in the sample led to the conclusion that the sample was predominantly disordered nanoparticulate ceria. The covering layer of nanoparticles prevented a DDP being obtained to deduce the accurate pore spacing for this particle. Measuring the pores from the image manually gave a pore spacing of 11-12 nm. Figure 6.3.7B shows a HRTEM image of the structure of the nanorods that comprise the mesoporous particle. In this particle they were made up of single crystals of ceria that had formed irregular shapes. The shapes of the nanorods were similar to the shapes of the pores of the SBA-15 template, except at the ends where larger faceted crystals had grown. The lattice planes of the nanorods in this particle also had common crystallographic alignments. Predominant lattice alignments have been indicated on the diagram and it can be seen that adjacent nanorods have common crystallographic lattice alignments.

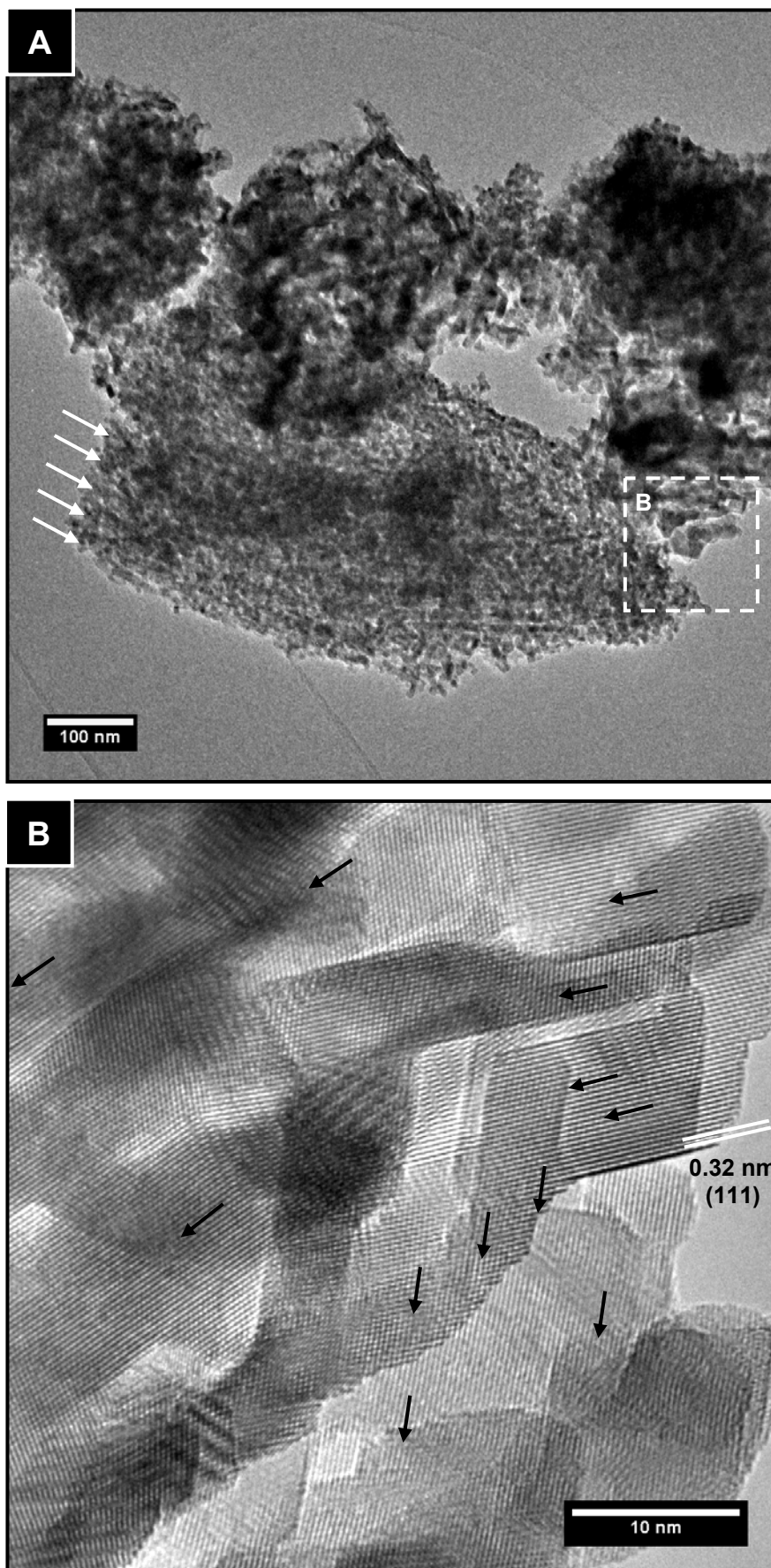


Figure 6.3.7: TEM images of Ceria-S-I: [A] TEM image of large mesoporous particle exhibiting a morphology similar to SBA-15 with the pore direction indicated with arrows; [B] HRTEM image showing the crystal structure of the pore walls with crystallographic planes indicated with arrows.

Figure 6.3.8A shows a large ordered mesoporous ceria particle that shows no curvature along the [100] mesopore zone axis. In this particle the nanorods were not single crystalline as described on the previous pages but were comprised of fused nanoparticles as shown by the HRTEM images (Figures 6.3.8B and C). A pore spacing of 8.5 nm was measured using DDPs from the (100) spots which was consistent with the SBA-15 pore spacing of 7.5-8.6 nm (Section 5.3.1).

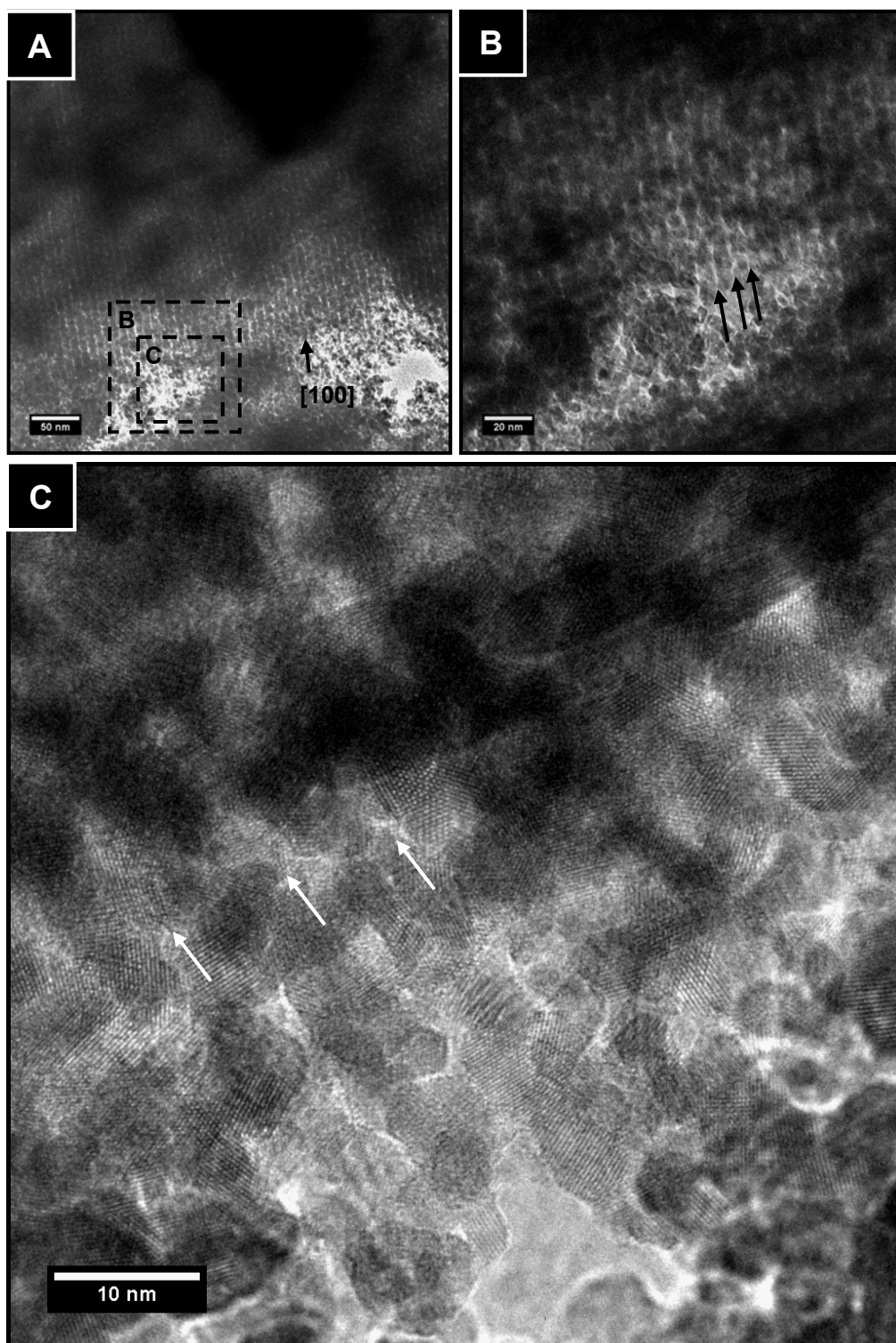


Figure 6.3.8: [A] TEM image of a large mesoporous particle viewed down the [100] zone axis; [B] enlarged image of [A] showing mesopores; [C] HRTEM image of [A] showing the pore walls are comprised of nanoparticles. Arrows indicate the direction of the pores.

Attempts at using the IWIT with a different solvent ($\text{Ce}(\text{AcAc})_3 \cdot x\text{H}_2\text{O}$ in acetone) were much less successful than using $\text{Ce}(\text{NO}_3)_3 \cdot 6\text{H}_2\text{O}$ in ethanol. $\text{Ce}(\text{AcAc})_3 \cdot x\text{H}_2\text{O}$ is only slightly soluble in acetone and insoluble in the other solvents investigated (water, ethanol, hexane and isopropyl alcohol). No ordered mesoporous material was visible in a TEM investigation. Large particles were observed that were consistent with the shape of SBA-15 particles, but no mesopores were visible (Figure 6.3.9A). HRTEM images showed that the sample was comprised of disordered nanoparticles and nanorods (Figure 6.3.9B).

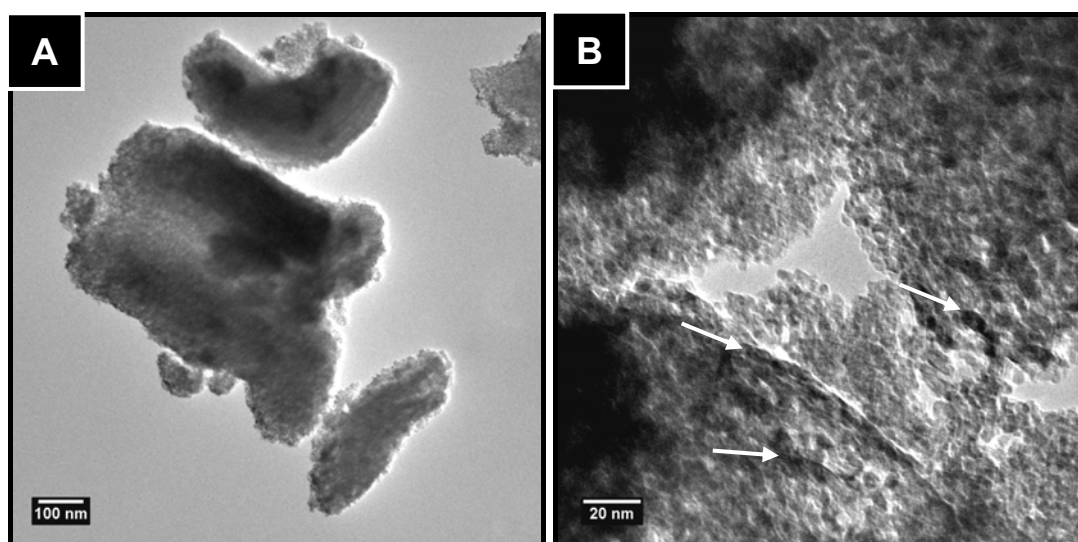


Figure 6.3.9: [A] TEM image of Ceria(AcAc)-S-I showing large particles in the shape of SBA-15 particles without mesopores; [B] TEM image showing the material is comprised of nanorods, as indicated with arrows, and nanoparticles.

6.3.3 Ceria Prepared Using KIT-6 and the IWIT

From physisorption results, the specific surface area and pore volume of Ceria-K-I were determined to be $129.1 \text{ m}^2\text{g}^{-1}$ and $0.25 \text{ cm}^3\text{g}^{-1}$, respectively. The adsorption-desorption isotherm was Type IV with Type H3 hysteresis (Figure 6.3.10). The pore-size distribution showed peaks in the 4-10 nm range and a tail at large pore diameters.

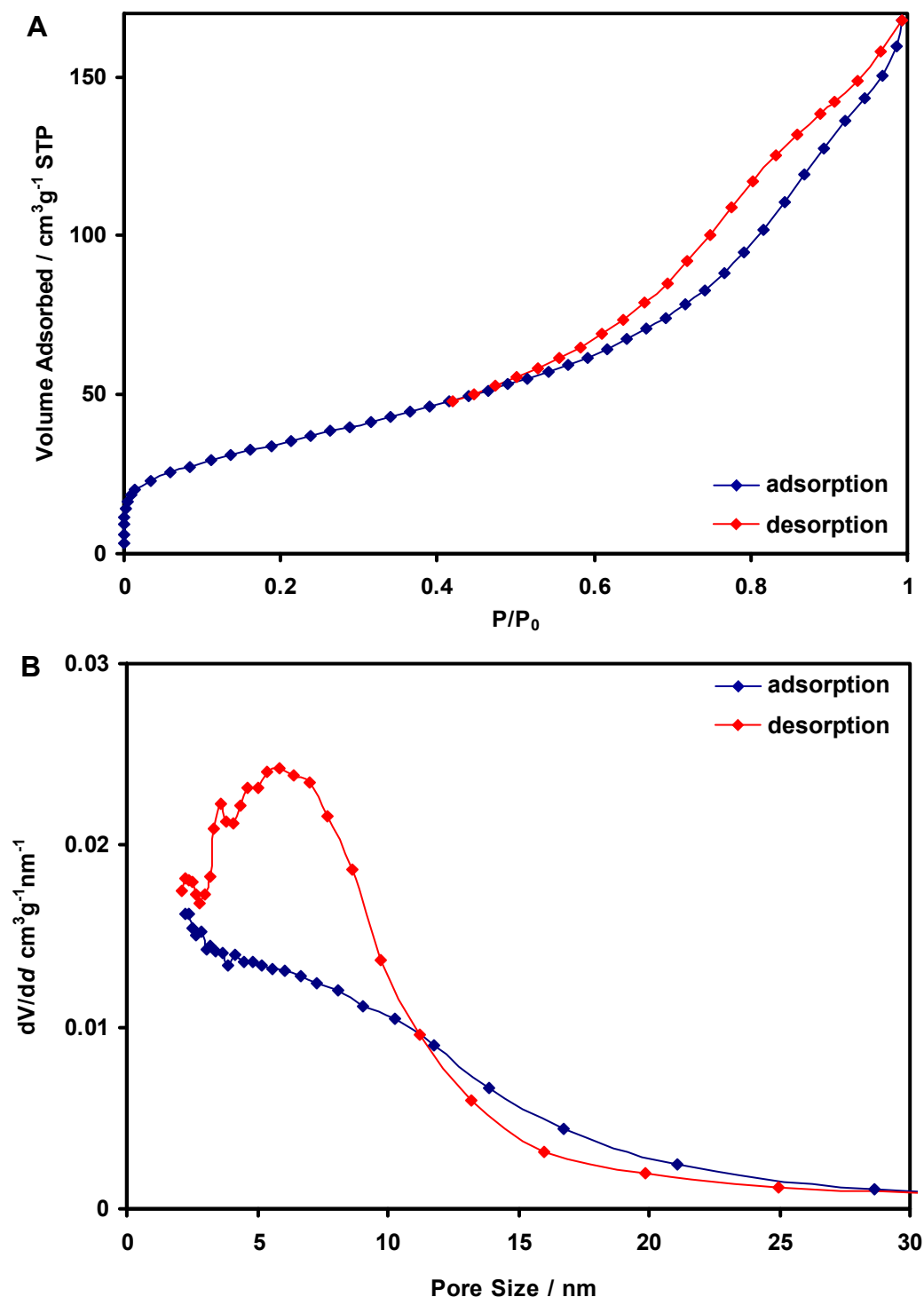


Figure 6.3.10: [A] Physisorption isotherm and [B] pore size distribution for Ceria-K-I.

TEM analysis of Ceria-K-I showed much more ordered mesoporous material than was seen in Ceria-S-I. Figures 6.3.11A-D show agglomerations in which multiple particles with ordered pores are visible. This was not seen previously in Ceria-S-I and had not been reported in the literature, where single, isolated particles were usually shown free of the nanoparticulate material that is evident in these images. The pore orientations visible had pore spacings within two ranges: $d = 14.7\text{-}17.6$ nm and $d \approx 9$ nm. The [211] pore spacings of approximately 9 nm coincided with the results for the KIT-6 template of 7.7-9.7 nm. The

larger pore spacing was attributed to the [111] zone axis. Most often the pore system was visible as a 1D network, meaning the pores were only aligned to the electron beam in one dimension. The only 2D representation is observed in Figure 6.3.11E. The pore arrangement could not be clearly seen but the pore spacings observed are likely to correspond to the [210] zone axis.

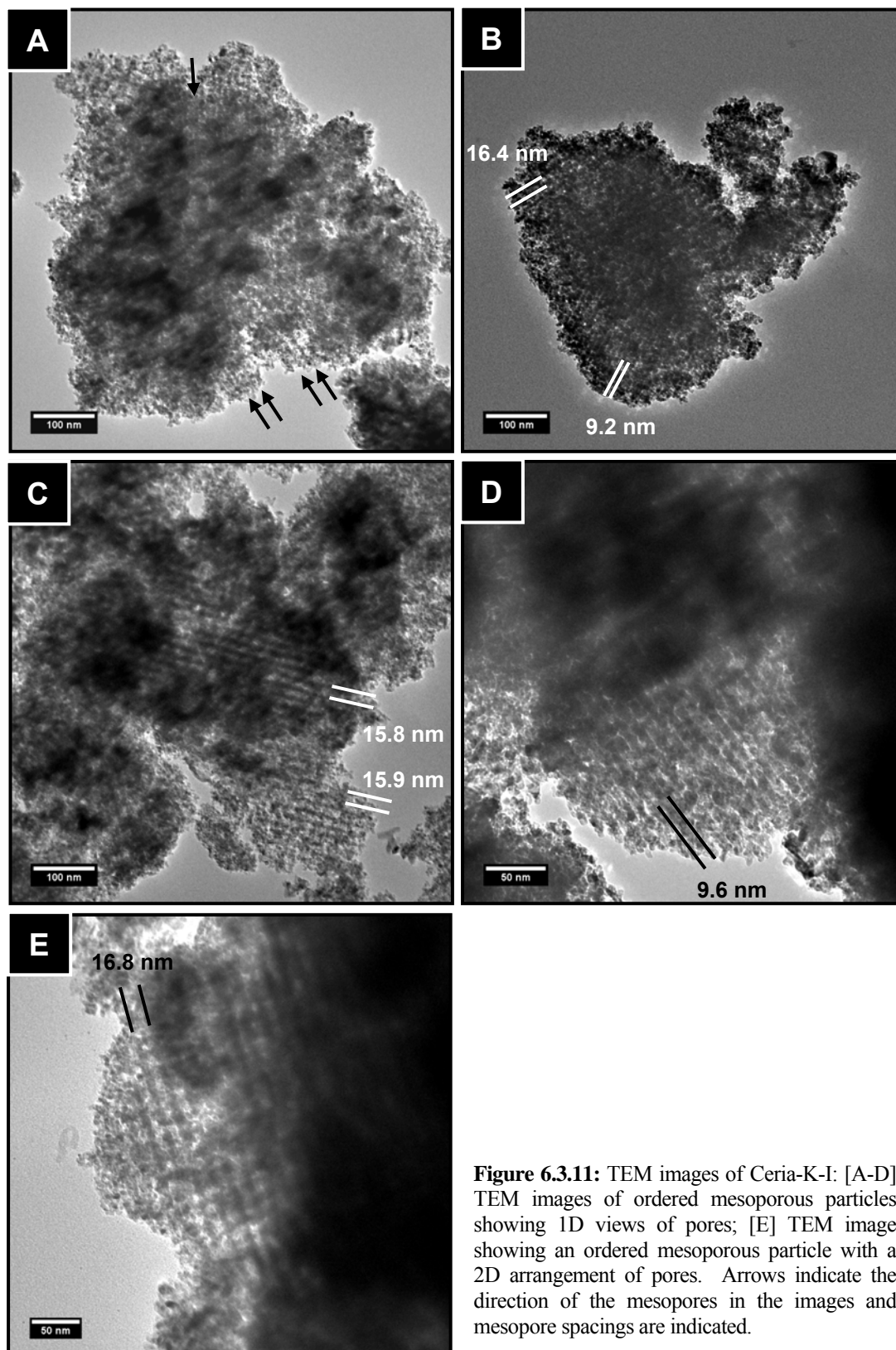


Figure 6.3.11: TEM images of Ceria-K-I: [A-D] TEM images of ordered mesoporous particles showing 1D views of pores; [E] TEM image showing an ordered mesoporous particle with a 2D arrangement of pores. Arrows indicate the direction of the mesopores in the images and mesopore spacings are indicated.

In all of these images, disordered nanoparticulate material could be observed around and on top of the ordered mesoporous ceria. Figures 6.3.12A and B show TEM images of nanoparticles and nanorods. The nanorods are similar in size to the size of the pores of the KIT-6 template. It would not be expected to see these structures form independently outside the silica template. Figure 6.3.1C shows a representative image of the material at sufficient magnification to resolve mesoporous material. As can be seen from the image, the sample was predominantly disordered and the particles with ordered mesopores had to be individually sought out.

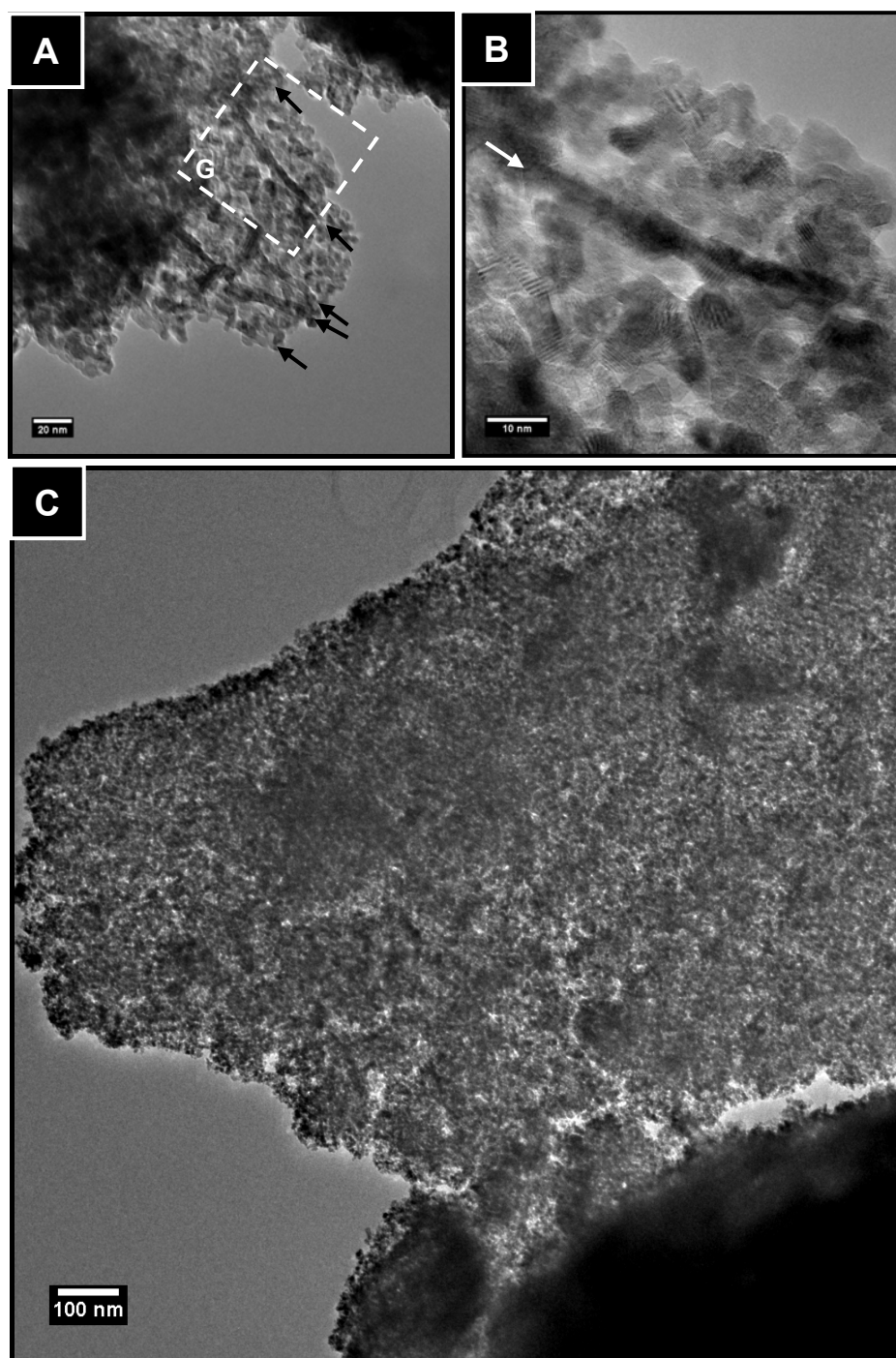
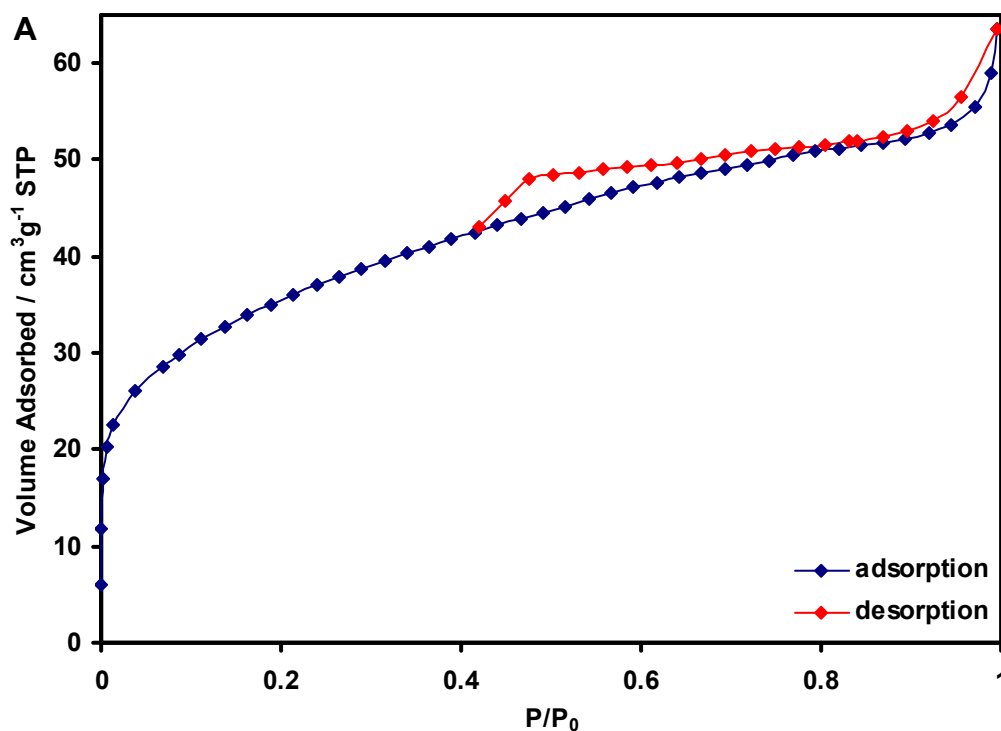


Figure 6.3.12: [A] TEM image of nanoparticles and nanorods typical of Ceria-K-I; [B] HRTEM of [A] showing nanoparticles and nanorods (indicated); [C] a representative TEM image of Ceria-K-I.

6.3.4 Ceria Prepared by Acid Hydrolysis

The addition of $\text{Ce}(\text{Cit})_{3(s)}$ to acidic solution at first resulted in no solid formation. Once a critical concentration was reached, the $\text{Ce}(\text{Cit})_{3(s)}$ added changed rapidly from cream to white and formed a precipitate.

From physisorption results, the specific surface area and pore volume for Ceria-S-A were determined to be $74.5 \text{ m}^2\text{g}^{-1}$ and $0.09 \text{ cm}^3\text{g}^{-1}$, respectively. The adsorption-desorption isotherm was Type IV with emphasis on low pressure adsorption (monolayer formation) with no hysteresis, consistent with the low pore volume. At higher pressures interparticle porosity was observed (Figure 6.3.14). The pore-size distribution showed peaks in the macropore range. The only peak in the mesopore range was at 3.8 nm for the desorption branch. This was attributed to the TSE due to the obvious forced closure of the hysteresis loop in the desorption branch of the physisorption isotherm at $P/P_0 = 0.45$ (see Section 5.4).



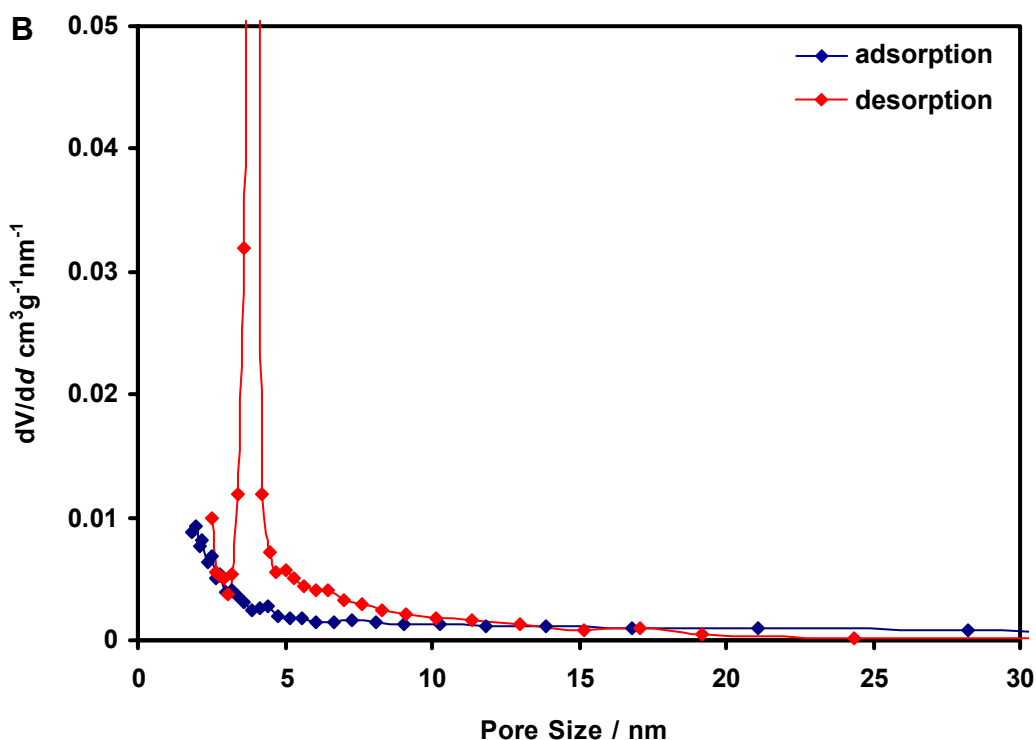


Figure 6.3.13: [A] Physisorption isotherm and [B] pore size distribution for Ceria-S-A.

No mesoporous particles or nanoparticulate ceria were found by TEM (images not shown). Large micrometre sized particles were observed.

Experiments testing the viability of $\text{Ce}(\text{AcAc})_3 \cdot x\text{H}_2\text{O}$ and $\text{Ce}(\text{OAc})_3$ as hydrolysis candidates produced no solid product. Investigation into other potential sol-gel candidates and further refinement of this technique was postponed due to the more promising results of vacuum impregnation experiments (described in detail in Chapter 7).

6.3.5 Ceria Prepared by Precipitation

The precipitation method was attempted for the synthesis of both mesoporous ceria and CGO. Both products were examined using TEM. However, only the ceria sample was examined using physisorption. From physisorption results, the specific surface area and pore volume of Ceria-S-P were determined to be $142.9 \text{ m}^2\text{g}^{-1}$ and $0.20 \text{ cm}^3\text{g}^{-1}$, respectively. The adsorption-desorption isotherm was Type IV with Type H4 hysteresis (Figure 6.3.14). The pore-size distribution showed a peak at approximately 8 nm in the desorption branch with a tail at larger pore diameters.

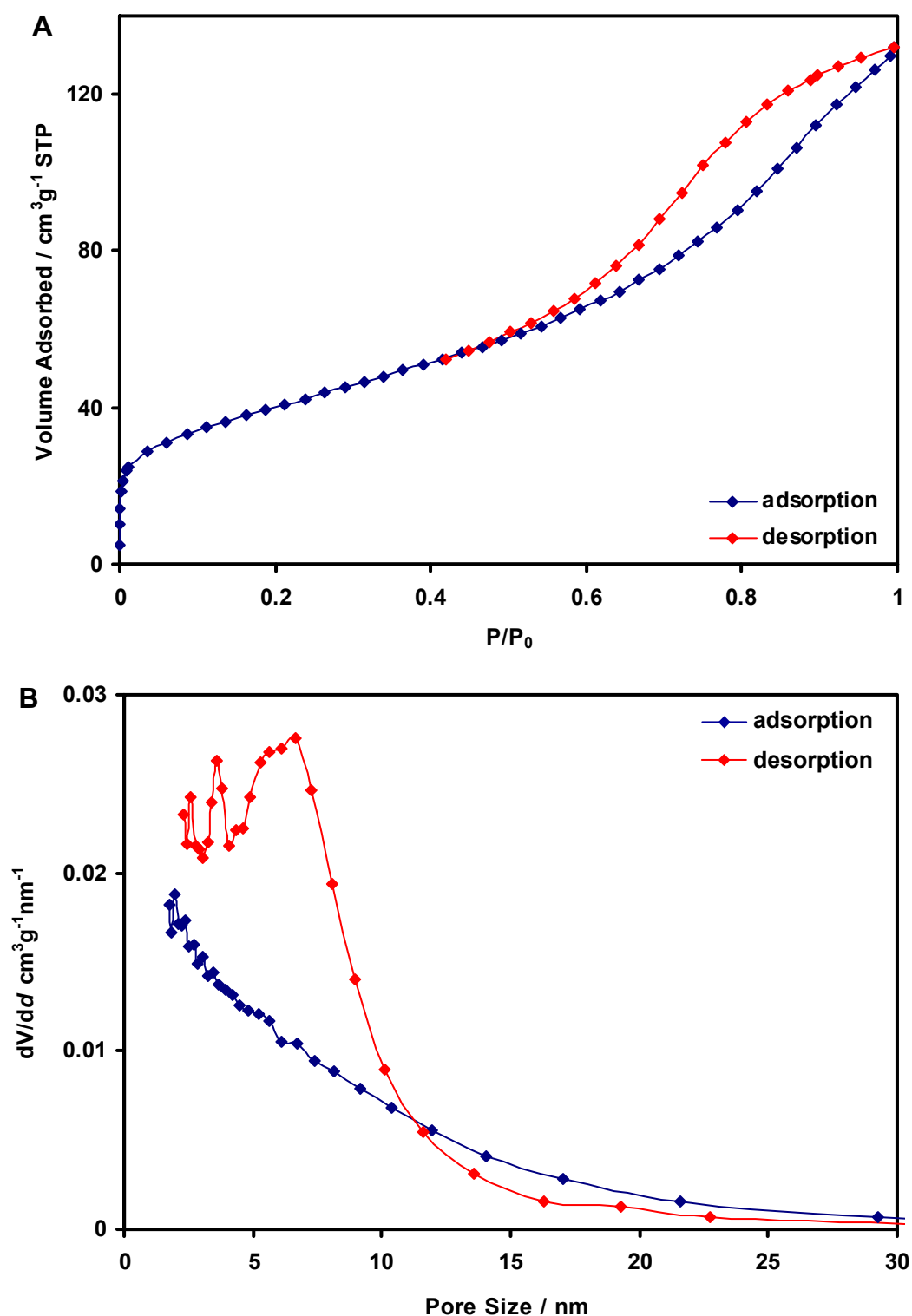
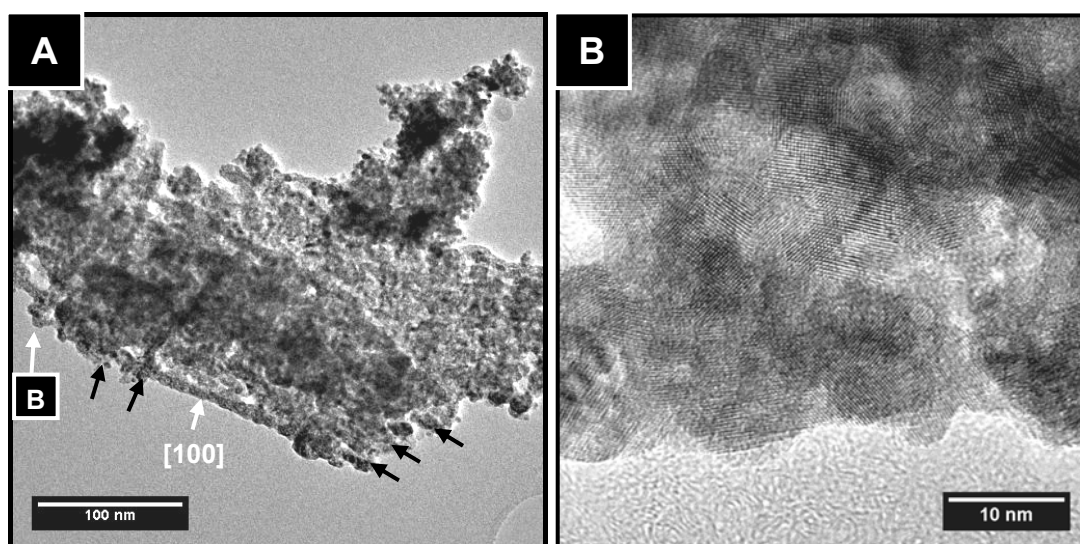


Figure 6.3.14: [A] Physisorption isotherm and [B] pore size distribution for Ceria-S-P.

TEM analysis showed that Ceria-S-P was comprised predominantly of nanoparticles with diameter of 5-20 nm. The morphology of the particles was similar to the reference materials described in Section 6.3.1 (Ceria-X-P and Ceria-X-Cit). The particles were loosely aggregated as in Ceria-X-P rather than formed into the large agglomerates that had

been seen in Ceria-X-Cit. After lengthy examination, some nanorods were found (Figures 6.3.14A and C). It can be seen that some of these rods are clearly in a pseudo-parallel arrangement similar to the pores in SBA-15 (Figure 6.3.15A), but this feature was very rare. Examination of different nanorods showed that some were polycrystalline (Figure 6.3.15B) - that is they were comprised of many nanoparticles sintered together in a linear fashion - while others were single crystalline (Figure 6.3.15C). As had been previously noted, ceria nanoparticles form polyhedral crystals, so these single crystal nanorods were an unusual shape for fluorite crystals. The particle imaged in Figure 6.3.15C indexed to ceria using the [111] crystallographic plane. The polycrystalline rods did not have aligned crystallographic planes between adjacent particles, as had been the case for some of the nanorods observed in Ceria-S-I.

Similar structures were observed using both $\text{NaOH}_{(aq)}$ and $\text{NH}_3_{(aq)}$ as the alkaline source.



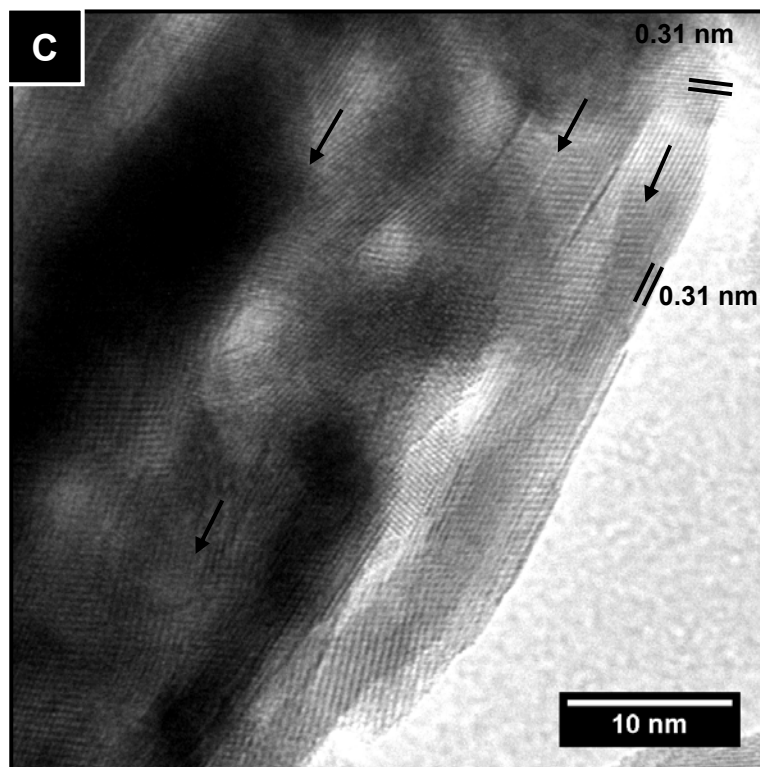


Figure 6.3.15: TEM images of Ceria-S-P: [A] TEM image showing a ceria particle with ordered mesopores similar in morphology to SBA-15 and comprised of nanoparticulate walls as indicated by arrows; [B] HRTEM image of a nanorod composed of nanoparticles; [C] HRTEM image of single crystal nanorods all aligned in the same direction as indicated by arrows, similar to the morphology to SBA-15.

TEM analysis of CGO-S-P shows a large amount of nanoparticulate material (Figure 6.3.16). Single-crystal nanorods were observed very rarely, but no large ordered mesoporous structures were found.

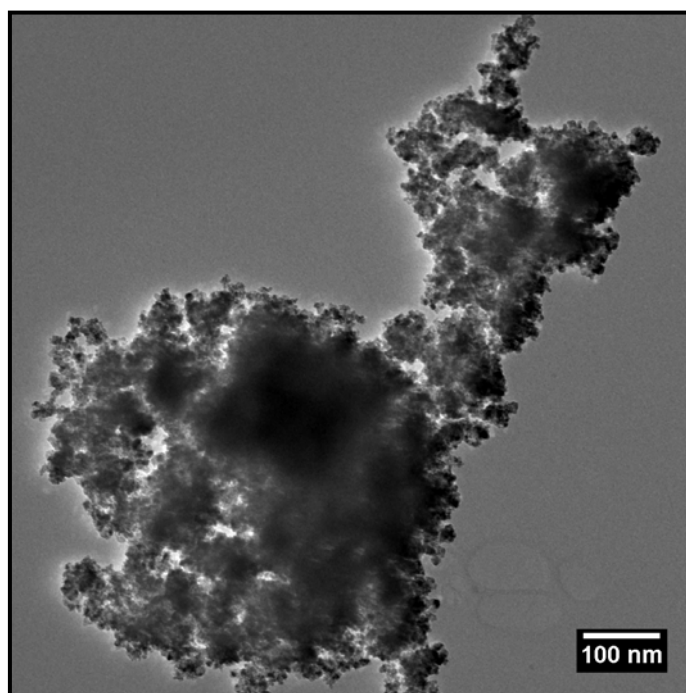
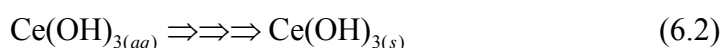


Figure 6.3.16: TEM image of CGO-S-P showing nanoparticulate nature.

6.4 Discussion

The one predominant feature shared by most of the results in this chapter was the formation of nanoparticles. The products designated Ceria-X-P and Ceria-X-Cit showed that ceria forms nanoparticles without the need for structure directing agents at low sintering temperatures. Nanoparticles are a favourable by-product of reaction as, while they may not have properties as favourable as an ordered mesoporous structure, the catalytic properties should be better than a low-surface area bulk material. Producing a hybrid material, for example, ordered mesoporous particles with nanoparticulate by-products, could mean the material is functionally active over a wider range of conditions such as temperature for catalysts, wavelength for photoactive materials or conductivity for electronic applications.

The attempt to produce mesoporous materials by the acid hydrolysis of cerium salts was unsuccessful. While there may be other cerium salts to examine for acid hydrolysis, the high solubility of ceria in acidic media will always restrict the experimental yields. Furthermore, observations made during the experiments, that the formation of the solid for both the acid hydrolysis and precipitation reactions was very rapid, suggested that the mechanisms for these reactions have a very rapid condensation component (Equation 6.1) relative to the condensation component in the synthesis of the mesoporous silica templates. This would mean that the solids may not have sufficient time to form a matrix around the structure-directing agent (the surfactant micelle) as they would condense too rapidly (Equation 6.2).



The mechanism shown here also appears to lack the synergy of the mesoporous silica syntheses described by Davidson, where the interactions between the protonated ether groups on the surfactant (due to the synthesis being carried out at low pH) with the chloride counter ions from the hydrochloric acid, may mediate the silicate oligomer (intermediate length polymer) condensation step.¹⁶⁷ This relative difference in the rate of the hydrolysis of silica and of metal sol-gel precursors has been discussed in the literature.¹⁶⁵

Some ordered mesoporous material was found in Ceria-S-P. This suggests that the precipitation reaction allows for some infiltration of the surfactant micelle but the relative yields of mesoporous material compared to those reported in Chapter 5 for the mesoporous silica templates were very low. The most significant result of this experiment was the large

difference the addition of a small amount of surfactant made to the physisorption results when Ceria-S-P was compared with Ceria-X-P (Table 6.2). These experiments were virtually identical in all other aspects. The addition of surfactant in this experiment increased the specific surface area and pore volumes 30 and 18 times, respectively. It should be noted that it is likely that there could be a large variation in the reproducibility of this result due to the number of environmental variables that could affect the precipitation experiments and the low values of the physisorption results for Ceria-X-P.

Table 6.2: Comparison of the effect of surfactant on specific surface area and pore volume of ceria nanoparticles.

	BET specific surface area (m^2g^{-1})	Pore volume (cm^3g^{-1})
Ceria-S-P	142.9	0.20
Ceria-X-P	4.8	0.011
Ceria-X-Cit	19.3	0.026

The ability of species to access active surfaces is an important factor in nanomaterials. Examples include gas adsorption at the active surface sites in catalysis, electron-transfer in bulk heterojunctions and in the impregnation of additional materials for making composite materials for devices such as dye-sensitised solar cells. A study of the thermal stability of Ceria-S-P materials would be necessary to determine how stable they would be at useful operating temperatures. This would depend on the potential application as not all applications require elevated temperatures, for example, photovoltaics.

Using the IWIT, nanorod crystals were observed that were atypical for conventional bulk fluorite materials. These crystals had a similar size and shape to the pores of the silica templates that had been used. It seems likely, therefore, that the pores of the template had been impregnated by the ceria precursor and that these nanorods formed inside the template. If there were areas inside the template that were not impregnated then, after the removal of the silica template, the disconnected sections would have formed the observed nanorods.

In analysing these materials it became apparent that non-ordered materials, for example Ceria-S-P, are capable of producing nitrogen physisorption results approaching those of materials with more ordered pores, for example Ceria-K-I (see Table 6.3). Usually a nanoparticulate material is characterised by a very high specific surface area and a low pore volume because of the absence of pores or the presence of closed pores and less than ideal stacking, for example, Ceria-X-Cit.

Table 6.3: Comparison of the physisorption results for nanoparticles and ordered mesoporous materials synthesised in this chapter.

	BET specific surface area (m ² g ⁻¹)	Pore volume (cm ³ g ⁻¹)
Ceria-X-P	4.8	0.01
Ceria-X-Cit	19.3	0.03
Ceria-S-P	142.9	0.20
Ceria-K-I	129.1	0.25
Roggenbuck <i>et al.</i> ⁴⁶	148	0.42
Theoretical Ceria-S-?	-	0.58*

* See Appendix 1 for theoretical calculations.

By using a synthesis that involved a structure-directing agent, even though the arrangement of nanoparticles under TEM observation appears random, the pore volume was increased dramatically. It is likely that the pore volume, as shown by the report by Roggenbuck *et al.* of the synthesis of ordered mesoporous ceria,⁴⁶ is the best indication of experimental yields of ordered mesoporous material. It is also worth noting that the pore volume measurements should be directly comparable with the pore volume of the original silica template if several considerations are taken into account. Firstly, the relative density of the two materials (silica $\rho = 2.63 \text{ gcm}^{-3}$, ceria = 7.21 gcm^{-3}) means that a ceria sample having the same volume of pores as the initial silica would have its pore volume decreased by a factor of 2.74. The nature of templating results in a negative copy of the original template, and therefore the volume occupied by the nanorods in the final product will be directly related to the pore volume of the initial template. Secondly, the density of the precursor impregnated must be approximated to give rise to the approximate final concentration of ceria in the template. In this thesis, $\text{Ce}(\text{NO}_3)_{3(s)}$ was assumed to be anhydrous for the calculation of the density of cerium in the silica template, as the material was generally kept above 100 °C after impregnation. Thirdly, changes in the unit cell should also be considered. During the synthesis there will likely be shrinkage of the mesoporous lattice. During calcination, water and $\text{NO}_{2(g)}$ are evolved which causes shrinkage of the impregnated material. This allows for sintering to occur. Finally, the contribution of the by-products of the synthetic procedure, such as nanoparticles, to the physisorption results should be considered. The product yield relative to the yield of by-products is discussed throughout this thesis. These assumptions

form the basis for the theoretical calculation shown in Table 6.3. The full calculation for the theoretical pore volume of ceria from a SBA-15 template is located in Appendix 1.

It was reported that experimental yields approaching the theoretically calculated value (though the theoretical value was not reported) for the impregnation of CMK-3 with ceria using the IWIT was achieved by Roggenbuck *et al.*⁴⁶ In the very best literature results, high pore volumes ($>0.25 \text{ cm}^3\text{g}^{-1}$) have been reported for the direct impregnation of silica templates with ceria precursors.^{46, 77-78} These values compare more directly to the ordered silica and carbon templates used (when adjusted for the difference in densities). Therefore, the pore volumes greater than $0.25 \text{ cm}^3\text{g}^{-1}$ for ceria may be a better indication of a material with bulk ordered mesopores than a high specific surface area.

Based on the experimental information, a mechanism was proposed for the IWIT and is summarised in Figure 6.4.1.

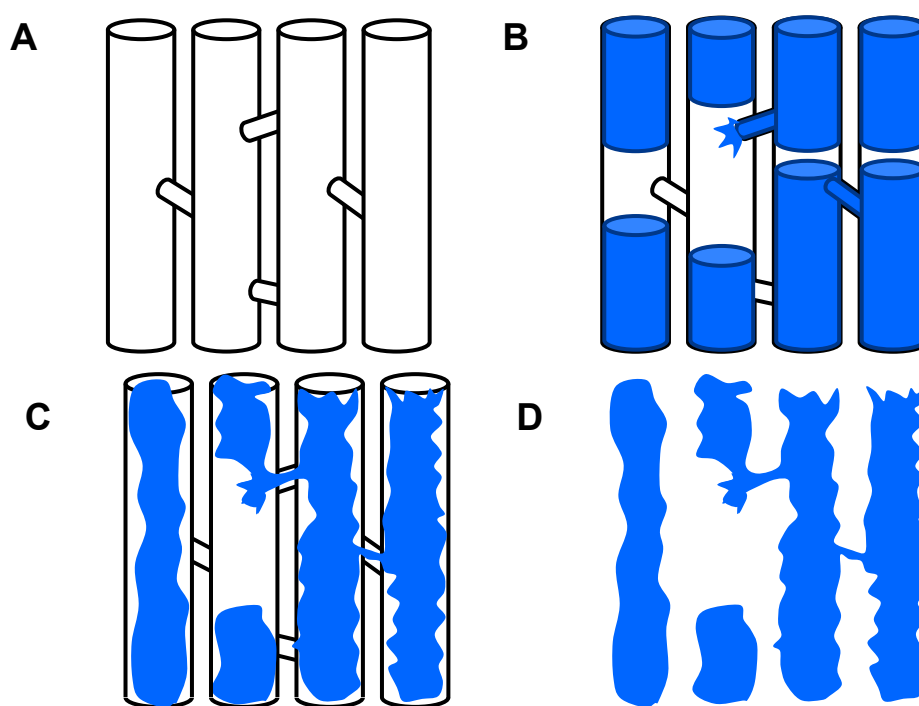


Figure 6.4.1: Proposed mechanism for impregnation based on experimental results: [A] SBA-15 template; [B] liquid impregnates the pores with some air pockets and micropores not impregnated; [C] sintering allows flow of material through pores connecting up material though some gaps remain; [D] after template removal nanoparticles and nanorods are produced as well as mesoporous material.

6.5 Summary

Two ceria materials (Ceria-X-P and Ceria-X-Cit) were synthesised and characterised to act as comparators for the other ceria-based materials that were synthesised in this investigation. Without structure-directing agents they had low specific surface areas and low pore volumes, and a TEM investigation showed that, while the ceria particles were nanocrystalline, there was no order to the way the crystals were arranged.

For the synthesis of ordered mesoporous materials the IWIT produced the best results of the methods examined, based on TEM observations. The other primary TEM observations were that the yield and quality of mesoporous material prepared by the IWIT were very low compared to the volume of nanoparticles present in the sample. The remainder of the sample in the IWIT preparation appeared to consist of disordered nanoparticles and nanorods formed from an incomplete impregnation.

Precipitation in the presence of a surfactant produced a material with both a high specific surface area and high pore volume. A TEM investigation concluded that the material did not have ordered pores and that the increased specific surface area and pore volume were likely caused by a looser packing arrangement of the nanoparticles which increased the space between the particles. This material would likely exhibit favourable functional properties compared to the reference materials, but would have low thermal stability as shown by literature reports.¹⁶⁹

The acid hydrolysis experiment was unsuccessful. While there may be scope for improving the solubility of ceria in acidic media by adjusting the reaction conditions, this was a major obstacle for producing any product in high yields.

Table 6.4 provides a summary of the analysis of the different preparative techniques used in this chapter for the synthesis of mesostructured ceria.

Table 6.4. Summary of the results from this chapter. The pore size was identified from the BJH pore size distribution plots, and the pore spacings were from DDPs of TEM images.

	BET specific surface area (m ² g ⁻¹)	Pore volume (cm ³ g ⁻¹)	BJH Pore size (nm)	d-spacing (nm)
Ceria-X-P	4.8	0.01	-	-
Ceria-X-Cit	19.3	0.03	-	-
Ceria-S-I				8.5
Ceria-K-I	129.1	0.25	4-10	~9
Ceria-S-A	74.5	0.09	-	-
Ceria-S-P	142.9	0.20	-	-

Chapter 7

Development of Vacuum Impregnation for Preparation of Mesoporous Ceria and CGO

7.1 Experimental Philosophy

To produce a high quality bulk ordered mesoporous ceria using a facile process, based on hard templates, for example, mesoporous silica or carbon, modification of the IWIT was required. Important factors that needed to be considered were:

- Capillary action. This is the primary mechanism for impregnation of the solution into the pores of the template and is summarised in Equation 7.1.

$$h = \frac{2\gamma \cos \theta}{\rho g r} \quad (7.1)$$

h is height of the column of liquid, m; γ is surface tension, N m^{-1} ; θ is contact angle, rad; ρ is viscosity, Pa s ; g is acceleration due to gravity, m s^{-2} ; r is pore radius, m.
Note: acceleration due to gravity term can be used as acceleration against viscosity.

- Solution viscosity. Decreasing the viscosity was important as it could affect two terms in Equation 7.1 (γ and g) and so increase impregnation.
- Increasing the precursor concentration. This was required to maximise the volume of solute impregnated as seen in the theoretical yield calculations in Appendix 1.
- Surface modification of the template to increase wetting of the surface and modification of the solute to effect the same result.
- Removal of air pockets from inside the template that would present a physical barrier to total impregnation.
- The mechanism of evaporation of the solvent and subsequent crystallisation of the solid. Whether crystallisation was initiated at the liquid-air interface or seeded on the template surface was a further consideration.

- Post-impregnation treatments. These were initially, but were not limited to, thermal treatments.
- Determining whether or not repeated impregnation was required.

A process was hypothesised that could potentially act on several of these factors to improve the overall procedure - vacuum impregnation (VI). As the current industrial applications for vacuum impregnation are for the elimination of porosity in materials,¹³²⁻¹³³ this method was expected to provide a good mechanism for facilitating the impregnation of material deep within the porous matrix of the template. Upon closer examination, applying a vacuum should impact on several of the aforementioned issues raised with the IWIT. By lowering the pressure in the pore network to below atmospheric, the external pressure forcing material into the vacuum in the pores could supersede capillary action as the driving force for impregnation. All of the air within the pore network should be removed prior to impregnation, increasing the yield of large particles with ordered mesoporous structures. Increasing the solute concentration in the precursor solution should increase the boiling point. This would be beneficial for a solution under vacuum as it would prevent the solvent from boiling off at low pressure. It would also increase the amount of precursor introduced into the template. The relationship between viscosity and concentration would need to be investigated, however, since increasing the precursor concentration would cause the viscosity to increase, which might decrease the level of impregnation. It was hoped that an increased viscosity would also decrease the ion mobility and so ensure that the solute remained in the porous template. This would decrease ion migration out of the template when the solvent left the template during evaporation. Increasing the impregnating forces would hopefully physically increase the surface wetting without having to revert to the more expensive and time consuming surface-modification methods that had been reported in the literature²⁷ (though this would remain as an option to test in tandem if required). The effects of post-synthesis treatments and the question of whether a second impregnation was required could be tested independently of the vacuum impregnation method.

7.2 Experimental

Since it is a new method for this application, the setup of VI is discussed in-depth in this section. The method outlined is for the developed VI method, identified as V₂. Preliminary conditions were slightly different and are referred to as V₁. Notes are made throughout this thesis where experiments used alterations to this method during the development stages of VI.

Depending on the scale of the experiment, different types of apparatus could be used, but the basic components used were a test tube with a sintered glass neck plus a vacuum adaptor (a Schlenk tube could be used here), a dropping funnel, and taps to isolate and release the vacuum as shown in Figure 7.2.1.

To begin an experiment, all taps were closed. A particle trap was placed in line with the vacuum pump to prevent contamination of the rotary pump. In a typical VI experiment a volume of template (0.1-2.0 g depending on the experiment) was placed into the test tube. The apparatus was then assembled as per Figure 7.2.1. The rotary pump was switched on and tap T2 was opened slowly to ensure no template was sucked down the vacuum line (due to the light and voluminous nature of the template). The test tube was tapped lightly to help remove air pockets during the early stage of the evacuation process. The template was then left to evacuate for 4-6 h. A precursor solution consisting of the impregnating salt (or other precursor material), was stirred for at least 6 h at 30-60 °C to ensure it was a homogeneous mixture. The solutions used in the work described in this chapter were ethanol saturated with $\text{Ce}(\text{NO}_3)_6 \cdot 6\text{H}_2\text{O}$, or ethanol with replacement of 10 mol% of the cerium salt by $\text{Gd}(\text{NO}_3)_6 \cdot 6\text{H}_2\text{O}$. The volume of precursor solution used in the impregnation step exceeded the volume required to impregnate all of the pores in the template in order to ensure the vacuum was not compromised during impregnation by ingress of air through the dropping funnel. The solution was placed in the dropping funnel and left for any air bubbles to dissipate. T2 was closed and the pump was switched off. T1 was opened slowly at first to allow the solution to completely cover the template and then, once sufficient volume of solution was admitted to completely impregnate the template, T1 was closed. T2, and then T3 were opened to return the system to atmospheric pressure and complete the impregnation. This could be observed by rapid infiltration of the precursor solution into the template. Excess solution was then decanted before the sample was dried at 95-105 °C in air in an oven. The sample was calcined typically at 400 and 600 °C in air for 5 h at each temperature (ramp rate 1 °C min⁻¹) using a tube furnace. The silica template was dissolved by stirring with approximately 20 cm³ of 1-2 M NaOH. Centrifugation was used to recover the product from the solution. This step was repeated three times. The product was then dried in an oven at 105 °C overnight.

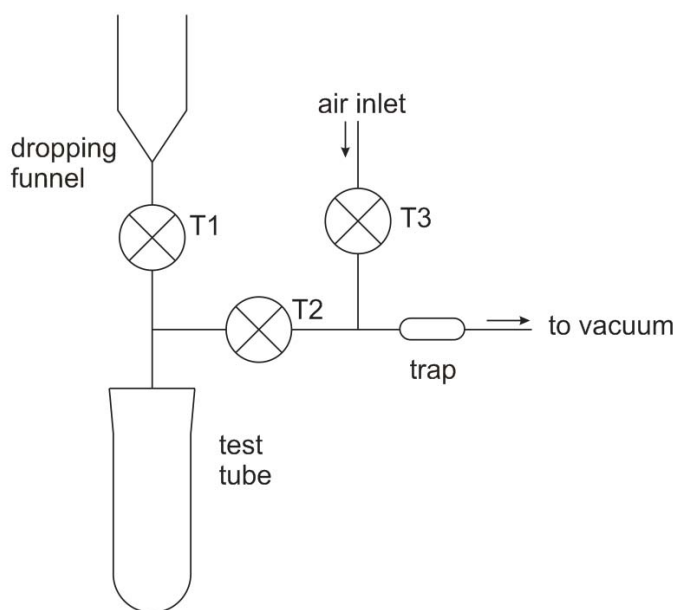


Figure 7.2.1: Schematic setup of a VI experiment.

For the preliminary experiments (V_1) there were several experimental differences from the above (V_2). A vacuum desiccator was used instead of a test tube and a water pump was used instead of a rotary pump. The precursor solution was added directly into the air inlet (see Appendix 1 for more information). After the product was dried at 95-105 °C in air in an oven, the sample was calcined at 400 °C in air for 5 h (ramp rate 1 °C min⁻¹), and then impregnated a second time (similar to the IWIT method in 6.2.2). After this the sample was calcined at 400 and 600 °C in air for 5 h at each temperature (ramp rate 1 °C min⁻¹), before the silica template was dissolved by stirring with approximately 20 cm³ of 1-2 M NaOH. Buchner filtration was used to recover the sample from the solution. The sample was sucked dry. This step was repeated three times.

7.2.1 Additional Observations

During evacuation of the template it was possible to see the air being evacuated as surface eruptions. In the initial stage, when the template was first exposed to vacuum, the amount of air removed was sufficient for a large proportion of the template to float up the test tube as in a flocculation experiment. This meant extreme care had to be taken to prevent loss of material down the vacuum line. After the initial settling period, exhaust flumes of air exited from the template for 10-15 min. Agitation of the test tube assisted in releasing the air pockets.

When the dropping funnel was opened to vacuum the lower pressure in the test tube caused the liquid to enter rapidly. If care was not taken the liquid would enter too quickly and air would enter before a complete liquid layer was formed over the template. Also, rapid liquid

passage through the tap appeared to facilitate boiling of the solvent, possibly through a nucleation process (gas bubbles were observed in the solution) so it was important that care was taken at this stage.

When solution was added to the vessel it did not immediately enter the template but remained on the surface. When the entire vessel was opened to atmospheric pressure the solution rapidly entered the template. Total impregnation could easily be identified because, when a viscous precursor was used, the solution and the silica template appeared to have a comparable refractive index making the composite translucent. A glass rod or spatula was used carefully to create a channel through which the solution could penetrate further into the gel if the composite was not completely clear within 1-2 min. This allowed for the rapid infiltration of the solution to deeper regions of the template rather than it having to diffuse through the entire pore structure.

7.3 Characterisation Studies

7.3.1 Ceria Prepared from KIT-6 Using VI

Ceria-K-V₁ was the first material prepared using VI. It is reported separately because the apparatus used was significantly different and therefore comparisons can be drawn to later experiments which used a more advanced setup (e.g. Ceria-K-V₁ versus Ceria-K-V₂).

From physisorption results, the specific surface area and pore volume of Ceria-K-V₁ were determined to be 105.7 m²g⁻¹ and 0.33 cm³g⁻¹, respectively. The adsorption-desorption isotherm was Type IV with Type H3 hysteresis (Figure 7.3.1). This type of isotherm is consistent with mesoporous materials. The pore-size distribution showed two sets of peaks: narrow peaks at 2.6-3.0 nm and broader peaks at 9.6-13.8 nm.

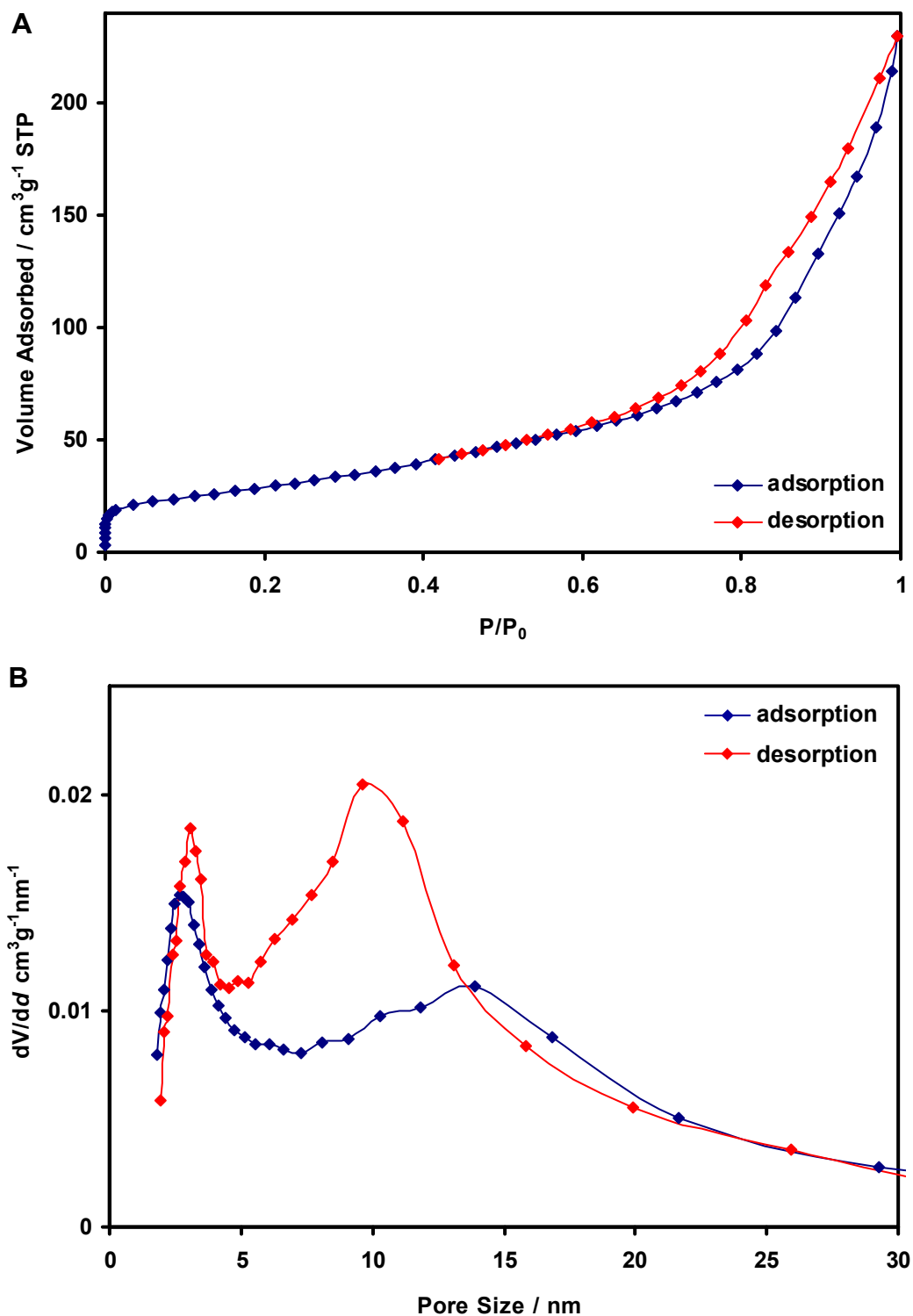


Figure 7.3.1: [A] Physisorption isotherm and [B] pore size distribution for Ceria-K-V₁.

High angle powder XRD showed the material to be single phase ceria with the fluorite structure (*Fm3m*, ICDD 43-1002). Extensive peak broadening was observed (Figure 7.3.2). By applying the Scherrer equation to the peak broadening, an average particle size of 24.6 nm was calculated.

Semi-quantitative EDS of the material showed it to be predominantly Ce (29.9 mol%) and O (64.7 mol%). C and Cu X-rays were presumed to be predominantly from the carbon grid

(Figure 7.3.3). Approximately 5.4 mol% residual Si, undoubtedly from the silica template, was detected across the sample (see Section **Error! Reference source not found.** regarding EDS accuracy). Al and Ca were also observed in the EDS spectrum. The most likely source of Al was from the alumina furnace boat. The residue of samples in subsequent work was not scraped out of the furnace boat to ensure the alumina was not being abraded. As noted in Section 1.3.1 ceria is an industrial polishing agent. A fraction of the detected C was assumed to be from absorbed $\text{CO}_{2(g)}$, but only as trace amounts.

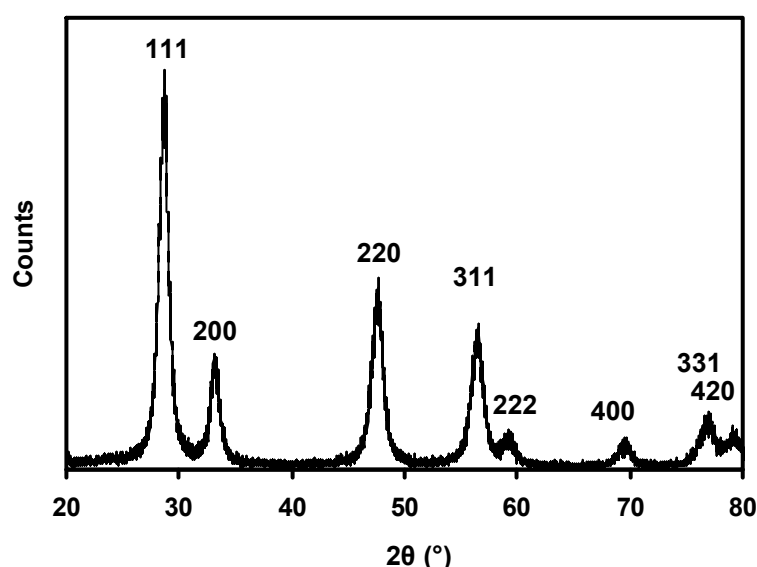


Figure 7.3.2: Powder XRD pattern for Ceria-K-V1.

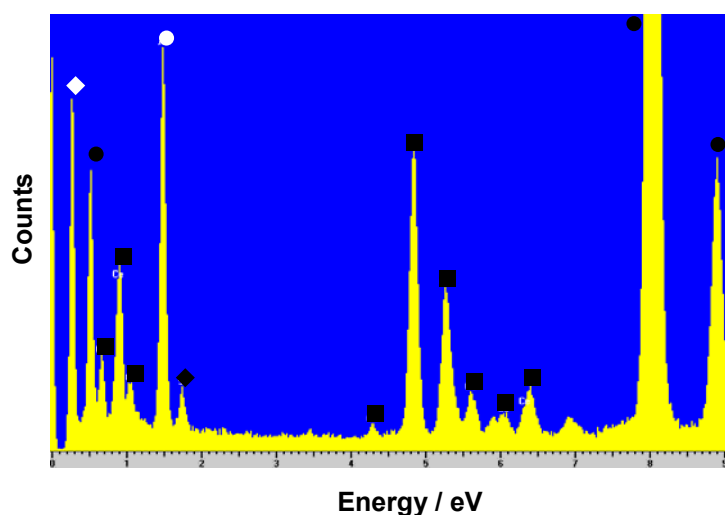


Figure 7.3.3: EDS spectrum for Ceria-K-V₁: ◇ O, ● Cu, ■ Ce, ○ Al, ◆ Si.

TEM images of Ceria-K-V₁ showed a large improvement in the quantity and quality of the ordered mesoporous material compared to Ceria-K-I. Figures 7.3.4A-D are representative images of the sample in which multiple pore orientations can be seen in most images. Figure 7.3.4A shows a low magnification image in which many mesoporous particles with ordered pores are visible, including 2D orientations viewed down the [211] zone axis ($d = 8.5$ nm) as well as the larger pore spacing ($d = 14.1$ - 14.7 nm) that corresponds to the

[110] zone axis. The particles themselves were 100-300 nm across and surrounded by disordered nanoparticles. Figure 7.3.4B shows a group of porous particles with at least two easily identifiable pore orientations, both corresponding to the [110] with $d = 14\text{-}14.9\text{ nm}$. At the right side of the image can be seen disordered nanoparticulate material. Figures 7.3.4C-D show further instances of ordered mesoporous particles to show that these were widespread in the sample. The pore spacings in these images were consistent with those reported above ($d = 8.4\text{-}8.6$ and $14.1\text{-}14.9\text{ nm}$).

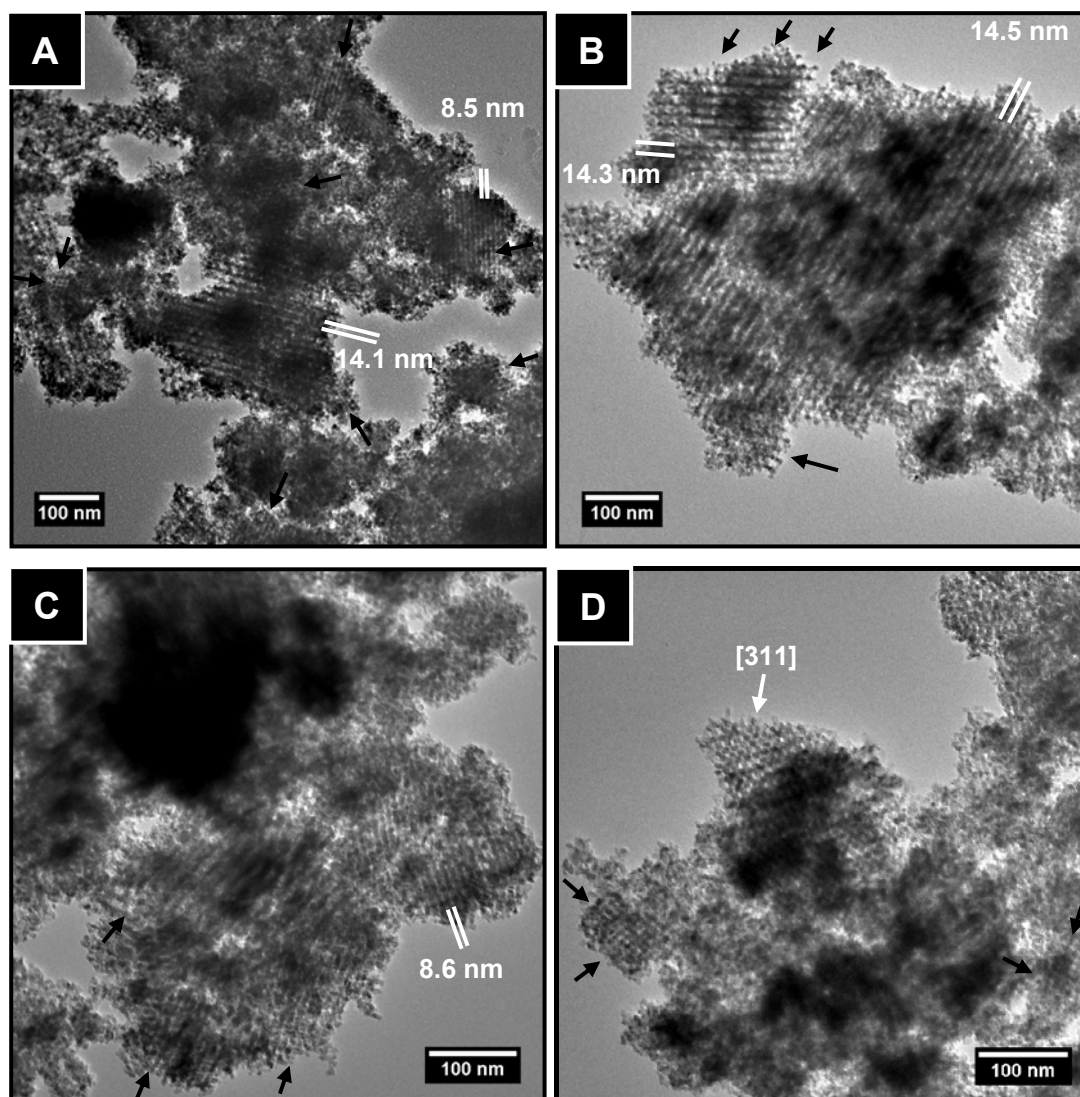


Figure 7.3.4: [A-D] Representative TEM images of Ceria-K-V₁ showing ordered mesoporous particles. Arrows indicate pore directions in mesoporous particles. Selected particles have zone axes and pore spacings identified where possible.

Figure 7.3.5 shows that there was still nanoparticulate material present in this sample. The image is devoid of ordered mesoporous particles, or contains material that is not aligned to the electron beam. The material that is present is comprised of 100-200 nm agglomerations of nanoparticles.

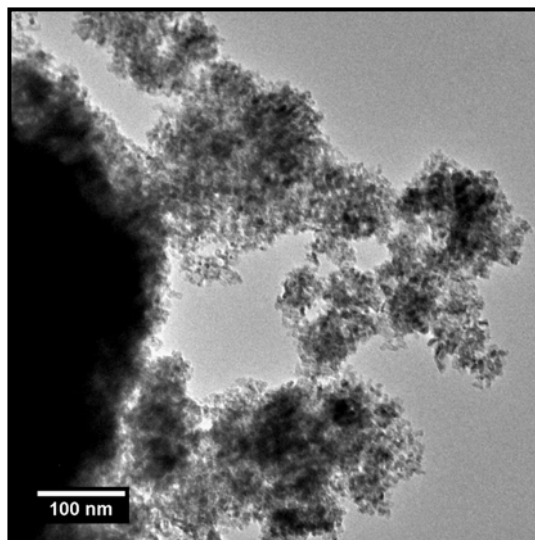


Figure 7.3.5: TEM image showing disordered nanoparticulate material present in Ceria-K-V₁.

Figure 7.3.6 shows a large (300×400 nm) porous particle viewed down the [311] zone axis. The DDP, which was taken of the entire image, shows that the particle exhibited a single pore structure viewed in a single orientation. The variation in the orientation of each family of planes in the pore structure was small since the angular range for each spot in the DDP was also small. The (211) spots had a d-spacing of 8.9 nm and the (110) spots had a d-spacing of 14.1-14.9 nm.

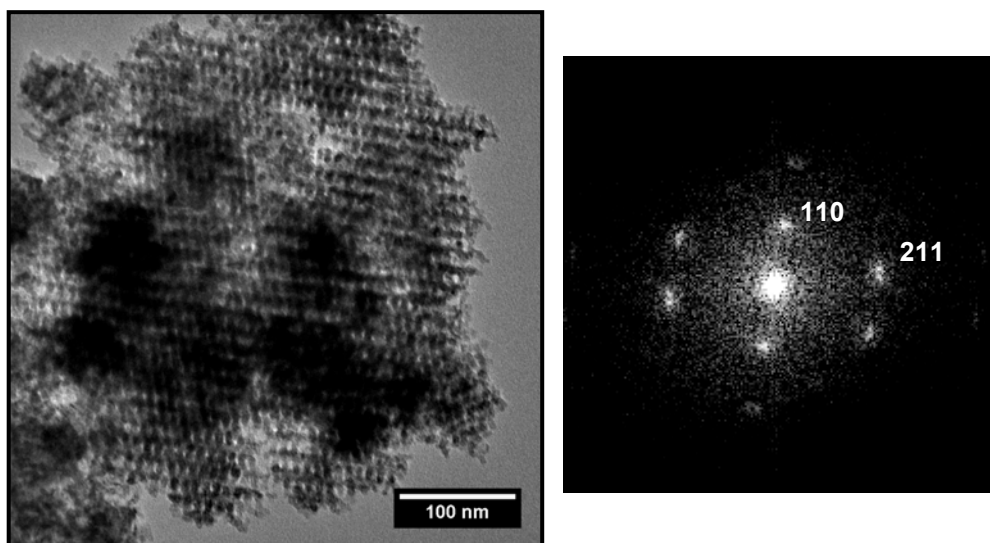


Figure 7.3.6: TEM image of Ceria-K-V₁ viewed down the [311] zone axis and DDP of this entire image.

HRTEM images of the ordered pores show that the crystallographic planes of ceria were aligned with respect to each other in adjacent pore walls. Figure 7.3.7 shows ordered mesoporous particle viewed down the [110] zone axis of the mesopore structure. The inset DDP shows that there were several predominant lattice plane orientations in the image rather than random crystallographic orientations. Due to the high magnification, the resolution of the mesopore spacing was low (measured as 8.5-9.1 nm) but the (111) reflection on the DDP

corresponded to the expected value for the crystal structure of ceria (0.32 nm measured, 0.31 nm reported in ICDD 43-1002).

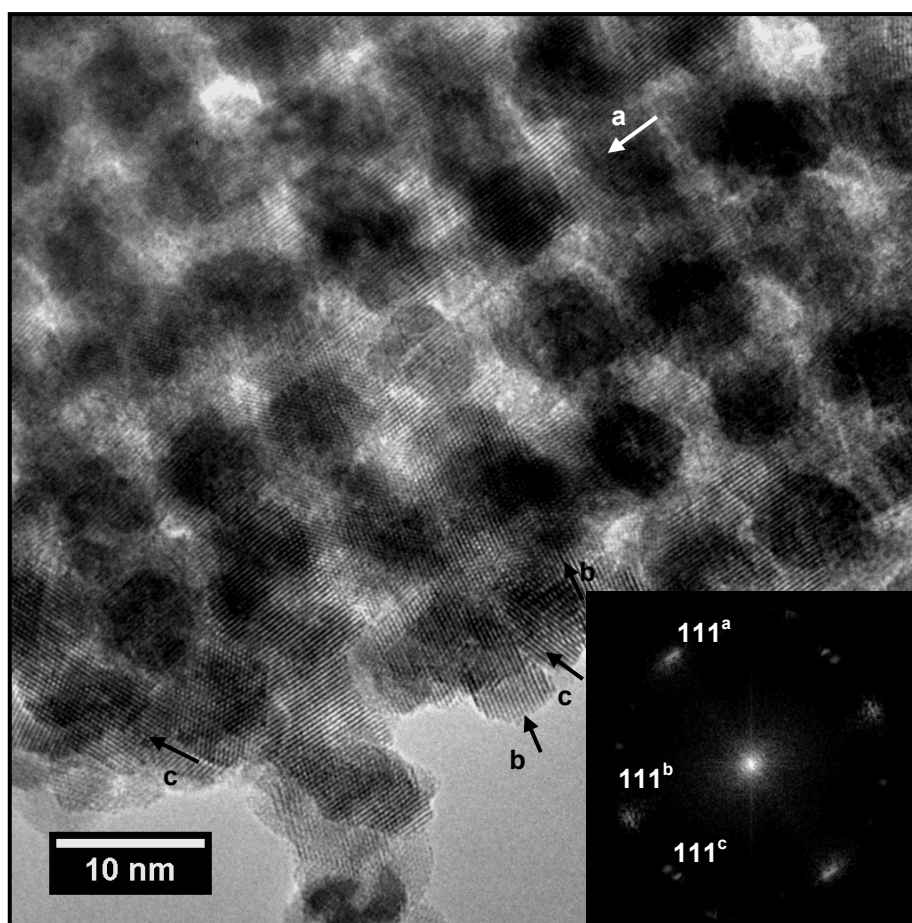


Figure 7.3.7: TEM image of Ceria-K-V₁ viewed down the [110] zone axis of the mesopore structure. The inset DDP was taken of the entire image. Arrows indicate the three predominant crystallographic planes in the image.

Figure 7.3.8A shows an image of a mesoporous particles viewed down the [111] zone axis of the mesopore structure. In this pore orientation the wormhole nature of the pores can be seen. Vertical pore walls (coming out of the image) link to three diagonal pore walls arranged in a hexagonal array. The layered arrangement of the pore network can be fully appreciated, unlike in images of the other zone axes. The pore spacing for the hexagonal repeating units was 16.2 nm, which indexed to the (110) planes in the pore network. This is consistent with the [111] zone axis in which (220) reflections would be expected. The HRTEM image of the pore walls shows that they were also essentially single crystalline (Figure 7.3.8B). The (111) reflections were all $70^\circ \pm 3^\circ$ which corresponds to the [110] crystallographic zone axis. These have not been indexed on the DDP as the crystallographic planes were misaligned and no single ceria crystals were observed clearly aligned in more than one direction.

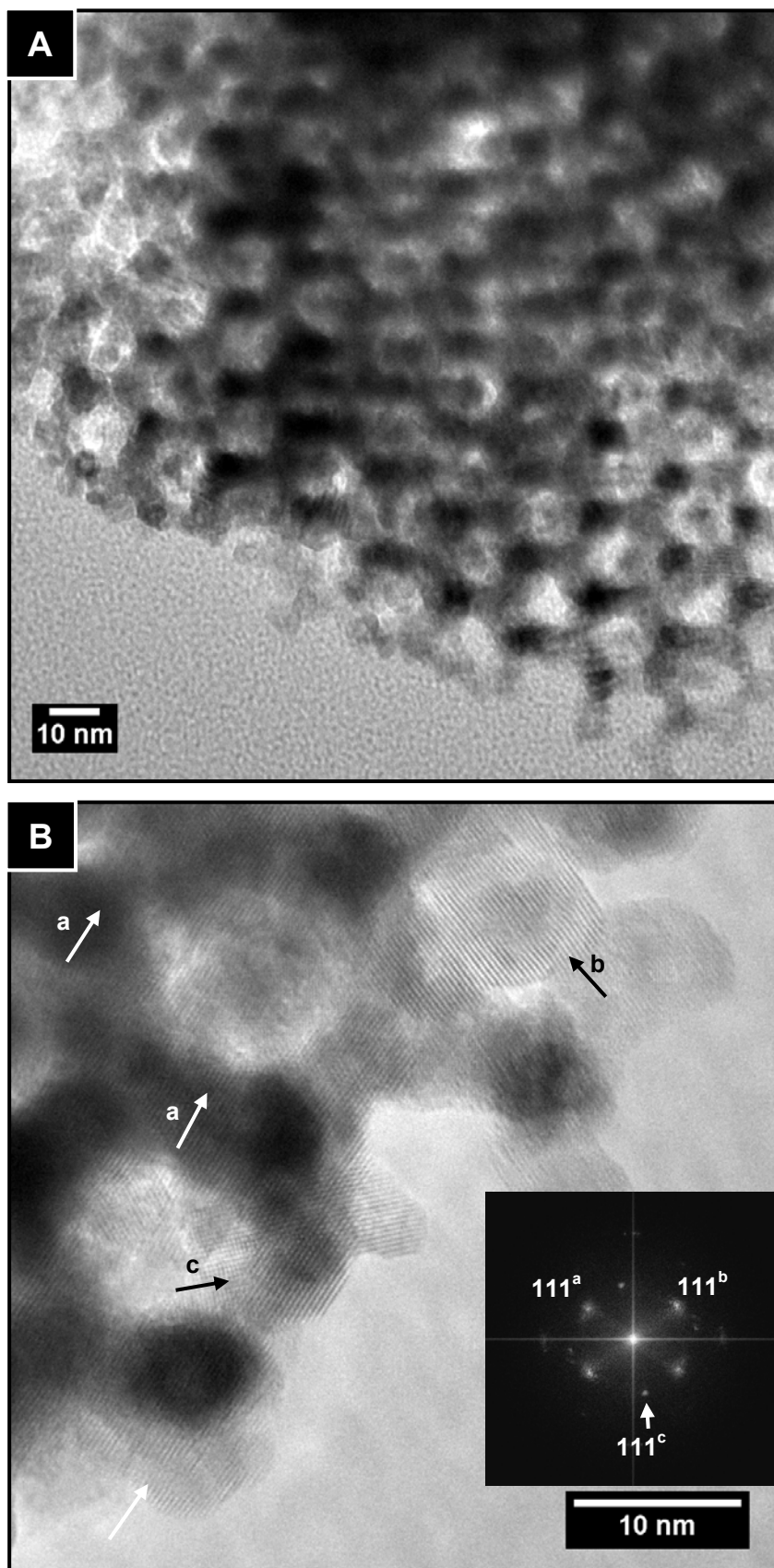


Figure 7.3.8: [A] TEM image of Ceria-K-V₁ viewed down the [111] zone axis of the mesopore structure; [B] HRTEM image of [A] showing the crystal structure of the nanorods comprising the pore walls. The inset DDP is of the entire image. Arrows indicate the three predominant crystallographic planes in the image.

Figure 7.3.9A shows a mesoporous particle viewed down the [210] zone axis. It is difficult to visualise this zone axis: the dark circles are cylinders coming out of the image and the HRTEM image (Figure 7.3.9B) shows how the wormhole nanorods alternate at angles throughout the depth of the particle. The inset DDP showed that there were many crystallographic orientations in this image, all which corresponded to ceria (ICDD 43-1002).

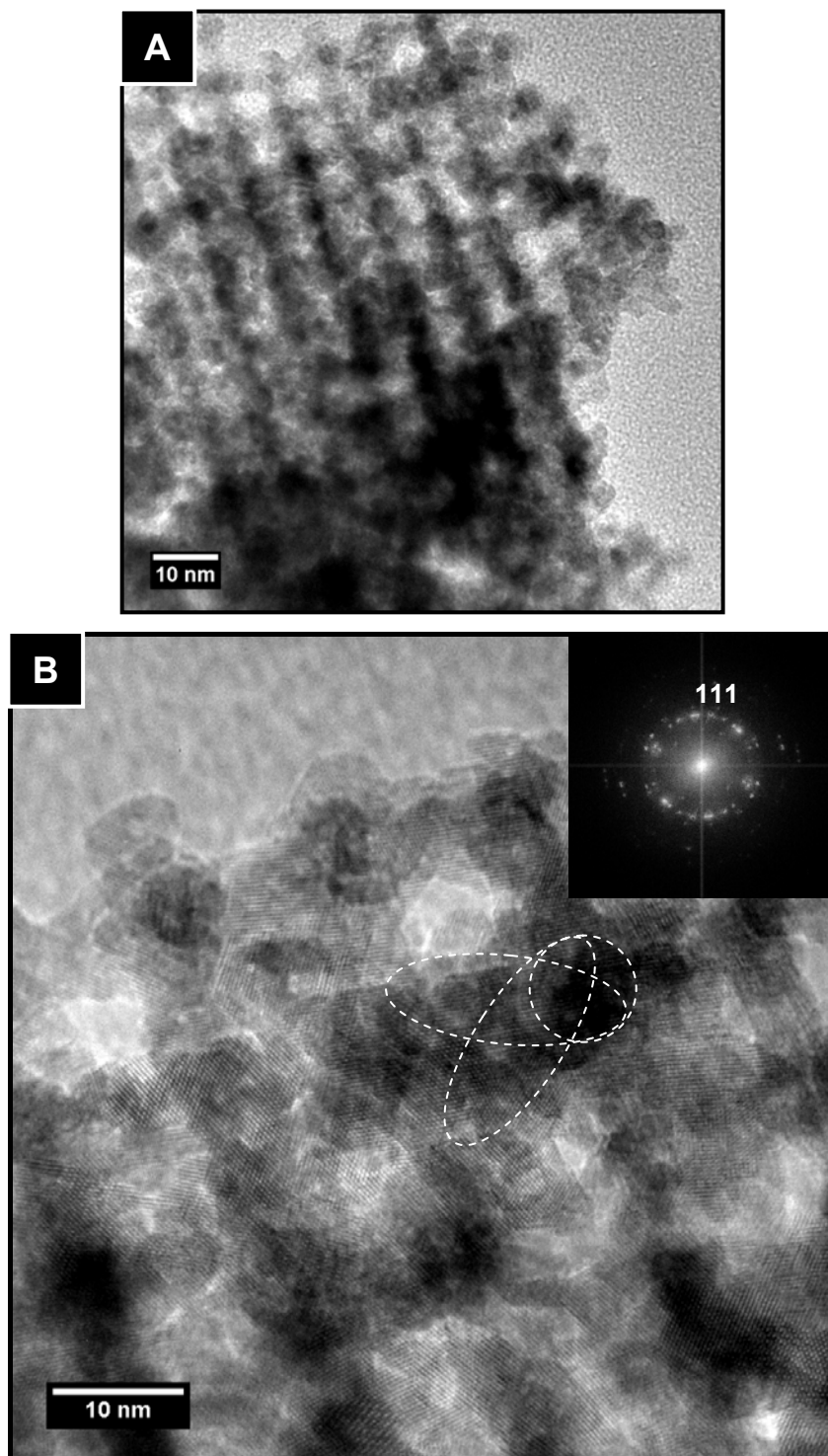


Figure 7.3.9: [A] TEM image of Ceria-K-V₁ viewed down the [210] zone axis of the mesopore structure; [B] HRTEM image of [A] showing the atomic structure of the nanorods that comprise the pore walls. The inset DDP is of the entire image. The wormhole nature of the pore walls is indicated.

Figure 7.3.10A shows a TEM image of a misaligned mesoporous particle. Only one pore orientation was aligned to the electron beam. The nanorods had a pore spacing of 8.0-8.3 nm derived from the (211) reflections in the DDP, Figure 7.3.10(i). The DDP taken of the entire image, Figure 7.3.10(ii) shows that the image indexed to a single crystallographic orientation for ceria with only two spots observed. This DDP clearly shows that the (111) lattice planes have a 23° variation and span this entire range of angles. A HRTEM image (Figure 7.3.10B) clearly showed the lattice variation. While it appears that the image contains nanorods, it can be interpreted as an image of a stepped orientation as shown by the inset schematic.

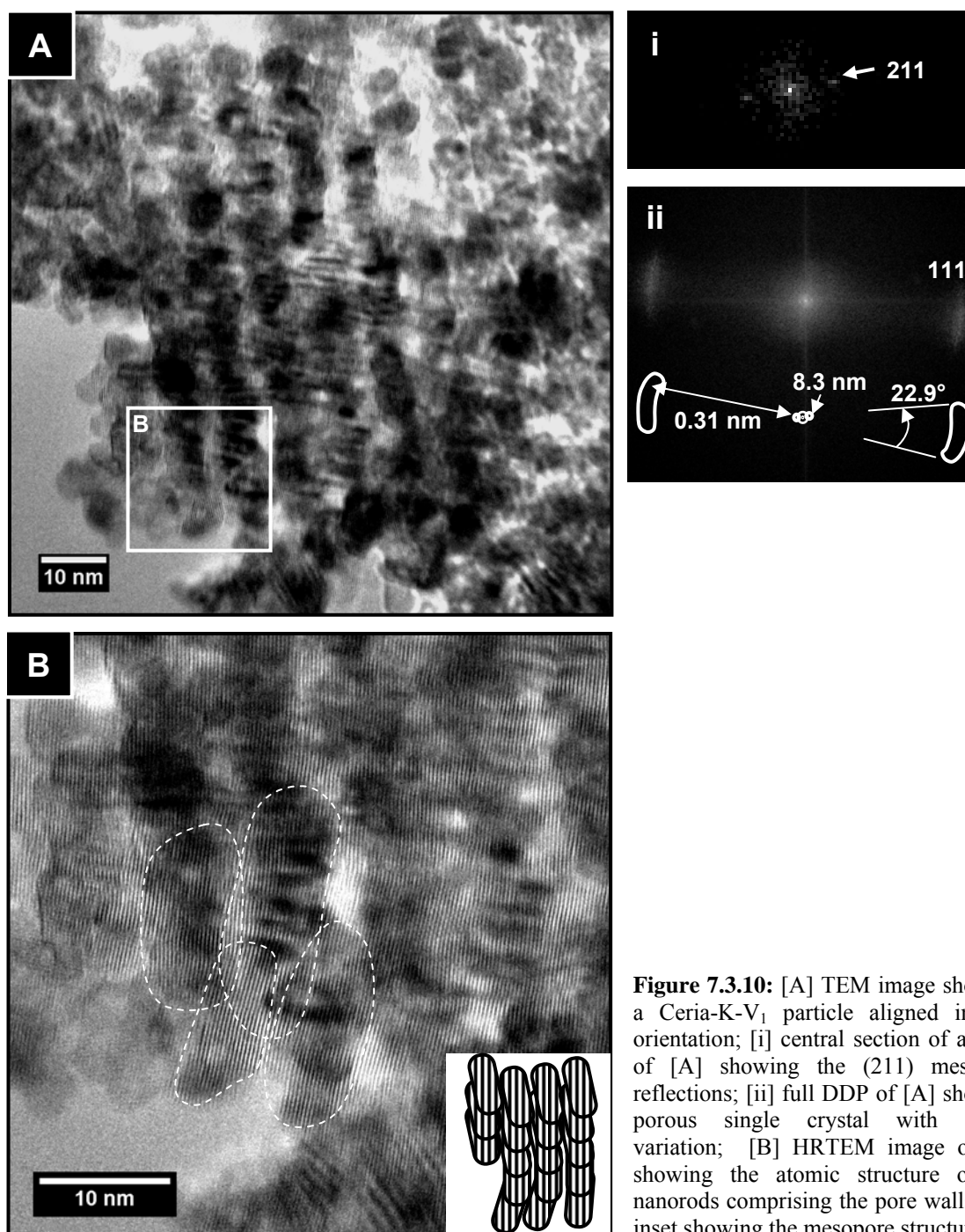


Figure 7.3.10: [A] TEM image showing a Ceria-K-V₁ particle aligned in one orientation; [i] central section of a DDP of [A] showing the (211) mesopore reflections; [ii] full DDP of [A] showing porous single crystal with lattice variation; [B] HRTEM image of [A] showing the atomic structure of the nanorods comprising the pore walls with inset showing the mesopore structure.

Investigations into using $\text{Ce}(\text{AcAc})_3 \cdot x\text{H}_2\text{O}$ with the VI method were unsuccessful, as with the earlier experiments with the IWIT.

7.3.2 Ceria Prepared from SBA-15 Using VI

From physisorption results, the specific surface area and pore volume of Ceria-S- V_2 were determined to be $85.7 \text{ m}^2\text{g}^{-1}$ and $0.29 \text{ cm}^3\text{g}^{-1}$, respectively. The adsorption-desorption isotherm was Type IV with Type H3 hysteresis (Figure 7.3.11). This isotherm is typical of mesoporous materials. The pore-size distribution showed sharp peaks at 2.4-3.0 nm and broader peaks at 9.6-13.8 nm. t-plot analysis showed that none of the pore volume was attributed to microporosity.

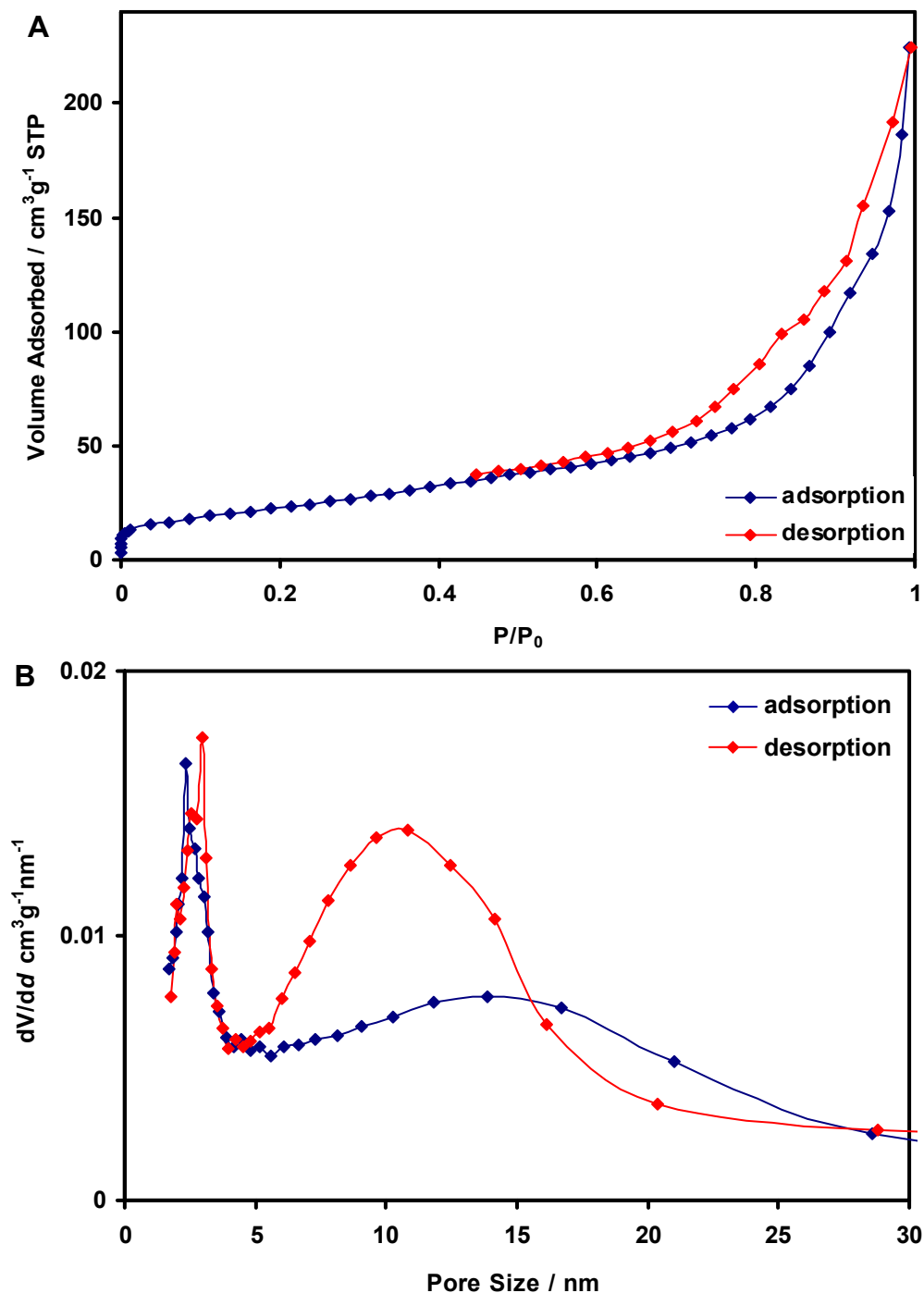


Figure 7.3.11: [A] Physisorption isotherm and [B] pore size distribution for Ceria-S- V_2 .

High angle powder XRD showed the material to be single-phase ceria with the fluorite structure ($Fm3m$, ICDD 43-1002). Extensive peak broadening was observed (Figure 7.3.12). By applying the Scherrer equation to the peak broadening, an average particle size of 34.2 nm was calculated.

SAXS performed on this sample showed a smooth curve with no defined peaks (Figure 7.3.13).

Semi-quantitative EDS of the material showed it to be predominantly Ce (40.7 mol%) and O (54.8 mol%), with C and Cu presumed to be from the carbon grid. Approximately 4.5 mol% residual Si, undoubtedly from the silica template, was detected across the sample (Figure 7.3.14).

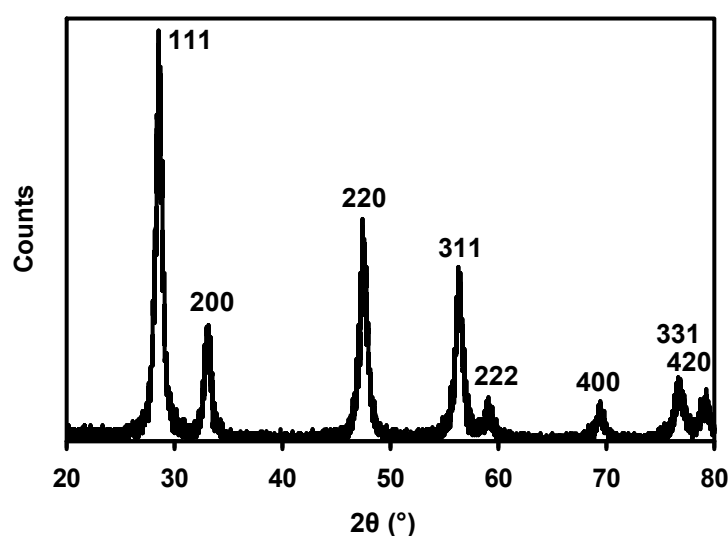


Figure 7.3.12: Powder XRD pattern for Ceria-S-V₂.

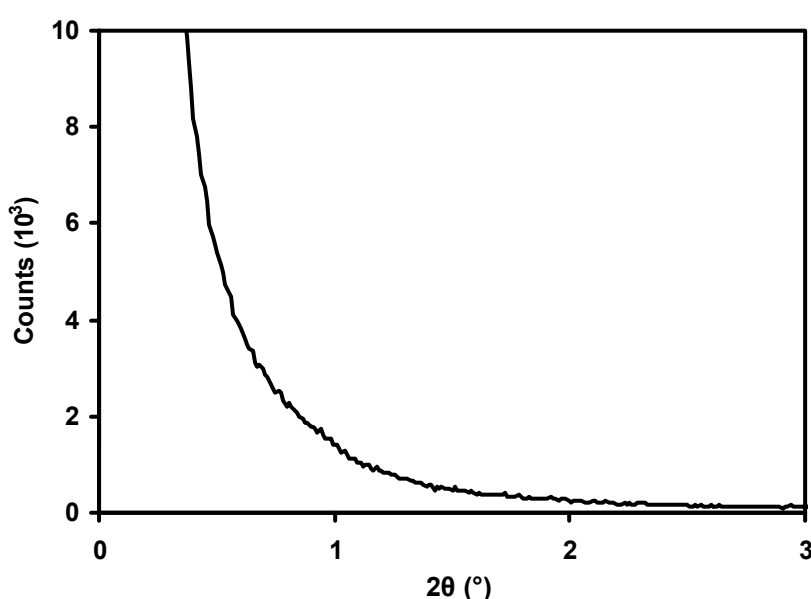


Figure 7.3.13: SAXS pattern of Ceria-S-V₂.

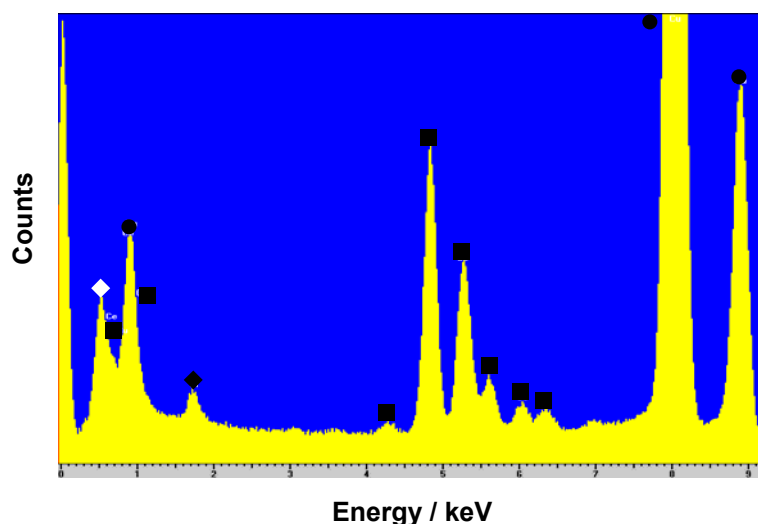
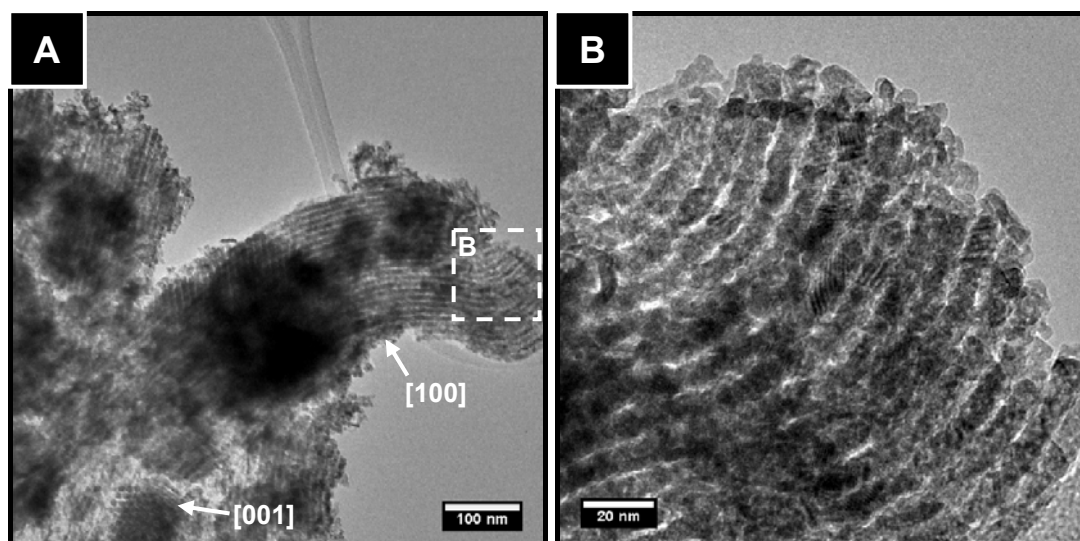


Figure 7.3.14: EDS spectrum for Ceria-S-V₂: ◇ O, ● Cu, ■ Ce, ○ Al, ◆ Si.

TEM images of Ceria-S-V₂ showed the sample to be comprised of predominantly ordered mesoporous material. DDPs of the crystalline material confirmed that the pore walls were comprised of ceria (by referencing the (111) diffraction spots to ICDD patterns), and the pore morphology was analogous to SBA-15 with [100], [110] and [001] zone axes clearly visible. Figure 7.3.15A shows a large (>600 nm) particle with parallel pores (d = 9.1 nm for the [100] pores) along its length that bent with the particle shape while maintaining their pore width. Figure 7.3.15B shows a magnified image of the aforementioned particle showing details of the curvature of the pores. Figure 7.3.15A also shows a particle viewed down the [001] zone axis where the hexagonal arrangement of the nanorods can be seen.

Figures 7.3.15C and D show that the product yield was high as both images show multiple ordered mesoporous particles. The pore spacings in these images were 8.9-9.7 nm for the [100] pore spacings, derived from DDPs. It must be noted that in all of these images disordered nanoparticulate material remained present.



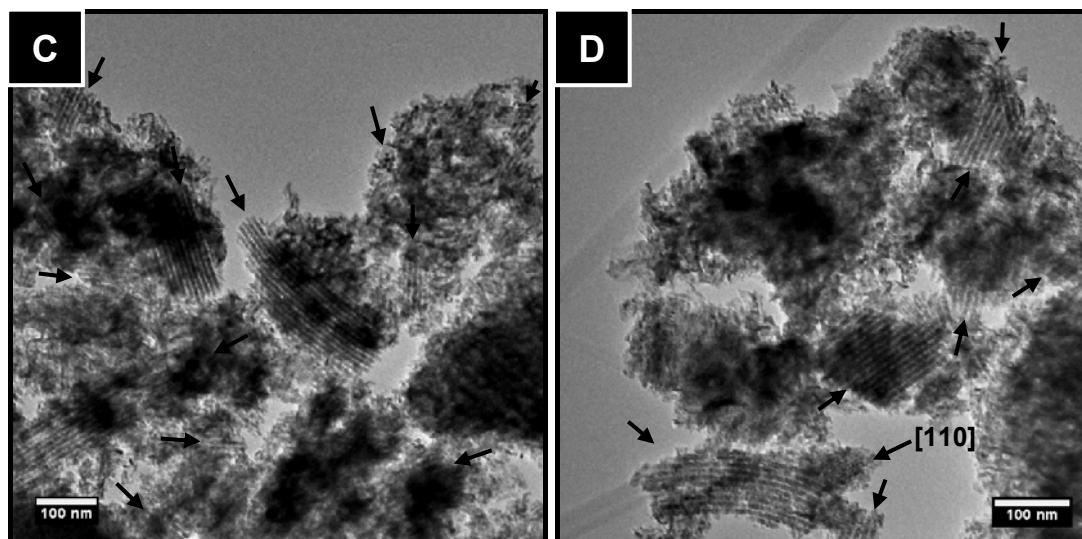
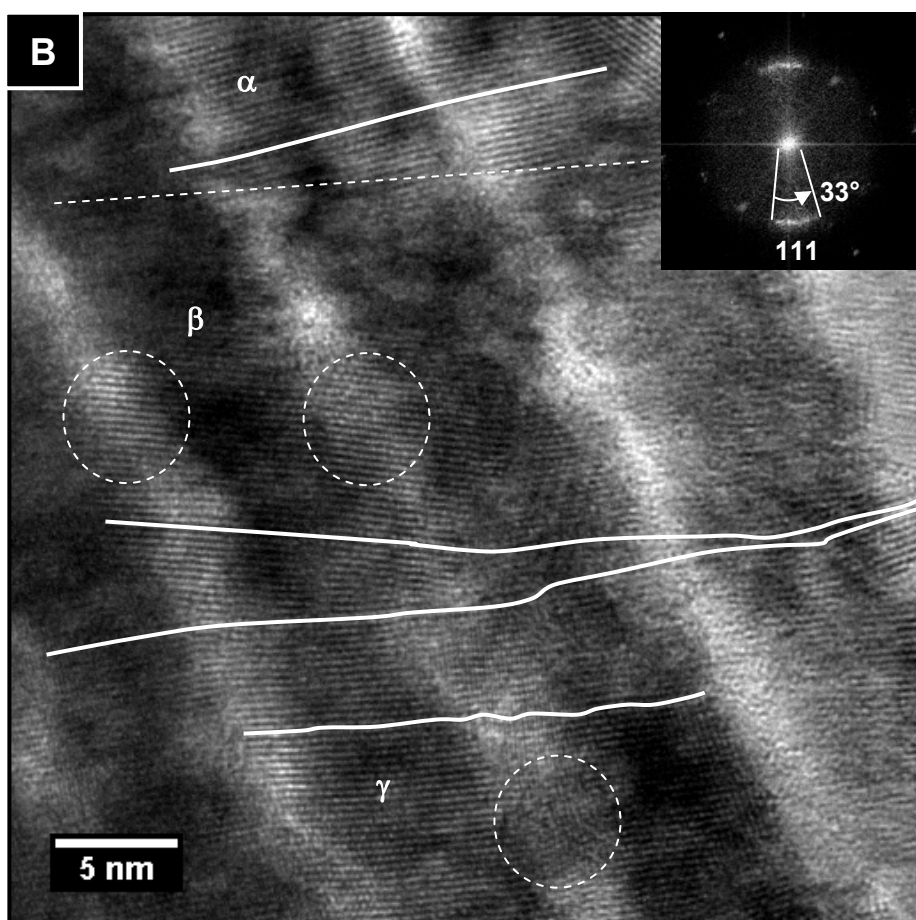
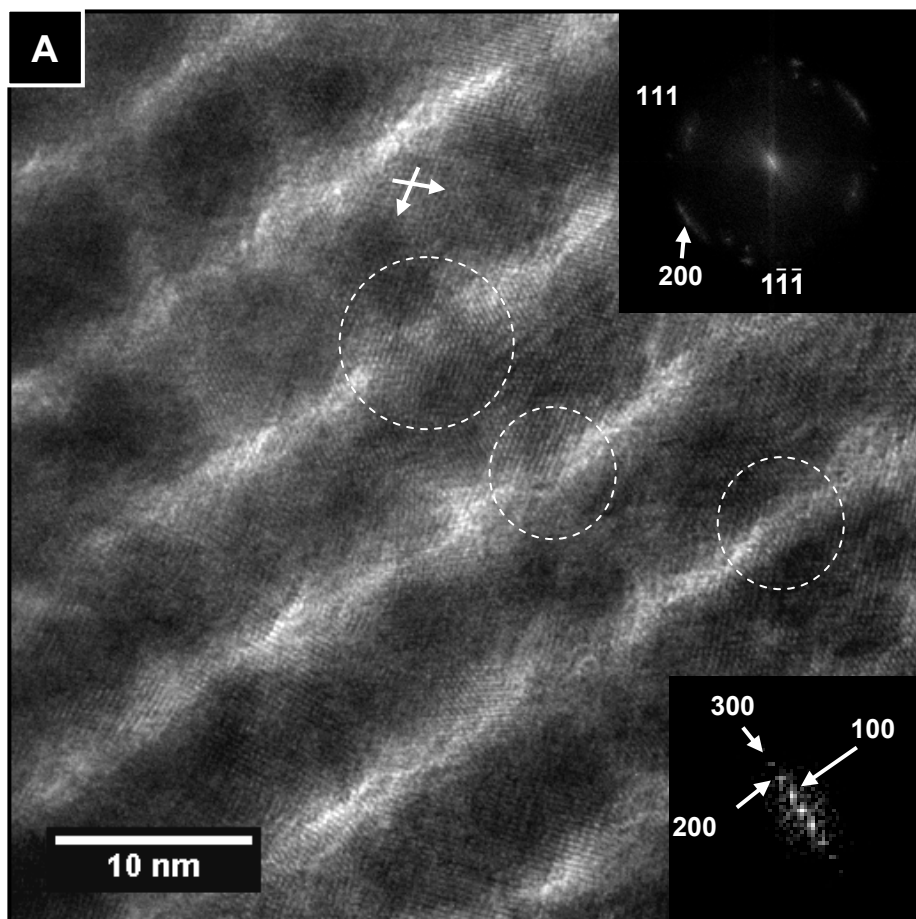


Figure 7.3.15: [A-D] Representative TEM images of Ceria-S-V₂ showing ordered mesoporous particles. [100], [110] and [001] mesopore zone axes are identified in images [A] and [D] for comparison purposes - in other images the pore directions are indicated with arrows. [B] is an enlargement of [A] as indicated.

Figures 7.3.16A-C show three HRTEM images of the pore walls. Several interesting features could be noticed from these images. Firstly, the pore walls were rough when compared to the SBA-15 template. Secondly, the crystallographic planes in adjacent pore walls were aligned with respect to each other. Thirdly, the pores look very narrow (<5 nm). And finally, the expected bridges between the pore walls, which were integral for binding the structure together, were very rarely identified. Areas identified as potential bridges using image contrast have been indicated on the HRTEM images. The inset DDPs show that there was a single predominant crystallographic orientation in each image and that, in each case, there was substantial variation in the angular orientation of the lattice planes across the image (Figure 7.3.16A 19°, B 33°, C 18°). The widest range observed was in Figure 7.3.16B but in this instance it appeared more likely that there were at least two plane defects rather than a gradual change in the lattice orientation. The lattice planes have been stencilled in, and while there is significant variation in the planes across the image, there are clearly two sharp changes (the three orientations are indicated in the image as α , β and γ).



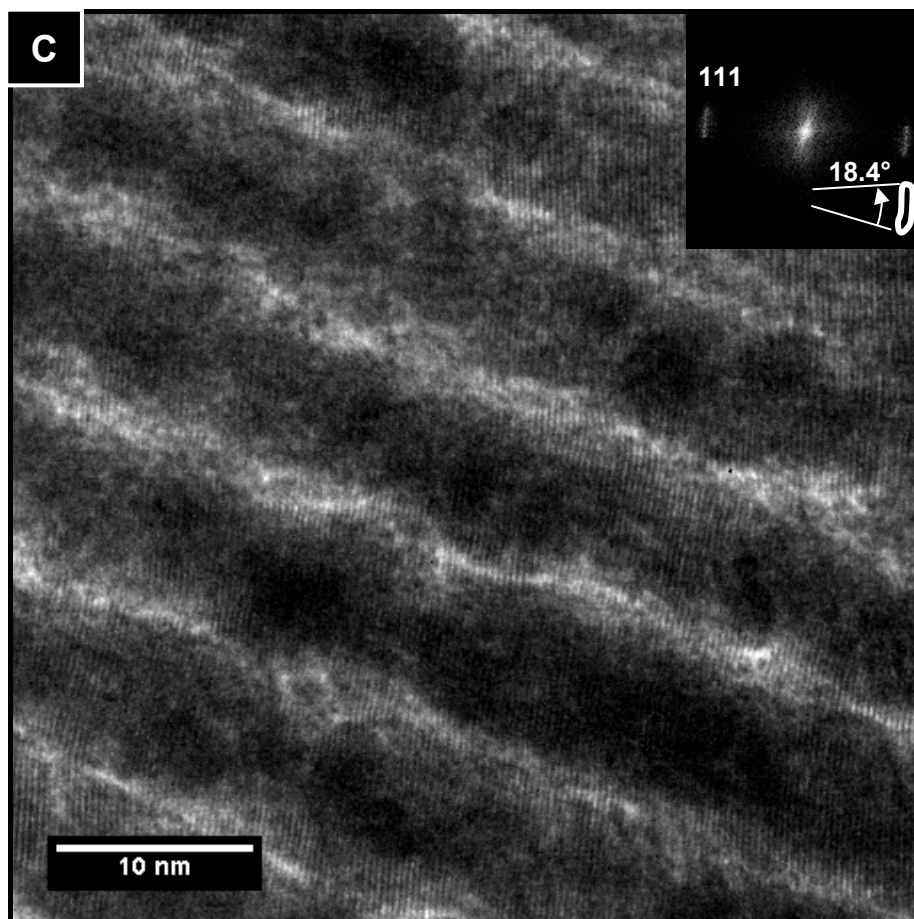


Figure 7.3.16: [A-C] HRTEM images of Ceria-S-V₂ particles viewed down the [100] mesopore zone axis showing the crystal structure of the nanorods. Inset DDPs are of the entire images. Arrows indicate crystallographic planes. Traced lines follow the lattice planes across the image. Nanobridges between the nanorods are identified where possible.

7.3.3 Ceria Prepared from KIT-6 Using VI (II)

From physisorption results, the specific surface area and pore volume of Ceria-K-V₂ were determined to be 114.7 m²g⁻¹ and 0.35 cm³g⁻¹, respectively. The adsorption-desorption isotherm was Type IV with Type H3 hysteresis (Figure 7.3.17). The pore-size distribution showed narrow peaks at 2.2-3.0 nm and poorly defined peaks around 8 nm.

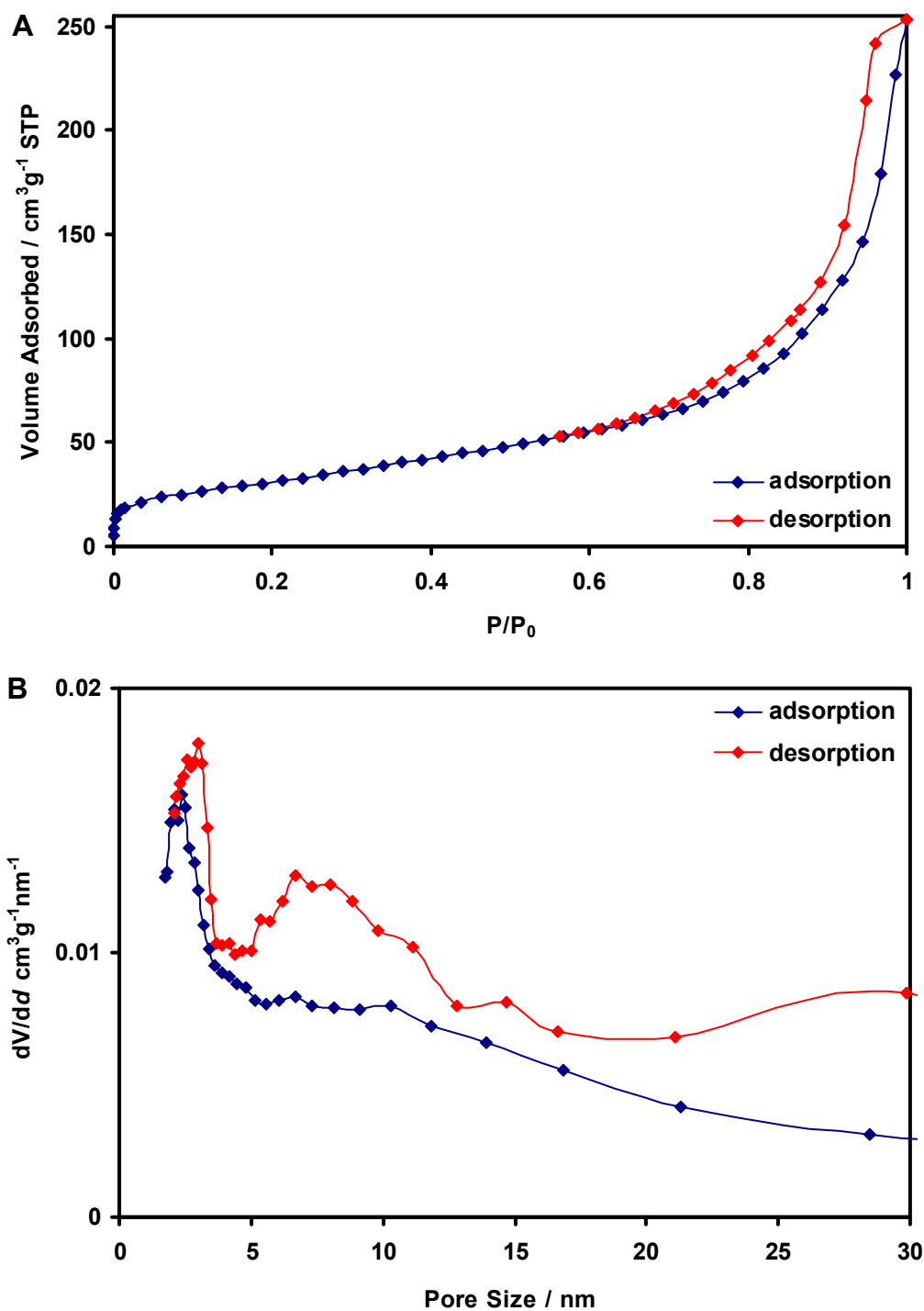


Figure 7.3.17: [A] Physisorption isotherm and [B] pore size distribution for Ceria-K-V₂.

High angle powder XRD showed the material to be single-phase fluorite ceria (*Pm3m*, ICDD 43-1002). Extensive peak broadening was observed (Figure 7.3.18). By applying the Scherrer equation to the peak broadening, an average particle size of 24.3 nm was calculated.

SAXS performed on this sample showed a smooth curve with no resolved peaks (Figure 7.3.19).

Semi-quantitative EDS of the material showed it to be predominantly Ce (52.4 mol%) and O (41.4 mol%). C and Cu X-rays were presumed to be predominantly from the carbon grid. Approximately 6.2 mol% residual Si, undoubtedly from the silica template, was detected across the sample (Figure 7.3.20).

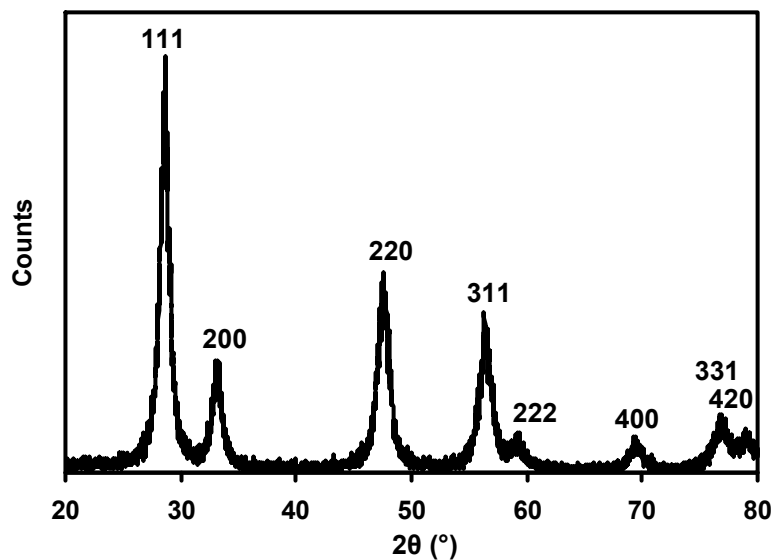


Figure 7.3.18: Powder XRD pattern for Ceria-K-V₂.

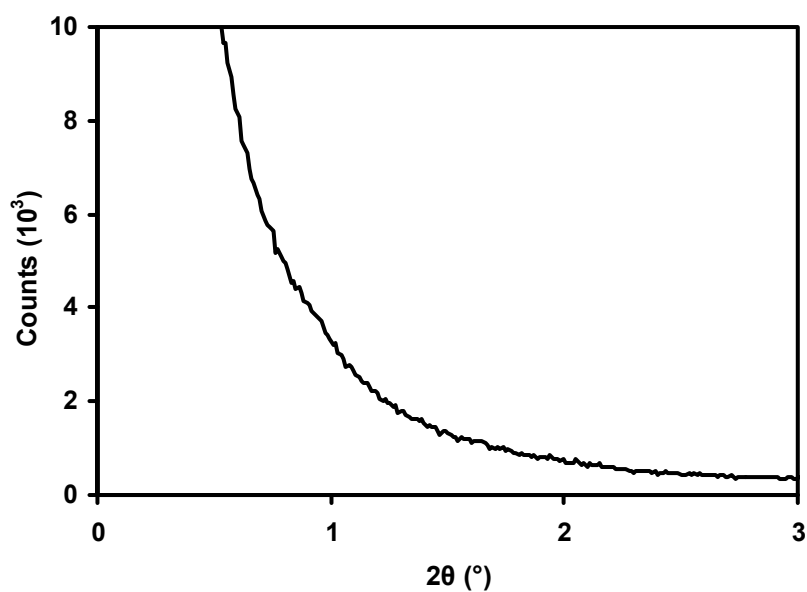


Figure 7.3.19: SAXS pattern for Ceria-K-V₂.

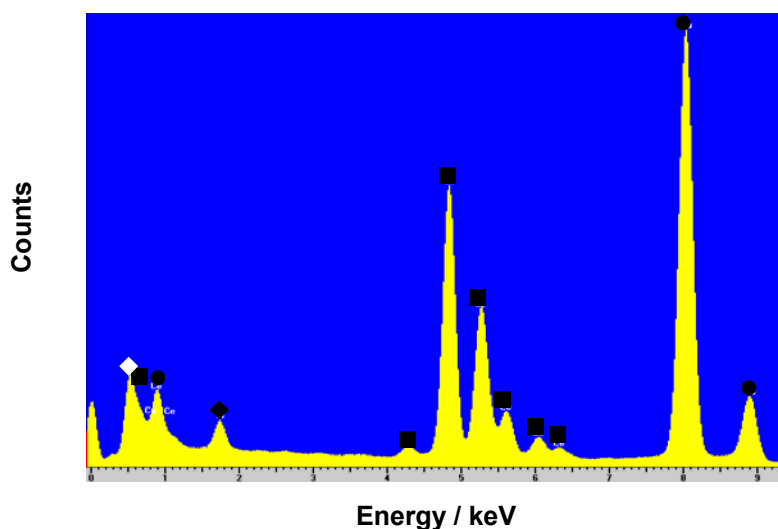


Figure 7.3.20: EDS spectrum for Ceria-K-V₂: ◇ O, ● Cu, ■ Ce, ◆ Si.

TEM images showed that the sample was predominantly comprised of ordered mesoporous particles. These were up to 200 nm across and were porous throughout their entirety. The pores could be seen in one and two dimensions showing that this material was analogous to the 3D KIT-6 template. Around the porous particles, disordered nanoparticulate ceria could be seen in the TEM images (Figures 7.3.21A and B). Mesoporous particles could be indexed to the pore structures observed for Ceria-K-V₁ in some instances, including the two [311] structures indicated. Figure 7.3.21(i) shows a DDP of a particle (c) from Figure 7.3.21B for the [311] zone axis used to obtain pore spacings. The pore spacings most often identified were the [211] with $d = 8.5\text{--}9.4$ nm and the [110] with $d = 14.1\text{--}15.7$ nm. Figure 7.3.21C shows a HRTEM image of the sample where a series of nanorods were aligned in one pore orientation. Figure 7.3.21(ii) shows a DDP taken of this entire image where it can be seen that there are two primary crystallographic orientations. The nanorods which comprised the mesoporous structure exhibited a single crystallographic orientation with material at the bottom of the image exhibiting another. The material at the bottom of the image can faintly be seen to carry on the pore structure throughout the entirety of the image.

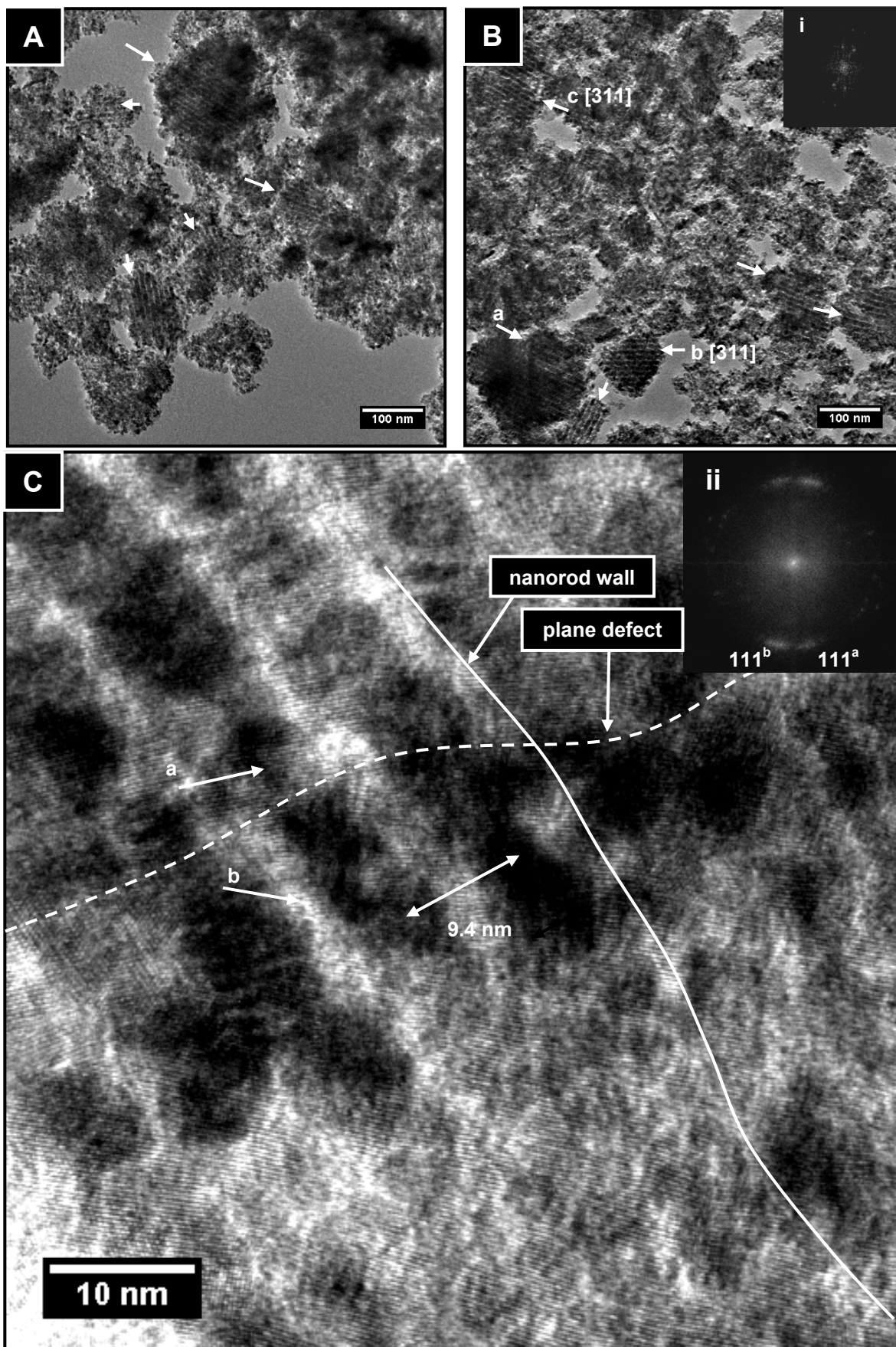
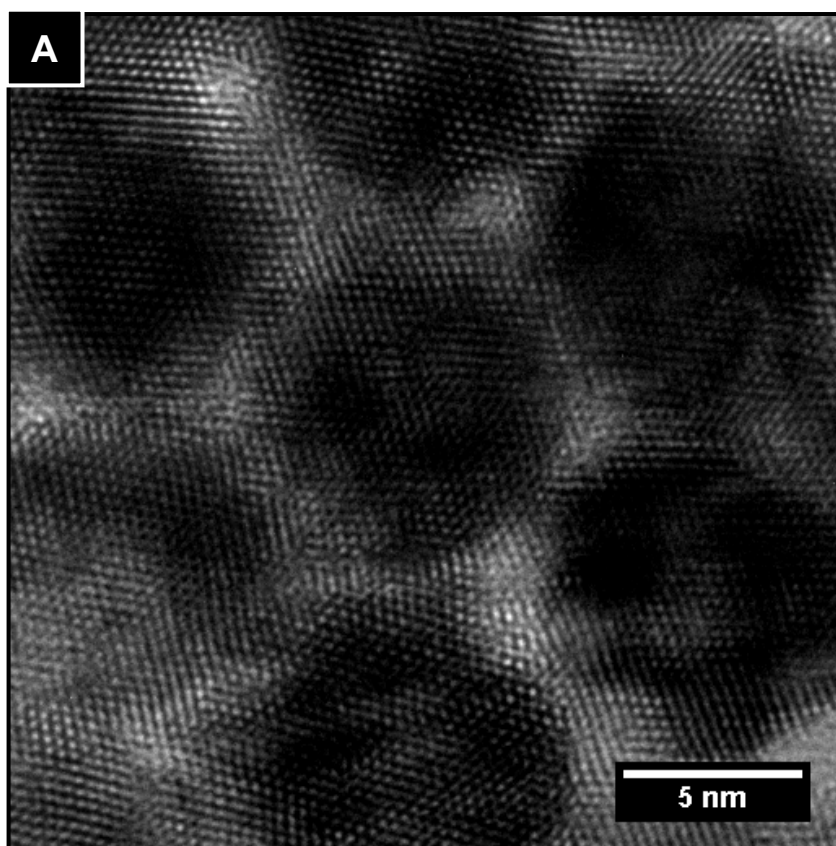


Figure 7.3.21: [A,B] Representative TEM images of Ceria-K-V₂ showing ordered mesoporous particles (Arrows indicate porous particles and zone axes are indicated where possible); [i] DDP of particle (b) in image [B] for the [311] zone axis; [C] HRTEM image of an ordered mesoporous particle showing porous single crystal morphology (pores and plane defect are indicated); [ii] DDP of entire image [D].

Figure 7.3.22A shows a HRTEM image of a particle of Ceria-K-V₂ aligned in the [110] zone axis. As can be clearly seen from the image both the pores and crystallographic planes are aligned in a ‘porous single crystal’.¹⁷⁰ The lower magnification image (Figure 7.3.22B) shows that the alignment of the pores and lattices extended over a significant distance. From both images the variation in the lattice plane orientation can be seen. The lattice planes in different vertical nanorods are at slightly different orientations. The DDP shown in Figure 7.3.22(i) confirmed, however, that the entire TEM image contained one crystallographic alignment in all three directions. The DDP confirmed that the material indexed to ceria using the (111) and (200) reflections (referenced to ICDD 43-1002) and the variation of the lattice planes was measured to be 29°.



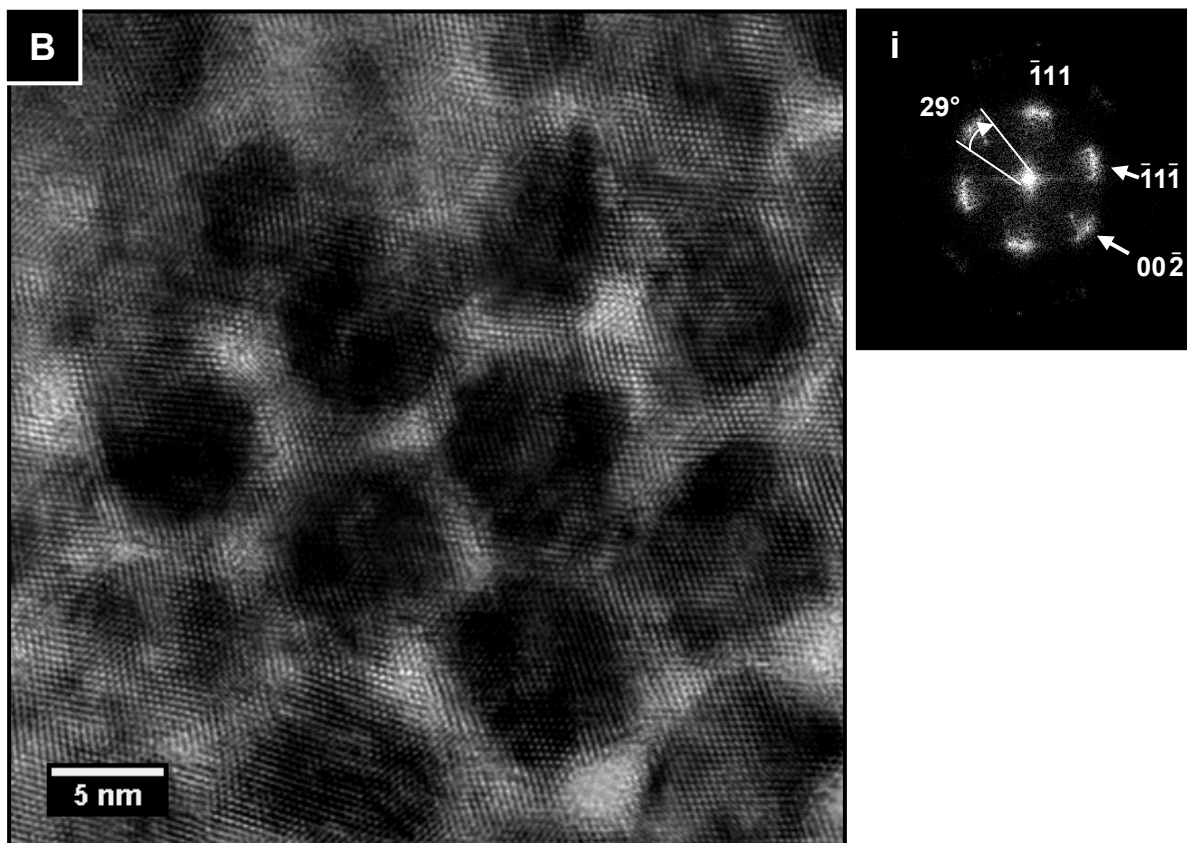
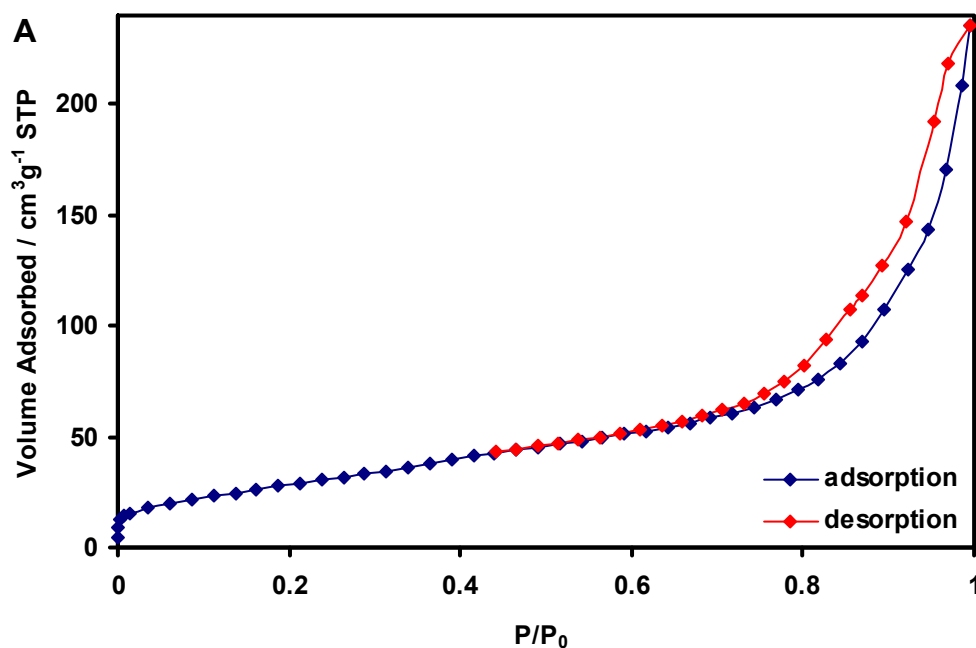


Figure 7.3.22: HRTEM images of a porous single crystal of Ceria-K-V₂: [A,B] images showing the [110] zone axis of the mesopores and the [110] crystallographic zone axis; [i] DDP of the image [B]

7.3.4 CGO Prepared from SBA-15 Using VI

From physisorption results, the specific surface area and pore volume of CGO-S-V₂ were determined to be 108.6 m²g⁻¹ and 0.32 cm³g⁻¹, respectively. The adsorption-desorption isotherm was Type IV with Type H3 hysteresis (Figure 7.3.11). The pore-size distribution showed sharp peaks at 2.5-3.0 nm and broad peaks at 11-17 nm.



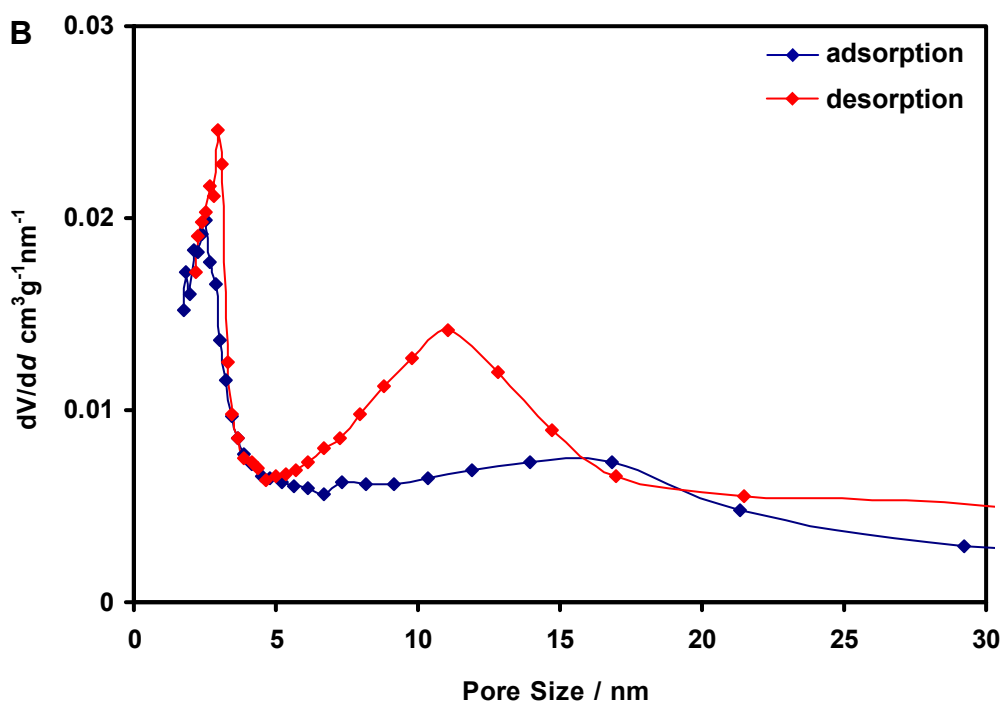


Figure 7.3.23: [A] Physisorption isotherm and [B] pore size distribution for CGO-S-V₂.

High angle powder XRD showed the structure of the material to be a single phase consistent with CGO with the fluorite structure ($Pm3m$, ICDD 75-0161). Extensive peak broadening was observed (Figure 7.3.24). By applying the Scherrer equation to the peak broadening, an average particle size of 23.5 nm was calculated.

SAXS performed on this sample showed two broad shoulders that could be resolved by subtracting the background (Figure 7.3.25). The background subtraction was done by eliminating the peaks of interest from the data set, and then fitting a curve to the zero loss peak. The calculated curve was then subtracted from entire data set to resolve the sample peaks. The peaks appear at equivalent angles to the SBA-15 SAXS pattern (Figure 5.3.2), with $2\theta = 0.96^\circ$ and $1.96\text{--}2.06^\circ$ equating to $d = 9.2$ (100) and 4.3–4.5 nm (200), respectively.

Semi-quantitative EDS of the material showed it to be predominantly Ce (35.5 mol%), O (55.2 mol%) and Gd (3.3 mol%). C and Cu X-rays were presumed to be predominantly from the carbon grid. Approximately 6.0 mol% residual Si, undoubtedly from the silica template, was detected across the sample (Figure 7.3.26).

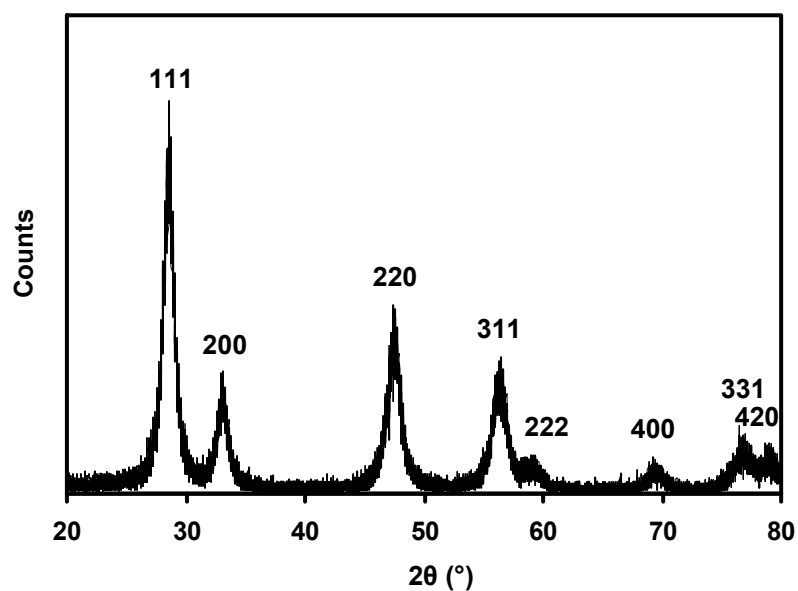
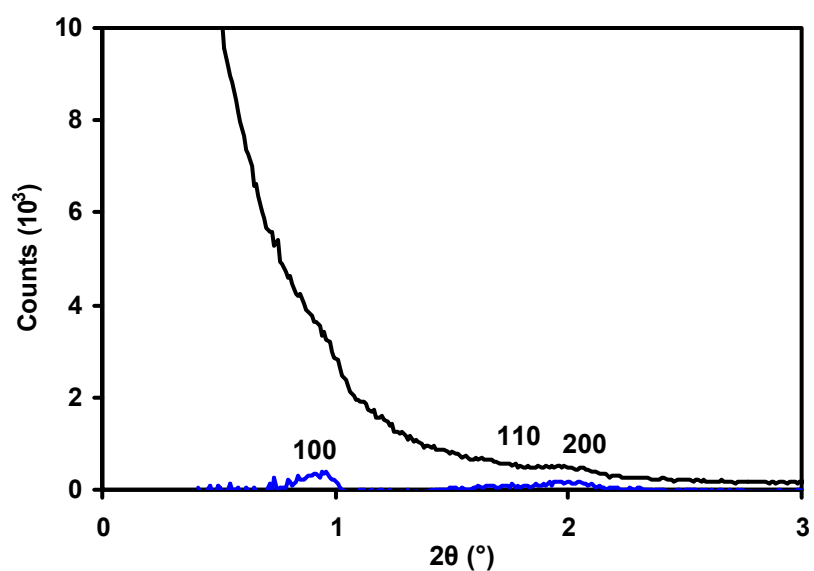


Figure 7.3.24: Powder XRD pattern for CGO-S-V₂.



Peak 2θ (°)	Indices	d-spacing (nm)
0.96	100	9.2
1.96-2.06	200	4.3-4.5

Figure 7.3.25: SAXS pattern for CGO-S-V₂ (■ background subtracted plot).

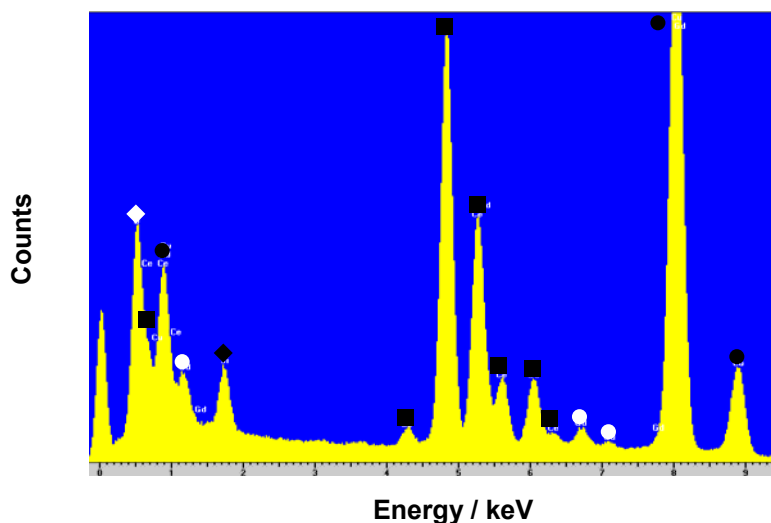
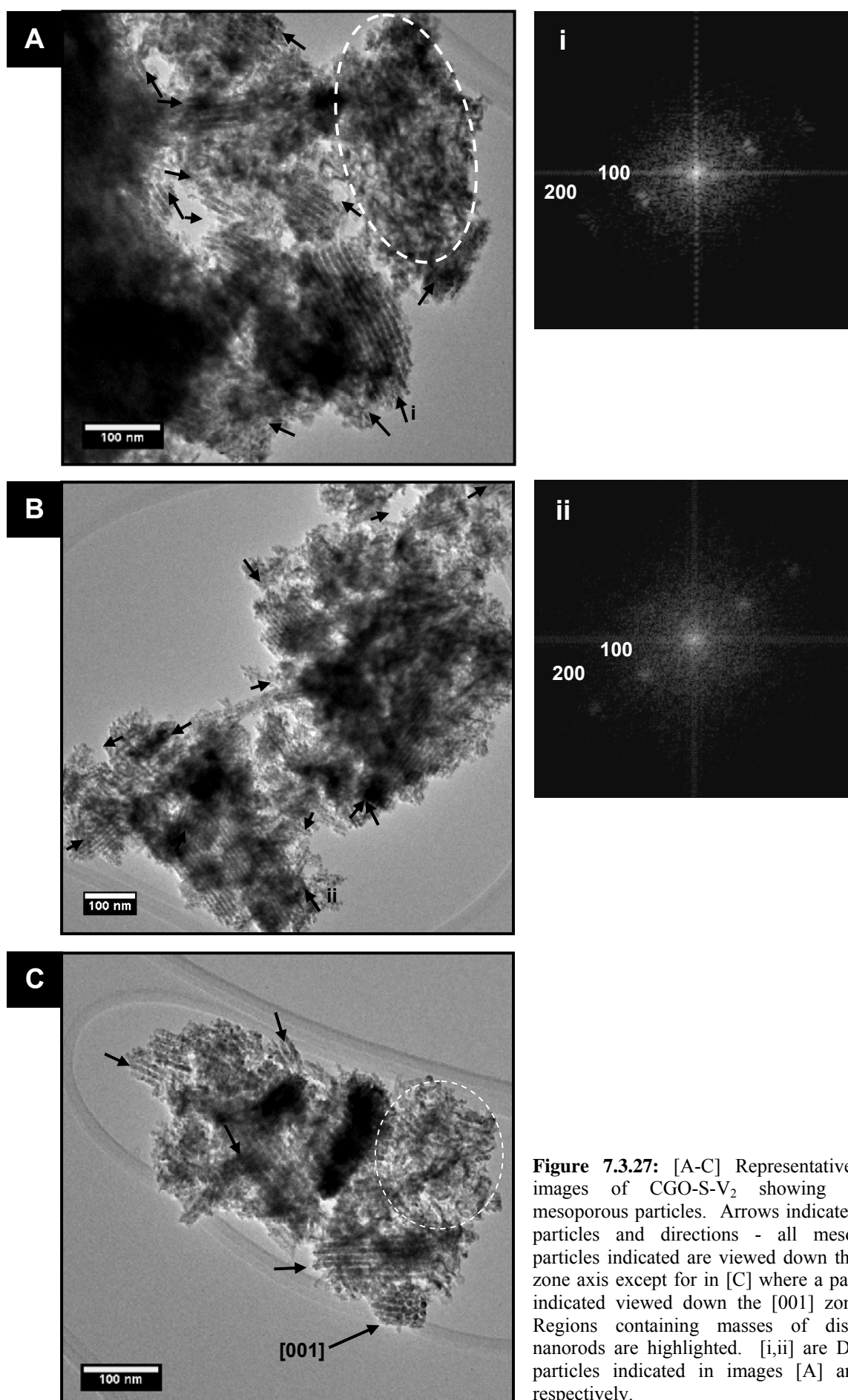


Figure 7.3.26: EDS spectrum for CGO-S-V₂: ◇ O, ■ Ce, ● Cu, ○ Gd, ◆ Si.

Figures 7.3.27A-C shows TEM images of CGO-S-V₂ in which high yields of ordered mesoporous particles (up to 250 nm long) can be seen. While the ordered mesoporous structures were not as large as observed in Ceria-S-V₂, they exhibited the same morphology - parallel pores of high aspect ratio in hexagonal arrays. The images clearly present these particles viewed down the [100] and [001] zone axes. The pore spacings ranged from 8.7 to 9.3 nm for the [100] pore orientation derived from DDPs such as those of Figures 7.3.27(i) and (ii). Surrounding the ordered material were disordered nanoparticles (observed in Figures 7.3.27A and C) as well as small agglomerations of nanorods. These nanorods were aggregated in bundles. The diameter of the nanorods in these bundles was equivalent to that of the pores from the template (discussed in more detail in Section 7.6.1).



The HRTEM image, Figure 7.3.28, shows that the pore walls were porous single crystals, or were comprised of a small number of crystallographic orientations as shown by the DDPs (i-iv). The (111) reflections from the DDPs confirmed the material was consistent with CGO (referenced to ICDD 75-0161). As with the ceria materials, Ceria-S-V₂ and Ceria-K-V₂, the pore walls were made from nanorods rather than sintered nanoparticles. The DDP (iv) gave a pore spacing of 9.0 nm for the image. Variation in the crystallographic lattice planes for the bulk of the mesoporous particle was observed and measured to be up to 17°.

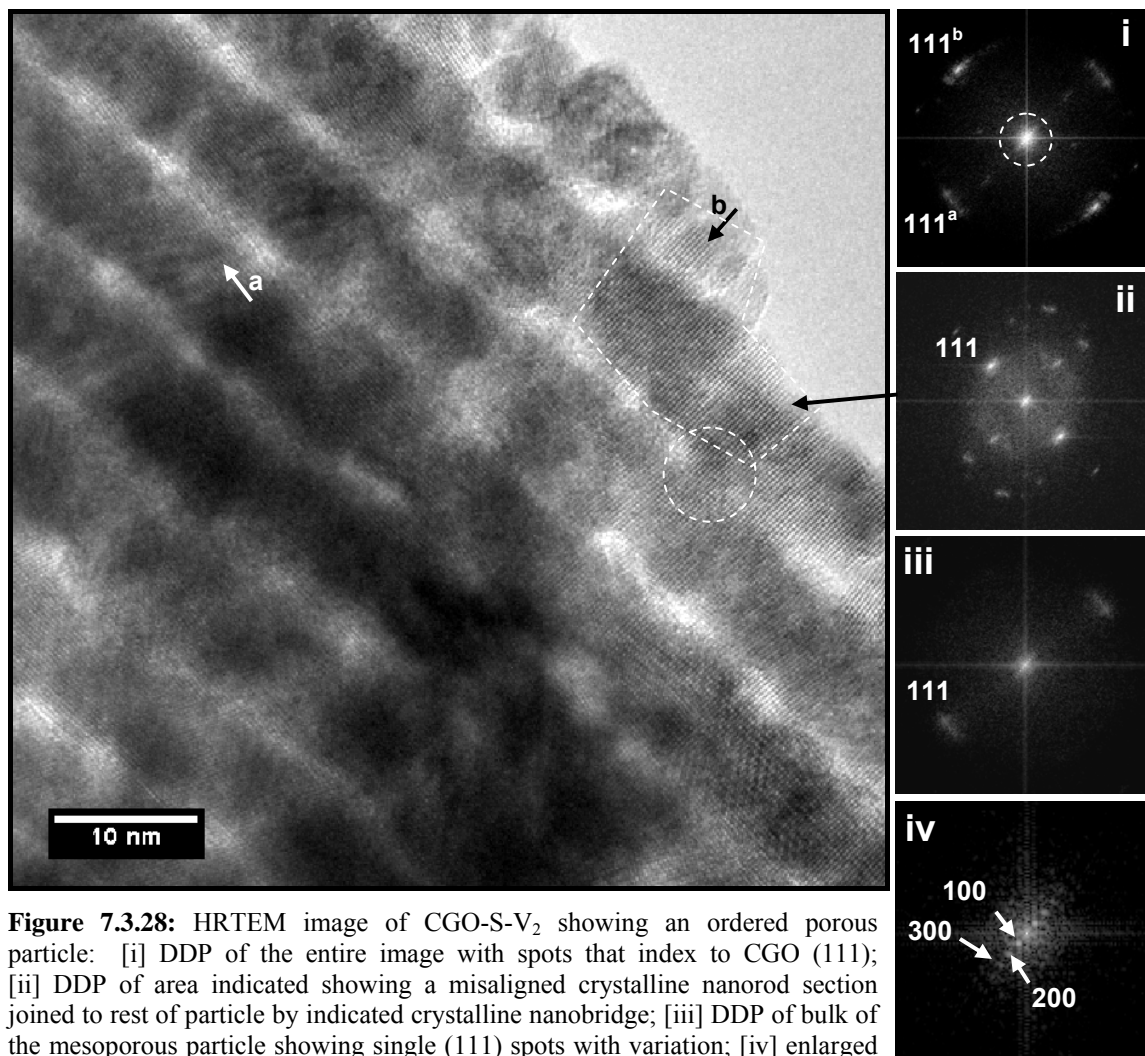


Figure 7.3.28: HRTEM image of CGO-S-V₂ showing an ordered porous particle: [i] DDP of the entire image with spots that index to CGO (111); [ii] DDP of area indicated showing a misaligned crystalline nanorod section joined to rest of particle by indicated crystalline nanobridge; [iii] DDP of bulk of the mesoporous particle showing single (111) spots with variation; [iv] enlarged central section of [i] showing the spots corresponding to the mesopores.

Figure 7.3.29A shows a porous single crystal viewed down the [100] zone axis with respect to the mesopores and the [110] zone axis of the CGO crystal structure. Figure 7.3.29(i) showed that the variations in lattice orientations were large (24°). These have been traced along two dimensions to show how the lattice planes vary across the image. The pore spacing was measured to be 9.8 nm. Figure 7.3.29B shows nanorods with a set of (111) crystallographic planes aligned approximately perpendicular to the length of the pores and exhibiting significant variation in their crystallographic lattice orientation. These variations in

orientation can be seen clearly as slight undulations in the angle of the planes across the image. The range of lattice planes was measured to be 28° from the DDP, Figure 7.3.29(iii).

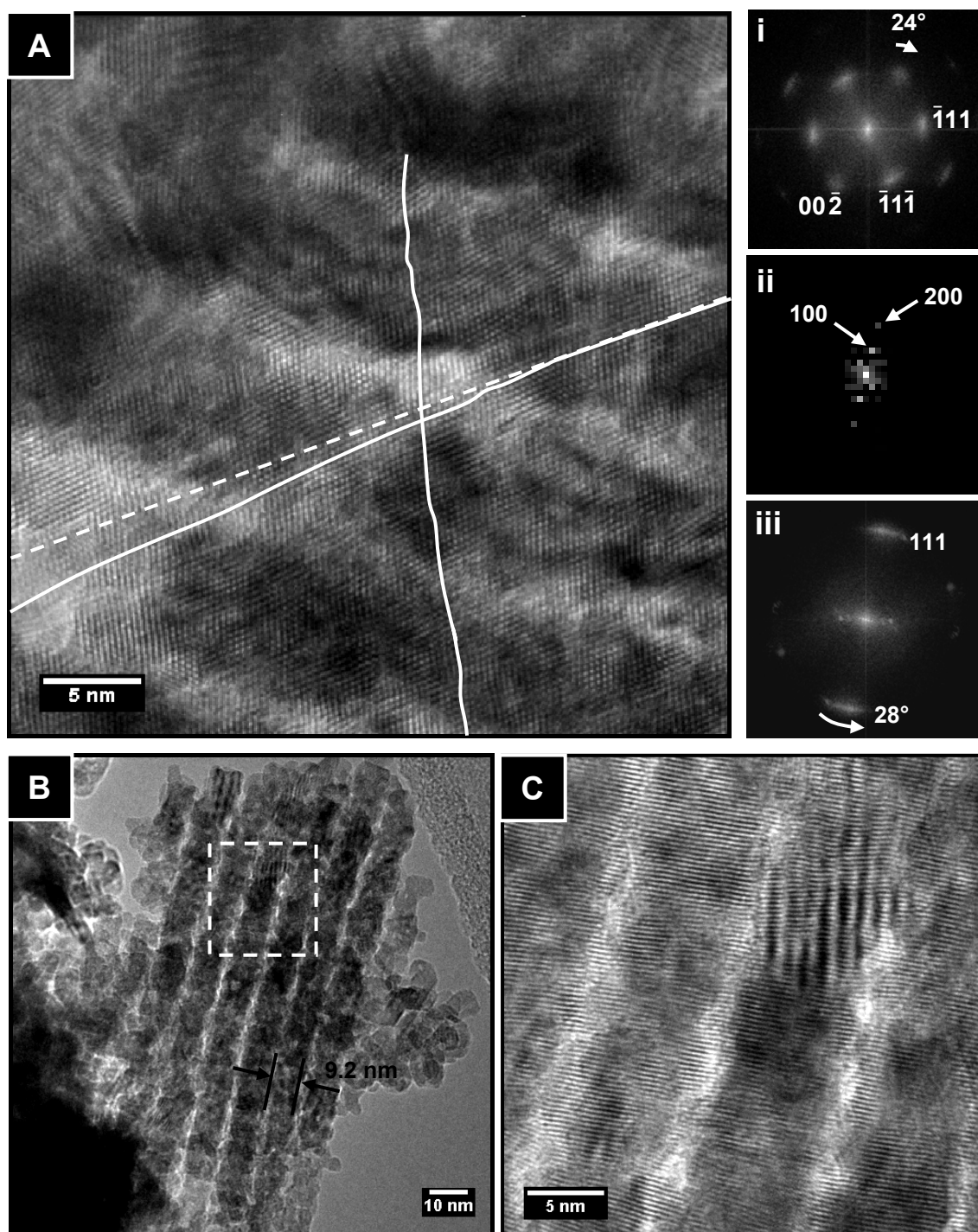
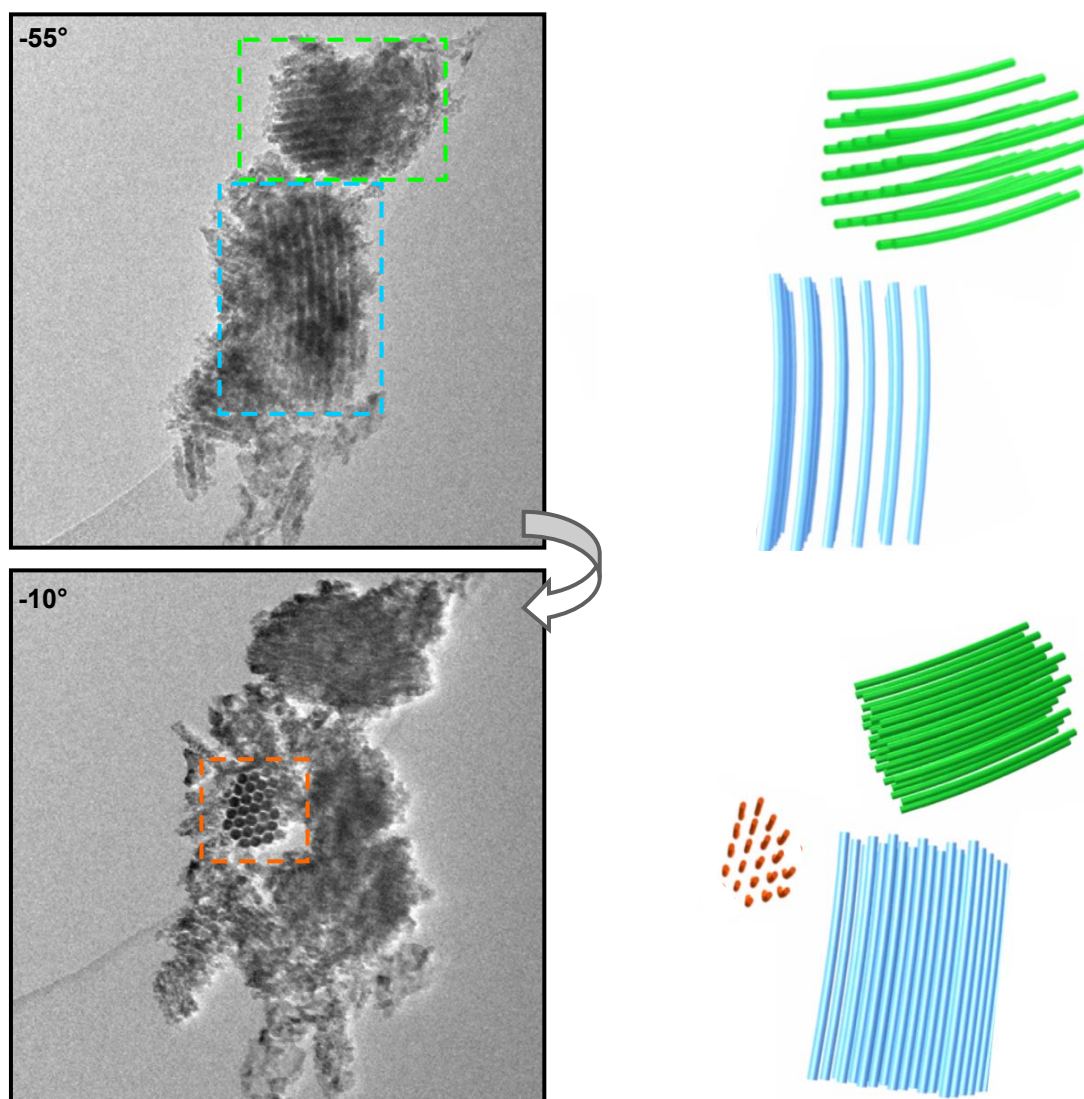


Figure 7.3.29: [A] HRTEM image of a CGO-S-V₂ porous single crystal viewed down the [100] pore, and [110] crystallographic zone axis (the lattice planes were traced to show the variation across the image with a straight line drawn for reference); [i] DDP of entire image [A] indexed to the [110] zone axis for CGO; [ii] enlargement of the centre of [i] showing the spots corresponding to the [100] mesopore zone axis; [B] TEM image of a mesoporous particle of CGO-S-V₂; [C] HRTEM image of section indicated in [B] showing that this was a porous single crystal; [iii] DDP of entire image [C] showing it is predominantly a single orientation.

7.3.4.1 Tomography Study of CGO-S-V₂

Tomography studies allowed the 3D structure of CGO-S-V₂ to be probed in more detail. Figure 7.3.30 shows TEM images taken from a tilt series. The sample was rotated from -55 to +55° in the sense indicated after having been placed at the eucentric point in the microscope. The ordered mesoporous particles that go through multiple orientations are highlighted. Graphical models are used to illustrate the particle orientations during rotation. This tilt series shows that these particles were curved more highly along one axis [100] than the other [010]. The full tilt series can be viewed on-line.¹⁷¹



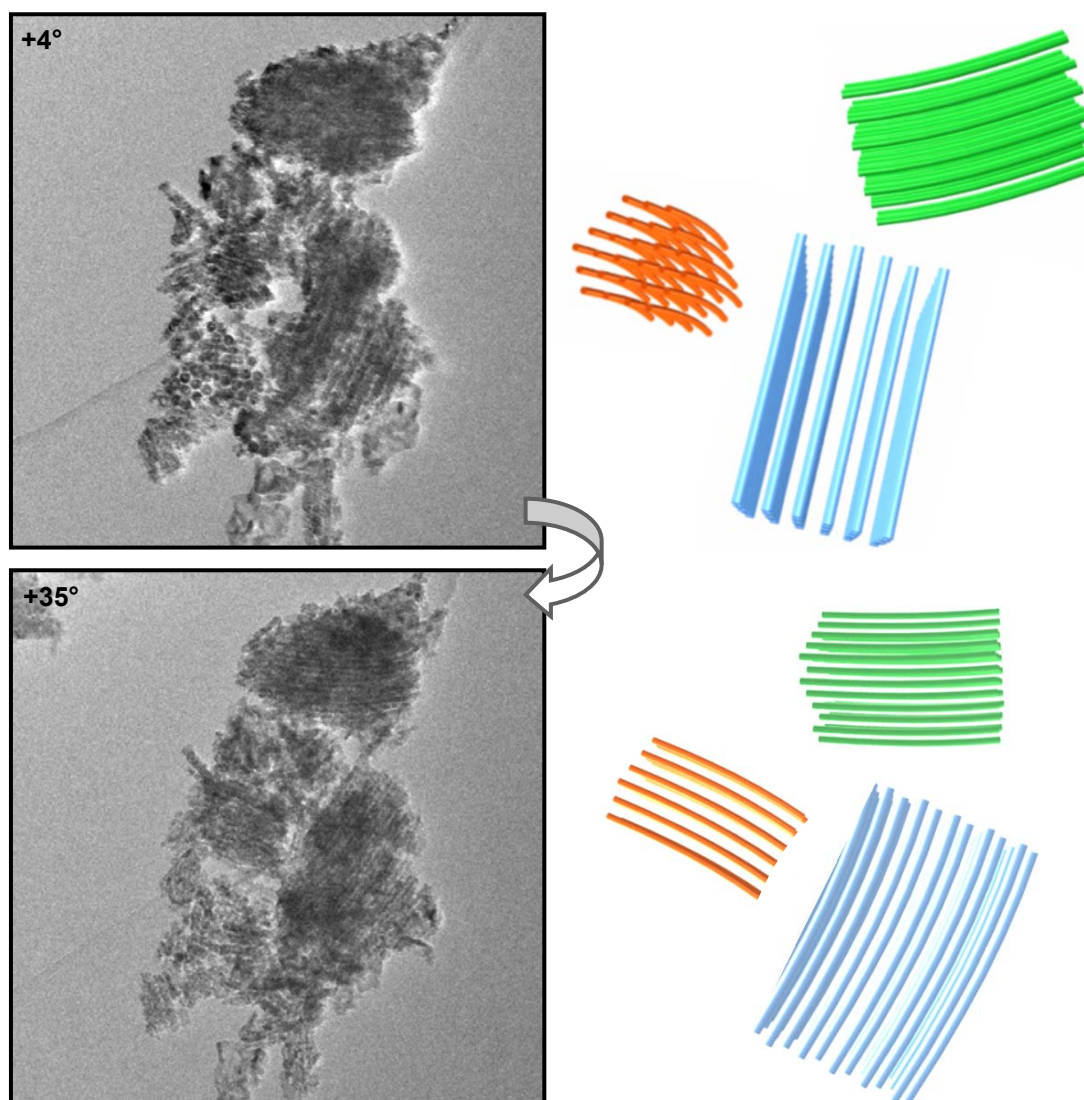


Figure 7.3.30: Images taken from a tilt series obtained for TEM tomography showing different pore orientations for a sample of CGO-S-V₂. Models prepared using Blender™ 2.49b.¹⁷²

7.3.5 CGO Prepared from KIT-6 Using VI

From physisorption results, the specific surface area and pore volume of CGO-K-V₂ were determined to be 137.5 m²g⁻¹ and 0.38 cm³g⁻¹, respectively. The adsorption-desorption isotherm was Type IV with Type H3 hysteresis (Figure 7.3.11). The pore-size distribution showed peaks at 2.1-2.7 nm.

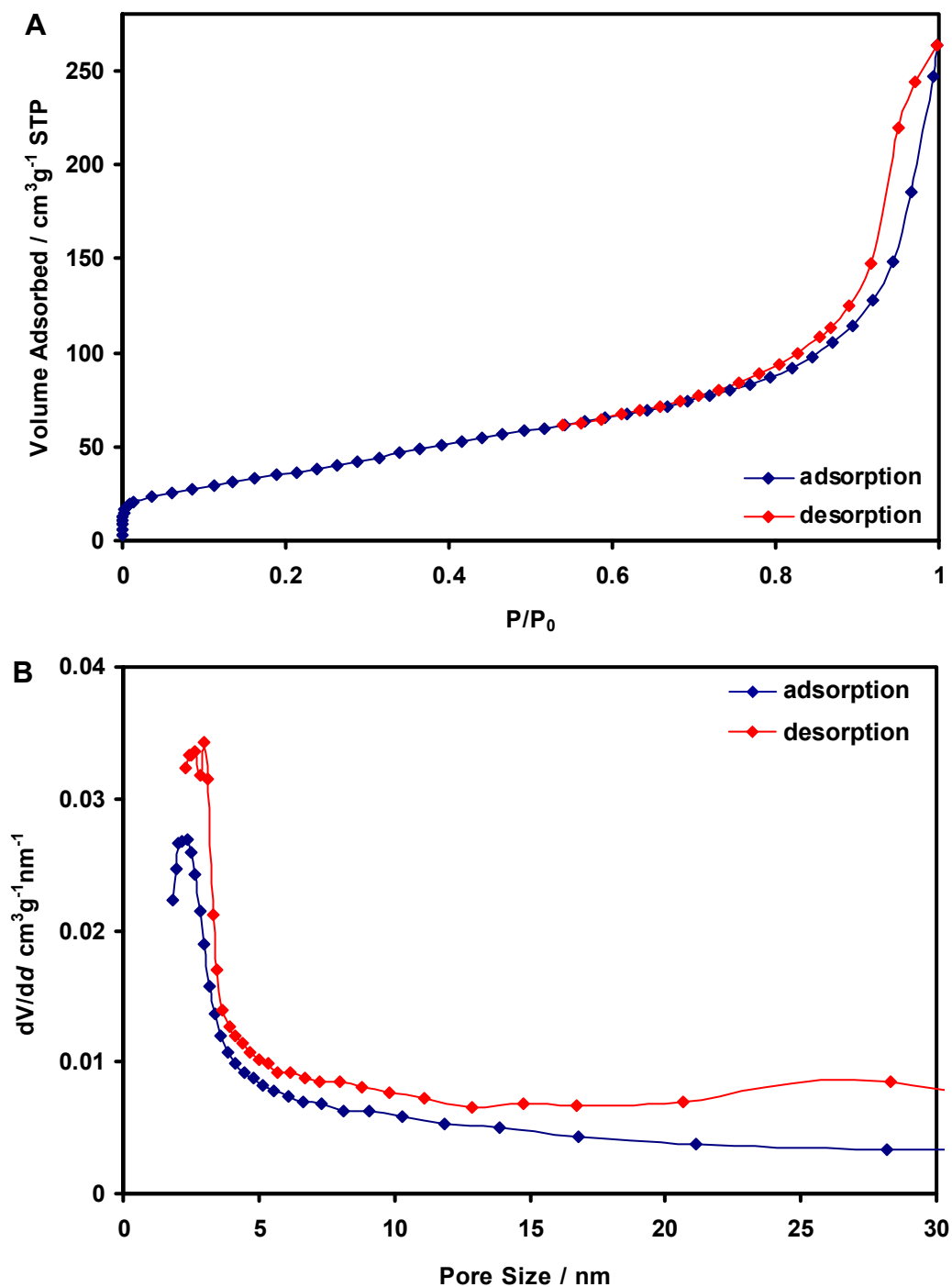


Figure 7.3.31: [A] Physisorption isotherm and [B] pore size distribution for CGO-K-V₂.

Powder XRD showed the material to be a single-phase consistent with CGO with the fluorite structure (ICDD 75-0161). Extensive peak broadening was observed (Figure 7.3.32). By applying the Scherrer equation to the peak broadening, an average particle size of 22.5 nm was calculated.

SAXS performed on this sample showed two broad shoulders that could be resolved by subtracting the background (Figure 7.3.33). The background subtraction was done by eliminating the peaks of interest from the data set, and then fitting a curve to the zero loss peak. The calculated curve was then subtracted from the entire data set to resolve the sample

peaks. The peaks appear at equivalent angles to the KIT-6 SAXS pattern (Figure 5.3.7), with $2\theta = 1.01^\circ$ equating to a pore spacing of 8.8 nm {211}, and the broad peak centred at 2.0° equating to pore spacings of approximately 4.2-4.7 nm $\{14 \leq (h^2+k^2+l^2) \leq 26\}$. This range of {hkl} was calculated using the lattice constant and corresponds to {321}, {400}, {420}, {332}, {420} and {431} from the KIT-6 SAXS pattern.

Semi-quantitative EDS of the material showed it to be predominantly Ce (46.1 %), O (42.9 %) and Gd (4.6 %). C and Cu X-rays were presumed to be predominantly from the carbon grid. Approximately 6.3 % residual Si from the silica template was detected across the sample (Figure 7.3.34).

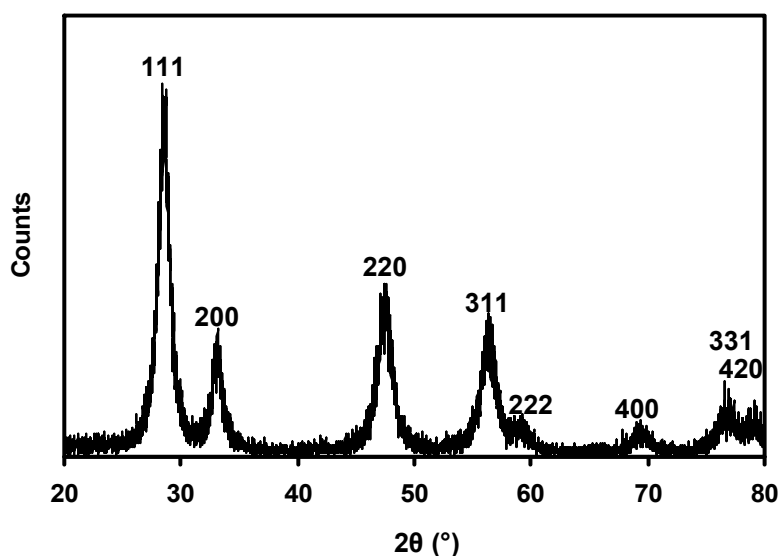
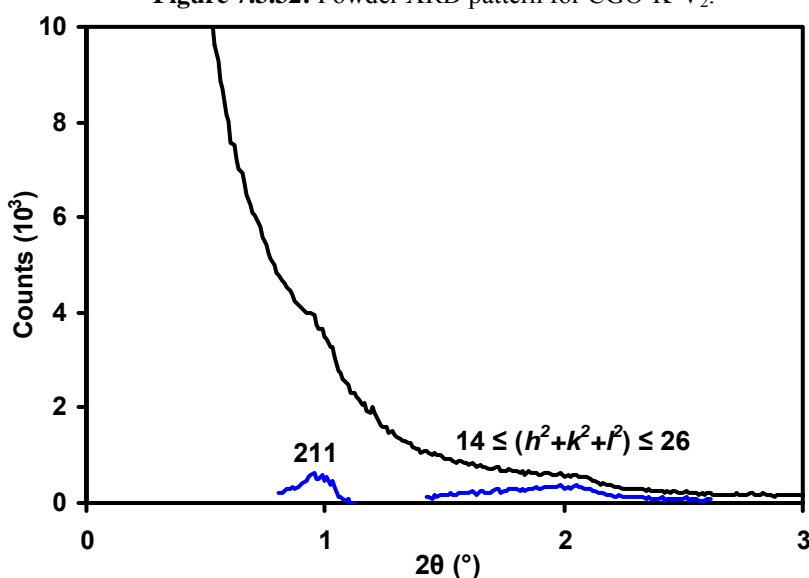


Figure 7.3.32: Powder XRD pattern for CGO-K-V₂.



Peak 2θ (°)	Indices	d-spacing (nm)
1.01	211	8.8
1.87-2.12	321, 400, 420, 332, 420, 431	4.2-4.7

Figure 7.3.33: SAXS pattern for CGO-K-V₂ (■ background subtracted plot).

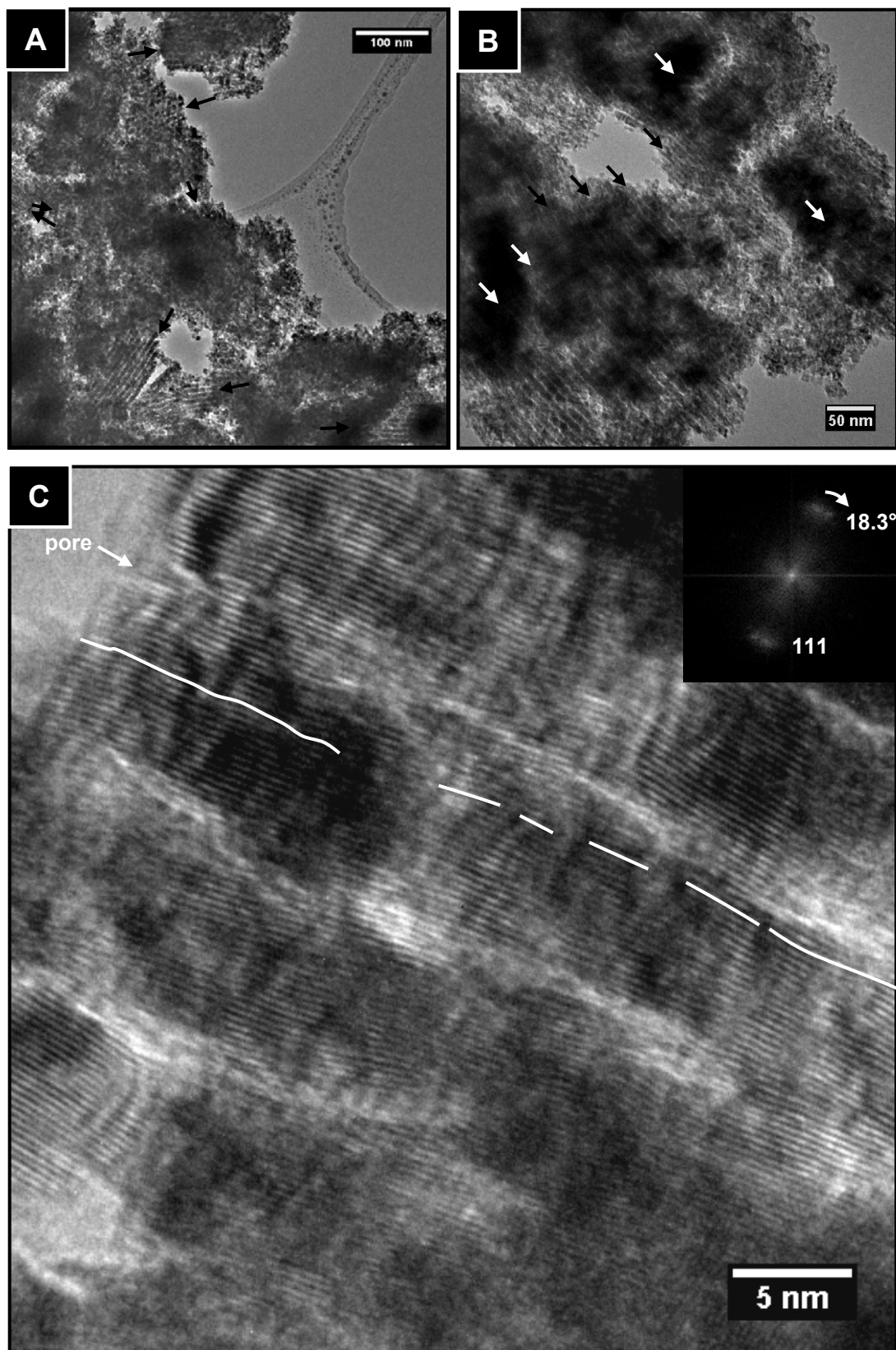


Figure 7.3.35: [A,B] representative TEM images of CGO-K-V₂ showing multiple ordered mesoporous particles (arrows indicate direction of mesopores in particles); [C] HRTEM image of a porous single crystal exhibiting the porous single crystal morphology with inset DDP of the entire image (the traced line follows a crystallographic plane, where possible, across the entire particle).

Figure 7.3.36A shows a large particle with the pores slightly misaligned, viewed down the [210] zone axis. Figure 7.3.36B presents a HRTEM image of this particle. The lattice planes

are visible in three directions. The inset DDP shows that there was significant variation in the crystallographic lattice orientation across the entire image without there being any other crystallographic orientations. This was measured to be 21° from the DDP. The (111) and (200) spots confirmed that the material was consistent with crystalline CGO (referenced to ICDD 75-0161).

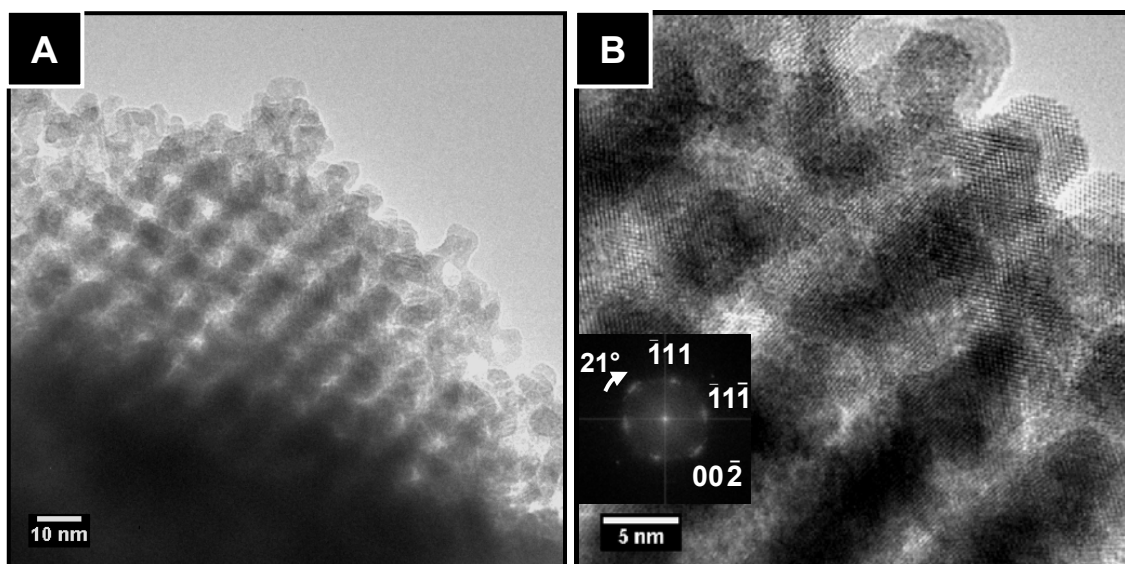


Figure 7.3.36: [A] TEM image of a ordered mesoporous particle of CGO-K-V₂ viewed down the [210] zone axis; [B] HRTEM image of [A] showing porous single crystal morphology with inset DDP showing [110] crystallographic zone axis.

7.3.5.1 Tomography Study of CGO-K-V₂

Tomography studies allowed the 3D structure of CGO-K-V₂ to be probed in more detail. Figure 7.3.37 shows TEM images from a tilt series. The sample was rotated from -55° to $+55^\circ$ in the sense indicated after having been placed at the eucentric point in the microscope. The ordered mesoporous particles that go through multiple orientations are highlighted. Graphical models are not used for this structure as the pore structure was too complex to resolve from this series. The series showed that the particles exhibited regular pores through three dimensions. At -55° the particle is oriented in the [311] zone axis, while at 0° and $+55^\circ$ it passes through two [210] zone axes. The full tilt series can be viewed on-line.¹⁷¹

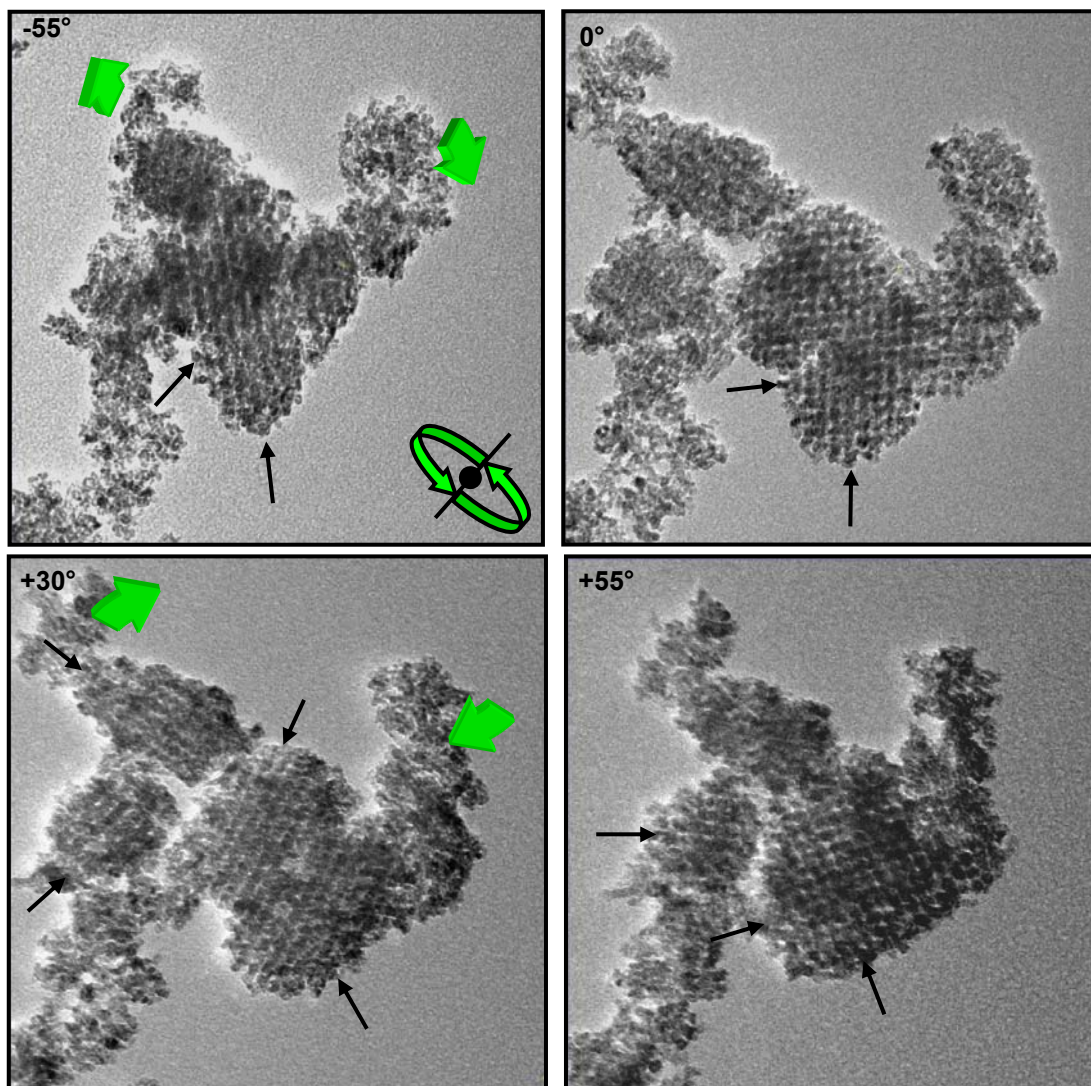


Figure 7.3.37: Images from tilt series obtained for TEM tomography showing different pore orientations for a sample of CGO-K-V₂. Sense of rotation is indicated in the first panel. Arrows indicate the direction of mesopores.

7.3.6 Compositional Analysis

Studies of the compositions of two types of mesoporous materials (Ceria-S-V₂ and CGO-S-V₂) using high resolution EDS (at the NNNC) utilised three main techniques of EDS analysis: spot analysis, area analysis, and line scanning analysis. The detector recorded a spectrum for each pixel in the image and amalgamated the spectra based on user-defined parameters for subsequent analysis. Cu, C and Au peaks were deconvoluted from the quantitative analysis except where specified.

Figure 7.3.38A shows a STEM image of a particle of Ceria-S-V₂ with the pore structure presented in the [100] zone axis. From the EDS maps (Figure 7.3.38B) the outline of the entire particle could be distinguished but no pore walls could be resolved in the elemental maps. Attempts at quantitative analysis of the features observed in the image produced results with significant variation. The previously measured value of 4.5 mol% Si (using the University of St Andrews TEM), was at the highest end of the quantitative data (Table 7.1)

with the channels showing a lower Si content than the pore walls. It is worth noting that one of the channels also showed a higher Ce content than the pore walls.

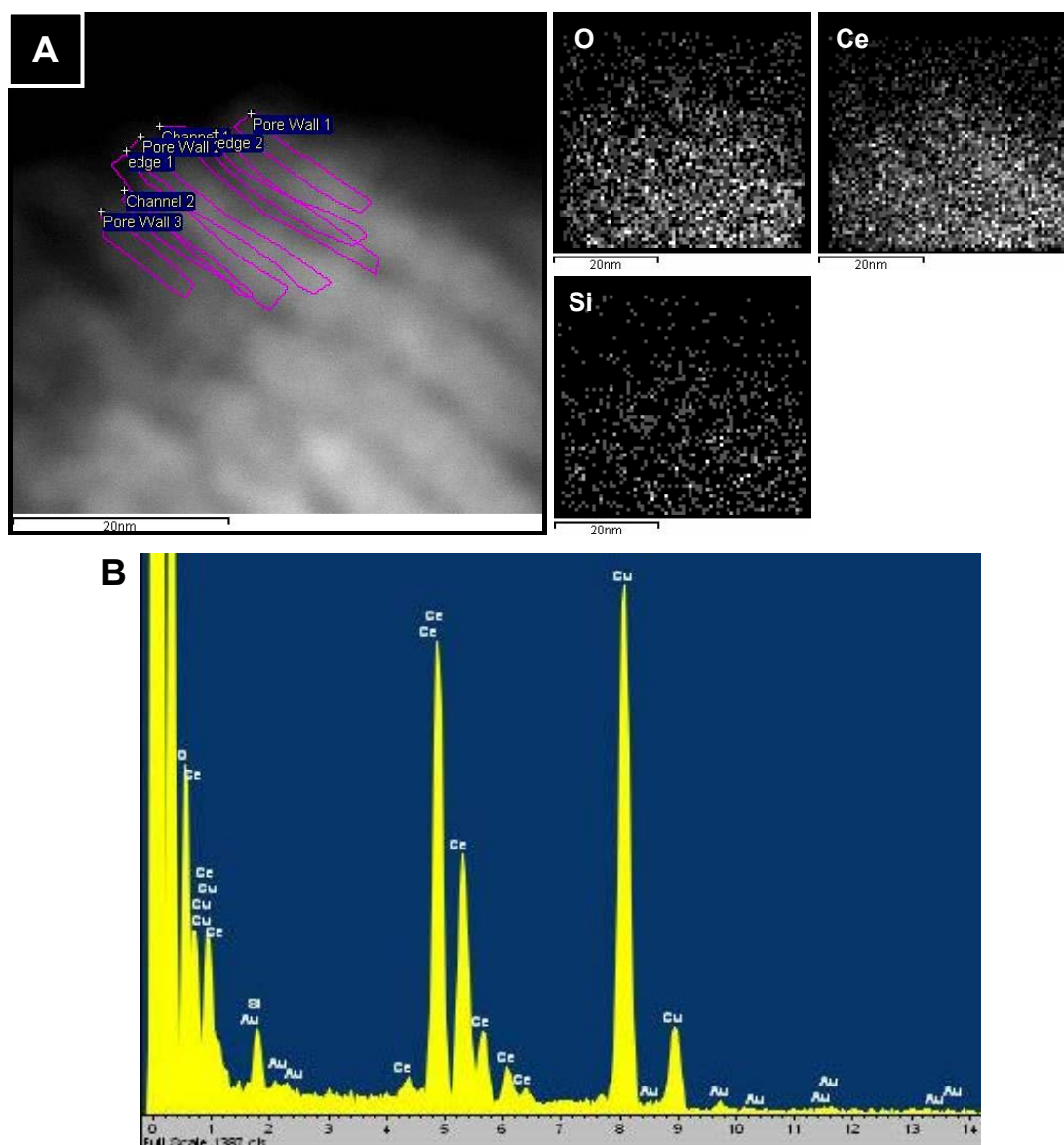


Figure 7.3.38: [A] STEM image of Ceria-S-V₂ with EDS maps. Selected areas indicate the EDS mapped regions in Table 7.1; [B] EDS sum spectrum of the entire image.

Table 7.1: Quantitative EDS results from spectra taken in Figure 7.3.38A in mol%.

Spectrum	O K Series	Si K Series	Ce L Series
Sum Spectrum	65.15	4.28	30.57
Channel 1	62.02	2.75	35.23
Channel 2	71.20	0.42	28.39
Pore Wall 1	67.43	3.79	28.78
Pore Wall 2	63.69	5.43	30.87
Pore Wall 3	67.58	4.03	28.39
Edge 1	68.35	2.84	28.80
Edge 2	55.67	4.44	39.89

Using a line scan across a set of pores showed no notable variation in any EDS spectral lines to indicate a variation in the composition across the image (Figure 7.3.39).

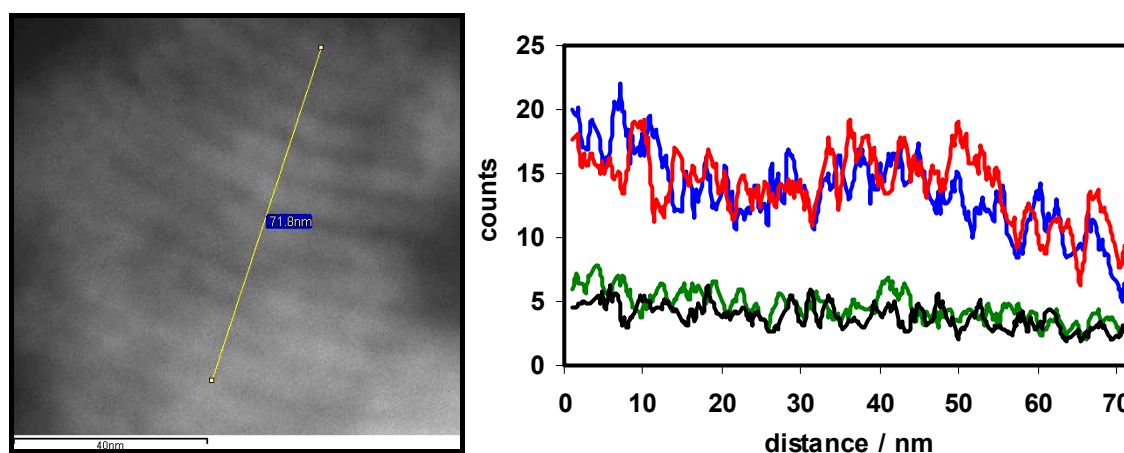
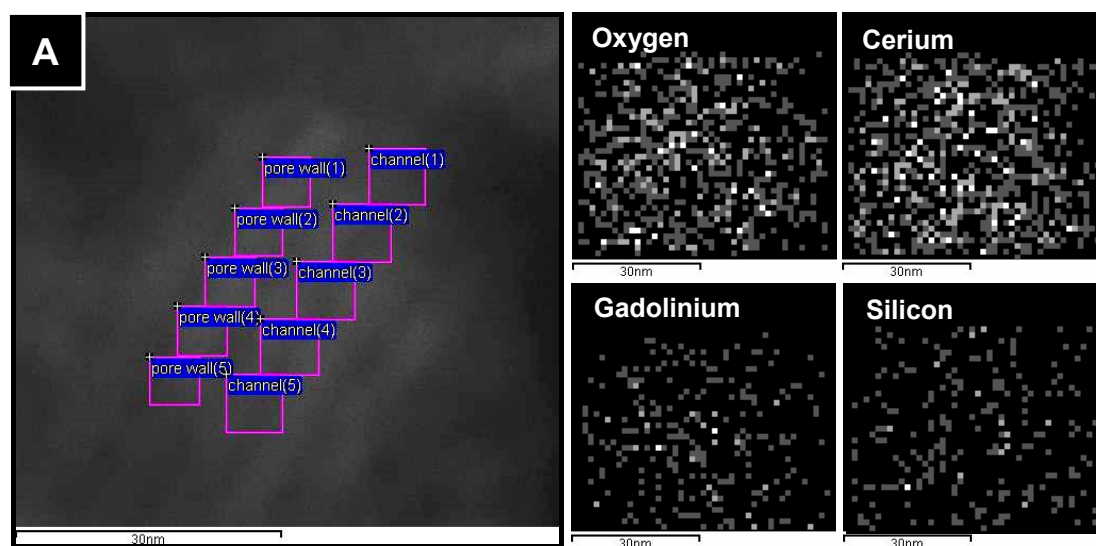


Figure 7.3.39: STEM image showing line scan across the [100] zone axis of a mesoporous particle and the corresponding EDS spectra for this line scan: **Ce** **Gd** **Si**. All data points are plotted as a 5 point moving average.

Figure 7.3.40 shows a similar series with CGO-S-V₂. The variation in the quantitative data (Table 7.2) can be evaluated as the values for Ce range from 64.4-110.0 mol% while the Gd values ranges from -7.0-13.3 mol%. The reported value for Si in this sample is also high, averaging 18.9 mol%.



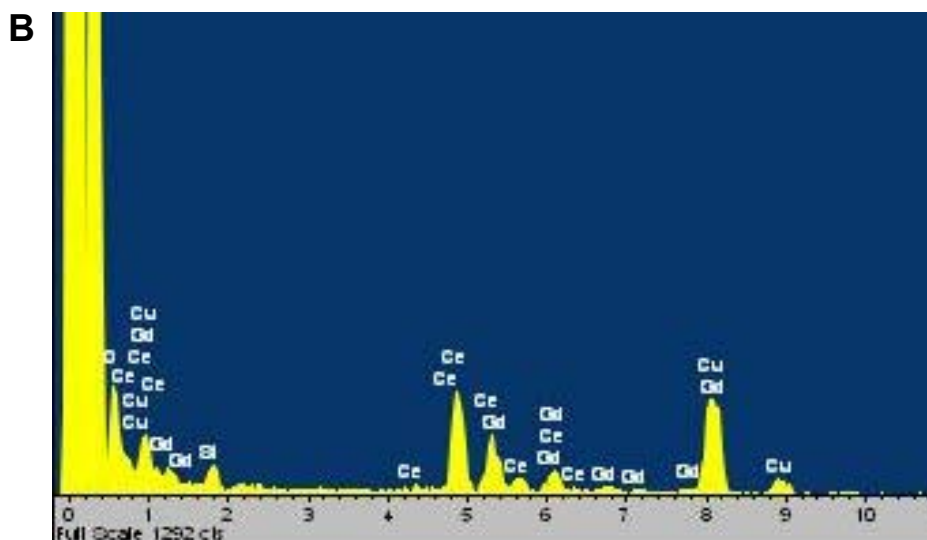


Figure 7.3.40: [A] STEM image of CGO-S-V₂ with EDS maps. Selected areas indicate the EDS mapped regions in Table 7.2; [B] EDS sum spectrum of the entire image.

Table 7.2: Quantitative EDS results from spectra taken in Figure 7.3.38 in mol%.

Spectrum	Ce L Series	Gd L Series	Si K Series
Sum Spectrum	71.09	10.05	18.86
Pore wall(1)	75.08	8.34	16.59
Pore wall(2)	65.87	0.87	33.26
Pore wall(3)	64.43	11.92	23.65
Pore wall(4)	72.64	6.72	20.64
Pore wall(5)	74.81	-0.91	26.10
Channel(1)	109.95	2.72	-12.67
Channel(2)	103.25	-7.03	3.78
Channel(3)	64.73	13.27	22.00
Channel(4)	70.35	12.35	17.31
Channel(5)	80.52	0.40	19.08

Figure 7.3.41 shows low-magnification EDX mapping of particles to compare the quantitative data (Table 7.3) from mapping particles, spot analyses of the centre of particles, maps from the centre of particles, and maps of the carbon film. All of the spot analyses and maps from the centre of the particle, except Spectrum 8, showed dramatically reduced Gd content (mol%). The carbon film was confirmed to give rise to only C and Cu X-ray signals. There was significant variation in the quantitative results between the quantitative data in the other spectra for Ce, O and Si signals.

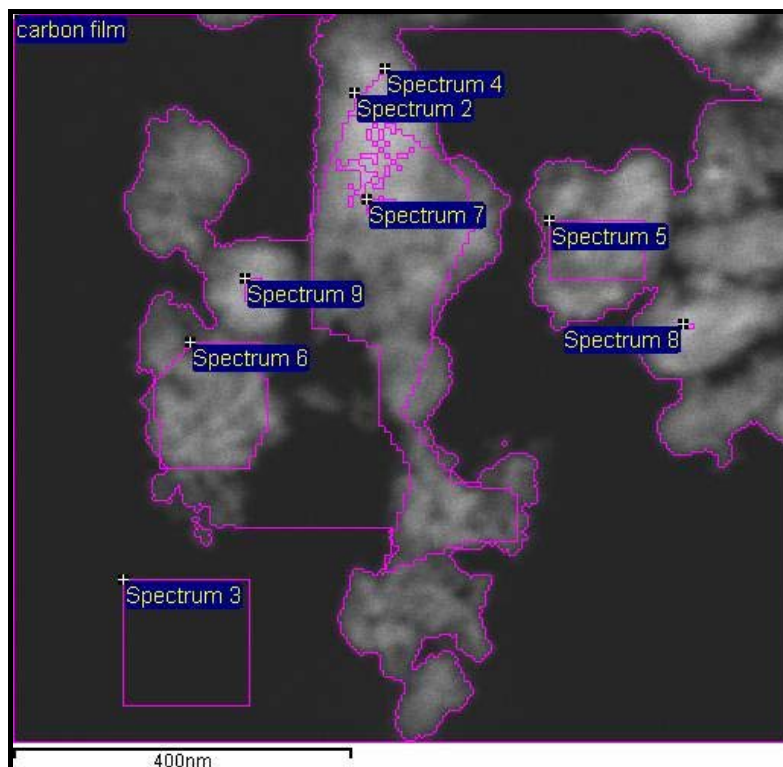


Figure 7.3.41: STEM image showing EDS maps of various CGO-S-V₂ particles corresponding to Table 7.3.

Table 7.3: Quantitative EDS results from spectra taken in Figure 7.3.38 in mol%.

Spectrum	Ce L Series	Gd L Series	Si K Series	Au L Series
Sum Spectrum	85.99	0.40	12.37	1.23
Spectrum 2	92.70	-0.25	5.45	2.10
Spectrum 3	90.47 C 10.36 Cu			
Spectrum 4	85.11	0.34	12.87	1.69
Spectrum 5	91.99	1.70	6.00	0.30
Spectrum 6	90.95	0.18	8.22	0.66
Spectrum 7	100.41	-8.69	4.20	4.08
Spectrum 8	76.32	6.74	10.07	6.87
Spectrum 9	105.26	-6.47	3.60	-2.39

Analysis of the compositions of Ceria-S-V₂, Ceria-K-V₂ and CGO-K-V₂ using ICP-MS showed the silicon contents to be 2.0 ± 0.7 , 2.5 ± 1.7 and 3.9 ± 1.5 mol%, respectively.

7.3.7 Discussion

Using TEM it was observed that the mesostructures of the materials were directly related to the templates used to make them. Multiple zone axes of each structural type were observed that were identical to those observed in the templates as well as those reported in the literature

for other mesoporous oxides. Low magnification images showed yields to be high though it should be noted that TEM can only image thin, electron transparent particles. A potential method for analysing the order of the mesopores in larger particles might utilise focussed-ion beam milling to produce electron-transparent cross-sections.

Using tomography it was possible to probe the structure in more detail and confirm that the 3D structure of individual particles was consistent with both of the original templates. The porous single crystal morphology was observed in all materials. A large lattice variation was also observed in all materials. This could have benefits with regards to catalytic activity as it would lead to exotic lattice planes being exposed on the surface of the nanorods or to a strained crystal structure.

By using DDPs it was possible to measure mesopore spacings. These were consistent with those measured for the templates and with the results of physisorption experiments (Table 7.4).

Table 7.4: Comparison of the physical properties of the mesoporous particles synthesised in this chapter with templates synthesised in Chapter 5.

Sample	BJH pore size (nm)	TEM d-spacing (nm)	SAXS d-spacing (nm)
SBA-15	*	7.5-8.6	9.3
KIT-6	*	7.7-9.7	9.6
Ceria-K-V ₁	2.6-3.0, 9.6-13.8	8.4-8.9	
Ceria-S-V ₂	2.4-3.0, 9.6-13.8	8.9-9.7	-
Ceria-K-V ₂	2.2-3.0, ~8	8.5-9.4	-
CGO-S-V ₂	2.5-3.0, 11.0-17.0	8.7-9.8	9.2
CGO-K-V ₂	2.1-2.7	8.5-9.2	8.8

* the pore size of the silica templates is not included as these pores become the nanorods in mesoporous ceria and CGO and, therefore, the pore sizes are not directly related.

Analysis of the surface structure using physisorption showed the materials to have an improved pore volume across the range of materials synthesised, compared to the materials described in Chapter 6, but lower specific surface areas than Ceria-K-I and Ceria S-P. The pore volumes presented were comparable with the highest reported in the literature using hard-templates, though the specific surface areas were, again, lower. The theoretical pore volume for materials synthesised from SBA-15 and KIT-6 templates was calculated using the method outlined in Appendix 1. It was assumed that impregnation was complete, the precursor templated crystallised into anhydrous $\text{Ce}(\text{NO}_3)_{3(s)}$, the $\text{Ce}(\text{NO}_3)_{3(s)}$ was only located

inside the pores of the template, the volume of the $\text{Ce}(\text{NO}_3)_{3(s)}$ unit cell was equivalent to the volume of the $\text{La}(\text{NO}_3)_{3(s)}$ unit cell, the physisorption measurements were consistent and only mesoporous ceria contributed to the measured pore volume. Using these assumptions the theoretical pore volumes for ceria templated from SBA-15 and KIT-6 were 0.58 and $0.44 \text{ cm}^3\text{g}^{-1}$, respectively. As these assumptions are unlikely to all be valid based on experimental observations, the experimental results achieved for these experiments were satisfactory ($0.29\text{-}0.38 \text{ cm}^3\text{g}^{-1}$). It should be noted, however, that there were significant contributions towards the total pore volume from pores larger than 4 nm – pore volume arising from structural by-products and interparticle porosity (see below).

The inverse relationship between pore volume and specific surface area suggested a change in product morphology from nanoparticles to mesoporous material. Figure 7.3.42 shows a schematic representation of the effect on surface and pore volume in this transformation. Nanoparticles, such as the faceted particles observed for Ceria-X-Cit and Ceria-X-P [A], can be approximated as spheres with a surface area of $4\pi r^2$ and zero pore volume [B]. When the nanoparticles are packed together [C], pore volume is created. If they are close-packed the pores are approximately tetrahedral, though the aggregates seen in this investigation were not close-packed. The pore volume is much smaller than the material volume of the nanoparticles. When structure directing agents are used in the synthesis of nanoparticles, the nanoparticles are not close-packed, but packed into arrays around the surfactants, increasing the pore volume, for example, in Ceria-S-P. Upon sintering [D], the surface liquefies and the pore volume is reduced. Grain growth will occur at relatively low temperatures because the small crystals have a low equilibrium melting temperature relative to the bulk material with a large crystal or grain size. The effect is that at each nanoparticle contact a surface area equivalent to twice the contact area is lost (one from each nanoparticle). This is multiplied throughout the material. This gives the partly-fused nanoparticles high specific surface area and low pore volume. As the temperature is increased, the smallest pores begin to fill in to decrease surface tension and then disappear. This dramatically lowers the pore volume and specific surface area. In comparison, ordered mesoporous materials [E] would have a lower specific surface area than nanoparticles, as all particles in the material are already sintered, and therefore surface area on each particle is lost where individual particles are in contact. Where the pore walls are nanorods the surface area would be expected to be lower relative to an equivalent mass of dispersed nanoparticles i.e. a $10\times 100 \text{ nm}$ nanorod of ceria has a calculated surface area of 3300 nm^2 , whereas the equivalent mass of 10 nm ceria nanoparticles has a surface area of 4700 nm^2 (ignoring sintering effects). The pore volume of the ordered mesoporous materials could be very high compared to that of nanoparticles, often

exceeding the volume of the solid in the structure, and upon sintering [F] grain growth in the walls would cause a less significant effect than in nanoparticles until such time as complete structural collapse occurred.

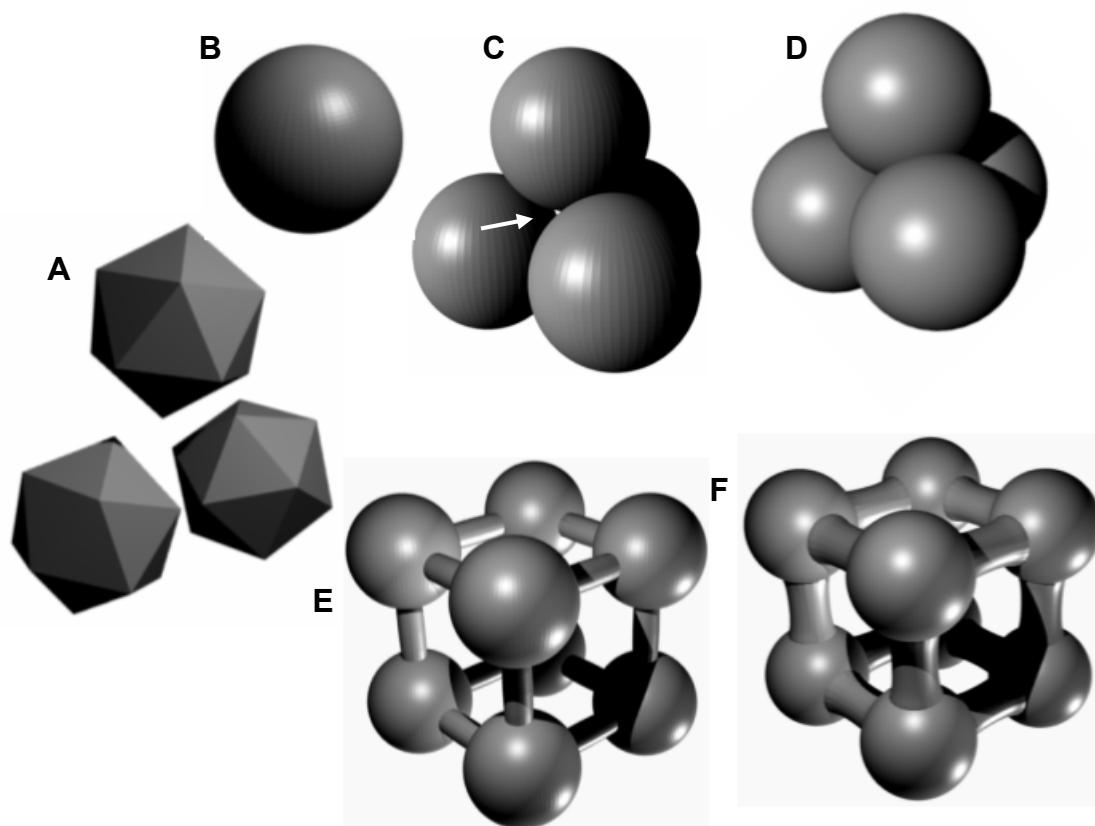


Figure 7.3.42: Schematic representations of [A] faceted nanoparticles, [B] spherical nanoparticle, [C] close-packed spherical nanoparticles, [D] sintered spherical nanoparticles, [E] ordered mesoporous cage, and [F] sintered ordered mesoporous cage.

Both the KIT-6 and SBA-15 templates synthesised in this investigation had a comparable specific surface area, but the SBA-15-derived ceria and CGO materials both had lower specific surface areas compared to the corresponding KIT-6-based materials. The theoretical specific surface areas for the product are exactly the same as the template multiplied by the change in density. Any other changes in the specific surface area are a function of the impregnation process or a change in the structure. Significant contributions towards the specific surface area in SBA-15 are from nanopores but not in the replicated ceria⁴⁶ – at least not in high yields. The proportion of the nanopores that were impregnated could not be determined by direct observation or physisorption analysis. Some of these were observed in the TEM images for Ceria-S-V₂ and CGO-S-V₂ but not a sufficient quantity to analyze total nanopore impregnation. The nanopores were not observed for the SBA-15 template. It is considered likely though, that impregnation of these nanopores was not complete, leading to a lower specific surface area for the SBA-15-derived materials than was expected.

The pore-size distributions showed a bimodal distribution for most materials prepared using VI. As both the adsorption and desorption traces matched in all plots the bimodal distributions were treated as being real and not artifacts. The differences in peak positions between the adsorption and desorption traces were attributed to hysteresis which caused the adsorption peaks to be at slightly higher values and the desorption peaks to appear sharper and at lower values. The sharp peaks at approximately 3 nm were attributed to the mesopores inside the porous single crystals. This pore size is in good agreement with the TEM images which showed narrow gaps between the nanorods and with calculations of the expected pore size based on the silica templates. The peak in the pore size distributions at 11-17 nm was attributed to the porosity of structural by-products. This included nanoparticles, bundles of nanowires (see Section 7.7) and agglomerations of nanorods that did not form coherent porous single crystals. Ceria-K-V₁ also had a larger peak at 11-17 nm than Ceria-K-V₂. This may suggest an improvement in the yield of ordered mesoporous material between the preliminary V₁ method and the more developed V₂ method. The peak at 11-17 nm was also more prevalent in the materials templated from SBA-15 and in materials comprised of ceria compared to CGO. It was calculated that if total impregnation of SBA-15 did not occur, a cylindrical mesopore of SBA-15 that was not impregnated would result in a larger mesopore in the final oxide of approximately 12 nm. This could have led to an increase in this peak in the materials synthesised from SBA-15. The materials synthesised from CGO would be expected to contain less structural by products – gadolinia acts as a sintering aid and would increase the mobility of the oxide during calcination, increasing the yield of ordered mesoporous oxide.

Attempts to confirm the bulk structure using SAXS were inconclusive. No peaks were observed for the ceria materials and only very weak reflections were obtained for the CGO materials despite repeated attempts. The data obtained for the CGO materials was in good agreement with the SAXS results for the SBA-15 and KIT-6 templates. Regarding the low intensities, it is possible that the irregularity of the porous structure lead to low intensities. Gd₂O₃ is known to enhance ceria grain growth,¹⁷³ so could increase the bulk formation of ordered mesoporous structures, increasing the bulk structural order. DDPs showed that the large mesoporous particles had regular pores so peaks in SAXS experiments had been expected. It is also possible that local variations in pore widths, and the roughness of the walls led to inhomogeneities in local d-spacings, causing a decreased peak signal. All previous investigations using hard-templating to synthesise ceria and CGO have also given rise to weak SAXS reflections. In some cases there have been no SAXS patterns reported. Using soft-templating methods produces stronger SAXS patterns for the synthesis of

mesoporous ceria.^{66, 71} It is possible that during nanocasting structural order is lost: liquid crystals give very strong SAXS reflections, materials synthesised from liquid crystals tend to give broader SAXS reflections and nanocast materials tend to give weak reflections.

The crystal structures of the materials were confirmed to be cubic with the fluorite structure using both XRD and DDPs referenced against ICDD patterns. As ceria and gadolinia form solid solutions, localised variations at the nanometre scale were possible but this was not significant enough to be observed in the XRD or DDP patterns. In XRD the ceria and CGO structures could not be distinguished from each other since differences in peak position were within the experimental error (Table 7.5). Longer scan times and smaller step sizes in XRD may allow the structures to be distinguished.

Table 7.5: Powder XRD results for mesoporous ceria and CGO (Chapter 7). The experimental patterns were indexed to ICDD reference patterns.

Sample	2 θ (111)	\pm (%)
Ceria-X-Cit	28.6	0.2
Ceria-K-V ₁	28.7	0.4
Ceria-S-V ₂	28.5	0.0
Ceria-K-V ₂	28.7	0.1
CGO-S-V ₂	28.6	0.2
CGO-K-V ₂	28.7	0.8

Using the peak broadening from the XRD patterns, crystal size analyses were conducted using the Scherrer equation. The results of the TEM investigation showed that the value of the Scherrer constant, K_w , would likely need to be reassessed because of the nature of the samples in this work. A K_w of 0.855 assumes the sample to consist of spherical nanoparticles. In the materials in this work there were also porous single crystals, nanorods and nanowires which each would reflect X-rays differently along different axes. The variations seen in the lattice planes would also increase the broadening of the XRD peaks. In some particles the lattice planes were clearly bending, though in others there may be many lattice defects. In both cases the particles would broaden the XRD peaks due to decreased long range crystal lattice order, increasing b , and therefore decreasing the p value (true size) calculated. For these reasons the Scherrer equation was determined to be inapplicable for correctly determining the accurate particle size of porous single crystals.

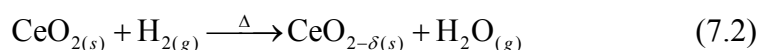
Semi-quantitative EDS was used as a tool to determine the elemental composition of the materials but the results were ultimately inconclusive. In the CGO samples, the detected amount of Gd spanned a range from zero to beyond the synthetic target of 10 %. EDS had insufficient spatial resolution in the instruments used to determine whether the silicon was located on the surface or throughout the material. The results from the University of St Andrews TEM showed the materials to contain approximately 6 mol% silicon while those from the NNNC TEM had a large variation spanning this value. The results from ICP-MS showed the silicon content to be lower (2-4 mol%), though the variation in the ICP-MS results was significant.

The silica content may be detrimental to the conductivity of the material. However, silica as a dopant has been shown to increase the thermal stability of ceria materials significantly (as do most tetravalent cations).¹⁷⁴⁻¹⁷⁵

The Al peak that was detected in Ceria-K-V₁ was attributed to material scraped from the alumina furnace boat. In subsequent experiments, where hard tools were not used to extract residual sample from the furnace boat, Al was no longer detected.

7.4 Temperature Programmed Studies

TP methods were used to study the redox properties of the mesoporous materials Ceria-K-V₁, Ceria-S-V₂, Ceria-K-V₂, CGO-S-V₂ and CGO-K-V₂, discussed in Section 7.3. The full experimental details are outlined in Section 4.4.4. These materials were compared with the reference material, Ceria-X-Cit (Chapter 6). The MS traces are presented in partial pressures (P/P₀). This produces a plot, essentially in arbitrary units, from the fragmentation of the gas mixture downstream from the reactor. Due to differences in the relative values of P/P₀ for different m/z fragments, the m/z = 18 (H₂O) fragment is plotted on a second axis to allow for features in the other m/z traces to be observed. The m/z = 40 (Ar) trace has been ignored as it was ≈ 95 % of P/P₀. As the MS is less sensitive to lighter fragments, the m/z = 2 (H₂) fragment has been smoothed using a 20 point moving average in an attempt to resolve features. A material's reduction peaks are observed as water peaks according to Equation 7.2.



All TPR spectra were run using identical experimental conditions and settings on the MS to ensure that the results would be comparable. In the materials studied, it was found that

TPR spectra contained up to four characteristic water peaks. These could be related between different samples and are labelled T_1 to T_4 , in order of increasing temperature in what follows.

The TPR-MS trace of the reference material, Ceria-X-Cit, shows that there was a small amount of H_2O produced at 100 °C (T_1) and CO_2 at approximately 100-500 °C (Figure 7.4.1). The H_2O trace began to rise at 600 °C and peaked at 745 °C (T_4) indicating reduction of the sample. A steady increase was also observed in the N_2 -CO trace which was attributed to instrument drift. This was observed in several TP spectra (see below).

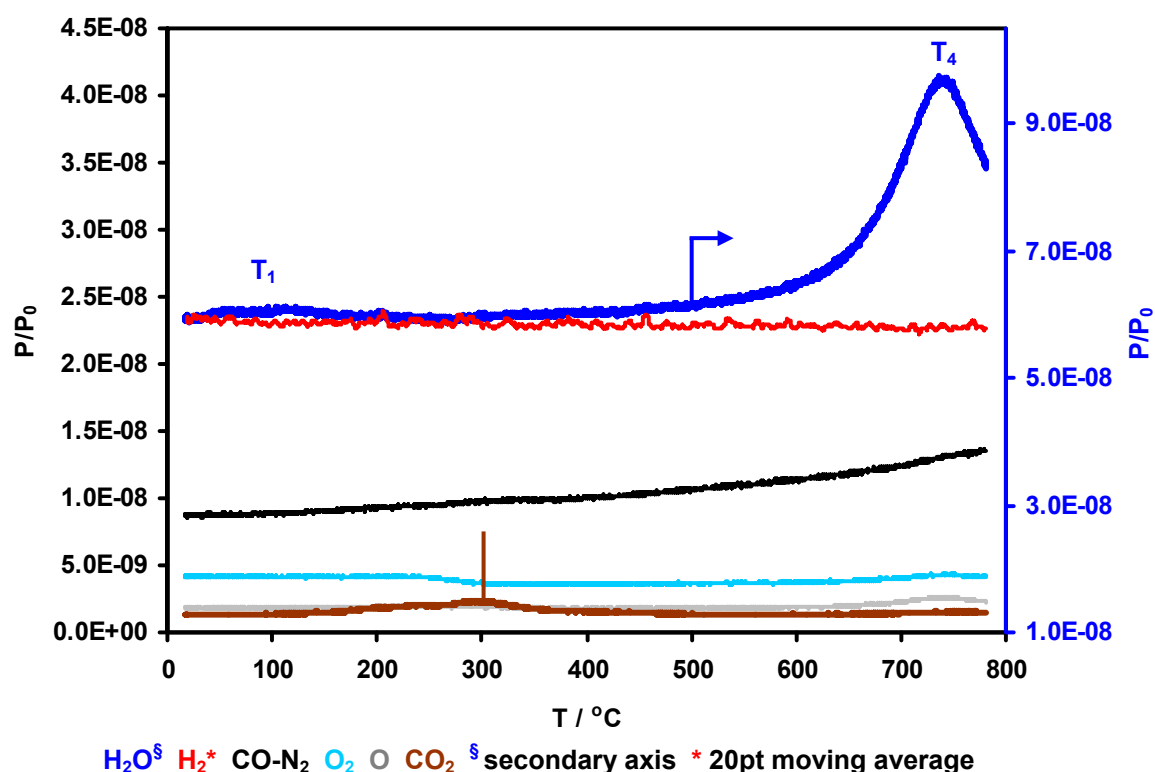


Figure 7.4.1: TPR-MS traces for Ceria-X-Cit. The arrow indicates the start of the T_4 reduction peak.

7.4.1 Ceria-K- V_1

In the TPR-MS traces for Ceria-K- V_1 (Figure 7.4.2), the T_1 H_2O and CO_2 peaks were noticeably larger than for Ceria-X-Cit. At 100-150 °C there was an O_2 peak coinciding with the T_1 peak. The N_2 -CO trace showed peaks at 570 °C (starting at 500 °C) and 725 °C.

These peaks were mirrored in the C trace and therefore the gas was CO, not N_2 . The H_2O trace showed four peaks: T_1 (90 °C), T_2 (446 °C), T_3 (508 °C; beginning at 370 °C), and T_4 (727 °C). There was notable drift in the H_2O and N_2 -CO traces with increasing temperature (indicated by the linear trend line in the figure). This drift was a result of environmental temperature effects on the MS (and was the reason for the later modifications made to the MS to prevent backflow). There was a direct correlation between experiments with an increasing H_2O baseline and an increasing external environmental temperature, and importantly for this

conclusion, vice versa (noticed in blank MS experiments to monitor the m/z baselines over several days while simultaneously plotting the external temperature). Many of the TPR traces presented were conducted during summer months when this effect was most noticeable (all windows on this side of the laboratory were insulated with reflective material in an attempt to prevent this feature in future experiments - this resulted in a dramatic reduction in the cyclic environmental temperature).

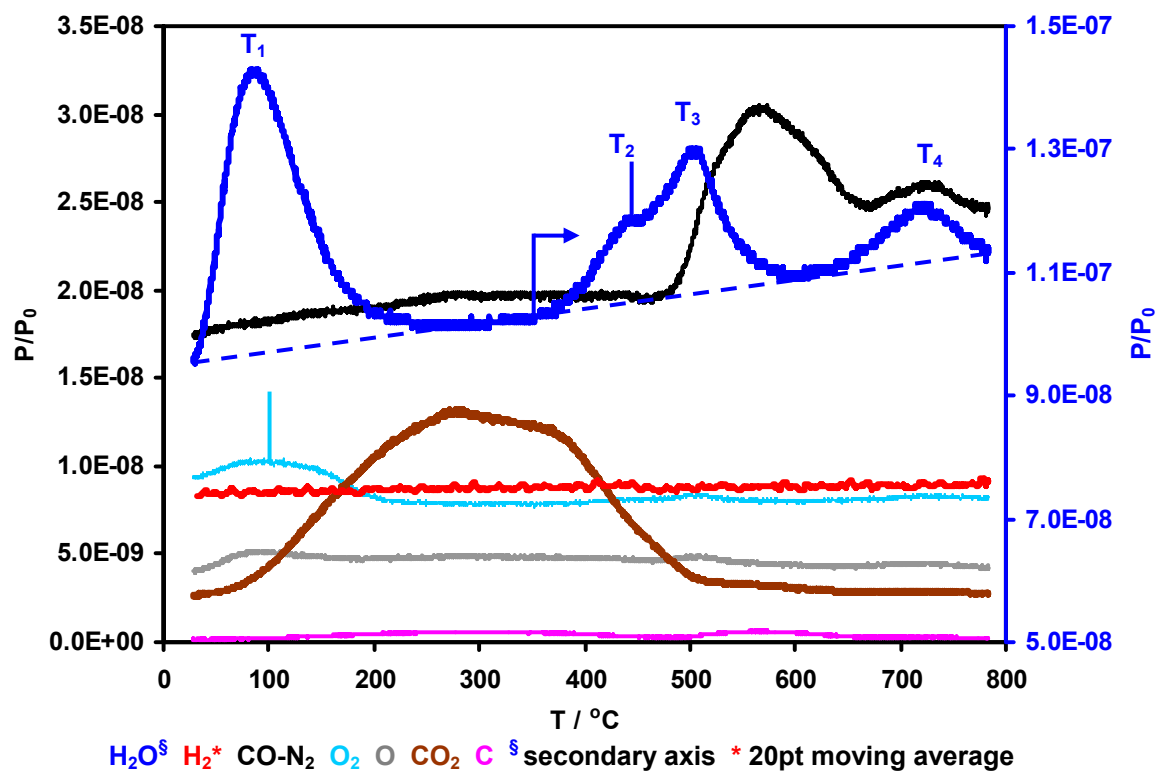


Figure 7.4.2: TPR-MS traces for Ceria-K-V₁. Peaks are indicated. The arrow indicates the start of the T_2 reduction peak.

7.4.2 Ceria-S-V₂

The TPR-MS traces observed for Ceria-S-V₂ were very similar to those for Ceria K-V₁. All of the same general features were observed (Figure 7.4.3). The signals of N₂-CO, O₂ and CO showed more noise as they were at lower P/P₀ values. The three observable H₂O peaks were at 125 °C (T₁), 514 °C (T₂, T₃) and 712 °C (T₄). The skew of the middle peak suggested that there was a shoulder at approximately 420 °C (T₂) which would make it consistent with the TPR trace seen for Ceria-K-V₁. The T₂-T₃ feature started at a lower temperature than for Ceria-K-V₁ (300 °C).

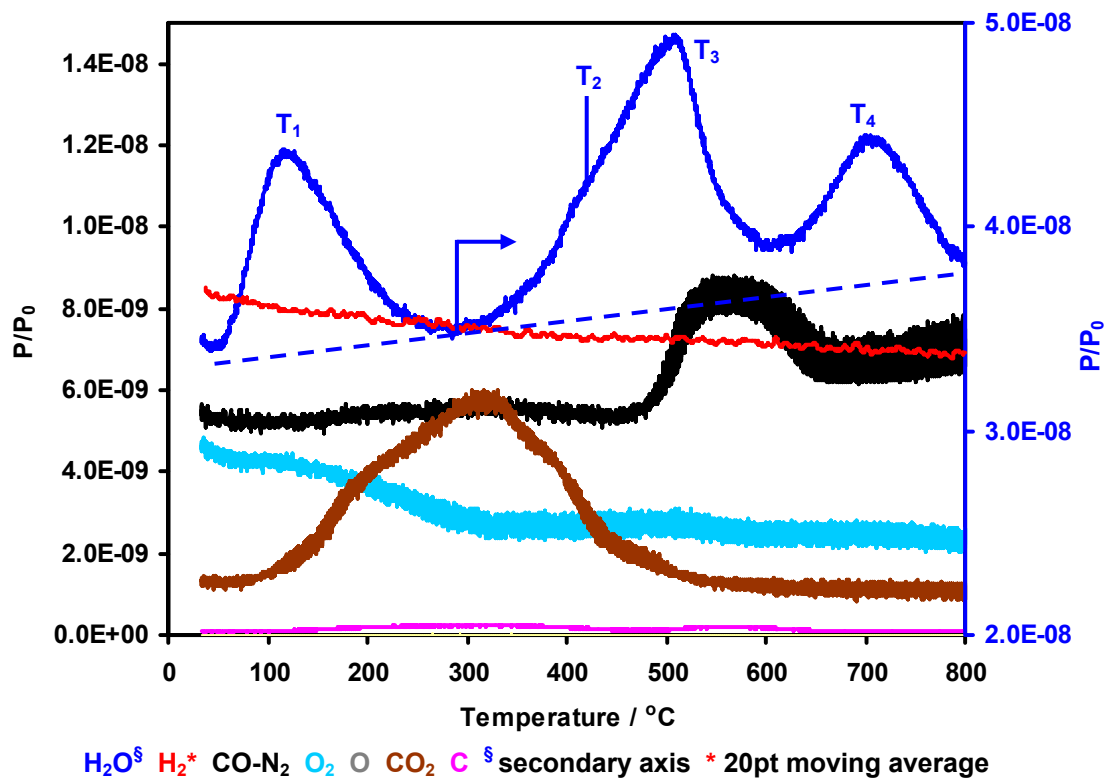


Figure 7.4.3: TPR-MS traces for Ceria-S-V₂.
The arrow indicates the start of the T₂-T₃ reduction peak.

7.4.3 Ceria-K-V₂

The TPR-MS trace for Ceria-K-V₂ had a much larger T₂-T₃ feature relative to the other H₂O peaks (Figure 7.4.4). The overlap of the T₃ and T₄ peaks made them even less easy to distinguish than in the TPR for Ceria-S-V₂. The peak maxima were at 154 °C (T₁), 523 °C (T₂-T₃) and 696 °C (T₄). The O₂ peak matched the H₂O peak at 148 °C.

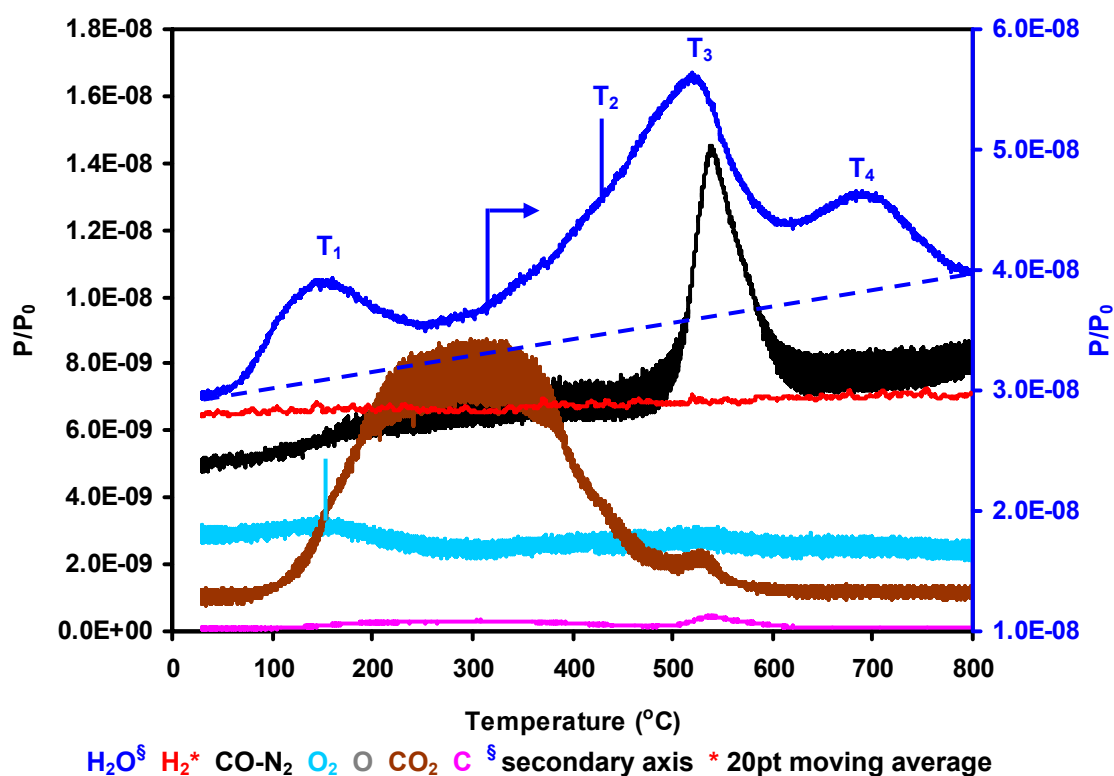


Figure 7.4.4: TPR-MS traces for Ceria-K-V₂. The arrow indicates the start of the T₂-T₃ reduction peak. O₂ peak indicated.

7.4.4 CGO-S-V₂

The TPR-MS traces for CGO-S-V₂ had features in common with both of the above materials made using the V₂ method (Ceria-S-V₂ and Ceria-K-V₂): a high T₁ peak with corresponding O₂ peak and overlapping features for both T₂-T₃ and T₃-T₄ (Figure 7.4.5). The four H₂O peaks were all distinguishable either as separate peaks or shoulders at 94 °C (T₁), 435 °C (T₂), 525 °C (T₃) and 664 °C (T₄). The T₄ peak was smaller than in the spectra of the previously tested ceria materials (Ceria-K-V₁, Ceria-S-V₂ and Ceria-K-V₂).

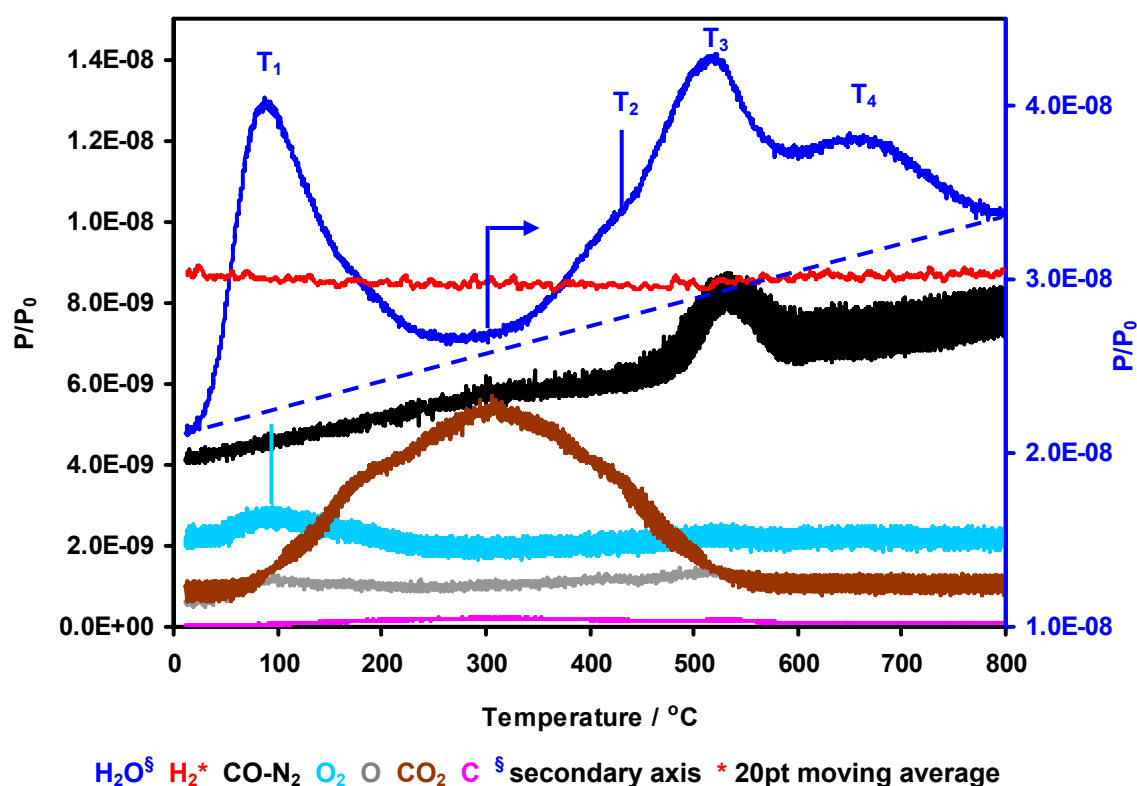


Figure 7.4.5: TPR-MS traces for CGO-S-V₂. The arrow indicates the start of the T₂-T₃ reduction peak. O₂ peak indicated.

7.4.5 CGO-K-V₂

The TPR-MS trace of CGO-K-V₂ (Figure 7.4.6) closely resembled that of Ceria-K-V₂. The T₁ peak at 156 °C was less pronounced relative to the other H₂O peaks and was mirrored by an O₂ peak. The T₂, T₃ and T₄ peaks appear to overlap to give one continuous feature with a maximum at 519 °C. Two shoulders could be observed at approximately 450 °C and 665 °C which are assigned to T₂ and T₄, respectively. As with CGO-S-V₂, the T₄ peak was smaller than the other reduction peaks relative to the peaks which had been observed in the pure ceria materials.

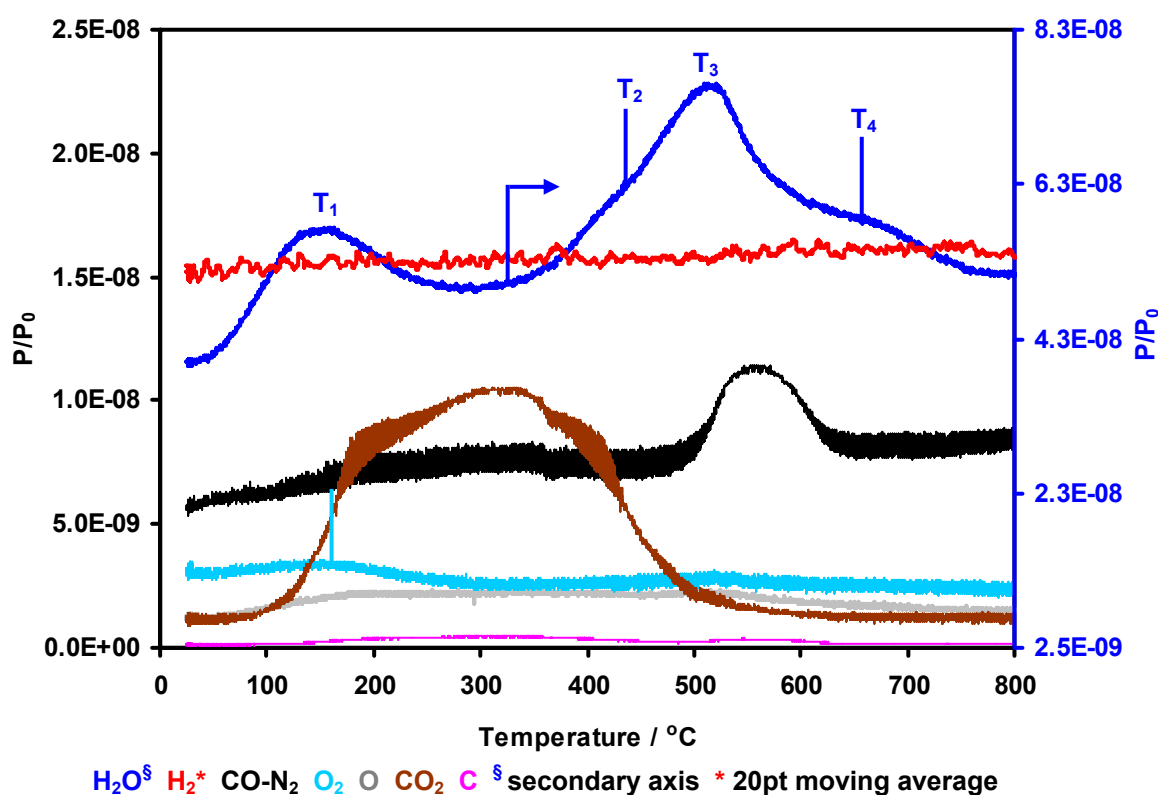


Figure 7.4.6: TPR-MS traces for CGO-K-V₂. The arrow indicates the start of the T₂-T₃ reduction peak. O₂ peak indicated.

7.4.6 TP Cycling

A cycling experiment comprising a TPD to 500 °C, TPR to 500 °C (TPR₁), TPO to 300 °C and a final TPR to 800 °C (TPR₂) was conducted on a sample of Ceria-S-V₂. The full experimental details were outlined in Section 4.4.4. There was the possibility of peaks at higher temperatures than in the TPD, TPR₁ and TPO traces presented, but temperatures were kept low initially to prevent sintering of the material. The results are presented in Figure 7.4.7 and show that during TPD H₂O was desorbed in the T₁ region at 77 °C. This was a lower temperature than previously observed. The subsequent TPR₁ on the same sample showed a

T_1 peak at 95 °C. The shoulder of a T_2 peak could be seen to begin at 331 °C and was still rising when the TPR experiment ended. This peak had not been observed in the TPD. Reoxidation of the sample during a TPO showed that the sample began oxidation at 60 °C and had completed a re-oxidation feature by 248 °C (though there may be additional oxidation peaks at higher temperatures). The final TPR₂ showed a T_1 peak at 113 °C and a T_2 - T_3 feature at 488-561 °C. A trough in the H_2 trace can be seen to coincide with the T_2 - T_3 feature. Further cycling was prevented by equipment failure.

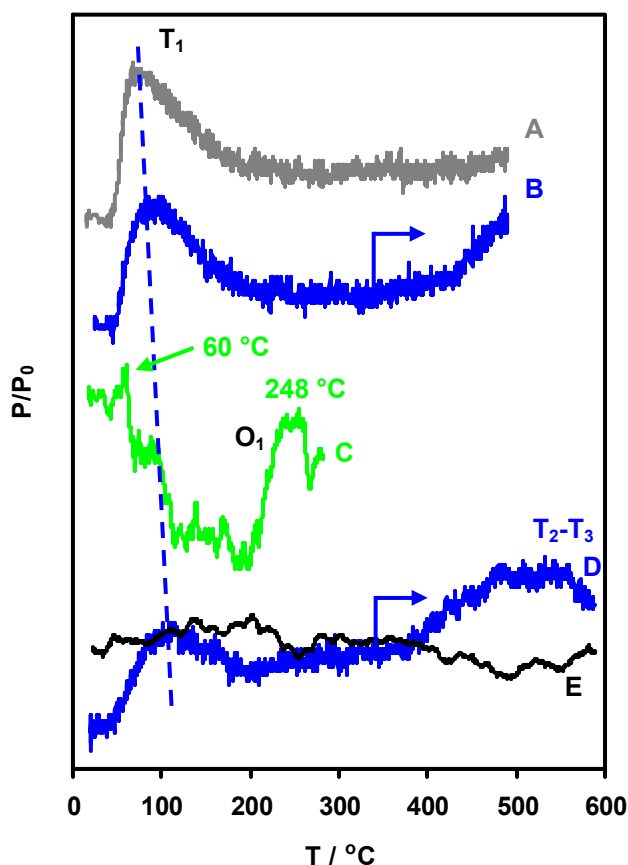


Figure 7.4.7: MS traces from a cycling TP experiment on Ceria-S-V₂: [A] H_2O trace in TPD; [B] H_2O trace in TPR₁; [C] O_2 trace in TPO; [D] H_2O and [E] H_2 (20 point moving average) traces in TPR₂. The y-axis units are arbitrary for comparison purposes. The start of the reduction peaks is indicated.

Table 7.6: Peaks extracted from TPR-MS traces in the cycling experiment presented in Figure 7.4.7.

	T_1 (°C)	T_2 start (°C)
TPD	78	-
TPR ₁	91	≈331
TPO	-	-
TPR ₂	113	≈347

All of the materials tested using TPR experiments changed from yellow to grey upon the completion of an 800 °C reduction experiment.

7.4.7 Discussion

Ceria is known to be hygroscopic and therefore desorption of absorbed water would be expected to occur at temperatures close to its boiling point of 100 °C. Water would be expected to adsorb at quantities, and absorb at rates roughly proportional to the specific surface area of the material. In the mesoporous materials there was also an O₂ peak at the same temperature as the T₁ peak. In the MS, fragmented molecules do not recombine so the O₂ peak represented the evolution of molecular oxygen from the sample. According to a literature report,¹⁷⁶ the strained or curved lattice plains observed under TEM examination, as well as the formation of unfaceted holes, may have lead to innate surface features capable of producing superoxide (O₂⁻) and peroxide (O₂²⁻) species. In this report a ceria sample underwent surface modification to induce unusual lattice planes which, under a reducing atmosphere, produced O₂⁻ and O₂²⁻. This could explain the O₂ trace in the TPRs. These species could also be the reason for the H₂O peak at 90 °C in TPR₁ in the cycling experiment since physisorbed water would have been desorbed during the prior TPD experiment. If present, these species would also be a contributing factor to the larger than expected water peaks as the reactive dioxide species would oxidise the hydrogen during the TPR experiment.

Ceria also absorbs atmospheric CO₂. In all of the experiments, and especially in the mesoporous materials, there were significant CO₂ and CO peaks. The only significant source of carbonaceous material during the experimental synthesis was during the silica template synthesis. The surfactant would have undergone two calcinations at temperatures between 400 and 600 °C over a total period of at least 18 h. On this basis, the carbonaceous peaks were attributed to absorbed CO₂. At approximately 100 °C CO₂ begins to desorb from the sample. This peaks at 250-300 °C. At 350-400 °C the desorption of CO₂ declines to coincide with the reduction (water evolution) peak. At 500 °C the CO₂ peak has levelled off and the ceria has become highly reduced, at which point the remaining CO₂ is reduced to CO (by the sample) and desorbed from 500 to 800 °C (typically 500 to 600 °C). This is essentially the reverse reaction of steam reforming.

The TPR results suggested that there were up to three different reduction processes occurring in these materials. The reference material, Ceria-X-Cit, showed a single reduction peak at 745 °C. This peak (T₄) was attributed to the oxidation of hydrogen by nanoparticulate ceria. The three mesoporous ceria materials examined (Ceria-K-V₁, Ceria-S-V₂, and Ceria-K-V₂) had a similar T₄ peak, though in all cases it was at a lower temperature by 18 to 49 °C. This decrease in temperature could be attributed to either a smaller particle size (where the silica template has restricted the nanoparticle grain growth), to the effect of

impurities in the sample (primarily silicon), or to another mechanism. The two mesoporous CGO materials examined (CGO-S-V₂ and CGO-K-V₂), had a T₄ peak 80 °C lower than in Ceria-X-Cit. This was expected as CGO has an increased ionic conductivity compared to ceria¹⁷⁷ and therefore, oxygen ions are more mobile in CGO. This would be expected to increase the oxide ion activity.

The intermediate-temperature T₂ and T₃ peaks were attributed to oxidation caused by the mesoporous material, as these peaks were too high for physisorbed water (>156 °C) and significantly lower (435-525 °C), and separately distinguishable from the T₄ peak (>664 °C). The reason for the two separate peaks, often identifiable as shoulders, was not identifiable from the experiments conducted in this report. Synthesis of further materials, which may separate these peaks out by targeting specific mesoporous structures, may allow it to be determined whether these two peaks are intrinsic to mesoporous materials or caused by two separate phases both active at lower temperatures. It was expected that mesoporous ceria would oxidise hydrogen at a lower temperature than nanoparticulate ceria. As shown by Terribile *at al*, high specific surface area ceria oxidises hydrogen at lower temperatures than bulk ceria (Figure 7.4.8).⁶² However, the ordered mesoporous materials made by VI oxidised the hydrogen stream at consistently lower temperatures than even the results described by Terribile *et al*. The low temperature oxidation activity could be explained by the mesostructure. In an ordered structure there may have been an increased proportion of open pores that were accessible to the reducing gas. The large pore volume allowed a large volume of gas to fill the voids in the material and the large specific surface area meant that the phase boundary, where the reaction must take place, would be larger, increasing the reaction rate. Other factors influencing the low temperature oxidation behaviour could include the observed lattice variations and the possibility of exotic lattice planes being exposed on non-faceted pore walls because the material crystallised in constrained conditions. In the TEM images the lattice planes on the edges of holes inside the matrix could not be directly observed, though Figure 7.6.3C shows the ends of a porous particle in which it can be seen that the crystal is not faceted.

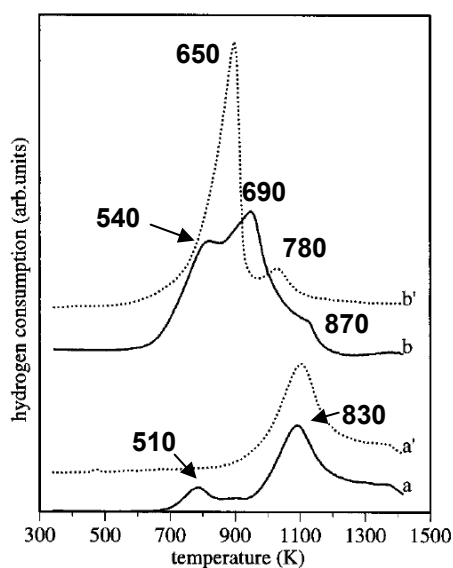


Figure 7.4.8: TPR-MS results from Terribile et al. H_2 consumption plots for [a] conventionally precipitated ceria, [a'] after TP cycling; [b] mesoporous ceria synthesised using soft templating, [b'] after TP cycling. Approximate peak maxima annotated in °C.⁶²

As the areas under the TP-MS peaks are directly related to the quantity of the gas evolved, it is possible that once the different peaks were correctly attributed to different material phases (ordered mesoporous material versus nanoparticles) that the product yield of mesoporous material could be calculated. A general application of this technique to the H_2O curves of Ceria-K- V_1 and Ceria-K- V_2 shows that the $T_{2/3}:T_4$ ratio for Ceria-K- V_2 was larger, implying the quantity of ordered mesoporous material in the latter is higher. This is consistent with the expected result since the V_2 method was an improvement on the V_1 method. A general observation of the relative sizes of the peaks of all of the mesoporous products would suggest that CGO-K- V_2 had the highest yield of mesoporous product, using this method. This was consistent with the results from the physisorption analysis where CGO-K- V_2 had the highest pore volume.

When plotted together the six H_2O MS traces showed that there were similarities and differences between the different compositions and structures (Figure 7.4.9 and Table 7.6). The T_1 peaks were not at a consistent temperature of 100 °C. This could be attributed to several factors. Firstly, ceria is hygroscopic and therefore the water is not simply adsorbed on the surface. As the temperature increases water migrates from the material and this would happen over a wider range of temperatures than surface adsorbed water alone. Secondly, the mesoporous nature of the material means that there could be a lag time between water

desorption and diffusion of the water sufficiently far from the material to enter the gas stream. Thirdly, there could be contributions from superoxide and peroxide species that may react over a wider temperature range.

During the cycling experiment it was observed that a single sample exhibited three different water peaks from 78-113 °C during a TPD and two TPRs. Physisorbed water would be expected to desorb during the TPD. The water peak during the subsequent TPRs was attributed to the superoxide and peroxide species. Further experimentation would be required to verify this. The shift in the peaks between the T_4 peaks, summarised in Table 7.7, can be attributed to the differences between the samples. Firstly, Ceria-K-V₁, Ceria-S-V₂, and Ceria-K-V₂, were ceria-based while CGO-S-V₂ and CGO-K-V₂ were CGO-based. The change in chemistry would affect the desorption of water and the production of superoxide or peroxide species. The addition of gadolinia would also affect the morphology of the materials as it increases the sintering of ceria. This would also affect the surface morphology. Ceria-K-V₁, Ceria-K-V₂, and CGO-K-V₂ were based on the KIT-6 structure while Ceria-S-V₂ and CGO-S-V₂ were based on the SBA-15 structure. As TPR is a transient technique the diffusion of species from the site of desorption out of the porous matrix will affect the peak position, and therefore, the change in the pore morphology will affect the peak position.

During the cycling experiment, TPR₂ showed a reduction peak at 400-600 °C. The initial experiment (Figure 7.4.3) showed a reduction peak at 300-600 °C. This may suggest that there has been a small alteration to the surface of the material, though the resolution of the H₂O MS trace was low (the MS filament failed shortly after this cycling experiment).

The CGO materials, and also the KIT-6-based materials, appear to exhibit the largest T_2 - T_3 features relative to the size of the T_4 peaks. Due to the lower T_4 temperature, the CGO materials did not exhibit a shoulder between the T_3 and T_4 peaks. This may give the CGO materials better catalytic activity over a range of temperatures. It is worth noting that all materials had comparable reduction maxima (T_3). Gadolinia enhances ceria sintering and therefore, if it is not beneficial to a device application, Ceria-S-V₂ and Ceria-K-V₂ may offer better thermal stability leading to higher catalytic activity by operating at 10-20 °C higher than CGO-S-V₂ and CGO-K-V₂.

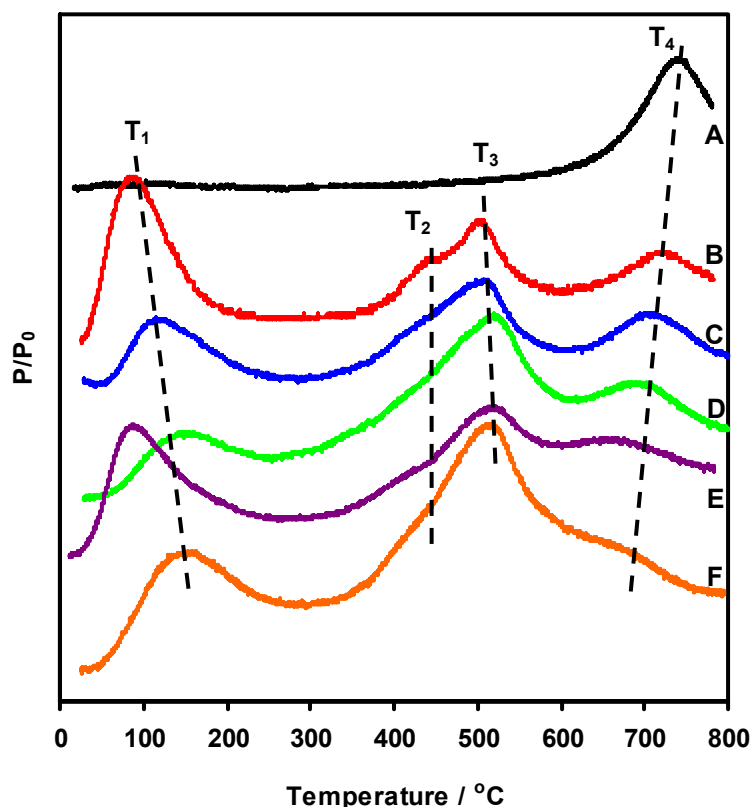


Figure 7.4.9: Comparison of H₂O traces from TPR-MS traces for [A] Ceria-X-Cit, [B] Ceria-K-V₁, [C] Ceria-S-V₂, [D] Ceria-K-V₂, [E] CGO-S-V₂, [F] CGO-K-V₂. y-axis adjusted for comparison.

Table 7.7: Peak positions from TPR spectra from Section 7.4 (in °C).

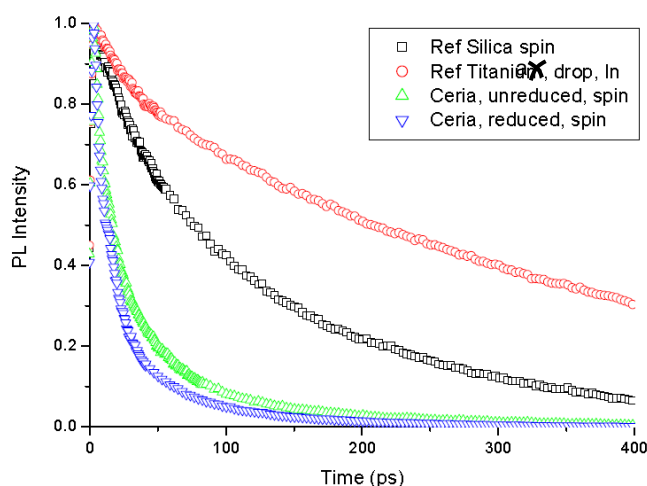
	T ₁	T ₂	T ₃	T ₄
Ceria-X-Cit	≈100			745
Ceria-K-V ₁	90	446	508	727
Ceria-S-V ₂	125	-	514	712
Ceria-K-V ₂	154	-	523	696
CGO-S-V ₂	94	435	525	664
CGO-K-V ₂	156	450	519	665

7.5 Photovoltaic Studies

PV studies were conducted to investigate ordered mesoporous ceria as a potential bulk heterojunction material for dye-sensitised solar cells. This experiment was conducted during preliminary VI experimentation and therefore the material studied was Ceria-K-V₁. Two samples of Ceria-K-V₁ were used to construct a dye-sensitised solar cell. One sample was reduced in 5 % H₂/Ar at 450 °C for 1 h (Ceria, reduced) to increase [Ce³⁺], the other sample

examined was untreated (Cer_{ia}, unreduced). The reduced sample was expected to have a higher conductivity. Two parameters were examined: the PL quenching (described in detail in Section 3.7), and the quenching efficiency which measured the efficiency of the material to separate the exciton charges to prevent exciton annihilation.

Preliminary photoluminescence experiments showed that Cer_{ia}-K-V₁ quenched the excitons produced in the organic dye rapidly (Figure 7.5.1). This meant that, compared to reference materials, the excitons were easily extracted from the dye before recombination occurred. The reduced ceria quenched the excitons faster than the standard (unreduced) Cer_{ia}-K-V₁ sample. This may be due to the increased [Ce³⁺] which would lead to an increased electronic conductivity. The quenching efficiency of both materials was high (90-93 %).



	τ (ps)	Quenching efficiency (%)
Reference silica	334	-
Reference titania	126	-
Ceria-K-V ₁	34	90
Reduced Ceria-K-V ₁	23	93

Figure 7.5.1: Photoluminescence results for standard and reduced Cer_{ia}-K-V₁ and reference materials.

7.5.1 Discussion

The PL experiment showed that the ordered mesoporous matrix had a great affinity for exciton quenching even though its properties had not been rigorously developed for solar cell applications. As effective exciton quenching occurs if the excitons can be removed from the

dye before they have time to recombine, a small distance between the dye and semiconductor of 5-20 nm is ideal (Ceria-K-V₁ had a half-pore width of 1.5-2 nm with structural by product half-pore widths of 7-10 nm). This means that materials with this morphology could potentially increase dye-sensitised solar cell efficiencies. As the pore morphology could potentially be tailored for the application, and the composition could be designed for the application, synthesising ordered mesoporous titania (or another material), based on SBA-15 may increase the quenching further while maintaining good semiconducting properties. As during the VI method material can be thermally treated up to 600 °C using a silica template (or higher with a carbon template) the material could be prepared in a crystalline form, as were the ceria materials, so decreasing grain boundary resistances. To improve the organic dye impregnation (itself a viscous liquid when in solution because of its high M_r), and the contact with the semiconductor, VI could be used again. Ceria has an additional benefit in this application in that it absorbs ultra-violet (UV) radiation, and would therefore provide additional protection for the organic dye against UV degradation.

7.6 Thermal Resistance Studies

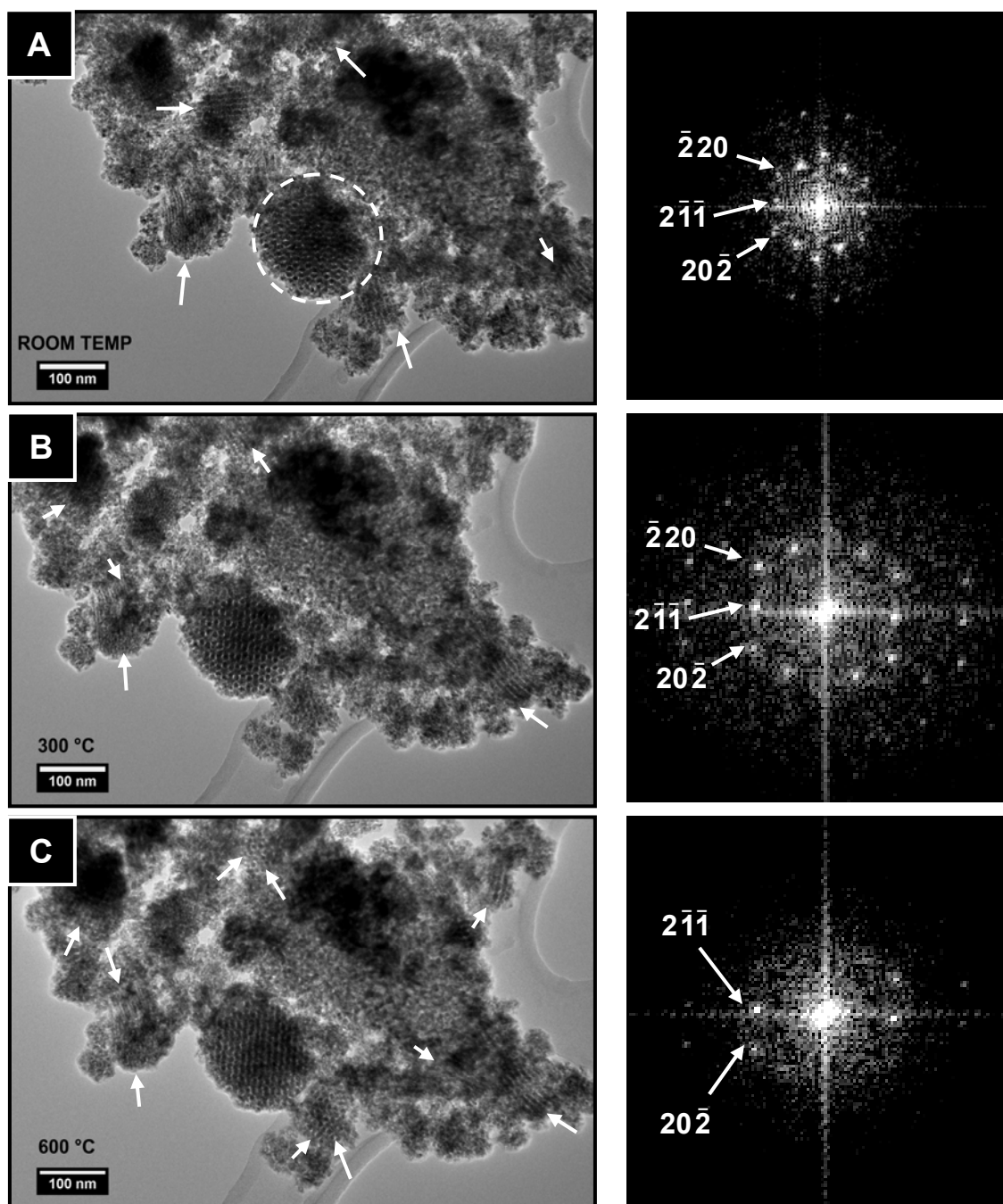
Materials being examined for applications in heterogeneous catalysis are required to be thermally stable at their operating temperatures. CGO-K-V₂ was studied by heating the material to 1000 °C inside a TEM in vacuo over a period of 4 h. CGO-S-V₂ was studied by calcining the material to 500 °C and 650 °C for 48 h and 72 h, respectively, in air. These samples were then characterised using TEM and nitrogen physisorption.

7.6.1 *In-situ TEM Heating of CGO-K-V₂*

The results for the in-situ heating experiments are presented in Figures 7.6.1-3. A large agglomerate was selected for observation based on its composition of ordered mesoporous particles and nanoparticulate material. The sample was heated to 1000 °C inside the TEM over a period of about 4 h. After a short period at 1000 °C the carbon grid failed.

Figure 7.6.1 presents an area of the agglomeration which features a 150×150 nm particle, presented in the [111] zone axis of the mesopore structure, that was selected for observation during the experiment (indicated in Figure 7.6.1A). Surrounding this particle were other mesoporous particles as indicated in the image. Upon heating, it is shown that either different mesoporous particles became visible or the particles visible at room temperature rotated to present a different pore axis. The primary feature, of which DDPs were taken at each temperature, can be seen to pass from the [111] zone axis in Figure 7.6.1A into a misaligned [111] orientation in Figure 7.6.1B. In Figures 7.6.1C and D all but two of the primary spots disappeared due to this misalignment. In Figure 7.6.1E new spots appeared that were

consistent with the (303) reflection, though this was not certain as there was large variation in the measurements. In Figure 7.6.1F the particle is again in the [111] orientation. After the carbon grid failed a new orientation can be observed, though the spacings could not be attributed with certainty due to large variation in the data. It was confirmed that the orientation of particles within the sample had not altered in Figure 7.6.1F by taking reference points in the image and comparing them to the other images. The lattice constants extracted from the DDP reflections did not decrease, within experimental variation, when increasing the temperature up to 1000 °C.



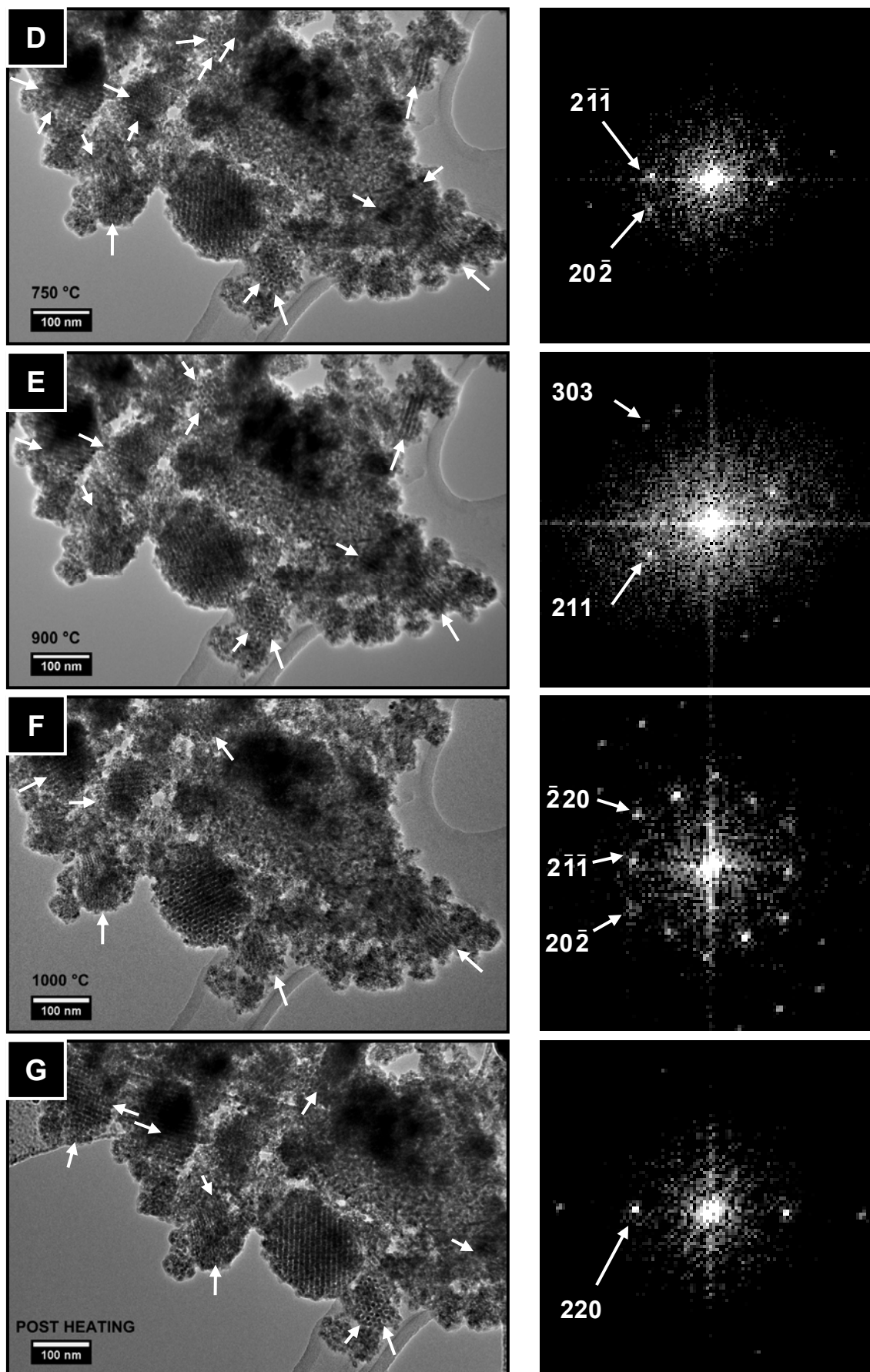
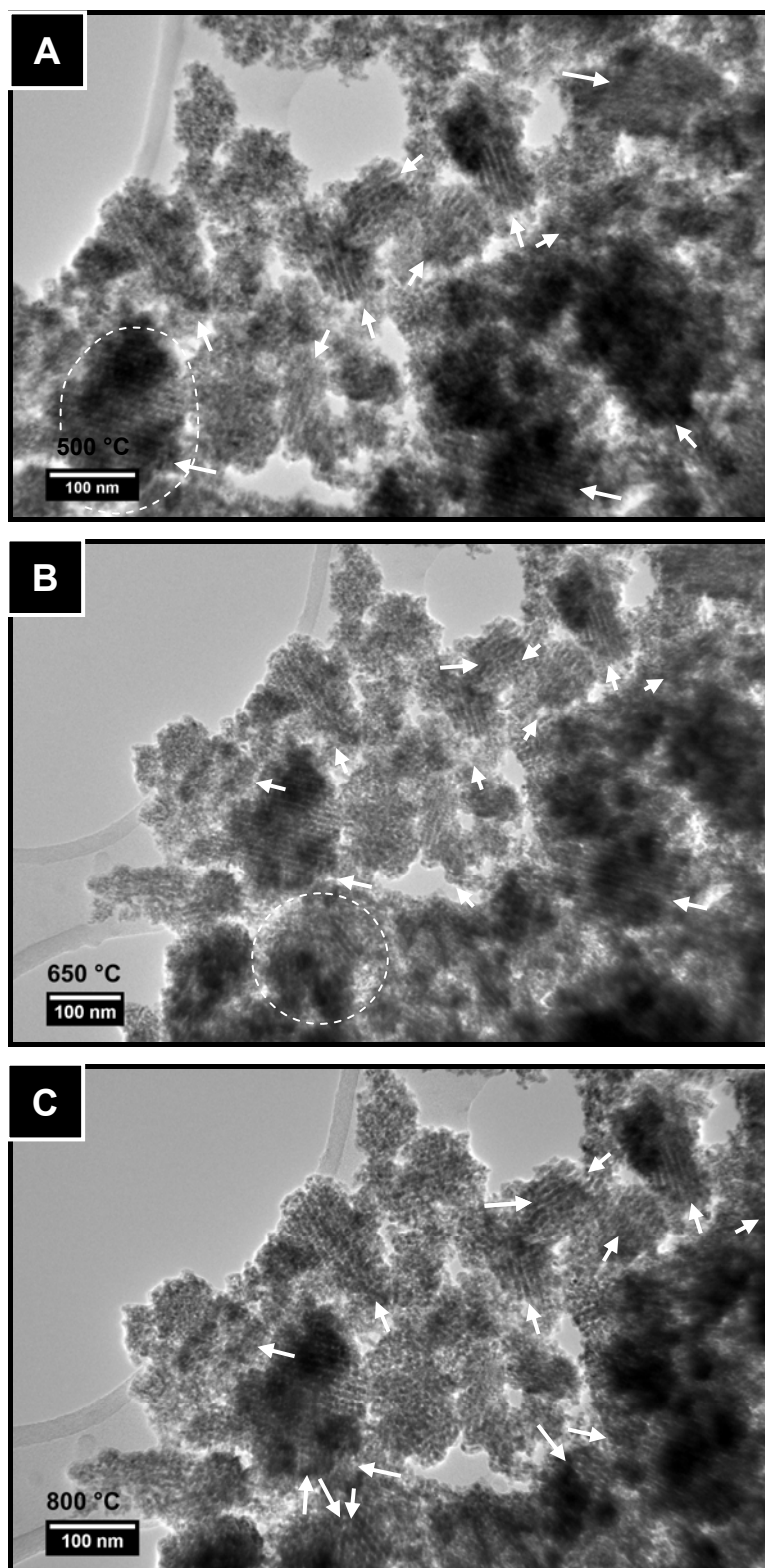


Figure 7.6.1: [A-F] TEM images from in-situ heating experiment. The series of images was taken as the temperature was increased from room temperature to 1000 °C. [G] TEM image of sample after heating experiment. Arrows indicate the arrangement of pores in mesoporous particles. The DDPs adjacent the images are taken of the particle indicated in image [A]. DDPs showed that the particle was presented in the $[111]$ zone axis in images [A], [B] and [F], misaligned $[111]$ zone axis in [C-E], and in [G] the zone axis could not be determined due to discrepancies in the measured d-spacings.

Figure 7.6.2 presents a series of TEM images from a separate area of the sample. There were no images taken below 500 °C of this region as there were no visible mesoporous particles below 500 °C. Figure 7.6.2A clearly shows that the region was almost entirely comprised of ordered material above 500 °C. This phenomenon was observed several times in different locations in the sample. At 900 °C this region remained unchanged except that the mesoporous structures circled in Figure 7.6.2A became better resolved.



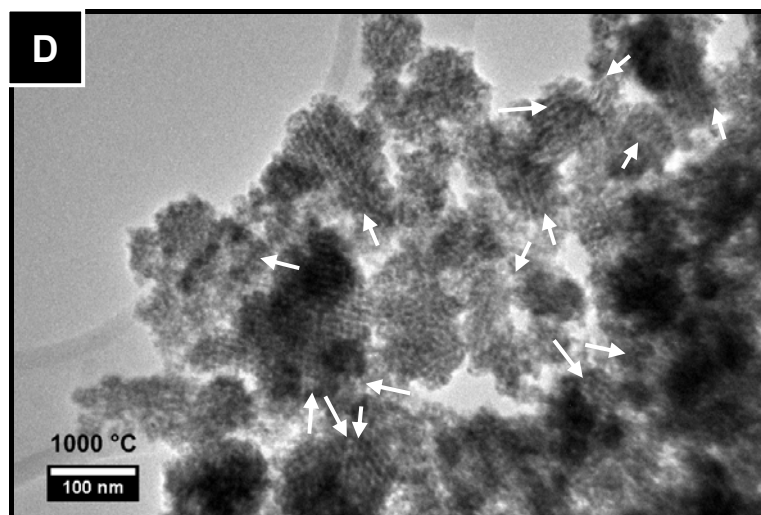


Figure 7.6.2: TEM images showing ordered mesoporous particles that appeared at temperatures above 500 °C and remained stable until 1000 °C: [A-D] series of images from a single region with direction of pores indicated. As temperature increases the clarity of the mesoporous particles can be seen to increase, specifically two particles circled. Arrows indicate pore direction in mesoporous particles.

7.6.2 Examination of the Thermal Stability in Air

An investigation into the thermal stability of CGO-S-V₂ by heating it to 500 °C for 48 h in air undertaken for comparison with the results from in-situ TEM heating experiments. Figure 7.6.3 shows a series of TEM images of this sample after heating. Figure 7.6.3A shows that the material was still comprised of ordered mesoporous particles. Above the ordered mesoporous particle were some nanorods (circled) that may have been distorted by heating or be a product of the original synthesis. There were not many agglomerations of nanoparticles visible with respect to the original images of CGO-S-V₂ (Figure 7.3.27). The inset DDP gave a (100) pore spacing for the mesoporous particle, presented in the [100] zone axis, of 8.3-9.8 nm.

Figures 7.6.3B and C show HRTEM images of two sections of Figure 7.6.3A, as indicated. These show that the particle had porous single-crystal domains. Figure 7.6.3B shows the crystallographic planes twinning in the porous crystal. Above the indicated nanorod the nanorods had one crystallographic plane aligned to the electron beam, as indicated in the inset DDP. Below this nanorod the alignment changed by 73° as shown by the lower DDP. Figure 7.6.3C shows that the ends of the nanorods were thicker than their centres. This has been indicated in the image for a nanorod.

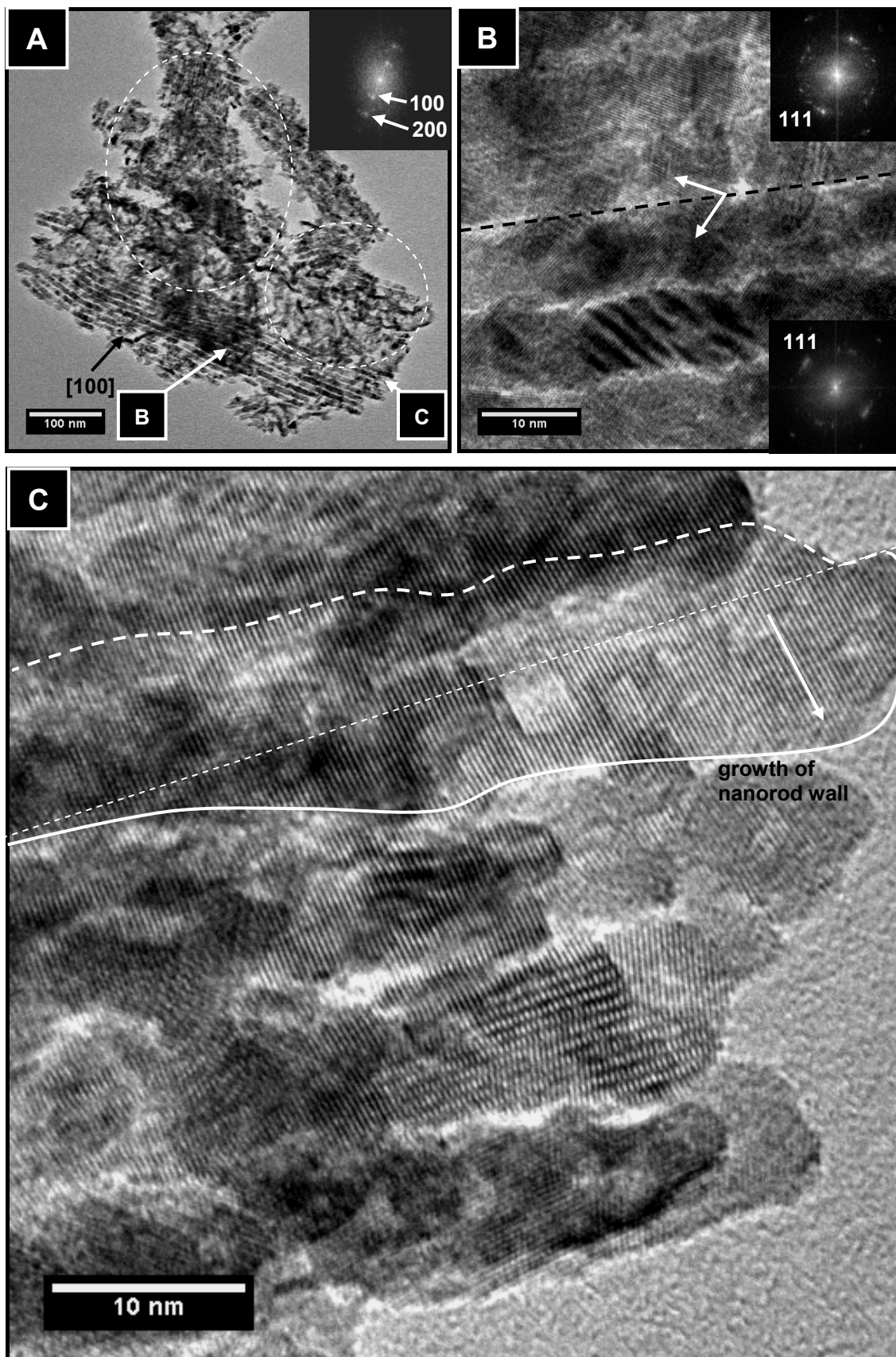


Figure 7.6.3: TEM images of CGO-S-V₂ heated to 500 °C for 48 h in air: [A] TEM image of an ordered mesoporous particle in the [100] zone axis with inset DDP of this particle; [B] HRTEM image of [A] showing porous single crystal morphology with plane defect indicated - DDPs are of regions above and below the indicated plane defect; [C] HRTEM image of [A] showing growth of tips of nanorods

Figure 7.6.4A shows another large ordered mesoporous particle that had retained its pores alongside an agglomeration of porous particles and twisted nanorods. There were no visible nanoparticles unlike the material before heating. The DDP of the ordered porous particle gave a d-spacing of 8.4-10.3 nm for the (100) mesopore reflection. As above, HRTEM images show the ordered particle to be a porous single crystal (Figure 7.6.4B). The inset DDP shows that there was still significant variation (up to 18°) of the crystallographic planes in the porous single crystal.

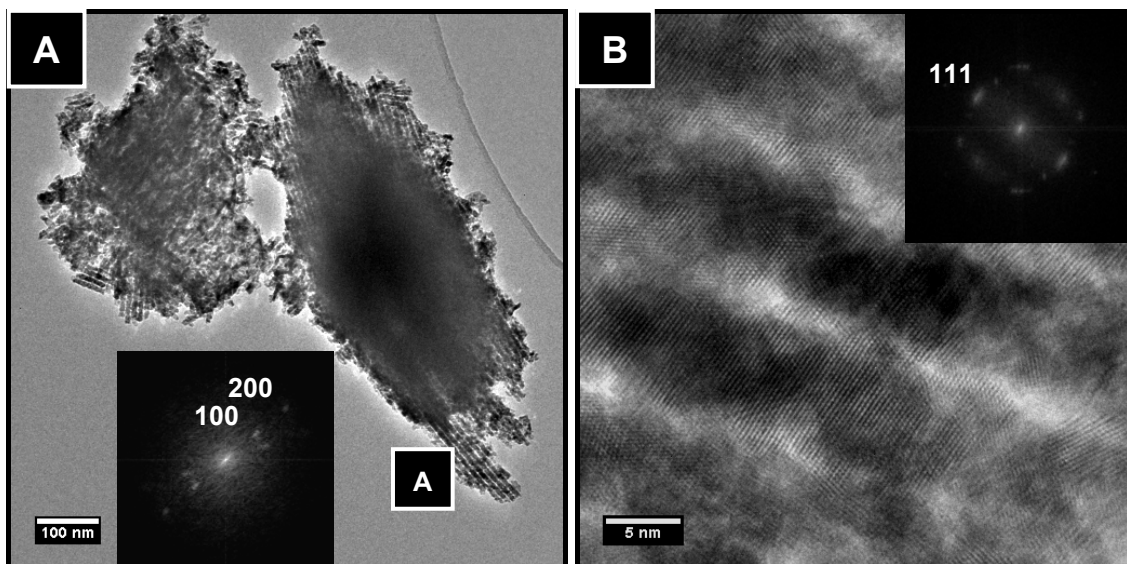


Figure 7.6.4: [A] TEM image of ordered mesoporous particles of CGO-S-V₂ with inset DDP of the mesoporous particle shown in the [100] zone axis; [B] HRTEM image of particle in [A] confirming the porous single crystal morphology.

Figure 7.6.5 shows a representative lower magnification image of a large agglomeration of material containing ordered mesopores and twisted nanorods.

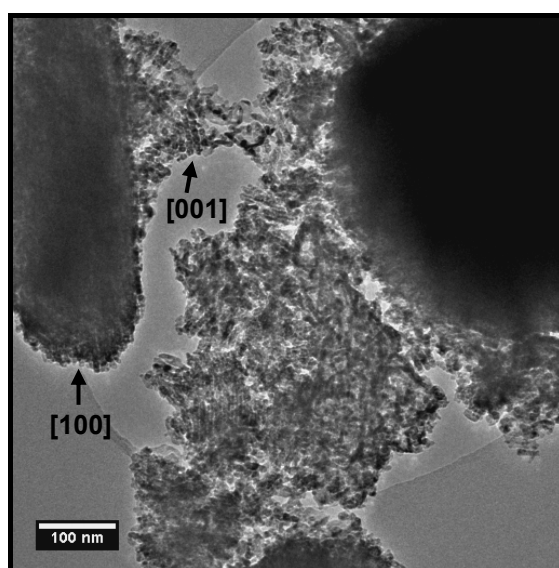


Figure 7.6.5: TEM image showing agglomeration of nanorods or nanowires as well as ordered mesoporous particle in the [001] zone axis as indicated.

From physisorption results, the specific surface area and pore volume of CGO-S-V₂, thermally treated to 500 °C for 48 h, were determined to be 86.7 m²g⁻¹ and 0.30 cm³g⁻¹, respectively. The adsorption-desorption isotherm was Type IV with Type H3 hysteresis (Figure 7.6.6). The pore-size distribution showed sharp peaks at 2.8-3.0 nm and broader peaks at 12-16 nm.

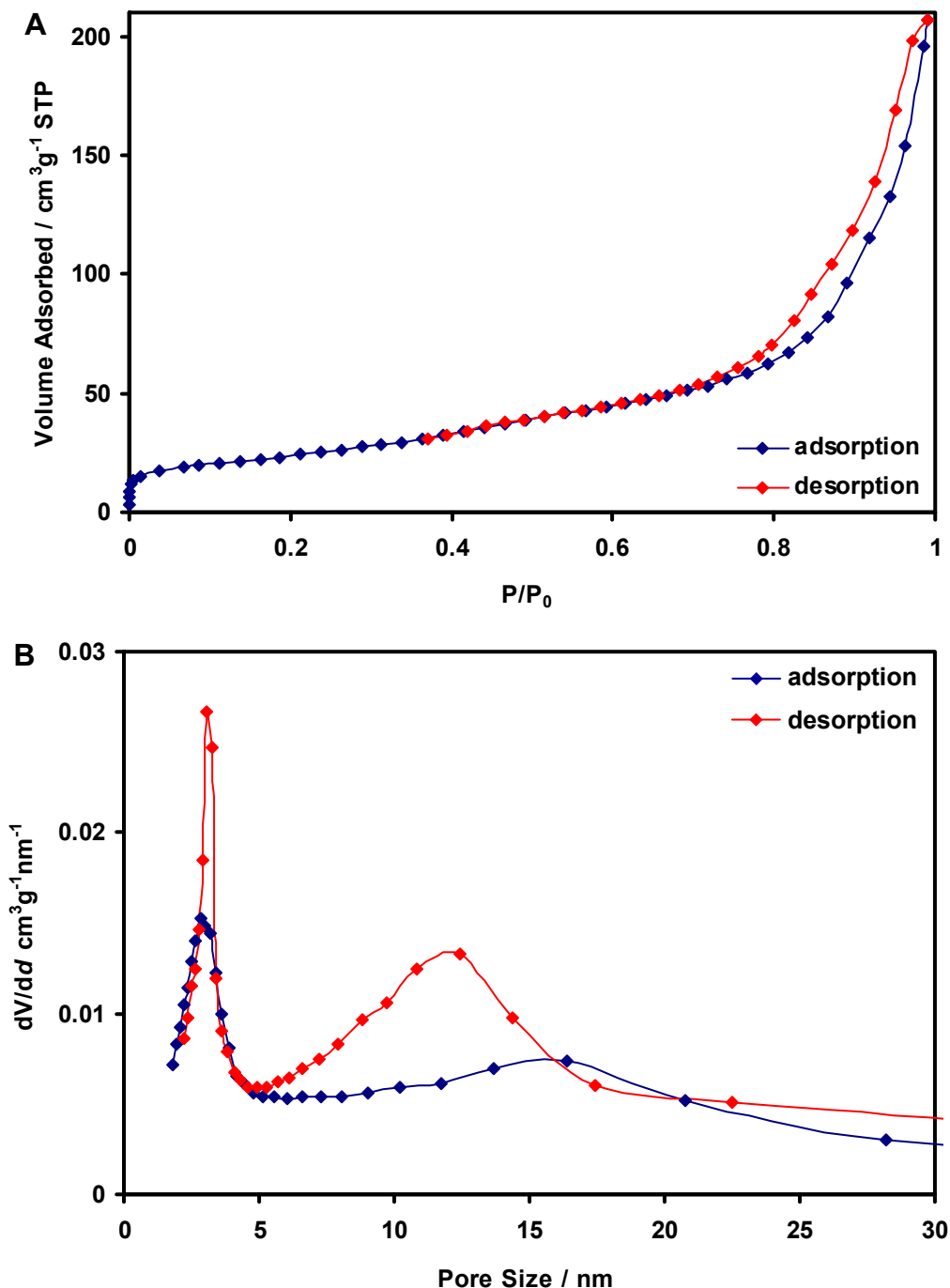


Figure 7.6.6: [A] Physisorption isotherm and [B] pore size distribution for CGO-S-V₂ thermally treated at 500 °C for 48 h.

An investigation into the effects of thermal treatment of CGO-S-V₂ at 650 °C for 72 h in air was carried out. The images in Figures 7.6.7A and B show that the mesoporous structure had been degraded significantly. No ordered mesoporous particles were evident.

The material had not degraded into the agglomerations of random twisted nanorods seen after treatment at 500 °C for 48 h, though this material had not been heated to 500 °C first. Instead, the parallel pore structure was still visible but the nanorod walls had distorted and twisted while remaining as coherent particles. HRTEM images showed that significant grain growth had occurred in some areas. CGO crystals were present that were much larger (> 150 nm across) than any that had previously been observed during this investigation (Figure 7.6.7C).

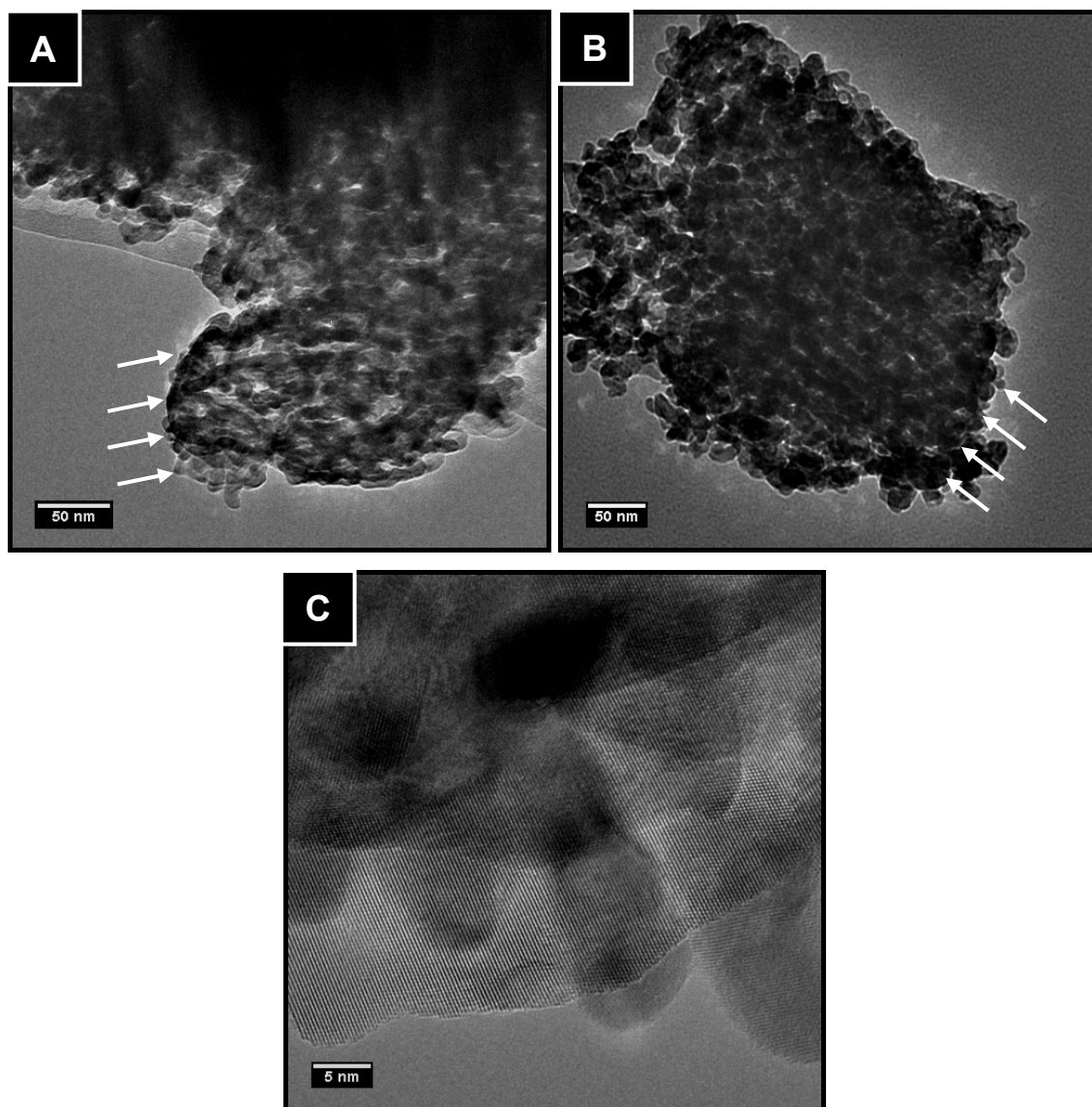


Figure 7.6.7: TEM images of CGO-S-V₂ heated to 650 °C for 72 h in air: [A,B] TEM images of mesoporous particles showing degradation caused by thermal treatment with arrows indicating the direction of mesopores; [C] HRTEM image showing sintering of CGO.

From physisorption results, the specific surface area and pore volume of CGO-S-V₂, thermally treated to 650 °C for 72 h, were determined to be 40.6 m²g⁻¹ and 0.25 cm³g⁻¹, respectively. The adsorption-desorption isotherm was Type IV with Type H3 hysteresis (Figure 7.6.6). The pore-size distribution showed no peak at 3 nm and broad peaks at 18-35 nm, at low adsorption values, in the range of interparticle porosity.

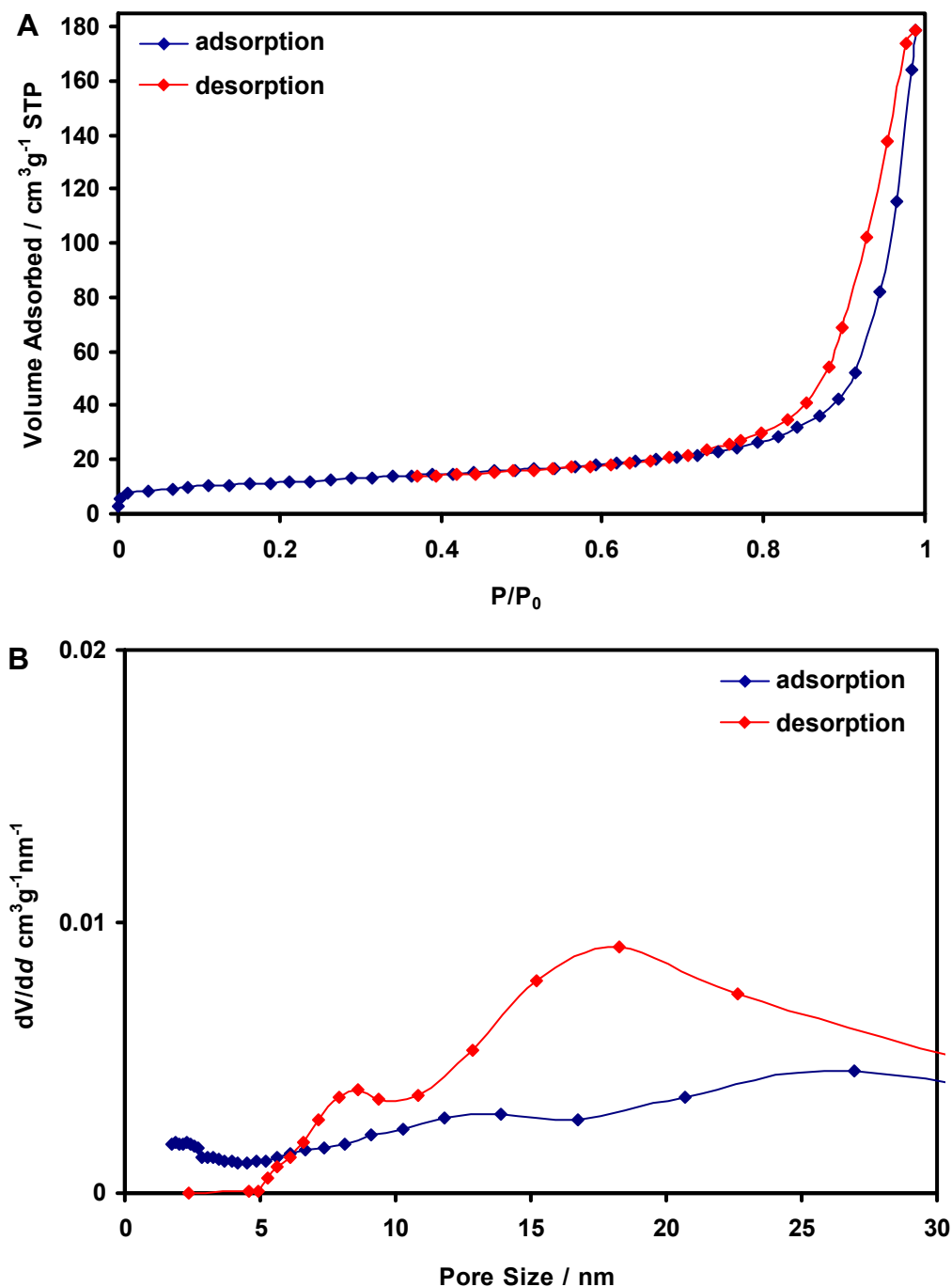


Figure 7.6.8: [A] Physisorption isotherm and [B] pore size distribution for CGO-S-V₂ thermally treated at 650 °C for 72 h.

7.6.3 Discussion

The ordered mesoporous materials showed high thermal stability at temperatures coinciding with the lower edge of the reduction peak (determined by TP studies to be approximately 500 °C). When heated above this temperature for prolonged periods there was clear evidence of sintering. In-situ heating in the TEM showed that over short periods (≈ 4 h) the materials could be heated up to 1000 °C, and cooled down again to room temperature, without loss of structure. It is possible that the mesoporous crystals had already grown sufficiently large that their equilibrium melting temperature made them stable at intermediate

temperatures. Nanoparticles have a lower equilibrium melting temperature and add to the mass of larger particles in the process known as Ostwald ripening. After heating CGO-S-V₂ to 500 °C the only change in the pore size distribution was to the feature at 6-18 nm which was attributed to the structural by-products. When compared to the pore size distribution of the original sample (Figure 7.3.23B), the peak maxima had shifted slightly from 12-17 nm to 13-17 nm. The peak attributed to the porous single crystals is still evident at 3 nm. This may suggest that the by-products have been more affected by the thermal treatment than the porous single crystals. The sintering of the by-products would cause the mass of the mesoporous crystals to rise and consequently their equilibrium melting temperature. As the temperature rose above the equilibrium melting temperature the mesoporous crystals would sinter into the structures observed in the TEM images taken after prolonged heating at 650 °C. The equilibrium melting temperature would vary depending on the size of the mesoporous particle.

Previous literature reports on the thermal stability of mesoporous ceria have shown a steady decrease in the specific surface area with increasing temperature (Figure 7.6.9A: Note that the cause for the increase in the specific surface area in the report from Wang *et al.*⁶⁵ was due to incomplete removal of the template at 200 °C - at 400 °C the template had been fully removed causing the pores to become unblocked, increasing the specific surface area). Unlike all of the mesoporous ceria materials previously reported, ordered mesoporous CGO (CGO-S-V₂) appeared to have a plateau up to approximately 500 °C where the specific surface area decreased only a small amount. It should also be noted that CGO-S-V₂ was heated for between 12-24 times longer than the other samples in this plot. In the comparison of pore volume there is limited data available (Figure 7.6.9B). Comparing CGO-S-V₂ with the ceria synthesised by Lundberg *et al.* using P123 in cooperative self-assembly⁷³ it can be seen that initially there is much less pore volume lost in CGO-S-V₂.

For a conclusive study more data points should be gathered, but the physisorption results were consistent with the proposed sintering mechanism described in Section 7.3.7. Samples with high concentrations of nanoparticles (the literature materials), were more affected by lower temperatures than the ordered mesoporous material tested in this thesis, and the ordered mesoporous material appears to be capable of maintaining a high pore volume even after being subjected to high temperatures for extended periods of time.

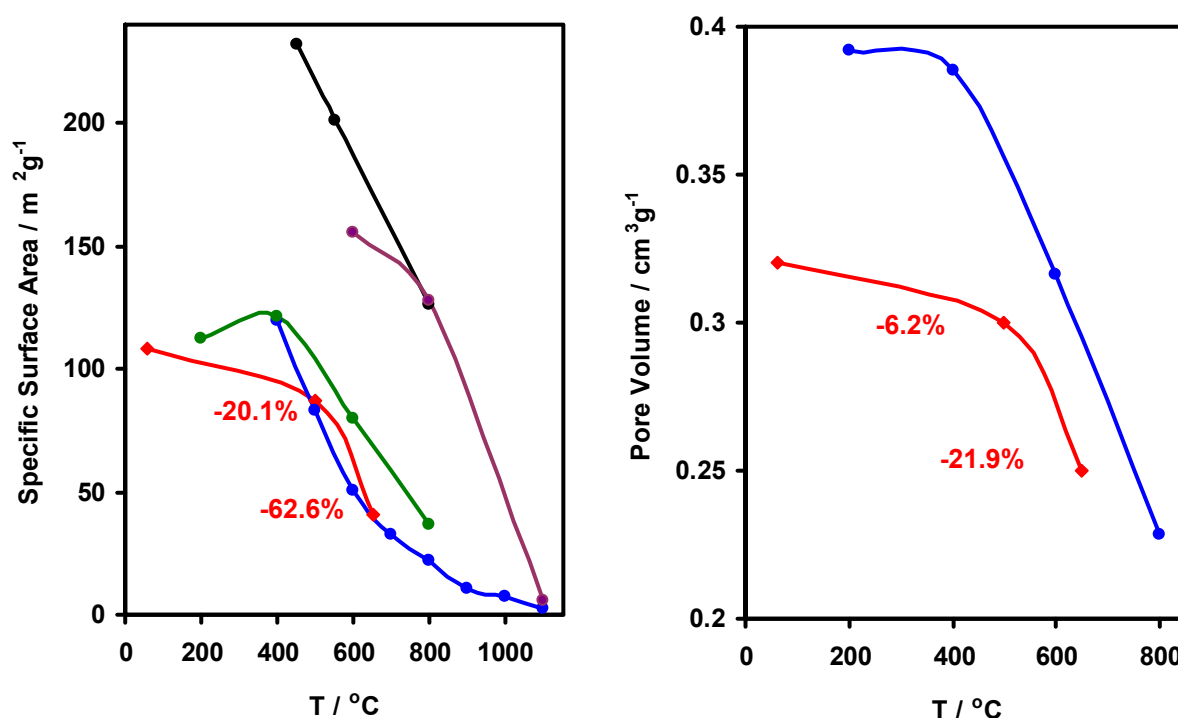


Figure 7.6.9: Plots comparing the effect of thermal treatment on [A] specific surface area and [B] pore volume for various mesoporous ceria-based materials with specific surface area and pore volume losses shown. Many of these are not directly comparable due to different heat treatments, but an indication of the thermal stability can be given. (—♦—) CGO-S-V₂ synthesised in this investigation (heated for at least 48 h), (—●—) ceria synthesised using P123 non-ionic surfactant (unspecified heating time),⁷³ (—●—) ionic templated ceria (heated for 4 h),⁶⁵ (—●—) ionic templated ceria (heated for 2 h),⁶⁴ (—●—) ionic templated ceria (heated for 2h).⁶⁹

7.7 Studying the VI Method

The VI method was studied by examining a sample of CGO-S-V₂ using TEM and HRTEM. This sample had been impregnated by the precursor solution and calcined but the silica template had not been digested. This was in order to examine the nanostructure of the material prior to template removal. The TEM images of this material are presented in Figures 7.7.1-3.

The images in Figure 7.7.1A show that the impregnation of the SBA-15 pores by the precursor material was comprehensive. The mesoporous structure of SBA-15, and the final material, CGO-S-V₂ (Figures 5.3.3 and 7.3.27, respectively), is clearly evident. There was very little nanoparticulate material covering the structure, in contrast to what had been observed in the final product. From the edge of the particle there were nanowires (differentiated from nanorods in that they are not linear) that appeared to be extruded from the

mesoporous silica. These nanowires originate at the mesoporous particle and formed bundles approximately 100 nm away. This feature has been expanded in Figure 7.7.1B. The bundles appeared to be loosely associated. The diameter appeared to be equivalent to that of the nanorods inside the mesoporous silica.

The HRTEM image Figure 7.7.2C confirmed that in the SBA-15 structure had been filled with CGO material. This is in the form of nanorods and these exhibit lattice planes which are consistent with the CGO structure, calculated using the DDP presented in Figure 7.7.2(ii). The lattice planes in adjacent CGO planes are seen to be aligned with each other. There was no evidence of empty voids between the CGO and silica materials.

A HRTEM image of a bundle showed that the nanowires were crystalline (Figure 7.7.2D). When a DDP was taken of this entire image, it was noticed that there were four prevalent crystallographic orientations Figure 7.7.2(ii). Three of these reflections measure 0.31 nm which is equivalent to the CGO (111) reflection. The other orientation, presented in Figure 7.7.2(iii) indexes to the CGO [111] zone axis.

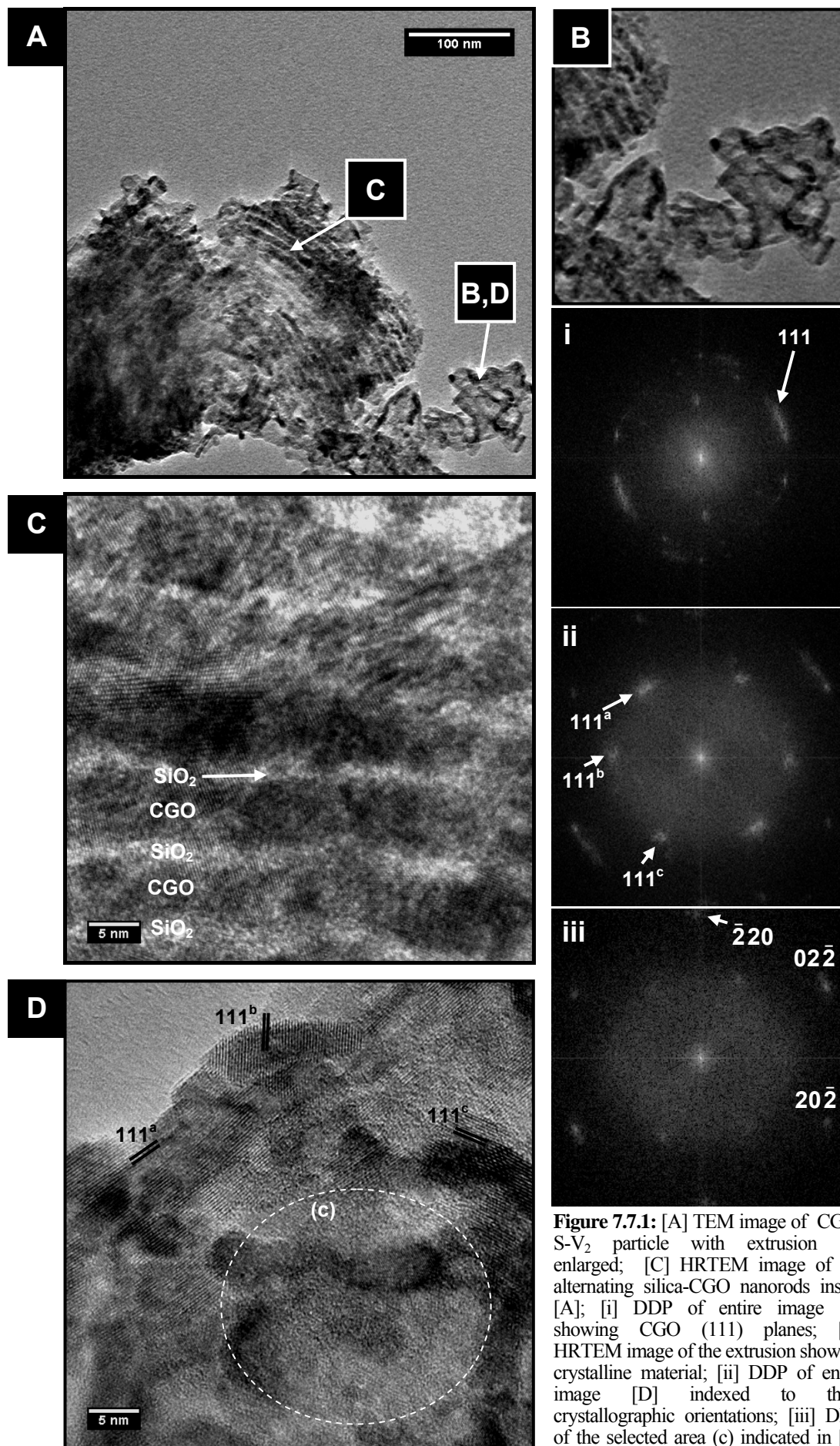


Figure 7.7.1: [A] TEM image of CGO-S-V₂ particle with extrusion [B] enlarged; [C] HRTEM image of the alternating silica-CGO nanorods inside [A]; [i] DDP of entire image [C] showing CGO (111) planes; [D] HRTEM image of the extrusion showing crystalline material; [ii] DDP of entire image [D] indexed to three crystallographic orientations; [iii] DDP of the selected area (c) indicated in [D] indexed to the [111] zone axis for crystalline CGO.

Figure 7.7.2A shows a defocused TEM image of mesoporous particles in which many of these extrusions were observed (as indicated). Two observations could be made from this image. These observations are clarified in the enlarged TEM image, Figure 7.7.2B. Firstly, the nanowires were not linear. They appeared to have grown up to 50 nm before the direction of growth changes. This formed curved, coiled, and bundled structures as were observed in Figure 7.7.2A. Secondly, the nanowires appeared to be extruded from the mesopores of the silica template. The SBA-15 particle (indicated) was arranged in the [100] zone axis. The nanowires were concentrated near the pore entrances as indicated by the arrows. Other bundles of nanowires, however, appear to have originated from the side of SBA-15 particles in Figure 7.7.2A. It is not clear in this image if this could be due to pore defects or overlapping particles.

Nanowire extrusion from silica mesopores is observed again in Figure 7.7.2C. The Image contrast in the expanded image, Figure 7.7.2D, shows that the SBA-15 particle is filled by CGO material. The schematic representation shows the shape of the nanowires that were extruded from the end of the SBA-15 pores, with the edge of the SBA-15 particle also indicated.

The HRTEM image, Figure 7.7.2E, shows three short nanorods with a width equivalent to the SBA-15 pore diameter. The particles protrude partially outside the SBA-15 template which is the darker amorphous material.

The HRTEM image, Figure 7.7.2F, shows different nanostructures in adjacent SBA-15 pores. The SBA-15 can be identified as the lighter amorphous material. The pores are labelled 1-4 from left to right across the image. Pore 1 had a nanorod inside it that was only 20-25 nm in length. Below the nanorod there was a void in the SBA-15 template. Pore 2 had a nanorod approximately 20 nm in length below which was a void. Below the void was a nanoparticle inside the SBA-15 pore. Pore 3 was completely impregnated with CGO material. Pore 4 had only a single nanoparticle approximately 20 nm from the pore entrance.

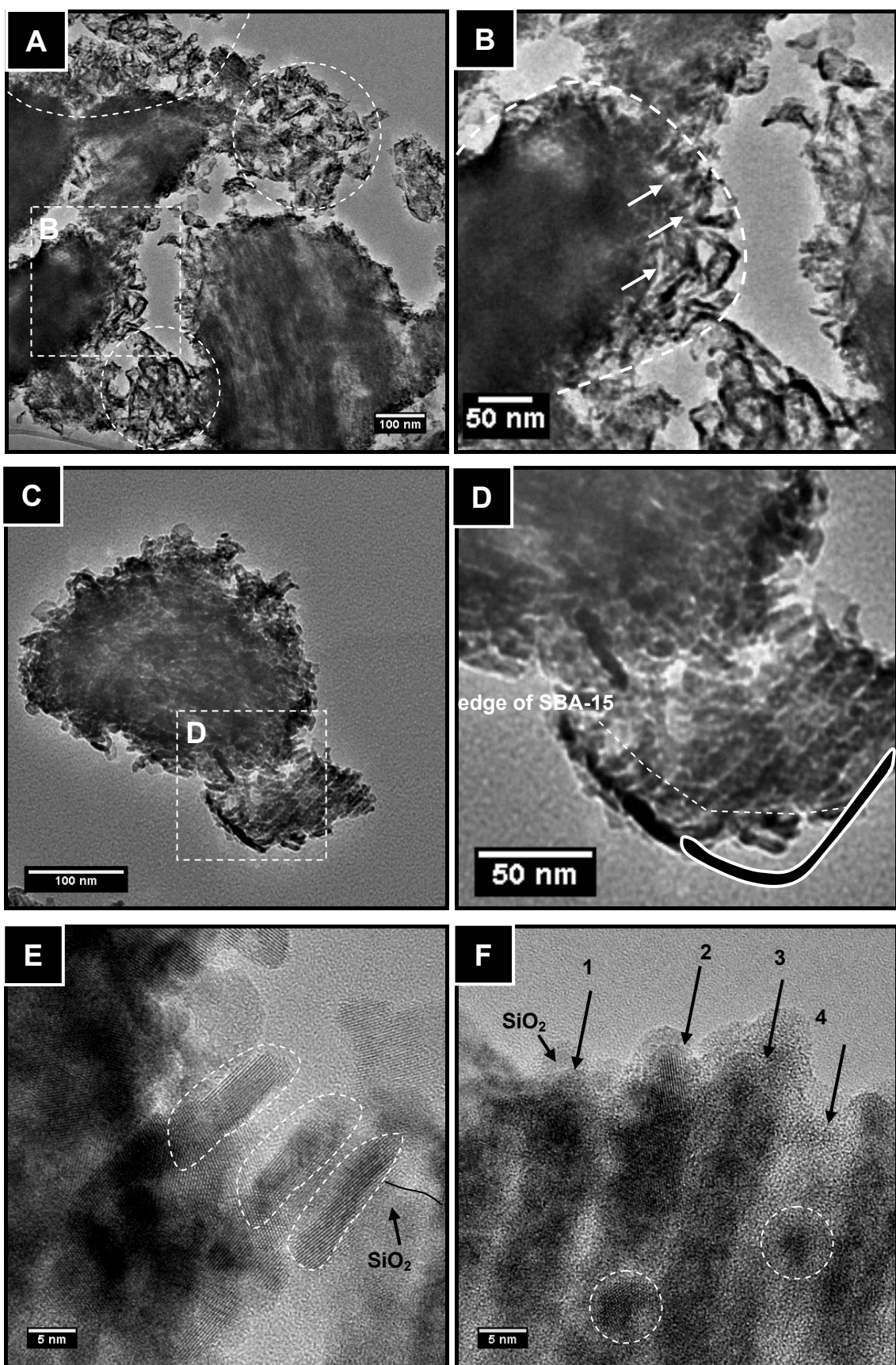


Figure 7.7.2: TEM images of CGO-S-V₂: [A] image of impregnated SBA-15 particles with extrusions (circled); [B] enlargement from image [A] where extrusions from the end of a particle, presented in the [100] zone axis, can be seen; [C] TEM image of a mesoporous particle presented in the [100] zone axis; [D] enlargement of [C] where extrusions from the end of the particle can be seen (with schematic); [E] HRTEM image of the edge of SBA-15 particle with three ceria nanocrystals partially outside the silica template; [F] HRTEM image of a SBA-15 particle showing the [100] zone axis with nanorods and nanoparticles inside adjacent pores.

7.7.1 Discussion

This section will discuss the VI method based primarily on the observations made in Section 7.6.1, the experimental observations made in Section 7.2 and the results discussed in Section 7.3.7. Section 7.3.7 suggested that VI overcame many of the issues raised with the IWIT in Section 7.1. It was noted in the observations that the template-precursor solution gel was clear in many instances when VI was used. This was likely caused by a decrease in the number of refracting surfaces when the precursor solution had a comparable refractive index (RI) to the template. For this phenomenon to occur, air pockets between the solution and the template (and within the matrix), must have been removed or the incident light would have been scattered sufficiently ($RI_{\text{SiO}_2} = 1.4\text{-}1.5$, $RI_{\text{air}} = 1.0$), for light to be scattered back out of the reactor and give the material a white appearance.

VI was shown to be a reproducible technique (Ceria-K-V₁ and Ceria-K-V₂). It was also used for both SBA-15 and KIT-6 templates as well as for both ceria and CGO materials. Preliminary attempts at using another salt ($\text{Ce}(\text{AcAc})_3$ in acetone at lower concentrations), showed that the method favoured the use of the initially-tested, highly-concentrated precursor solutions, despite the fact that these were highly viscous. Modifications of the apparatus to make the impregnation procedure simpler did not appreciably enhance results. The modifications were aimed at decreasing the pressure for the removal of gases and to improve the vacuum integrity. This could suggest that the removal of air from the pores is not difficult and other factors are less crucial. The other modifications made between the V₁ and the V₂ setup did, however, make the impregnation easier to carry out. The VI method was shown to successfully produce porous single crystals using a single impregnation. Similar methods often use two impregnations. This saved approximately 48 h in the synthetic procedure compared with IWIT. Processes that were not investigated and could enhance product quality and quantity could include modification of the template surface and modification of the solvent to increase the attractive forces between the template and the solute to ensure that material was retained in the pores during the drying and calcining steps. An investigation of the heating processes involved would also be of interest.

7.7.1.1 The Mechanism of the Vacuum Impregnation Method

In Section 7.6.1 it was observed that there was not much nanoparticulate material on the surface of the SBA-15 template. Disconnected nanoparticles were observed inside the pores of SBA-15. The final products contained a lot of nanoparticles. In Sections 7.6.1.2-3 nanoparticles were not observed on the surface of the SBA-15 template after heating the material in air. During in-situ TEM heating experiments it was observed that above

approximately 400 °C nanoparticulate material began to sinter and porous material remained. Therefore it was proposed that during the synthesis of ordered mesoporous materials the temperature is sufficient (400 and 600 °C) for small diameter ceria nanoparticles to sinter or be sufficiently mobile to sinter and form larger crystals.

In Section 7.7 it was observed that most pores in the oxide had been comprehensively impregnated and there were no air pockets visible even though volume would be expected to have been lost due to the decomposition of the nitrate. This suggests that there had been migration of solid material or shrinkage of the entire structure. This was difficult to verify as these observations were from a 2D image of a 3D structure. However, the d-spacing of all products were comparable with those of the templates implying that the materials had not undergone significant shrinkage. It is possible that these observations are a result of particle growth inside the pores. It is known that capillary action in mesoporous materials is sufficient to absorb molten solids as the temperature is increased slowly as this is the basis of the solid-liquid nanocasting method discussed in Section 1.2.2. There are two phases that could undergo molten or mobile phases during this synthetic procedure. Firstly the nitrates melt below their decomposition temperature and could migrate into the pores via capillary action. Secondly the oxide could migrate when small nanoparticles become mobile at their equilibrium melting temperature and become consumed in Ostwald ripening. The second process would likely be slower as it would involve mobile species rather than a true liquid phase.

It was observed that crystalline nanowires, of a diameter equal to the template pores, were extruded from the template pores in CGO-S-V₂ during the calcination process. It is proposed that the smaller particles became absorbed into larger crystals inside the pores until such time as the pores became completely filled. At this time Ostwald ripening continued particle growth of the porous single crystals inside the template. After a time material began to extrude from preferential sites - the pore entrances - producing nanowires that aggregated in coils outside the mesoporous particle. A schematic for this mechanism is shown in Figure 7.7.3.

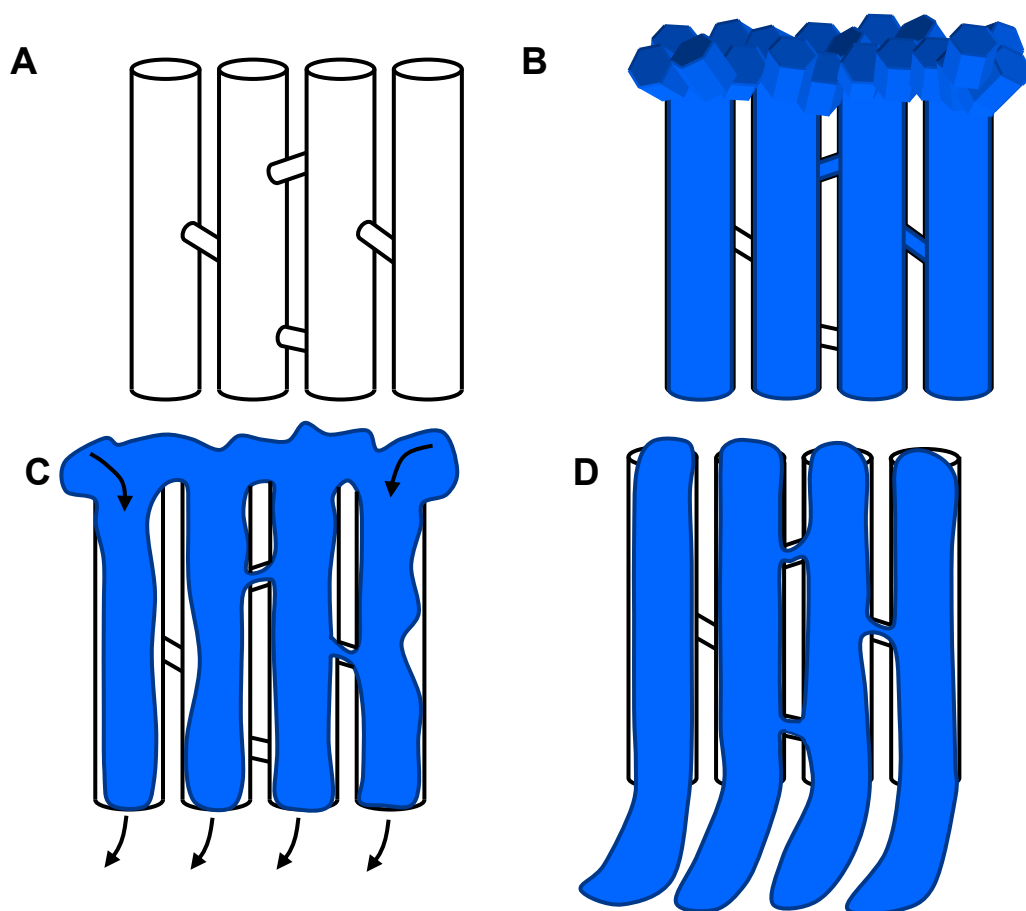


Figure 7.7.3: Schematic mechanism for VI: [A] SBA-15 template; [B] impregnation of the precursor solution is more comprehensive than with IWIT and after calcination there is residual material on top of the template; [C] during calcination the material is sufficiently mobile that capillary action and Ostwald ripening draws it into the pores, increasing the particle size of the mesoporous crystals; [D] this causes filling of the pores and then extrusion of the nanowires out of pores with a diameter equivalent to that of the pores.

7.8 Summary

The results presented in this chapter show that VI was a significant improvement on the IWIT for producing ordered mesoporous ceria and CGO. All of the compositions and templates examined produced ordered mesoporous materials in high yields showing that the method was reproducible (Table 7.8). The pore volume was determined to be high with respect to the theoretical value, though there were many assumptions to take into account in this calculation, and the pore size and spacings related well to the templates from which the materials were synthesised. TEM studies and tomography confirmed that the samples had a 3D structure, being the negative of the original template. At the time of its first use for this investigation the VI method had not been reported before, though several months afterwards a patent for a highly similar VI method was issued.¹⁷⁸ At the time of this report, while VI has

been applied to the in-situ growth of nanoparticles in a mesoporous template,¹⁷⁹ to the author's knowledge there are no publications using VI for producing ordered mesoporous materials.

Table 7.8: Table summarising the results from this chapter. The pore size was identified from the BJH pore size distribution plots, and the d-spacing from DDPs of TEM images.

	BET specific surface area (m ² g ⁻¹)	Pore volume (cm ³ g ⁻¹)	BJH pore size (nm)	d-spacing TEM (nm)	d-spacing SAXS (nm)
Ceria-K-V ₁	105.7	0.33	2.6-3.0, 9.6-13.8	8.0-9.1	
Ceria-S-V ₂	85.7	0.29	2.4-3.0, 9.6-13.8	8.9-9.7	
Ceria-K-V ₂	114.7	0.35	2.2-3.0, ~8	8.5-9.4	
CGO-S-V ₂	108.6	0.32	2.5-3.0, 11-17	8.7-9.8	9.2
CGO-K-V ₂	137.5	0.38	2.1-2.7	9.1-9.2	8.8

The materials were not only produced in high yields, but also displayed the porous single crystal morphology, with non-linear lattice planes. The pore walls were not faceted as was usual for fluorite crystals. This is likely to lead to unusual lattice planes being exposed on the surface. TEM images of CGO-S-V₂ prior to template removal showed nanorods being extruded from the pores. These nanorods appeared to be single crystalline. During the impregnation process, there were very few nanoparticles observed on the surface of the material. There was also noticeable loss of nanoparticles upon heating to 500 °C. These observations allowed a mechanism for the VI process to be proposed. It is hoped that in-situ TEM observations will allow for further study of this mechanism.

The highest specific surface areas were reported for materials impregnated using the KIT-6 template, and using the CGO precursor solution. These materials were characterised in detail using TEM, physisorption, TP studies, and powder XRD. SAXS analyses had a very low signal to noise ratio, but information regarding pore spacings was gained from DDPs. EDS results were inconclusive but it is hoped that elemental analysis will be achieved through ICP-MS.

The thermal stability of the materials was studied to determine their range of potential applications. It was determined that the porous single crystals were resilient to thermal shock up to at least 1000 °C for short periods (<1 h). After heating at 500 °C for 48 h the porous single crystal structure was maintained as well as most of the initial specific surface area and pore volume. After heating at 650 °C for 72 h there was a dramatic loss of structure, surface

area and approximately a 22 % loss of pore volume. The nanoparticles in the sample appeared to sinter well below these temperatures based on observations from the in-situ TEM heating experiment, which is consistent with the theory of sintering and grain growth presented above. The ability of the porous single crystals to maintain their integrity at high temperatures means that they could be useful in intermediate temperature applications (100-500 °C) in which high specific surface area materials have typically not been used, as nanostructures are prone to thermal instability. These materials may also be useful in low temperature applications, such as photovoltaics, since preliminary tests showed that the ordered mesoporous structure quenched photocatalytically produced excitons with a very high efficiency.

All of the materials prepared using VI showed a decreased oxidation temperature in TPR experiments. Further TP experiments, including the addition of active metal catalysts, could improve this further, as well as adding functionality to the materials.

Chapter 8

Mesoporous Carbon

8.1 Experimental Philosophy

Ordered mesoporous carbon has been investigated previously with a view to use in catalyst supports and as templates for nanocasting. Mesoporous carbons may also have applications in low temperature fuel cells, photovoltaics, supercapacitors and other emerging technologies, as discussed in Section 1.3.2. Therefore, being able to produce mesoporous carbon using a faster, simpler and more importantly, less expensive method compared to competing methods, for example, IWIT, could assist in the implementation of mesoporous carbon in these key areas. The main goal for the application of VI in the synthesis of mesoporous carbon was to maintain yields while simplifying the synthetic procedure. This might open a pathway for decreasing the production cost, while also investigating the possibility of tailoring both the pore morphology (by using different silica templates) and the structure of the pore wall (amorphous carbon versus graphitic) to control the electronic properties.

This chapter reports the first results for the application of the VI method to the synthesis of mesoporous carbon. Also reported are some potential modifications to VI which could be applied to the synthesis of materials such as, but not restricted to, mesoporous carbon.

8.2 Experimental

8.2.1 Mesoporous Carbon Using the IWIT

For the IWIT of SBA-15 to produce the mesoporous carbon product, CMK-3, the method described by Ryoo *et al* was used.⁹⁰ For consistency with the rest of this thesis this material will be termed C-S-I. In a typical experiment, 1.25 g d-sucrose was dissolved in 5 cm³ water. To this was added 1.43 mmol sulfuric acid. The sulfuric acid must be added once the sugar solution is homogenised, or diluted in water first, to prevent premature carbonisation of the sucrose. The precursor solution was added drop wise to 1 g of SBA-15. Once the impregnation was completed the material was dried at 100 °C and then at 160 °C in air using

an oven (typically overnight for each step) to ensure the catalytic carbonisation of the sucrose by sulphuric acid was complete. This was followed by a further impregnation step where a solution comprised of 0.8 g d-sucrose, 5 cm³ water and 0.92 mmol sulfuric acid was impregnated as above. The carbonization step was repeated and the material was calcined at 900 °C for 3 h (ramp rate 5 °C min⁻¹) in an Ar atmosphere. The silica was digested by stirring with 100-200 cm³ of 1-2 M NaOH at 60-80 °C. Buchner filtration was used to recover the product from the NaOH solution (the mesoporous carbon was insufficiently dense for centrifugation) and the sample was sucked dry. This step was repeated three times. The final product was washed with water, ethanol and then dried in an oven at 105 °C in air.

8.2.2 Preparation of Mesoporous Carbon Using VI

For the synthesis of CMK-3 using VI (C_x-S-V₂), the apparatus was set up as shown in Figure 7.2.1. SBA-15 was placed in the test-tube and this was then pumped down. Once the silica had been pumped down for 4-6 h, the precursor solution (described for individual experiments below) was admitted to the test tube as per Section 7.2. Once impregnated the material was carbonised, calcined, underwent template digestion using NaOH, was washed and finally dried, as per Section 8.2.1. There was no second impregnation - all VI syntheses to produce CMK-3 involved a single impregnation.

The experiments to prepare the product, C₁-S-V₂, employed a 2:1 w/w ratio of d-sucrose to water. The precursor solution was stirred overnight to create a homogeneous mixture. The quantity of precursor solution added was sufficient to impregnate the SBA-15 template used (as in the preparations of ceria and CGO materials). 4 drops of pure sulfuric acid were added to approximately 20 cm³ precursor solution in the dropping funnel. This was done immediately prior to impregnation to prevent premature carbonisation of the sucrose solution.

The preparation of the final material in this series, C₂-S-V₂, used a solution composed of 1:2 w/w ratio of d-sucrose to water with four drops of pure sulfuric acid added immediately prior to impregnation.

8.2.3 Molten Vacuum Impregnation

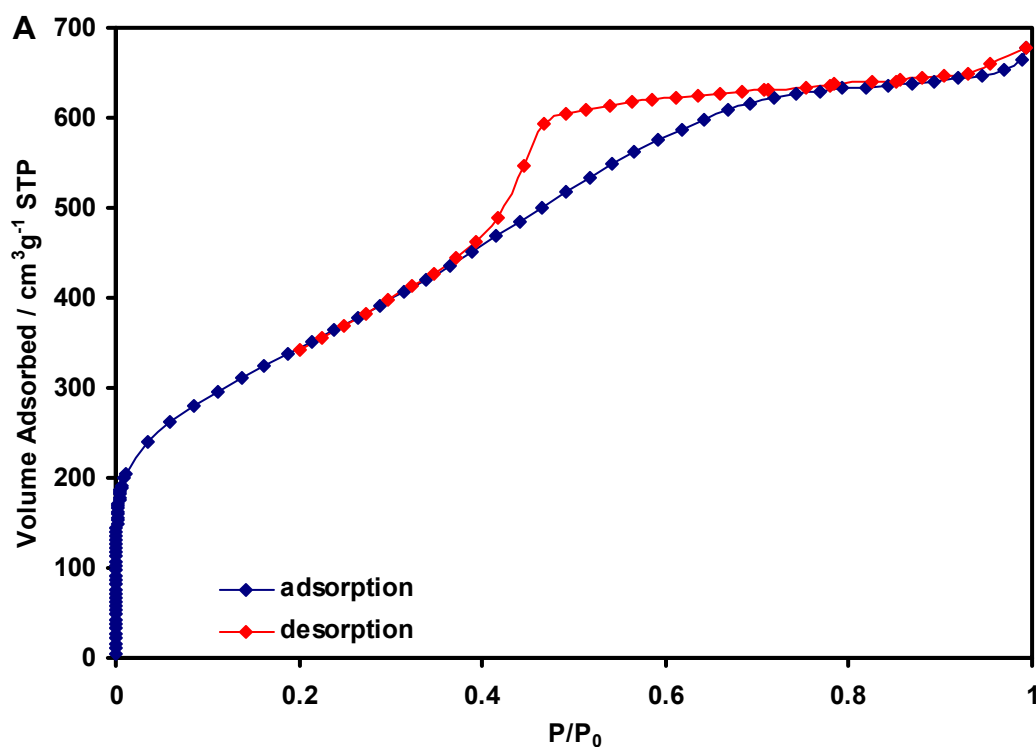
The motivation for the molten VI experiment was that by using a molten precursor, rather than a solution, the pure precursor could be heated beyond its melting point inside the test tube. This is similar in principle to the solid-liquid method described by Yue and Zhou,²⁶ except vacuum assisted. Once in molten form, the vacuum would be released and the molten liquid would impregnate the template. The sample would then be calcined directly after cooling. The molten VI schematic would be similar in design to the VI experiment, except that the impregnation chamber would be capable of being heated. It should be noted that the

modifications make the experimental setup similar to that reported by Benoit *et al.*,¹⁷⁹ though Benoit *et al.* used a vacuum system for in situ nanoparticle synthesis not for the preparation of mesoporous materials. Before applying the molten VI method with molten precursors for the synthesis of mesoporous materials, preliminary experiments were performed. In these, it was found that it was not possible to melt the sucrose precursor without it decomposing to glucose and fructose followed by immediate carbonisation of the sugars. Other sugars that could be tested in future studies include glucose, fructose and other saccharide-based compounds plus other materials capable of undergoing carbonisation, for example furfuryl alcohol and phenol resin.¹⁸⁰

8.3 Results

8.3.1 Mesoporous Carbon Using the IWIT

From physisorption results, the specific surface area and pore volume of C-S-I were determined to be $1248.1 \text{ m}^2\text{g}^{-1}$ and $1.02 \text{ cm}^3\text{g}^{-1}$, respectively. The adsorption-desorption isotherm was Type II with a small amount of Type H2 hysteresis. The shape of the isotherm is typical of carbons with micro- and mesopores, and the hysteresis indicated adsorbate effects at $P/P_0 = 0.45$, such as the TSE (Figure 7.3.11). The pore-size distribution showed a narrow peak at 2.4-3.5 nm.



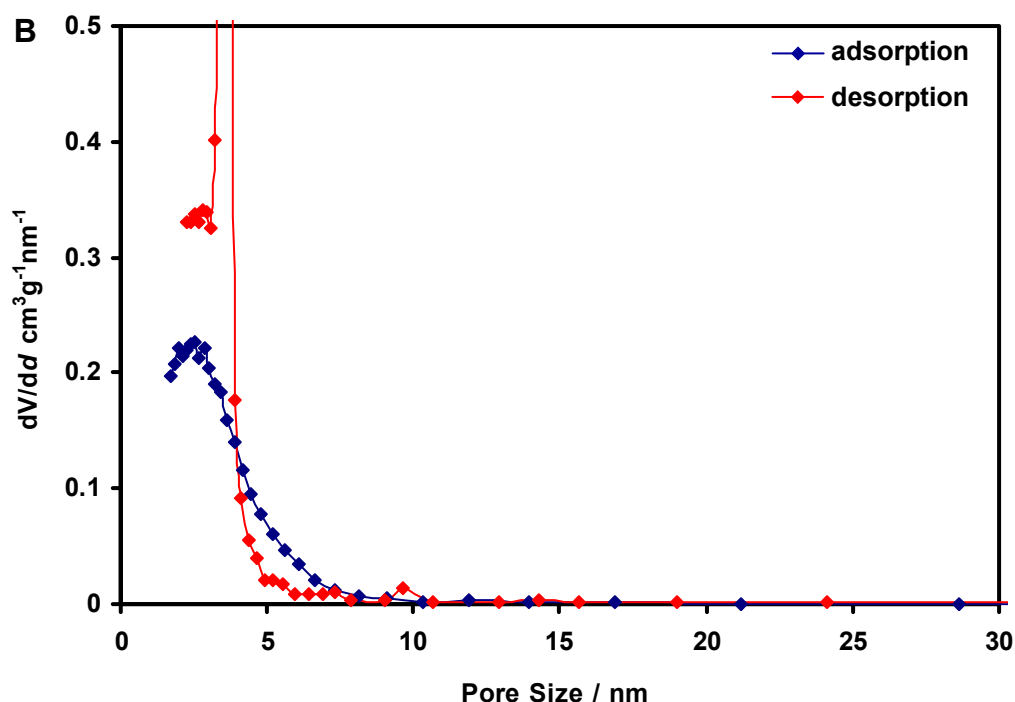


Figure 8.3.1: [A] Physisorption isotherm and [B] pore size distribution for C-S-I.

TEM analysis of C-S-I (Figure 8.3.2) showed the sample was comprised of large (300×1000 nm) mesoporous particles with a shape similar to the original SBA-15 template. These particles were shown to agglomerate together in large numbers (Figure 8.3.2A). The image contrast was lower than in previously observed samples but this is likely to be caused by decreased scattering by the carbon atoms which have a lower electron density than Si, Ce or Gd. The electron beam was found to cause damage to the sample. Therefore, only a limited time was allowed to capture images for each sampled area. The pores were highly ordered in parallel arrangements across the entire particle but showed curvature down their lengths (Figures 8.3.2C and D). The pore spacings were measured at 6.4–8.1 nm from the (100) spots in the DDPs. The spots in the DDPs show the variation in the (100) pore diameters and angles within the images.

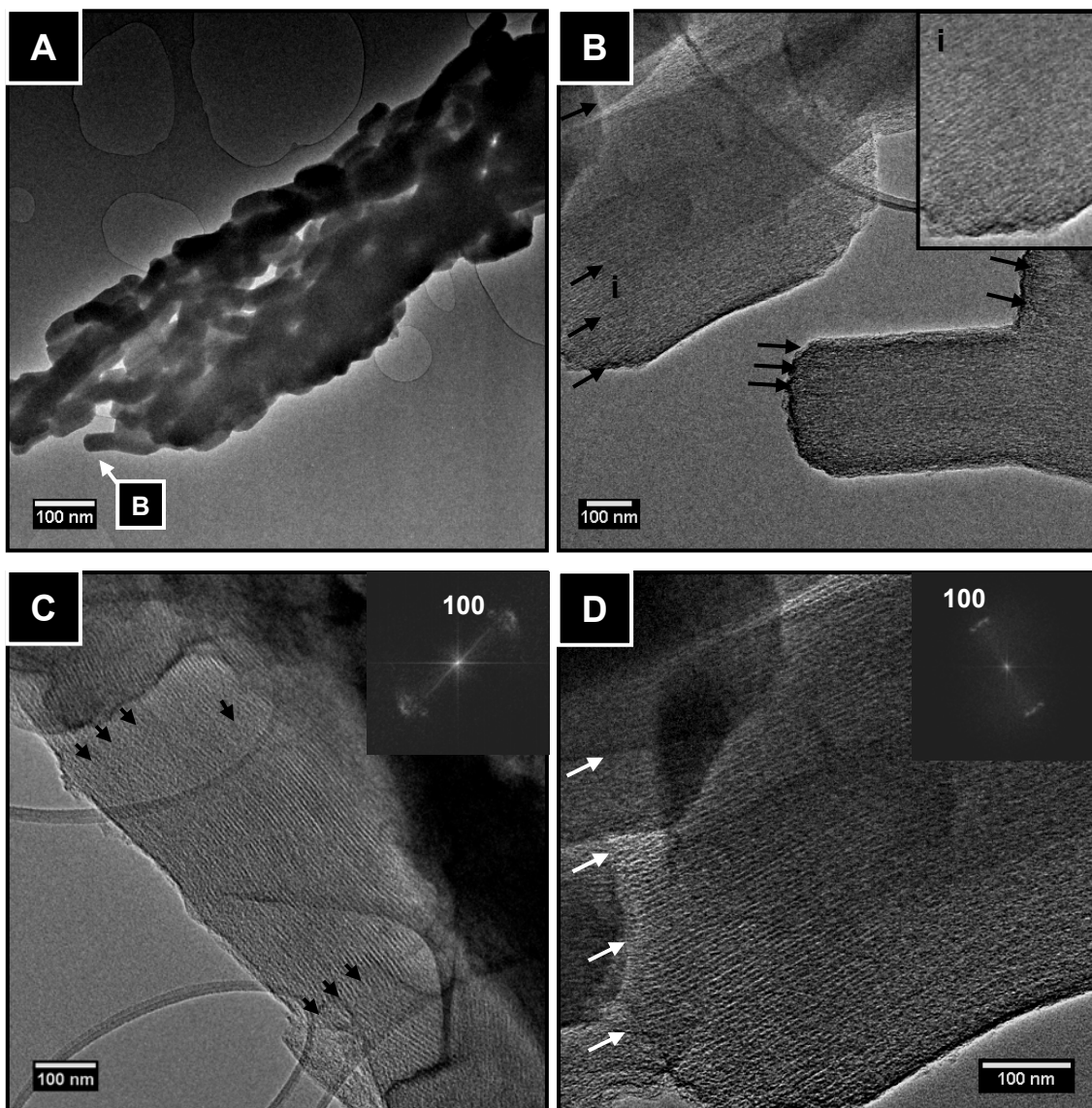


Figure 8.3.2: TEM images of C-S-I: [A] TEM image showing a typical cluster of CMK-3 particles; [B] TEM image of particles from image, with inset enlargement showing mesopores, from cluster [A]; [C,D] HRTEM images showing mesoporous particles viewed along the [100] zone axes showing pores with inset DDPs which were taken of the visible mesoporous regions. Arrows indicate the directions of mesopores.

8.3.2 Mesoporous Carbon Using VI

8.3.2.1 Mesoporous Carbon Using Concentrated Precursor Solution

From physisorption results, the specific surface area and pore volume of C₁-S-V₂ were determined to be 554.5 m²g⁻¹ and 0.27 cm³g⁻¹, respectively. The adsorption-desorption isotherm was Type II with almost no hysteresis. At high P/P₀ values there was further adsorption, likely to have been caused by interparticle porosity. The shape of the isotherm is typical of carbons with micro- and mesopores (Figure 8.3.3). The pore-size distribution showed no well defined peaks, except at approximately 3.5 nm on the desorption branch which was likely caused by the forced closure of the hysteresis loop by the TSE.

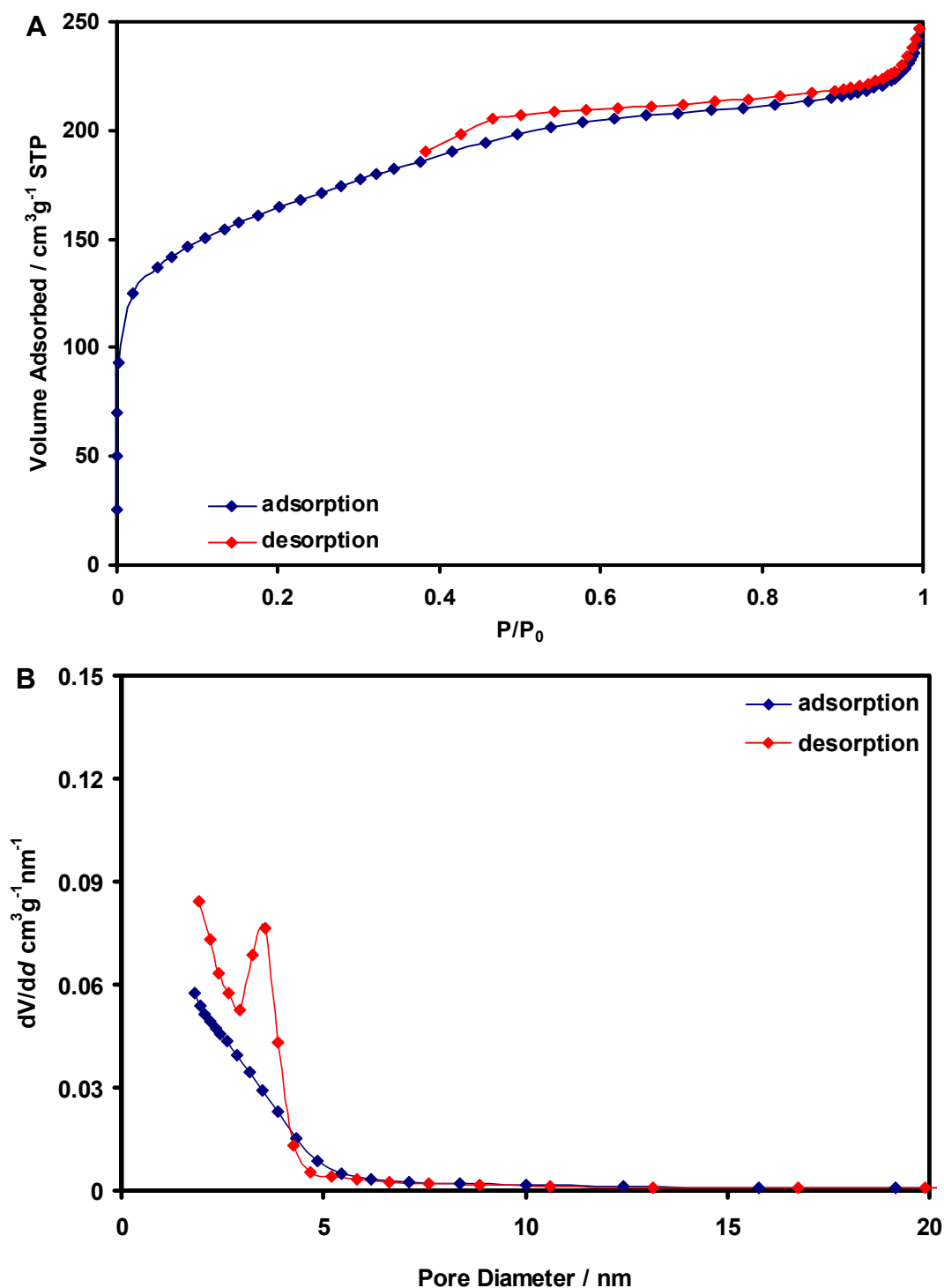


Figure 8.3.3: [A] Physisorption isotherm and [B] pore size distribution for C-S-V₂.

TEM images of C₁-S-V₂ showed large particles (>1 μm across) comprised of pores with a high aspect ratio similar to the C-S-I sample prepared using the IWIT (Section 8.2.1). Both the longitudinal [100] and hexagonally arranged [001] pore orientations were clearly visible in the TEM images (Figure 8.3.4). In Figure 8.3.4A multiple pore orientations were visible, likely to have been caused by multiple overlapping particles. The curving parallel pore structure could be seen in at least two particles. Pore spacings from the (100) reflections in

the inset DDP was measured to be 7.4-8.4 nm. Figure 8.3.4B shows an image in which the [001] zone axis of a C_1 -S- V_2 particle can be seen. The particle had approximately hexagonal morphology in cross-section and contained hexagonally arranged pores. The TEM resolution was insufficient to determine the pore shape from this image. The pore spacings, measured from the ($\bar{1}010$) reflections on the inset DDP, were 7.4-8.3 nm. Figure 8.3.4C shows another C_1 -S- V_1 particle viewed down the [001] zone axis. Here the regular hexagonally faceted particle, similar in shape to that observed in SBA-15 (Figure 5.3.4D), is seen. The pore spacings measured from the ($\bar{1}010$) spots in the DDP were 7.9-8.5 nm.

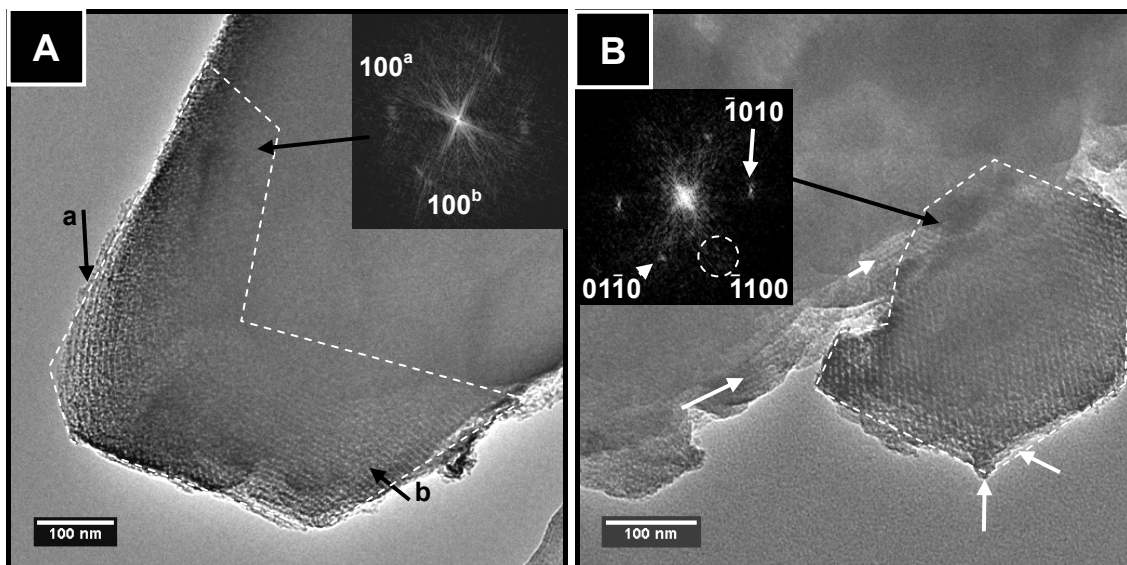


Figure 8.3.4: TEM images of C_1 -S- V_2 : [A] TEM image of multiple particles showing mesopores viewed down the [100] zone axis with inset DDP of the mesoporous regions; [B,C] TEM images of mesoporous particles viewed down the [001] zone axis with inset DDPs of the mesoporous regions as indicated. Arrows indicate the directions of mesopores.

8.3.2.2 Mesoporous Carbon Using Dilute Precursor Solution

The TEM images of C_2 -S- V_2 in Figure 8.3.5 show a large number of ordered mesoporous particles. Figure 8.3.5A shows an agglomeration of particles in which at least four particles have mesopores with the [100] zone axis aligned to the electron beam. The electron beam did not penetrate the thicker parts of the sample. The pores appeared to be parallel with a high aspect ratio and are curved along the length of their pores while maintaining their pore width. Figure 8.3.5B shows two adjacent mesoporous particles. The upper particle in the TEM image is aligned along the [100] zone axis of the pore structure with a pore spacing of 8.0-8.6 nm measured from the corresponding DDP. The pore structure in the lower particle is aligned along the [110] zone axis with a pore spacing of 4.8-5.2 nm measured from the corresponding DDP. The ratio for these two pore spacings of 1.66:1 was in good agreement

with the values of 1.71:1 for the SAXS pattern of SBA-15 (Figure 5.3.2) and 1.73:1 which was the theoretical value.

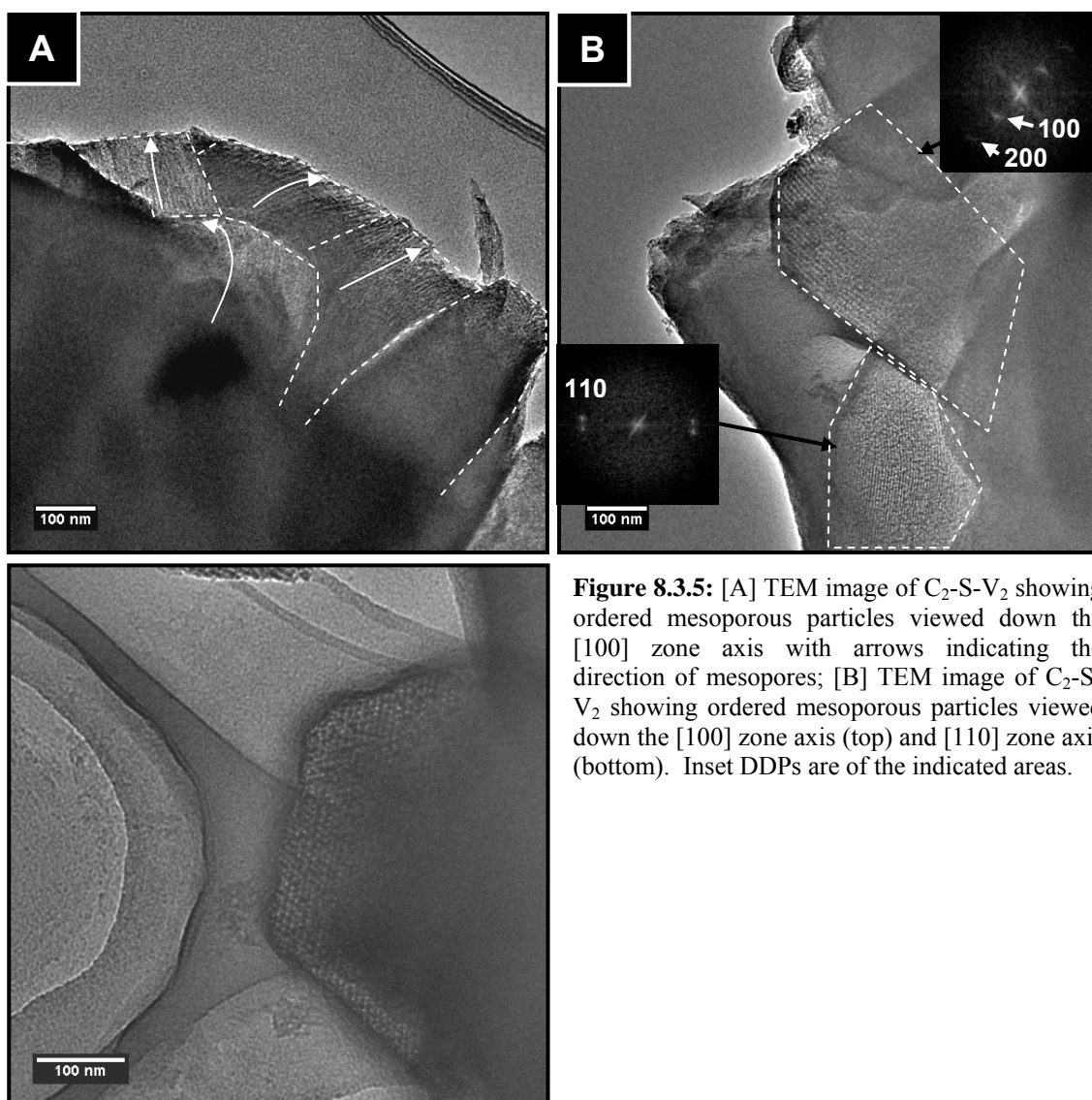


Figure 8.3.5: [A] TEM image of C₂-S-V₂ showing ordered mesoporous particles viewed down the [100] zone axis with arrows indicating the direction of mesopores; [B] TEM image of C₂-S-V₂ showing ordered mesoporous particles viewed down the [100] zone axis (top) and [110] zone axis (bottom). Inset DDPs are of the indicated areas.

Figure 8.3.6A shows a TEM image of the edge of a mesoporous particle. Mesopores can be seen throughout the image. It can be seen that the walls of the nanorods are rough, especially at the tips of the nanorods. The HRTEM image of the tips of the nanorods (Figure 8.3.6B) shows that the pore walls were comprised of sheets of 2-3 layers of carbon that were bound together in a twisted network. These appeared to bundle together to form the pore walls. Typically, layers did not extend beyond 2-3 nm. The pore walls often terminated with the exposed edge of these layers protruding rather than preferentially terminating at a crystal face. Figures 8.3.6C and D show another image series in which the nanorods exhibit a small number of graphitic nanoregions as indicated. In general though, this material is essentially amorphous.

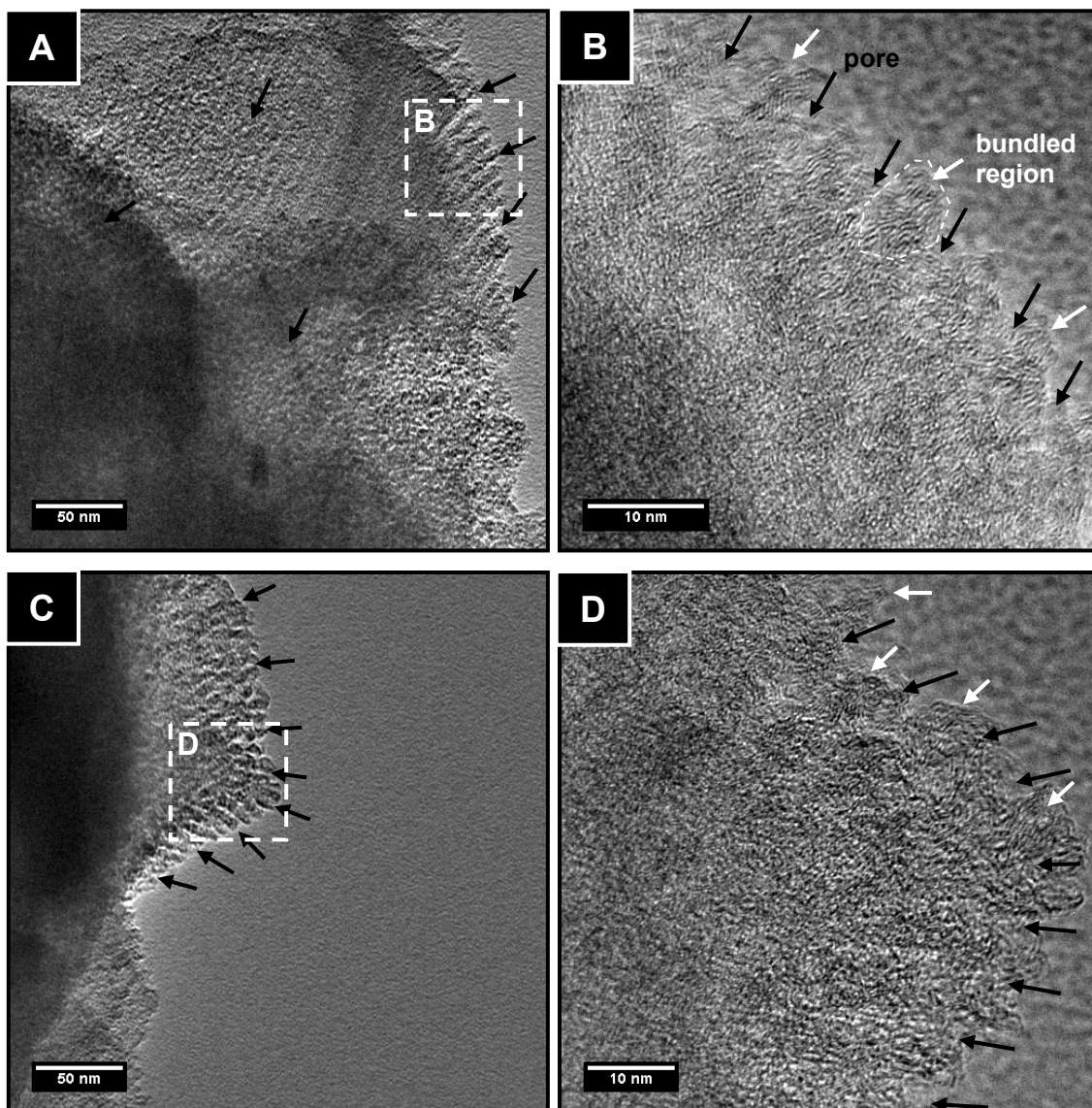


Figure 8.3.6: [A] TEM image of a mesoporous CMK-3 particle; [B] HRTEM image of [A] showing some graphitic nanoregions of the nanorods; [C] TEM image of the edge of a particle; [D] HRTEM image of [C] showing some graphitic nanoregions of the nanorods. Direction of mesopores is indicated with black arrows and some graphitic nanoregions are indicated with white arrows.

8.4 Discussion

8.4.1 Product Characterisation

The results for the IWIT synthesis of SBA-15 to produce C-S-I were consistent with literature reports for CMK-3 suggesting that this reference material was representative of the conventional method used for the synthesis of ordered mesoporous carbon.

The specific surface area and pore volume for C₁-S-V₂ were not as high as for C-S-I, as shown in Table 8.1. The theoretical yield for VI (C_x-S-V₂) would be expected to be higher than the theoretical yield using the IWIT (C-S-I). When synthesising mesoporous carbon the density of the product must be taken into account. C-S-I was impregnated twice. Therefore

the volume lost during carbonisation was partially replaced by more carbonaceous material during the second impregnation. VI-synthesised mesoporous carbon may have a lower final density, as it was only impregnated once. Therefore, a material produced using the VI method in comparable yield to the IWIT method may have a higher specific surface area and pore volume. It is uncertain at this stage whether or not this will be beneficial to the final product. It would produce a lighter material that may have less mechanical strength. Further study is required to investigate this fully.

Table 8.1: Comparison of the physisorption results of mesoporous carbons prepared in Chapter 8.

Sample	Specific Surface Area (m^2g^{-1})	Pore Volume (cm^3g^{-1})
C-S-I	1248.1	1.02
C ₁ -S-V ₂	554.5	0.27
C ₂ -S-V ₂		
Theoretical*		1.54

* The calculation of the theoretical yield for mesoporous carbon templated from SBA-15 is located in Appendix 1.

The shape of the physisorption isotherm for C₁-S-V₂ was consistent with mesoporous carbons and with the physisorption isotherm for C-S-I. The most significant difference between the two isotherms was the uptake of less adsorbate by C₁-S-V₂. The only peak discernible in the pore size distribution correlated to the same peak at 3.4-3.5 nm for C-S-I. This was consistent with the diameter of the mesopores observed for ceria and CGO (3 nm). Jun *et al.* reported 4.5 nm pores for mesoporous carbon and attributed the difference between the expected pore spacing and the observed pore spacing to the shrinkage of the lattice during calcination.⁹⁰

The pore spacings obtained in the TEM investigation were consistent with this observation. C-S-I had the lowest pore spacing and had been calcined twice. C₁-S-V₂ and C₂-S-V₂ both had larger average pore spacings. The difference in the materials represented a significant difference (Table 8.2) but the variation in the results was large.

Table 8.2: Comparison of the pore spacings of mesoporous carbon materials synthesised in this chapter. Pore spacings are derived from TEM images.

Sample	Pore Spacing (nm)
C-S-I	6.4-8.1
C ₁ -S-V ₂	7.4-8.5
C ₂ -S-V ₂	8.0-8.6
SBA-15	7.5-8.6
Ceria-S-V ₂	8.9-9.7

There would be several factors limiting the inclusion of carbonaceous material in the silica template compared to the ceria-based materials. The carbonaceous precursor did not go through a liquid intermediate phase during calcination as it had already been catalytically carbonised by the sulfuric acid. As carbon melts at approximately 4500 °C, it would be expected to be much less mobile than ceria. The implications of this mechanism are twofold. Firstly, less material inside the pores allows for shrinkage of the mesoporous lattice of the carbon-silica composite during calcination. This would cause the pore spacings to decrease in the final product. Secondly, as additional carbon is not drawn into the pores there is unoccupied pore volume. At this high calcination temperature, the silica structure would tend to shrink to occupy this unoccupied volume. This mechanism may explain the decreased pore spacings and increased pore sizes in the mesoporous carbon products with respect to the ceria-based materials.

HRTEM images also showed that the microstructure of the material contained small graphitic nanoregions within an essentially amorphous structure. An experimental objective was to produce a mesoporous carbon with crystalline walls and this was not achieved. The nature of the carbon - amorphous or graphitic - is of interest for applications where electronic conductivity is important. Graphitic structures would have higher electronic conductivities than amorphous or mixed phases. Future work would be required to examine how the phase of the carbon might be controlled by different preparative variables.

There are many parameters yet to experiment with to improve yields, and there was insufficient time for physisorption measurements to be taken for C₂-S-V₂. The TEM investigation suggested C₂-S-V₂ was superior in quality to C₁-S-V₂. This suggested that changing the precursor concentration had a large effect on the final product. Adjusting factors in the carbonisation process could also have contributed to the improved yield. Adding sulfuric acid drop-wise to the precursor solution immediately prior to impregnation meant that

after the carbonisation, but before calcination, the sample became brown, not black as in previous samples. The different colour of the material after carbonisation had been observed previously in the literature.⁹⁰ Therefore, precursor concentration and the carbonisation process should be investigated first with a view to improving the yield of mesoporous carbon.

8.4.2 Implications for the Vacuum Impregnation Method

Results for C₁-S-V₂ and C₂-S-V₂ suggested that VI is transferable to the synthesis of materials other than mesoporous oxides. There were many differences in the chemistry between the syntheses of CMK-3 materials and ordered mesoporous ceria. Firstly, the solute used in the precursor solution for carbon-based materials was a polar organic molecule rather than an inorganic ionic salt. The different solutes interacted with the template via ionic bonding in the synthesis of mesoporous ceria and by dipole-dipole and hydrogen bonding in the case of mesoporous carbon. Secondly, water was used as the solvent in the synthesis of CMK-3 whereas ethanol was used in the synthesis of mesoporous ceria. As water has been used in the conventional synthesis and was shown to be successful for C-S-I, surface wetting of silica with water appears to be efficient. As water has a higher polarity than ethanol, and has a low cost, it is a valuable solvent to be able to utilise in impregnation syntheses for precursor solids requiring a more polar solvent. Finally, mesoporous carbon was formed by catalytic carbonisation and reduction rather than decomposition, as in the case of ceria. This shows that there is scope for the movement of additional reactants within the mesoporous matrix after impregnation. This could allow for more complicated chemistry during the impregnation process, for example, ion exchange, redox reactions or electrolysis of reactants inside the mesoporous matrix.

8.4.3 Modifications to the Vacuum Impregnation Method

The molten VI experiment was designed to increase the density of solid in the nanorods. The experiments conducted showed that sucrose decomposed below its melting temperature and therefore other carbonaceous materials need to be investigated to examine whether or not this method is viable for the synthesis of ordered mesoporous carbon.

8.5 Summary

An initial investigation into the application of VI for the synthesis of mesoporous carbon showed that this method could be a viable pathway for the production of mesoporous carbon in high yields. It could also potentially remove time consuming steps from the conventional procedure. The results presented here showed promising product yields. Further investigation is required to optimise the experimental conditions in order to determine whether product

yields equivalent to those reported using the IWIT can be achieved. Some possible improvements to the method were discussed in Section 8.4.

The experiments conducted in this chapter showed that VI may be applicable to the syntheses of a range of materials using a range of synthetic conditions, rather than being restricted to the fabrication of mesoporous oxides.

Chapter 9

Other Mesoporous Materials

9.1 Experimental Philosophy

Ordered mesoporous materials other than carbon and ceria-based compositions of interest for SOFC electrode applications include YSZ and the perovskite materials based on the $\text{La}_x\text{Sr}_{1-x}\text{M}_y\text{O}_{3-\delta}$ system (where $\text{M} = \text{Ga}, \text{Cr}, \text{Mn}$ or Co). To determine whether the VI method could be employed to synthesise more complex mixed oxides than the ceria and CGO systems, it was decided to apply it to these materials in the first instance. YSZ and LSG were the materials whose syntheses were attempted first because of their attractive electrical properties. In this investigation, the syntheses of Cr- and Mn-based perovskites were not attempted as a brief literature examination suggested that the simple salts such as nitrates, hydroxides and halides were unsuitable for VI without further processing because their boiling or sublimation temperatures were lower than their temperature of decomposition to the oxides. A more in-depth examination, however, may identify suitable candidates for nanocasting these materials.

9.2 Experimental

9.2.1 *Lanthanum Strontium Gallate*

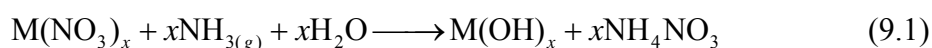
The water content of $\text{Ga}(\text{NO}_3)_3 \cdot x\text{H}_2\text{O}$ was determined to be 27.3 % w/w using thermogravimetric analysis. According to the literature, $\text{Ga}(\text{NO}_3)_3 \cdot x\text{H}_2\text{O}$ and $\text{Sr}(\text{NO}_3)_2$ were insoluble in ethanol and therefore water was used as the solvent.¹⁶⁸ The solubility of $\text{Sr}(\text{NO}_3)_2$ in water was lower than the other salts meaning that a less viscous solution was used compared to the solutions used in Chapter 7 to prevent $\text{Sr}(\text{NO}_3)_2$ crystals from forming. Heating the solution greatly increased the solubility of the $\text{M}(\text{NO}_3)_x$ salts (where $\text{M} = \text{La}, \text{Sr}$ or Ga).

LSG-X-X (a bulk material to examine the phase purity of LSG prepared by the sol-gel method), was made by preparing a solution comprising $\text{M}(\text{NO}_3)_x$ salts, where $\text{M} = \text{La}, \text{Sr}$ or

Ga, with a molar ratio of 0.85:0.15:1, respectively, with sufficient water to completely dissolve all of the solid. Once all of the solid had completely dissolved, the mixture was left stirring overnight to homogenise the solution. The solvent was removed by drying in an oven at 105 °C in air. The resulting solid was calcined at 1200 °C for 2 h (ramp rate 2 °C min⁻¹) in air.

LSG-C-V₂ was made by using the same solution as above in conjunction with the VI method for the impregnation of CMK-3. This CMK-3 itself had been prepared by the VI of SBA-15. Although its quality was rather poor (sample C₁-S-V₂) this LSG experiment was conducted in the hope of presenting a material that was the result of a double VI: VI to synthesise the C₁-S-V₂ followed by VI to synthesise the oxide. It was also conducted prior to the development of superior carbon structures by VI (for example, sample C₂-S-V₂). The impregnation itself was conducted as described in Section 7.2. Because mixed phases were observed in LSG-X-X, a different thermal treatment was used in this procedure. The sample was dried at 60 °C for 48 h and then calcined at 1200 °C for 10 h (ramp rate 2 °C min⁻¹) in a N₂ atmosphere. The C₁-S-V₂ template was removed during heating at 420-430 °C in air using a muffle furnace over a period of 12 h.

LSG-C-V₂/NH₃ was prepared using a new batch of solution to ensure that its composition was correct. The molar ratio was kept the same as above. The resulting solution was stirred overnight to homogenise. The solution underwent VI into C₁-S-V₂ followed by drying overnight at 105 °C in air using an oven. Following drying, an in-situ alkaline treatment was conducted to convert the nitrate salts to hydroxide salts. The purpose of this step was to alter the melting and boiling points of any volatile solids. This was conducted by placing the sample in a TP reactor with one end attached to a bubbler containing 30 % ammonium hydroxide solution, through which argon was passed, and the other end open to vent. The assumed reaction inside the mesoporous template is shown in Equation 9.1.



The experimental setup is schematically represented in Figure 9.2.1.

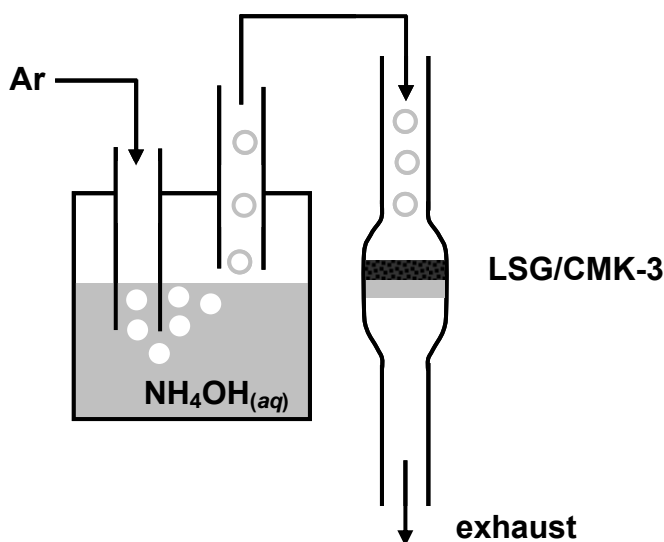


Figure 9.2.1: Schematic setup of the in-situ chemical modification of material inside a mesoporous template.

Visual inspection of the reactor and sample confirmed that the vapour was moist. This was important as it ensured that it was not simply $\text{NH}_{3(g)}$ being passed over the sample because water was required for the reaction. When removing the sample from the reactor it was obvious from the odour that significant amounts of ammonia had been transferred. For safety auditing it was confirmed that harsh thermal and mechanical treatment of the resultant material did not result in any problems with the by-product, NH_4NO_3 , a class 5 explosive (according to the University of St Andrews Chemical Hazard Database). The sample was then calcined at 1000 °C for 6 h (ramp rate 5 °C min⁻¹) in an Ar atmosphere. The C₁-S-V₂ template was removed during heating at 420-430 °C in air using a muffle furnace over a period of 12 h, as above.

9.2.2 Lanthanum Strontium Cobaltite

The material, LSC₁-C-V₂, was made by preparing a solution comprised of $\text{M}(\text{NO}_3)_2$ salts, where M = La, Sr or Co, with a molar ratio of 0.76:0.19:1, respectively, with sufficient water to completely dissolve all of the solid. Once all of the solid had been completely dissolved the mixture was left stirring overnight to homogenise the solution. VI was used to impregnate C₁-S-V₂ with the solution as in Section 9.2.1. The sample was dried at 80 °C overnight and then calcined at 1100 °C for 5 h (ramp rate 5 °C min⁻¹) in an Ar atmosphere. When removed from the furnace the sample was metallic grey, the alumina crucible which had contained it had turned blue (especially around the sample particles) and a significant portion of the furnace tube had also turned blue. Sample had been ejected from the alumina boat into the surrounding furnace tube.

LSC₂-C-V₂ was made by preparing three individual solutions of La(NO₃)_{3(aq)}, Sr(NO₃)_{2(aq)}, and Co(NO₃)_{3(aq)}, each at their saturation points at laboratory conditions. Once these solutions had been stirred overnight to homogenise, appropriate aliquots were taken to produce a solution of (La,Sr,Co)(NO₃)_x with the La:Sr:Co ratio of 0.76:0.19:1, respectively. This solution was stirred for 24 h to homogenise, then used to impregnate C₁-S-V₁ as above. This resulted in the further contamination of the furnace equipment.

Early experiments suggested that (La,Sr,Co)Cit_x could be synthesised easily by mixing a homogenised solution of nitrates with citric acid, using the method described in Section 6.2.1. At moderate temperatures - 30-60 °C in air - (La,Sr,Co)Cit_x melted to form a viscous gel and therefore could be a candidate for the molten VI experiment. The citrate complex was insoluble in all solvents tested (water, ethanol, acetone, ethanol/acetone, hexane, hexane/ethanol, isopropanol) except for acidic solution. The solubility in 2 M HCl was further investigated and it was found that at 50 °C the solubility increased dramatically. Increasing HCl concentration caused the solution to turn blue. This was attributed to the formation of CoCl_{3(aq)}. CoCl₃ boils and does not form an oxide. Using H₂SO₄ the solution remained red (Co₂(SO₄)₃ is blue) even at high concentrations. Therefore (La,Sr,Co)Cit_x could be a potential precursor solution candidate for VI experiments if H₂SO₄ is used.

9.2.3 *Yttria Stabilised Zirconia*

The product, YSZ-F-V₁, was made by preparing a solution comprised of ZrOCl₂.8H₂O and Y(NO₃)₃.6H₂O in a molar ratio of 0.92:0.08, with sufficient water to completely dissolve all of the solid. The target composition was partially stabilised zirconia. The solution was typically maintained at approximately 60 °C to increase the solubility of the Y(NO₃)₃. Once all of the solid had been completely dissolved, the mixture was left stirring overnight to homogenise the solution. VI was used to impregnate 15 cm³ of precursor solution into 2.05 g of FDU-12, as described in Section 7.2. As this product was prepared by a preliminary VI experiment, with the following amendments, it is denoted 'V₁'. After the sample had been impregnated, excess solution was gravity filtered rather than decanted. This was performed using a Buchner funnel and filter paper without suction. After drying at 100 °C overnight in an oven, the entire sample was milled for 20 min at 200 rpm in a planetary ball mill using zirconia milling balls (7 milling balls giving approximately 21 g of zirconia balls). The sample was calcined at 400 °C for 6 h (ramp rate 1 °C min⁻¹) in air. This was followed by a second impregnation under vacuum using 15 cm³ precursor solution. Excess solution was removed, as before, by gravity filtration. The sample was dried at 100 °C overnight and then ball milled as above. The sample was calcined at 400 and 600 °C for 6 h at each temperature

(ramp rate $1\text{ }^{\circ}\text{C min}^{-1}$) in air. The silica template was digested by stirring with approximately 20 cm^3 2 M NaOH . Buchner filtration was used to recover the sample from the solution. The sample was sucked dry. This step was repeated three times. The final product was washed with water and air dried.

YSZ-K- V_1 was prepared in an identical manner, substituting the FDU-12 template with KIT-6.

YSZ-S- V_2 was made by preparing a solution comprised of $\text{ZrOCl}_2 \cdot 8\text{H}_2\text{O}$ and $\text{Y}(\text{NO}_3)_3 \cdot 6\text{H}_2\text{O}$ with a molar ratio of 0.84:0.16, with sufficient water to completely dissolve all of the solid. The solution was typically maintained at approximately $60\text{ }^{\circ}\text{C}$ to increase the solubility of the $\text{Y}(\text{NO}_3)_3$. The target composition was cubic zirconia. Once all solid was completely dissolved the mixture was left stirring overnight to homogenise the solution. VI was used to impregnate SBA-15 as described in Section 7.2. The sample was dried at $105\text{ }^{\circ}\text{C}$ overnight and then calcined at 400 and $600\text{ }^{\circ}\text{C}$ for 5 h at each temperature (ramp rate $1\text{ }^{\circ}\text{C min}^{-1}$) in air. The silica template was digested by stirring with 20 cm^3 2 M NaOH at $80\text{ }^{\circ}\text{C}$. Buchner filtration was used to recover the sample from the solution (although there was no specific reason for not using centrifugation). The sample was sucked dry. This step was repeated three times. The final product was washed with water and air dried.

YSZ-C- V_2 was prepared as above except a CMK-3 template was used ($\text{C}_1\text{-S-}V_2$). The sample was calcined at $1200\text{ }^{\circ}\text{C}$ for 1 h (ramp rate $2\text{ }^{\circ}\text{C min}^{-1}$) in a N_2 atmosphere. The $\text{C}_1\text{-S-}V_2$ template was removed at $420\text{-}430\text{ }^{\circ}\text{C}$ in air using a muffle furnace over a period of 12 h .

9.3 Results

The results in this chapter do not represent a complete data set for every sample. This was primarily due to time constraints where the most important data for determining the success of a particular experiment were prioritised. While this has resulted in gaps in the analysis of individual samples it has allowed for the reporting of a wider range of samples for future research to build upon.

9.3.1 Lanthanum Strontium Gallate (LSG)

Figure 9.3.1 shows the high angle powder XRD patterns for LSG-X-X, LSG-C- V_2 and LSG-C- V_2/NH_3 in which it can be seen that all three have mixed phases from the $\text{La}_2\text{O}_3\text{-SrO}_2\text{-Ga}_2\text{O}_3$ system. The XRD pattern of LSG-X-X showed it to be predominantly

perovskite-type orthorhombic LaGaO_3 ($Pbnm$, ICDD 24-1102) with minor phases of La_2O_3 ($Ia3$, ICCD 22-369), $\text{SrLaGa}_3\text{O}_7$ ($P421m$, ICCD 45-637) and SrLaGaO_4 ($I4/mmm$, ICCD 24-1208). Several peaks referenced to a deleted reference pattern, $\text{La}_4\text{Ga}_2\text{O}_9$ (ICDD 37-1433), as indicated. It is possible that the LaGaO_3 phase was Sr-doped as this does not significantly affect the pattern - it only increases the lattice constant - and the change in the lattice spacings are small. In this section, the reference pattern, ICDD 24-1102, will be used to identify this phase as it was not possible to distinguish between two perovskite-type phases with and without Sr. There were also additional minor peaks that could not be attributed to peaks using the ICCD database and searching for phases in the La_2O_3 - SrO_2 - Ga_2O_3 -C system. Compared to the two patterns for LSG-C- V_2 and LSG-C- V_2/NH_3 , the XRD pattern for LSG-X-X had narrower peaks, implying larger crystallites, as would be expected for a non-mesoporous material. By applying the Scherrer equation to the peak broadening, an average particle size of 57.2 nm was calculated.

Powder XRD showed LSG-C- V_2 to be predominantly hexagonal La_2O_3 ($P3m1$, ICCD 5-602) with a minor phase of $\text{SrLaGa}_3\text{O}_7$. There were no peaks in this pattern that were not attributed to these two reference patterns.

Powder XRD showed LSG-C- V_2/NH_3 to be predominantly hexagonal La_2O_3 and orthorhombic LaGaO_3 with the perovskite-type structure (see above regarding possible Sr-doped perovskite phase). $\text{SrLa}(\text{GaO}_4)$ ($I4/mmm$, ICSD 80-1806) and $[\text{SrLa}]\text{Ga}_3\text{O}_7$ ($P-42/m$, ICSD 86-1839) were also identified as minor phases. By applying the Scherrer equation to the peak broadening, an average particle size of 32.8 nm and 22.6 nm were calculated for the La_2O_3 and perovskite-type phases, respectively.

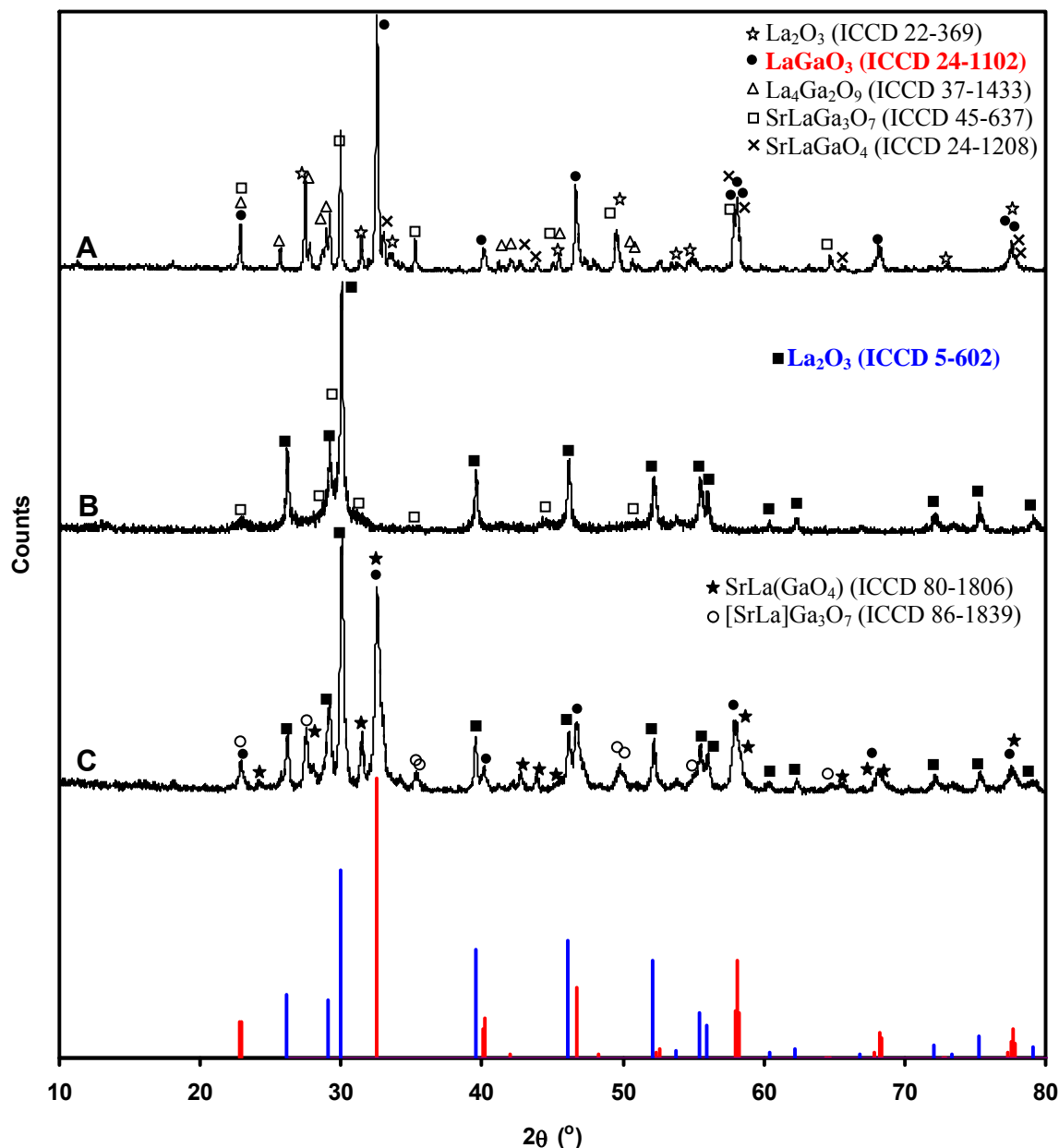


Figure 9.3.1: Powder XRD patterns for [A] LSG-X-X, [B] LSG-C-V₂, and [C] LSG-C-V₂/NH₃. The reference patterns **LaGaO₃** (ICCD 24-1102) and **La₂O₃** (ICCD 5-602) are also plotted for reference.

TEM analysis of LSG₂-C-V₂ showed large particles (>1 μm) that had a similar shape to the CMK-3 template that was used. The image contrast from Figure 9.3.2A showed that the particles were porous throughout their entirety. Figure 9.3.2B shows that the particle imaged is highly porous but that the pores were not aligned. The particle appears to have undergone significant sintering while maintaining some pore structure. Figure 9.3.2C shows a HRTEM image of Figure 9.3.2B showing that the pore walls were comprised of fused nanoparticles with different crystallographic alignments. The pore walls were 6-10 nm wide, the narrowest being in bridged sections. Selected area DDPs are indicated on the TEM image. All of the reflections corresponded to hexagonal La₂O₃ more closely than to any other materials that had been identified in the powder XRD analysis. DDPs (i) and (iv) were not sufficiently aligned,

or contained multiple orientations, so that zone axes could not be attributed. DDPs (ii) and (iii) were attributed to La_2O_3 viewed down the [001] zone axis (DDP (ii) being misaligned).

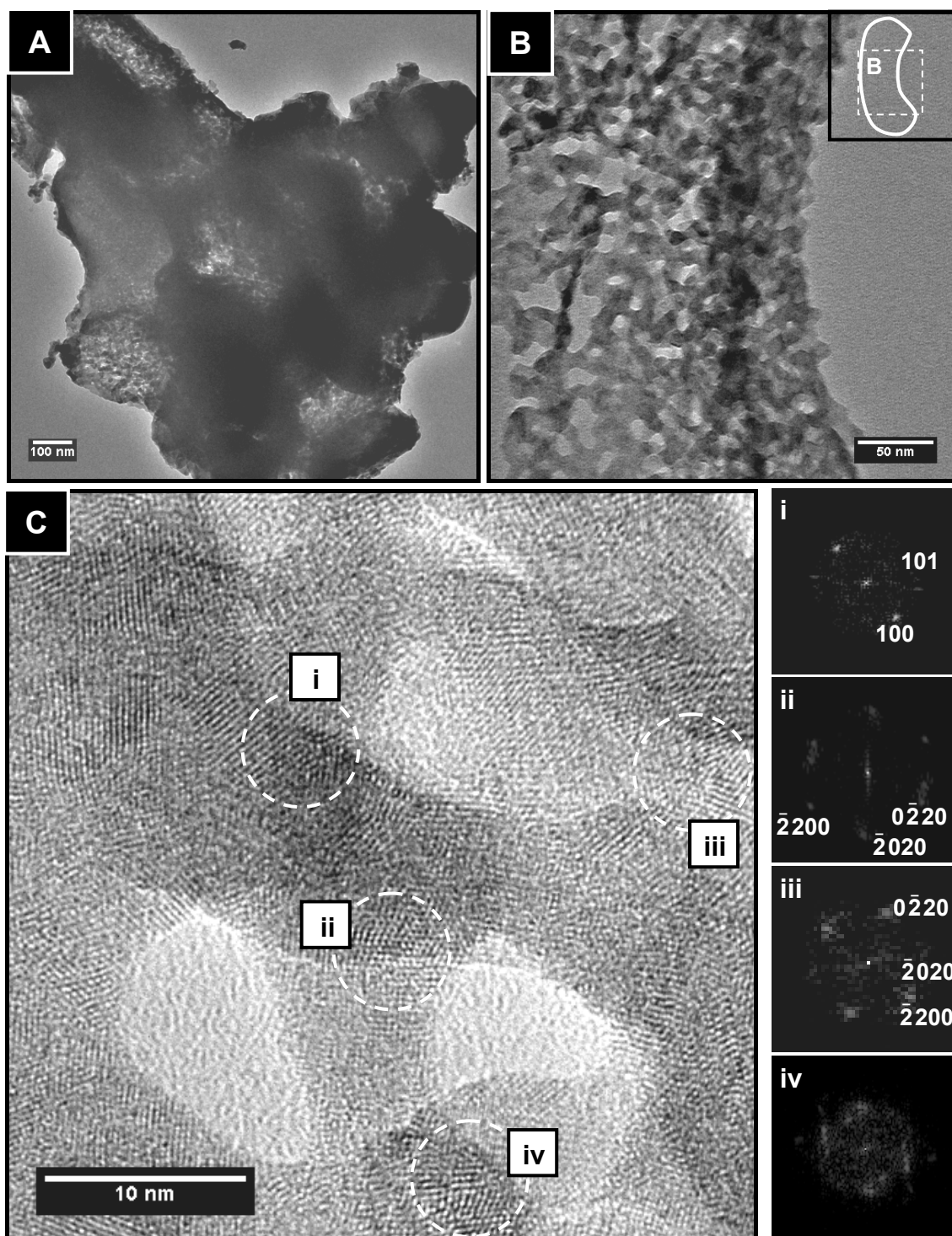


Figure 9.3.2: TEM images of mesoporous LSG: [A] representative image showing particle porosity; [B] image of a highly porous particle with shape of CMK-3 particle where it can be seen that the pores are not ordered, but maintain a similar morphology to the template; [C] HRTEM image of [B] showing the crystal structure of the pore walls, with selected area DDPs at right. All DDPs are assigned to the La_2O_3 structure.

9.3.2 Lanthanum Strontium Cobaltite

Observations from the calcination of LSC-C-V₂ determined that one of the precursor salts, likely to be $\text{Co}(\text{NO}_3)_3$, was volatile. The alumina boat had almost entirely turned blue, as had

a significant portion of the furnace tube, indicating cobalt oxide contamination. The resulting sample was dark grey. The nature of the contamination could be described as explosive in that material had been distributed over an area exceeding the size of the alumina boat, suggesting that the decomposition had not been gradual.

Attempts to determine whether the solution was inhomogeneous were terminated prematurely due to the furnace being further contaminated with cobalt oxide. At this point experiments were terminated until such time that either this problem could be resolved, or specialist furnace equipment could be dedicated to the synthesis of LSC.

Samples from both LSC₁-C-V₂ and LSC₂-C-V₂ were subjected to powder XRD study. Figure 9.3.3 shows that both samples had mixed phases as with LSG. LSC-C-V₂ had significant amounts of LSC present (ICDD 28-1224 and 46-706). In both samples there was an unidentified predominant phase (being common to both of the samples) as indicated. Study of various La₂O₃-SrO₂-Co₂O₃ phases suggested that this may be a SrLaCoO₄-based phase with a decreased unit cell as several ICDD reference patterns matched the pattern of peaks closely. There was a small shift in peak positions assigned to this phase between the LSC₁-C-V₂ and LSC₂-C-V₂ samples (approximately 0.15° at 30.7°, the most intense peak).

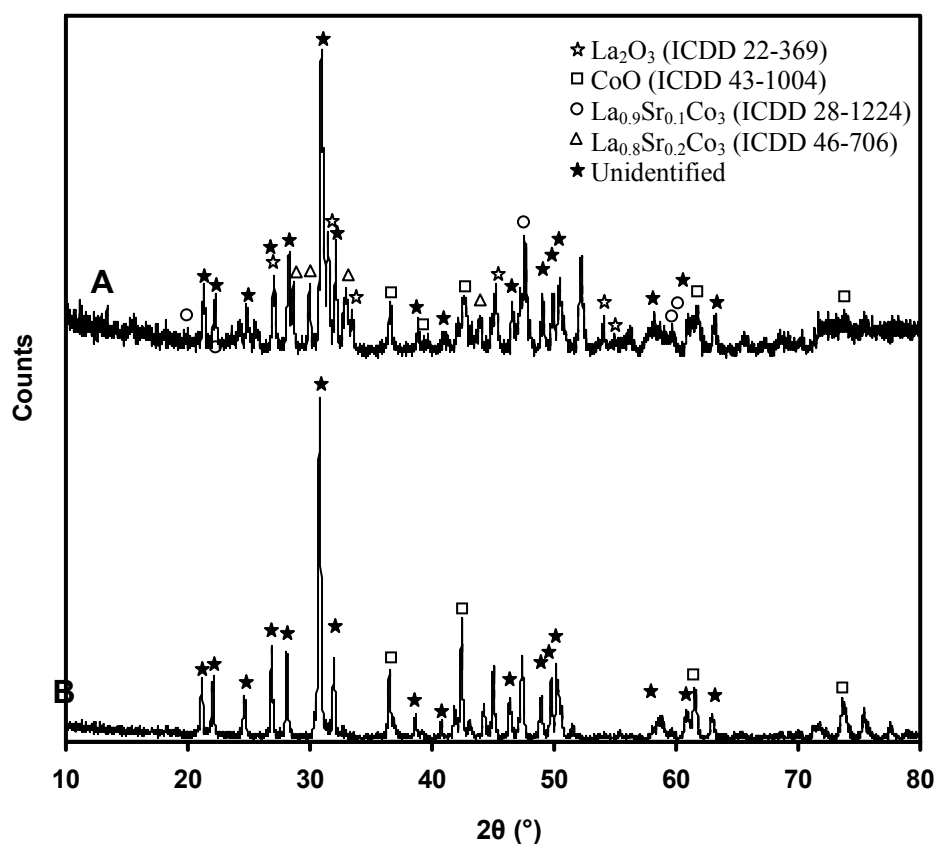


Figure 9.3.3: Powder XRD patterns for [A] LSC₁-C-V₂ and [B] LSC-C-V₂/NH₃.

9.3.3 Yttria-Stabilised Zirconia

9.3.3.1 Partially Stabilised Zirconia

From physisorption results, the specific surface area and pore volume for YSZ-F-V₁ were determined to be 38.75 m²g⁻¹ and 0.063 cm³g⁻¹, respectively. Subsequent examination of the FDU-12 batch used for this experiment suggested it was of insufficient quality for nanocasting (20 % lower specific surface area and pore volume than other FDU-12 batches and disordered pores observed in a TEM investigation).

From physisorption results the specific surface area and pore volume for the partially stabilised zirconia, YSZ-K-V₁, were determined to be 368.0 m²g⁻¹ and 0.29 cm³g⁻¹, respectively. The TEM investigation, however, did not find any ordered porous material and, therefore, this material is not reported in further detail (similar pore volume values had been achieved for Ceria-S-I and Ceria-K-I).

Powder XRD of YSZ-F-V₁ confirmed it was consistent with tetragonal YSZ (*P42/nmc*, ICDD 48-224, Figure 9.3.4A) except for the peak indicated. It is possible that this peak was caused by the presence of some cubic YSZ - it being the {311} cubic YSZ peak. The YSZ-C-V₂ pattern was consistent with the pattern for cubic YSZ (*Fm3m*, ICDD 30-1468, Figure 9.3.4B). This pattern could be distinguished from the tetragonal pattern because of the absence of the {110}, {102}, {200} and {202} peaks from the tetragonal pattern. The cubic phase also had the {311} peak at a 2θ value that was not present in the tetragonal pattern mentioned above. The XRD pattern for YSZ-S-V was also consistent with single phase cubic YSZ with the fluorite structure. Extensive peak broadening was observed indicating that the sample contained nanoparticles. Superimposed upon this was the pattern of a more crystalline phase with sharper peaks.

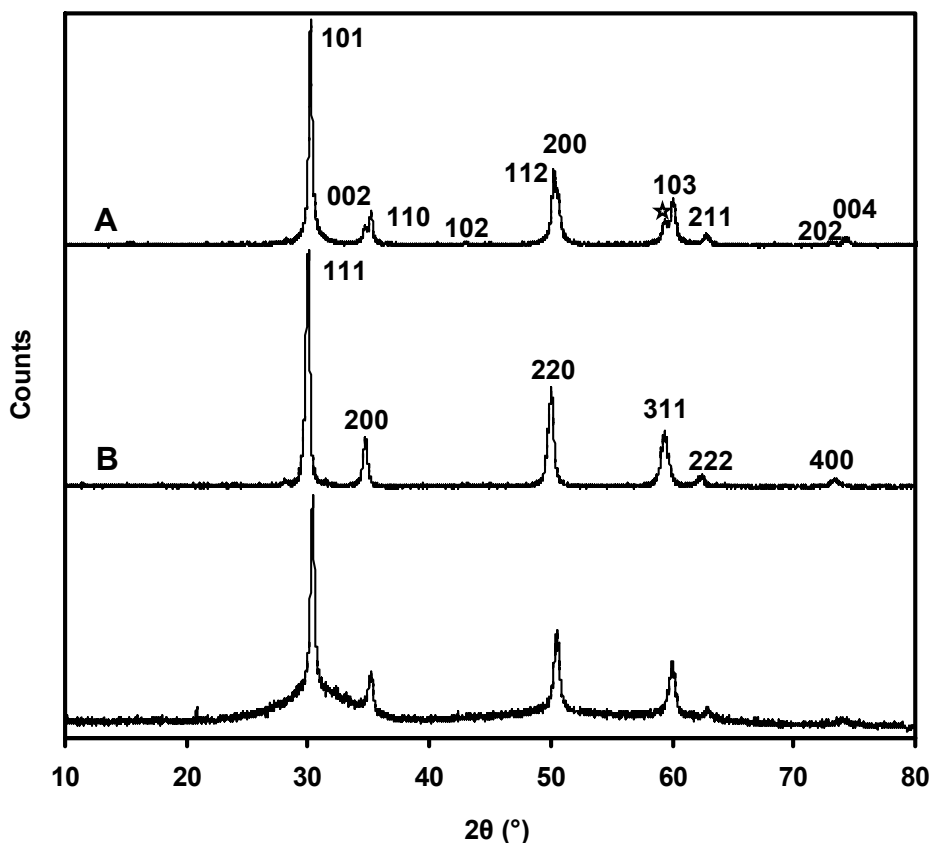


Figure 9.3.4: Powder XRD patterns for [A] YSZ-F-V₁ (mixed cubic and tetragonal YSZ), [B] YSZ-C-V₂ (cubic YSZ), and [C] YSZ-S-V₂ (cubic YSZ).

EDS of YSZ-F-V₁ showed the material to be predominantly Zr (41.5 mol%), O (47.9 mol%) and Y (5.5 mol%). Residual Si (5.1 mol%), presumed to be from the silica template, was also detected throughout the sample.

TEM analysis of YSZ-F-V₁ showed the material to be composed of large (>1 μm) particles with disordered pores. Much of the material was comprised of disordered nanoparticulate material (Figure 9.3.6A). Closer examination revealed regions which contained porous single crystals containing disordered pores (Figures 9.3.5B-D). It can be seen from the variations in image contrast that the pores were not in an ordered array, varied in size (3-10 nm diameter) and were highly faceted. It was not possible to determine whether these pores were created from the template or from contraction of the material during sintering.

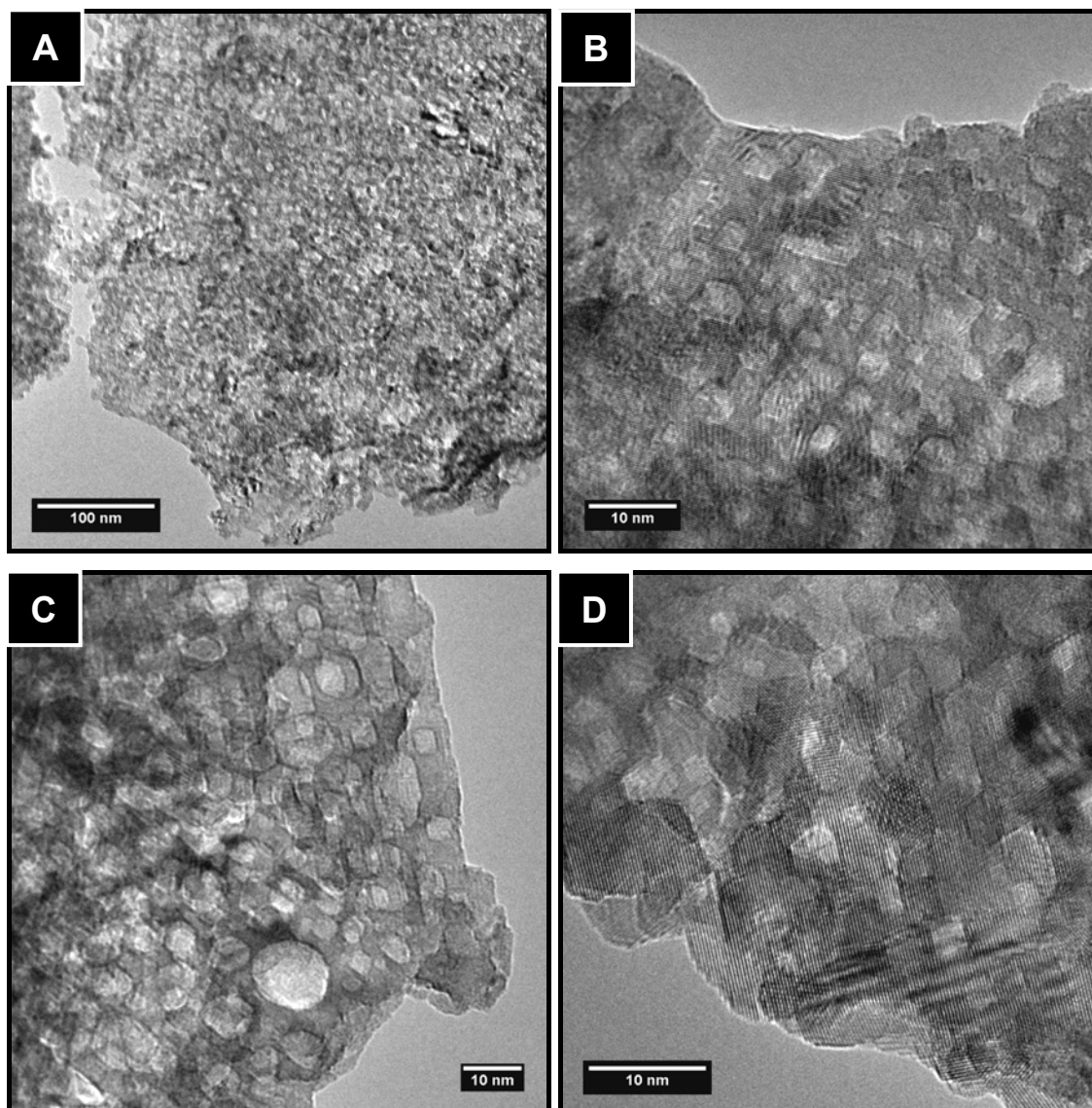


Figure 9.3.5: TEM images of YSZ-F-V₁: [A] representative TEM image showing disordered nanoparticulate material; [B-D] HRTEM images showing porous single crystals with disordered, highly faceted pores

HRTEM images of these crystals (Figures 9.3.6E and F) showed that the crystallographic planes were aligned over a large distance. The inset DDPs show that each TEM image corresponds to a single crystallographic orientation, which could be indexed to tetragonal YSZ.

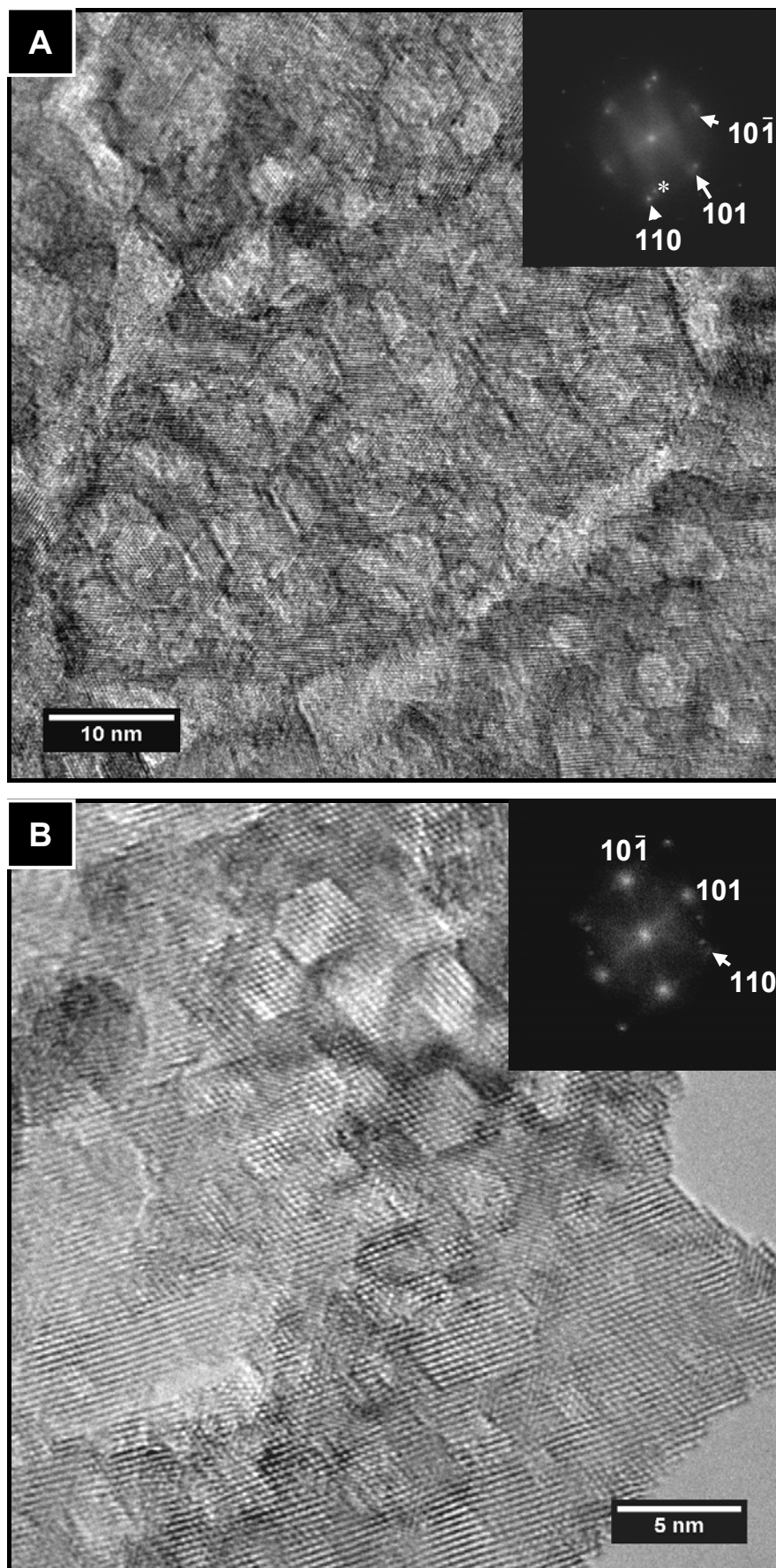
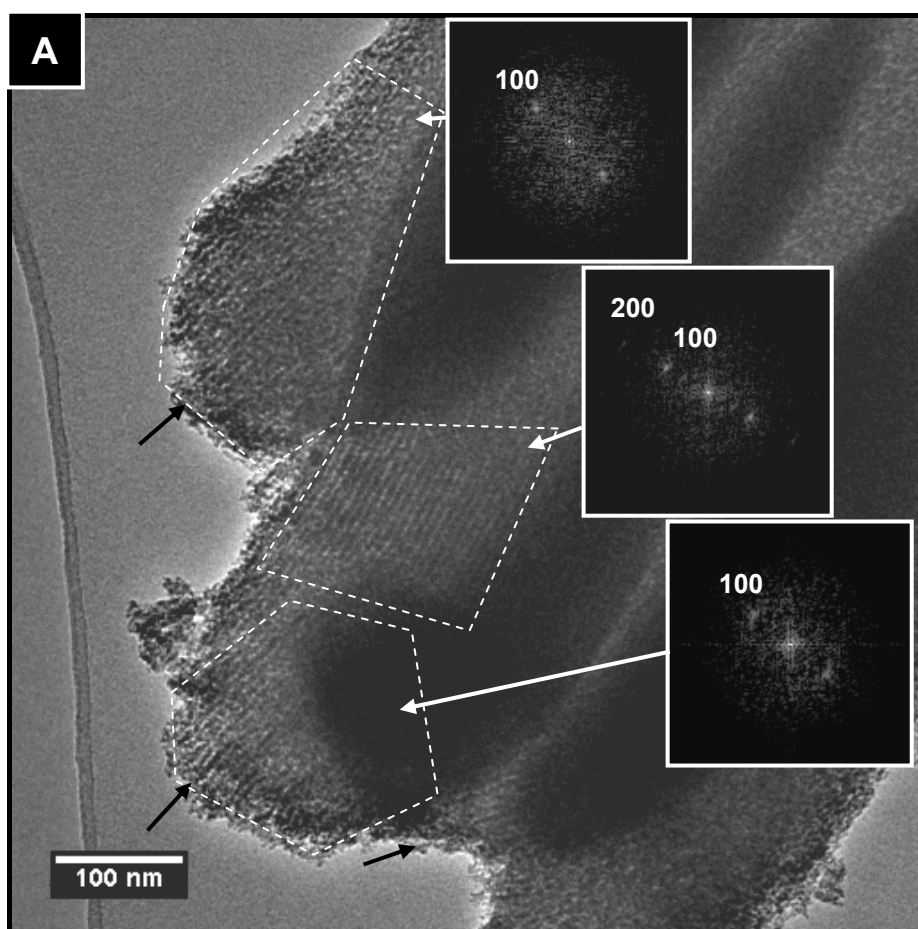


Figure 9.3.6: HRTEM images of YSZ-F-V₁: [A,B] HRTEM images of porous single crystals with disordered pores viewed down the [010] crystallographic zone axis. Inset DDPs are of the entire images. * indicates reflections that do not belong to the indexed pattern.

9.3.3.2 Cubic YSZ

TEM analysis of YSZ-S-V₂ showed the sample to be comprised of large (> 1 μm) particles that were similar in shape to the SBA-15 template. Figure 9.3.7A shows that the particles had the same parallel pore structure as the template. Here, three adjacent particles can be seen with aligned mesopores spanning large distances. The pores bend with the particle while maintaining their pore width. The pore walls also appeared rough. DDPs taken of selected areas (indicated) consistently gave pore spacings of 6.7-7.4 nm. The edges of the particles appeared rough which could be attributed to the presence of nanoparticles on the particle surface. Figure 9.3.7B shows another region of the sample in which ordered mesoporous YSZ was found. The material had the same morphology as described above and the pore spacings from the inset DDP were measured to be 5.8-6.3 nm. Figure 9.3.7C shows a highly curved mesoporous particle with similar morphology to the SBA-15 template. The pore spacing for this particle was measured to be 7.0-7.1 nm. There was a significant amount of nanoparticulate material visible on the surface of the mesoporous particle.



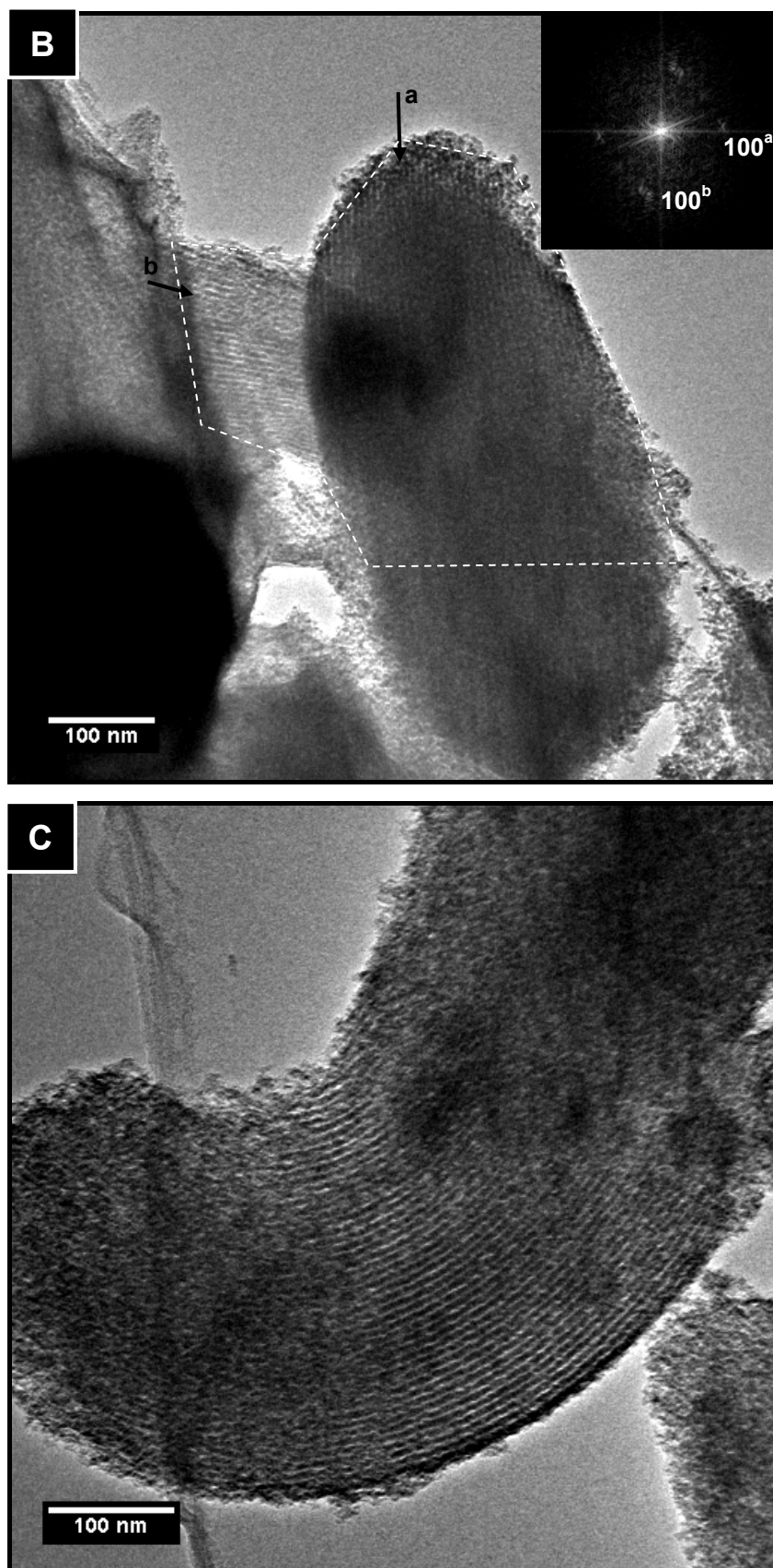


Figure 9.3.7: TEM images of YSZ-S-V₂: [A] TEM image showing multiple large particles with ordered mesopores, similar in morphology to the SBA-15 template with DDPs of selected regions as indicated; [B] TEM image showing two large mesoporous particles with ordered mesopores with inset DDP of indicated region; [C] TEM image of an isolated mesoporous YSZ particle showing curved mesopores. Black arrows in images indicate the directions of mesopores.

The HRTEM image in Figure 9.3.8 showed that the bulk of the pore walls were composed of nanoparticles of size <5nm. Some regions were porous single crystalline. The material was unstable under high electron beam dosage and therefore prolonged study of the crystal structure of these particles was not possible.

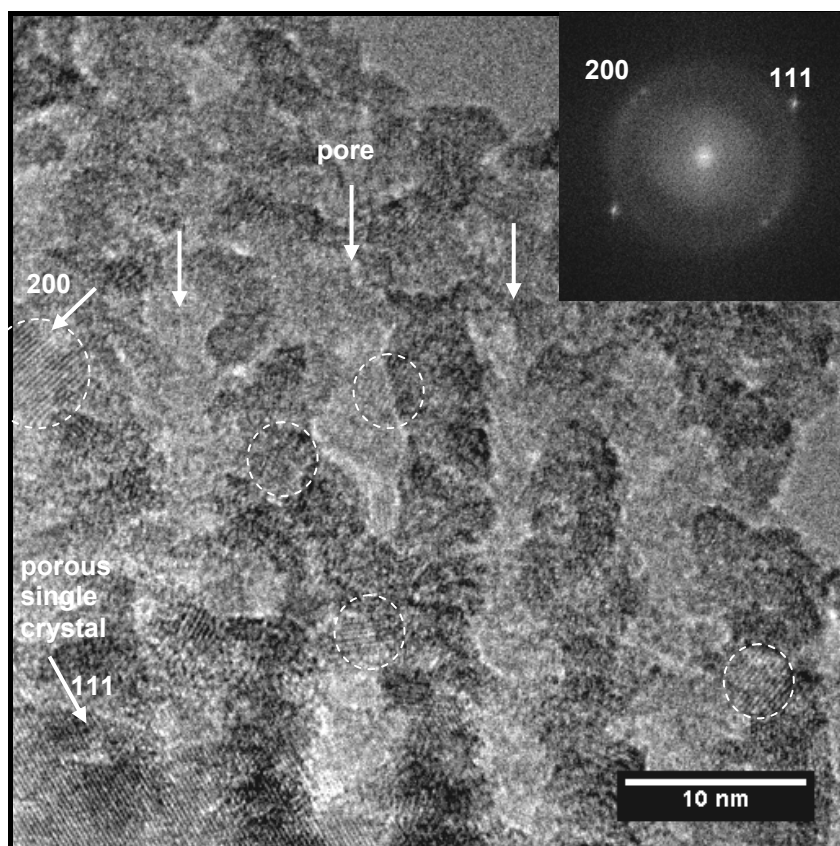


Figure 9.3.8: HRTEM image of YSZ-S-V₂ showing that the nanorods (indicated) are comprised predominantly of nanoparticles (circled) with isolated regions of porous single crystal. The inset DDP is of the entire image.

9.4 Discussion

9.4.1 Ordered Mesoporous Perovskites

Powder XRD results showed that all of the perovskite materials synthesised had phase impurities in them. While this is common for $\text{La}_x\text{Sr}_{1-x}\text{M}_y\text{O}_{3-\delta}$ syntheses, the phase impurities are typically in low concentrations. From the high levels of lanthana present in the LSG-C-V₂ and LSG-C-V₂/NH₃ products it was determined that $\text{Ga}(\text{NO}_3)_3 \cdot x\text{H}_2\text{O}$ (or one of its decomposition products) had volatilised. The orthorhombic LaGaO_3 phase identified was found to be almost identical to the calculated reference pattern for $\text{La}_{0.88}\text{Sr}_{0.12}\text{GaO}_3$ (ICDD 70-8312, *Ibmm*). However, this was a different pattern to a measured single-crystal reference pattern of $\text{La}_{0.88}\text{Sr}_{0.12}\text{Ga}_{2.94}$ (ICDD 53-0412, *Imna*). This could mean that it is possible that the phase observed in the XRD patterns was strontium substituted making LSG-C-V₂/NH₃ a LSG-La₂O₃ blend, deficient in Ga₂O₃. Further work would be required to

identify more stable gallium-containing precursors to increase the product yields. The TEM investigation suggested that the product was porous. However, the pores were disordered. This could be due to the poor quality of the template used (C_1-S-V_1).

The issues raised with LSG precursors also applied to the synthesis of LSC. While the XRD pattern did not show any obvious cobalt deficiencies, the blue contamination of the furnace equipment suggested that cobalt was evaporating from the reaction mixture in large quantities. This suggested that either $Co(NO_3)_3$ passed through a liquid phase that was volatile or that the $Co(NO_3)_3$ crystals themselves were thermally unstable under the reaction conditions. In either case this meant that phase purity was not achieved. An attempt at homogenising the solutions further before impregnation did not improve the results. The experimental observations suggested that the problem was likely to have been caused by the $Co(NO_3)_3$ since this was the only change from the LSG experiment. Therefore, for the further development of this material, other cobalt salts would need to be explored. Preliminary work into metal citrates may have found a complex suitable for the molten VI experiment as $(La,Sr,Co)Cit_x$ was observed to melt below 60 °C. $(La,Sr,Co)Cit_x$ was also found to be soluble in acidic solution, though careful consideration of the complexing anion is required to prevent formation of $(La,Sr,Co)X_x$, for example $CoCl_{3(aq)}$. The volatility of $(La,Sr,Co)Cit_x$ under reaction conditions still requires investigation.

9.4.2 Ordered Mesoporous YSZ

Experiments showed that partially-stabilised YSZ could be produced as porous single crystals, though the pores were not organised in an ordered array. The porous single crystal morphology may be important for increasing the thermal stability of the material, as was shown for ordered mesoporous ceria. The experiments involving the VI of mesoporous carbon showed that cubic YSZ can be produced in an inert atmosphere, although it is unclear whether or not the low concentration of porous single crystals was a result of the synthesis conditions or a carbon template of insufficiently quality. This meant, using this method, that the silica content of a final product could be reduced by using a carbon template synthesised using sol-gel methods (a VI-prepared CMK- n would likely retain trace amounts of silica). The more developed VI method (V_2) showed that, using a higher quality silica template (SBA-15), high yields of ordered mesoporous cubic YSZ were produced, though both powder XRD and TEM investigation suggested that the nanorods in this material were comprised of fused nanoparticles. The combination of these factors suggests that the synthesis of porous single crystal cubic YSZ may be possible using nanocasting by adjusting the synthesis conditions (see Chapter 12).

9.5 Summary

The VI method was applied to three mixed oxides in an attempt to determine the applicability of the method for synthesising mesoporous materials with complex compositions. Of these materials, progress was made towards synthesising ordered mesoporous cubic YSZ with the porous single crystal morphology. High yields of ordered mesoporous cubic YSZ were observed using TEM of a VI material templated from SBA-15. It was also shown that the cubic YSZ phase could be prepared in an inert atmosphere which means that templating YSZ from mesoporous carbon may be possible. This would produce YSZ without a silicon impurity. This may be important for electrical and catalysis applications such as in SOFC anodes.

Turning to the perovskites, while a LSG particle was observed the pores were not ordered and the pore walls were comprised of nanoparticles that indexed to La_2O_3 . An investigation into the phase purity of the products of the LSG experiments suggested that this was caused by the volatility of the $\text{Ga}(\text{NO}_3)_3 \cdot x\text{H}_2\text{O}$ or other gallium intermediates under the experimental conditions. Results from Chapter 8 suggested that the CMK-3 template had been made in only low yield. This may explain the quality of the mesoporous structure. Attempts at producing ordered porous LSC resulted in cobalt containing material evaporating from the sample. This was likely to have been caused by the volatility of $\text{Co}(\text{NO}_3)_3$. This prevented further experimentation on this material as lab-ware became contaminated with cobalt. For pure-phase porous single crystal perovskites to be synthesised a study is required to identify non-volatile precursors that can be used at high temperatures and that decompose to oxides under an inert atmosphere.

A summary of the results presented in this chapter is shown in Table 9.1.

Table 9.1: Table summarising the results from this chapter. The d-spacings were determined from DDPs of TEM images.

	BET specific surface area (m^2g^{-1})	Pore volume (cm^3g^{-1})	Pore size (nm)	d-spacing (nm)
LSG ₂ -C-V ₂	Only powder XRD patterns presented			
YSZ-K-V ₁	368.0	0.29	-	-
YSZ-F-V ₁	38.8	0.06	-	-
YSZ-S-V ₂				5.8-7.4

Chapter 10

Conclusions

1. Three mesoporous silica templates, SBA-15, KIT-6 and FDU-12, were synthesised in accordance with literature procedures. TEM images and nitrogen physisorption results were consistent with previously reported literature results. It was determined that the relatively simple, low cost and environmentally friendly synthesis of these materials may be an acceptable basis for nanocasting porous single crystals of ceria and $\text{Ce}_{0.9}\text{Gd}_{0.1}\text{O}_{2-\delta}$ (CGO), in high yields, for use in catalysts or other functional devices.
2. Application of the incipient wetness impregnation technique (IWIT) for nanocasting using these silica templates produced low yields of ordered mesoporous ceria, as determined by TEM and nitrogen physisorption, when compared to literature reports of the preparation of other ordered mesoporous materials using sol-gel or nanocasting methods.
3. By precipitating cerium salts in the presence of a surfactant using alkaline solution, followed by calcination at a moderate temperature (300 °C), ceria nanoparticles with a diameter of 5-20 nm were produced. This material had relatively high specific surface area and pore volume ($143 \text{ m}^2\text{g}^{-1}$ and $0.20 \text{ cm}^3\text{g}^{-1}$, respectively). This method was a fast, inexpensive and easily reproducible method for producing high specific surface area and high pore volume nanoparticulate ceria.
4. The acid hydrolysis route for the synthesis of ordered mesoporous ceria was deemed to be unsuccessful. While there is scope for further investigation of sol-gel ceria precursors, the solubility of ceria in acidic media fundamentally limits product yields using this approach.
5. Vacuum impregnation (VI) was used to successfully synthesise ordered mesoporous ceria and CGO using the silica templates, SBA-15 and KIT-6. TEM images showed that the VI method had significantly improved the product yield of ordered mesoporous

product with respect to the IWIT, with many ordered mesoporous particles often visible in any particular field of view. Nitrogen physisorption results showed these materials to have larger pore volumes ($0.29\text{--}0.38\text{ cm}^3\text{g}^{-1}$) than previously reported results for ceria templated from mesoporous silica ($0.18\text{--}0.24\text{ cm}^3\text{g}^{-1}$),^{40, 81} though the pore volume measured in this investigation included significant contributions from structural by-products and interparticle porosity. CGO templated on KIT-6 ($0.38\text{ cm}^3\text{g}^{-1}$) was determined to be approaching the theoretically calculated pore volume ($0.44\text{ cm}^3\text{g}^{-1}$). The experimental pore volumes of the materials templated using SBA-15 were lower. This was proposed to have been caused by the increased difficulty of micropore impregnation, the lower pore volume of the SBA-15 nanorods with respect to the open structure of KIT-6 or because of the formation of non-ordered structural by-products (Point 8).

6. Mesoporous ceria and CGO had relatively high specific surface areas for dense materials, ranging between approximately 86 and $138\text{ m}^2\text{g}^{-1}$. These were lower than the highest literature values for mesoporous ceria. It was proposed that ordered mesoporous materials would have a lower specific surface area than a loosely packed nanoparticulate system. Therefore, the pore volume was the best indication of the yield of mesoporous product.
7. From analysis of the pore size distributions of mesoporous ceria and CGO, it was determined that the pores had a diameter of approximately 3 nm . This was consistent with observations from TEM images, where the gap between nanorods had been observed to be narrow ($<5\text{ nm}$). This pore size is also consistent with reported literature results.^{6, 40} The overlapping of lattice planes in the 3D mesoporous structures complicated the direct measurement of the width of the pore walls and the size of the pores themselves in the TEM images.
8. Generally, the pore size distributions of the ceria-based materials synthesised using the VI method exhibited three peaks. The peak at 3 nm was attributed to mesoporosity inside the ordered mesoporous materials (described above). The broad peaks larger than 25 nm were attributed to interparticle porosity. The feature observed between 6 and 20 nm was attributed to structural by-products. These structural by-products could be loose, disordered nanoparticles, nanorods and nanowires identified in TEM images, as well as mesoporous particles with larger pores caused by incomplete impregnation of the template. This feature, at $6\text{--}20\text{ nm}$, was the only peak to change when heating to

500 °C. This implied that the loosely ordered nanoparticulate material, rather than the ordered mesoporous material, had sintered.

9. The pore structures of the mesoporous materials were shown to be related to the silica templates using TEM imaging, though only small, electron transparent particles, could be imaged. Multiple mesopore zone axes were identified where ceria or CGO nanorods had replaced the pores of the original silica structure. For the SBA-15 materials, the cylindrical pores were replaced by a material which had parallel nanorods arranged in a hexagonal array. These were linked with nanobridges which were identified in some TEM images. This arrangement of nanorods was confirmed in TEM images taken along the longitudinal [100] zone axis, in images taken of the hexagonal arrangement of pores in cross-sectional [001] zone axis and by rotating sample material in TEM tomography. For the KIT-6 materials, the bi-continuous wormhole structure was replicated to form a complex branching nanorod network. TEM images of ceria and CGO materials along the [110], [111], [210] and [311] mesopore zone axes were captured. These were consistent with the KIT-6 template, with previous literature reports on KIT-6 and on other mesoporous oxides templated from KIT-6.
10. Ceria and CGO materials were determined to have the fluorite crystal structure. This was the desired phase as it is the phase in which oxygen ion conduction occurs. Ionic conducting materials are typically good oxidation catalysts.
11. The pore spacings measured for mesoporous ceria, CGO and the original silica templates were found to be consistent within experimental error. Due to the loss of water and $\text{NO}_{2(g)}$ during the synthesis of mesoporous ceria materials a significant loss of volume was expected. However, no decrease was observed in the pore spacing in TEM images of ceria or CGO templated using SBA-15 or KIT-6. TEM images of CGO-S- V_2 before silica digestion revealed that, in some instances, the pores of entire template particles were completely filled. This was believed to have prevented shrinkage of the mesostructure during calcination. Near-total impregnation of the mesopore network of the templates using VI appeared to give rise to an increase in the number of ordered mesoporous particles in the final product.
12. Small-angle X-ray scattering (SAXS) was only partially successful as a method for the determination of the extent of ordering of the mesopores in ceria or CGO. Several factors may have contributed to this. These included the roughness of the pore walls, irregularities in the pore spacings, the presence of nanoparticulate material covering the mesoporous particles and the decreased regularity of the materials caused by

consecutive casting. The latter refers to the use of a template which itself had been formed by templating. The SAXS patterns of CGO templated using SBA-15 and KIT-6 gave very weak reflections that corresponded to the same peaks in the SBA-15 and KIT-6 patterns.

13. Residual silicon, undoubtedly from the silica template, was detected in the mesoporous ceria and CGO samples. This was measured to be approximately 5-6 mol% using semi-quantitative EDS and 2-4 mol% using ICP-MS. Silicon has been reported to increase the thermal stability of ceria. However, silicon is likely to have a detrimental effect on the electrical properties of the material.
14. In the case of ceria and CGO templated on SBA-15 and KIT-6, the mesoporous particles were observed to be porous single crystals. The crystallographic lattice planes were aligned in the contiguous nanorods that comprised the mesoporous particles. This morphology was considered to contribute to the thermal stability of the materials. This was found to be consistent with the theory of grain growth and with the experimental observations that the mesoporous structures exhibited unusually high thermal stability (Points 16-19).
15. The porous single crystals were observed to contain crystallographic defects. The predominant defect was a consistent variation (up to 30°) in the crystallographic lattice plane orientation in the material. These variations were observed, in some TEM images, to occur in three crystallographic lattice directions. The other observed crystallographic defects in the porous single crystals were plane defects, where the lattice planes abruptly changed direction, edge defects and twinning.
16. Temperature programmed experiments showed that ordered mesoporous ceria and CGO oxidised hydrogen at temperatures up to 250 °C lower than for nanoparticulate ceria produced using the citrate method. The ordered mesoporous materials were therefore active oxidising agents at 450-500 °C, making them of great interest for use in intermediate temperature SOFC anodes and in other catalytic systems. The increased catalytic activity was attributed to several factors. Firstly, the unfaceted surface of the porous single crystals, which grew under constrained conditions, were expected to have exotic lattice planes exposed on the surface which may have been more active. Secondly, the variation in the crystallographic lattice plane orientation may increase the activity of the material. Thirdly, the increased pore volume would increase the rate of diffusion of reactants to the active sites and of products away from the active sites. Also, the increase in the specific surface area would mean that more of the material was

in contact with the gas phase, essentially increasing the concentration of the active sites. Finally, the small size of the nanorods meant that the bulk of the material could oxidise the reaction gas more rapidly because the oxygen ions had less distance to diffuse to the surface of the material.

17. Temperature programmed reduction cycling experiments showed that after heating Ceria-S-V₂ to 500 °C twice it still gave rise to a reduction peak at 400-600 °C. This suggests that the nature of the material remained largely unchanged during heating to 500 °C. As the shape of the reduction peak was slightly altered after TP cycling, some modification of the surface of the material was suggested, however.
18. Thermal resistance studies showed that ordered mesoporous CGO (CGO-S-V₂) was thermally stable at 500 °C over 48 h. After this treatment there was a loss of approximately 6 % in pore volume and 20 % in specific surface area. The pore size distribution still showed the 3 nm peak attributed to the ordered mesoporous material. This temperature coincided with the lower edge of the oxidation peak observed in the TPR experiments and, therefore, this material could be thermally stable at catalytically-active temperatures.
19. Ordered mesoporous CGO (CGO-K-V₂) was found to be thermally stable when heated to 1000 °C for a short period (<1 h). While heating in-situ in a TEM instrument to 1000 °C, several porous single crystals of CGO were observed to retain their structure during, and after, the heating process.
20. Ordered mesoporous CGO (CGO-S-V₂) was not thermally stable at 650 °C over an extended period. After treatment at this temperature for 72 h the loss in the pore volume and specific surface area were measured to be approximately 32 % and 63 %, respectively. The pore size distribution no longer showed the 3 nm peak that had been attributed to porous single crystal mesopores. TEM imaging showed that the nanorods that comprised the porous single crystals had significantly distorted and a large amount of grain growth of the CGO material had occurred. It has been reported that gadolinium increases ceria grain growth and, therefore, the CGO materials tested should be the least thermally stable of the ceria-based materials synthesised in this work.
21. During in-situ TEM heating experiments it was observed that there was a significant loss of nanoparticles at 400-600 °C. It was determined that, between these temperatures, the 5-20 nm nanoparticles had sintered. This was consistent with other observations during the thermal resistance experiments in which the loss of nanoparticulate material had also been observed. The temperature range of 400-600 °C

coincides with the temperature used to synthesise ordered mesoporous ceria and CGO. This observation assisted in the formulation of a mechanism for the VI method. According to this mechanism, precursor material that was deposited on the surface of the silica template was absorbed into the template during calcination by capillary action. Residual nanoparticles that remained outside the template would migrate into the silica pores and sinter into the porous single crystals during calcination. The nanoparticles and isolated nanorods that were observed in the TEM images of mesoporous products were likely to have formed inside the silica template and to have been released upon digestion of the template.

22. Further investigations into the mechanism of VI revealed the existence of nanowires that appeared to have been extruded from the silica template during the calcination stage of the synthesis of the sample, CGO-S-V₂. These were observed in large quantities and were determined to be crystalline CGO. A mechanism was postulated to explain the formation of these nanowires. According to this mechanism, excess material was forced into the silica template by capillary action and Ostwald ripening, as mentioned above. Once the pores were filled, crystal growth persisted and the nanowires were extruded from the pores.
23. When evaluated as a bulk heterojunction in dye-sensitised solar cells, ordered mesoporous ceria exhibited rapid exciton quenching (half life of 23-34 ps) and a high quenching efficiency (90-93 %). This was considered promising considering that the material had not been specifically designed for this application. Tailoring a material for this application could enhance these properties further.
24. The synthesis of mesoporous carbon was attempted using the VI method. While the results did not improve on conventional methods for the synthesis of mesoporous carbons, they were still promising. TEM images showed high yields of ordered mesoporous materials with the desired cylindrical pore structure clearly evident in numerous particles. The specific surface areas and pore volumes were approximately 44 % and 26 %, respectively, of those measured for CMK-3 (mesoporous carbon produced using IWIT). This demonstrated that VI may be applicable to more than just mesoporous oxides.
25. The synthesis of mesoporous yttria-stabilized zirconia (YSZ) was attempted using the VI method. VI of a mesoporous silica, FDU-12, produced single crystals of tetragonal, partially-stabilized zirconia with disordered pores. The low quality of the mesostructure was likely to have been caused by the poor quality of the template. VI of mesoporous

silica, SBA-15, produced ordered mesoporous, cubic YSZ in high yields. TEM images of this material clearly showed multiple instances of ordered mesoporous YSZ with the desired cylindrical pore structure. An attempt was made to use VI and a mesoporous carbon template, itself made by VI, to synthesise ordered mesoporous YSZ. No ordered mesoporous structure was observed in the product. Again, this was likely because of the poor quality of the template. However, it was of interest that the cubic YSZ phase was achieved using a carbon template. This is important because templating with mesoporous carbon, rather than silica, should reduce the silicon content of the product. Low silicon material would be ideal for SOFC and catalysis applications. By combining the experimental conditions explored in this work, it may be possible to use VI for the synthesis of ordered mesoporous cubic YSZ, in high yields.

26. The syntheses of the mesoporous perovskite materials, lanthanum strontium gallate and lanthanum strontium cobaltite, were attempted using the VI method. The products of both syntheses contained major impurity phases. The loss of volatile precursors, or volatile intermediate compounds, containing gallium or cobalt, appeared to be the cause of this.

Chapter 11

Future Work

Mesoporous Ceria and CGO

As the VI of mesoporous silica to produce ordered mesoporous ceria and CGO was not rigorously developed, there is scope for investigating several fundamental parameters of this method to improve the yields of mesoporous material. Firstly, investigating of the effect of the precursor concentration, as this was shown to have a large effect on the product quality of mesoporous carbon. Secondly, changing the precursor solvent to alter the interactions between the precursor solution and the template, for example, increased surface wetting. Thirdly, impregnating the template under different temperatures to alter, for example, the viscosity of the precursor or investigating the molten VI method. Also, exploring some of the techniques used in industrial VI could be explored, such as introducing the precursor solution before lowering the pressure or increasing the pressure after impregnation to force the solution into the pores.

As discussed in Section 7.7.1.1 there were several questions raised regarding the mechanism involved in VI. Further in-situ TEM heating experiments to observe nanowire formation plus the migration of $\text{Ce}(\text{NO}_3)_3$ and ceria nanoparticles would assist in verifying the proposed mechanism.

Further TPR studies may provide more information on the catalytic properties of the ordered mesoporous materials. Of key interest would be the effects of thermal cycling to determine at what temperature the materials can continually operate. Addition of metals (e.g. nickel, copper, platinum, palladium/gold, platinum/palladium/gold) to investigate the catalytic properties of these materials in both oxidation reactions and for hydrogen generation should be investigated.

The capture of a reduced sample in-situ for FT-IR study to determine the presence of peroxide or superoxide species should also be conducted as these may have a large contribution towards oxidation reactions below 200 °C.

Mesoporous Carbons

The product yield could be improved using the same approach as described above for ceria and CGO. Some work has already been reported on the effect of heating rate on the product quality of mesoporous carbon produced by nanocasting.¹⁸¹

Mesoporous YSZ

It would be of interest to determine the silicon content of mesoporous YSZ made by VI to establish whether the single-step impregnation reduces the silicon content sufficiently for this material to be viable for fuel cell anode applications. If the silica content is too high then templating from mesoporous carbon should be investigated.

Mesoporous Perovskites

The volatility of some precursor materials was thought to have caused the mixed phases observed in the VI of perovskite materials. Therefore the development of mesoporous perovskites would require the identification of non-volatile precursors, or suppression of this volatility. Other, simpler perovskite materials could be investigated, such as SrTiO_3 or SrZrO_3 , to compare the change in properties when prepared as a porous single crystal.

Other Materials

Using VI, it is the author's opinion that the most interesting materials that might be investigated, using either silica or carbon templates as appropriate, to produce porous single crystals, would be TiO_2 (for organic solar cell applications), and mesoporous carbon with a sulphur coating (VI followed by VI-slip cast) for supercapacitors. Both of these materials would likely be based on the cylindrical pore morphology (similar to SBA-15). Once TiO_2 had been prepared it can be compared with ceria and CGO to determine whether these materials are worth developing for PV applications.

Environmental Impacts of Nanocasting

Literature reports show that by using block co-polymers more than 90 % of the surfactant can be recovered using solvent extraction.¹⁶ The silica template is often dissolved using NaOH, and mesoporous silica can be synthesised using sodium silicate. Therefore being able to produce ordered mesoporous silica from the waste sodium silicate would reduce the environmental impact of this method significantly. Literature reports show that mesoporous silica can be produced from industrial waste materials in high yields.¹⁸²

Appendices

Appendix 1 Calculations of Theoretical Pore Volumes

Theoretical yield for Ceria-S-()

$$\begin{array}{lll}
 \text{Ce(NO}_3\text{)}.0\text{H}_2\text{O} & M_r = 326.06 \text{ g mol}^{-1} & (1) \\
 \text{La(NO}_3\text{)} & \rho = 3.63 \text{ g cm}^{-3} \text{ (approximate r value used as no lit. value for } anhy. & \\
 & \text{Ce(NO}_3\text{)}_3 & (2) \\
 \text{CeO}_2 & M_r = 172.10 \text{ g mol}^{-1} \quad \rho = 7.21 \text{ g cm}^{-3} & (3, 4) \\
 \text{SBA-15 pore volume: } 1.05 \pm 0.05 \text{ cm}^3 \text{ g}^{-1} & & (5) \\
 1 \text{ g silica } (\rho 2.65 \text{ g}^{-1} \text{ cm}^3)^{168} \text{ takes up } 0.38 \text{ cm}^3 & & (6) \\
 V_{\text{silica}} & 1.43 \text{ cm}^3 & (5)+(6) \\
 3.81 \text{ g Ce(NO}_3\text{)} \text{ impregnates pores completely} & & (8) (2) \times (5) \\
 -\text{NO}_{2(g)} \text{ becomes } 2.01 \text{ g CeO}_2 \text{ which takes up } 0.28 \text{ cm}^3 & & (9) (3) \times (8) \div (1) \\
 V_{\text{TOT}} - V_{\text{ceria}} = V_{\text{pores}} = 1.17 \text{ cm}^3 & & \\
 V_{\text{pores}} \div m_{\text{ceria}} = 0.57 \pm 0.03 \text{ cm}^3 \text{ g}^{-1} & &
 \end{array}$$

This calculation assumes that there is no shrinkage of the template during calcinations. As this was observed in Figure 7.6.2 this will decrease the achievable pore volumes. The shrinkage cannot be assumed to consume the empty volume created in (9) as during sintering there is likely solid migration through Ostwald ripening that means the value of shrinkage will be between 0 and completely consuming this space.

Theoretical yield for CMK-3

$$\begin{array}{lll}
 d\text{-sucrose} & \rho = 1.587 \text{ g cm}^{-3}, M_r = 342.30 \text{ g mol}^{-1} & (1, 2) \\
 m_{\text{carbon}} \text{ (in sucrose)} & 144.12 \text{ g mol}^{-1} & (3) \\
 \text{carbon black} & \rho \approx 2.01 \text{ g cm}^{-3} & (4) \\
 \text{SBA-15 pore volume: } 1.05 \pm 0.05 \text{ cm}^3 \text{ g}^{-1} & & (5) \\
 1 \text{ g silica } (\rho 2.65 \text{ cm}^3 \text{ g}^{-1}) \text{ takes up } 0.38 \text{ cm}^3 & & (6) \\
 V_{\text{silica}} & 1.43 \text{ cm}^3 & (5)+(6) \\
 1.66 \text{ g sucrose impregnates pores completely} & & (8) (1) \times (5) \\
 -\text{H}_2\text{O becomes } 0.70 \text{ g C which takes up } 0.35 \text{ cm}^3 & & (9) (3) \times (8) \div (2) \\
 V_{\text{TOT}} - V_{\text{carbon}} = V_{\text{pores}} = 1.08 \text{ cm}^3 & & \\
 V_{\text{pores}} \div m_{\text{carbon}} = 1.54 \pm 0.07 \text{ cm}^3 \text{ g}^{-1} & &
 \end{array}$$

Appendix 2 The development of VI

A

2/2

1. load sample
2. evacuate to vacuum (maybe overnight)
3. put Ce^{3+} precursor in as liquid (enough to fill pores)
4. open to atmosphere to help soak into pores

2g of SBA-15 put in & evacuated overnight

23/2 20um² $\text{Ce}(\text{NO}_3)_3 \cdot 6\text{H}_2\text{O}$ added - sprayed abt...

sample returned to atmospheric pressure & dried at 60°C

NOTES ON METHOD

- would be good to use a contained vessel in desiccator i.e. r.b.f. to reduce spraying of precursor. Or a test-tube would be good as the silica would be deep rather than spread out. Light silica also gets blown about desiccator...

B

- will try w/ KIT-6
KIT-6 \Rightarrow 500°C (sh) to use in this exp.

20/2 Best would be a smaller desiccator that the entire bottom can have SiO_2 powder due to better w/ powder spraying all about the desiccator.

13/3 Got smaller desiccator put KIT-6 powder on bottom & vacuum.

1. vacuum overnight
2. impreg. atmosphere, filter, H^+ wash
3. dry
4. repeat

cont. p 52

C

27/4 VACUUM LINE SETUP

1. Insert sample (mesoporous silica) into desiccator
2. open pump ballast
3. turn pump on & close ballast
4. open taps 1 & 3
5. pump down c. 8 hrs
6. close tap 1
7. put impreg. soln in measuring cylinder
8. open tap close tap 3, open tap 2 to suck precursor up to tap. close tap 2
9. close tap 1, open tap 3

To clean

1. make sure $\text{N}_2(\text{l})$ trap full
2. open all taps
3. wash tubes w/ H_2O , EtOH
4. suck dry

D

1/10/7 Thror. Calc. for CeO_2 , GOO , YSZ , LSG Impreg.

7g KIT-6 = 0.92 cm³ pores

$\rho \text{ Ce}(\text{NO}_3)_3 \sim 3.63$

$\rho [\text{Ce.Gd}](\text{NO}_3)_3 \sim 3.64$

$[\text{Zr+Y}](\text{NO}_3)_3$

La Mg Sr Gd $(\text{NO}_3)_3$

$\text{ZrO}(\text{NO}_3)_2 \cdot \text{Y}(\text{NO}_3)_3$

for Ce^{3+} approx 4.4g in 1st impreg
3.5g in 2nd impreg
fills 0.402 cm³ of the pores

New Experiment setup

Pages taken from 2007 lab book of Troy Dougherty showing the progression of VI (A) V_1 setup, (B) modified V_1 setup, (C) proposed improvement to V_1 , (D) V_2 setup.

References

1. Reporting Physisorption Data for Gas Solid Systems with Special Reference to the Determination of Surface-Area and Porosity (Recommendations 1984), K. S. W. Sing, D. H. Everett, R. A. W. Haul, L. Moscou, R. A. Pierotti, J. Rouquerol and T. Siemieniewska, *Pure and Applied Chemistry*, 1985, **57**, 603-619.
2. The Preparation of Alkyltrimethylammonium-Kanemite Complexes and Their Conversion to Microporous Materials, T. Yanagisawa, T. Shimizu, K. Kuroda and C. Kato, *Bulletin of the Chemical Society of Japan*, 1990, **63**, 988-992.
3. Ordered Mesoporous Molecular-Sieves Synthesized by a Liquid-Crystal Template Mechanism, C. T. Kresge, M. E. Leonowicz, W. J. Roth, J. C. Vartuli and J. S. Beck, *Nature*, 1992, **359**, 710-712.
4. Ordered mesoporous materials in catalysis, A. Taguchi and F. Schuth, *Microporous and Mesoporous Materials*, 2005, **77**, 1-45.
5. Crystalline mesoporous metal oxide, W. B. Yue and W. Z. Zhou, *Prog Nat Sci*, 2008, **18**, 1329-1338.
6. Synthesis of highly ordered carbon molecular sieves via template-mediated structural transformation, R. Ryoo, S. H. Joo and S. Jun, *Journal of Physical Chemistry B*, 1999, **103**, 7743-7746.
7. Mesoporous materials for encapsulating enzymes, C. H. Lee, T. S. Lin and C. Y. Mou, *Nano Today*, 2009, **4**, 165-179.
8. Synthesis of ordered mesoporous materials using surfactant liquid crystals or micellar solutions, A. E. C. Palmqvist, *Current Opinion in Colloid & Interface Science*, 2003, **8**, 145-155.
9. Triblock copolymer syntheses of mesoporous silica with periodic 50 to 300 angstrom pores, D. Y. Zhao, J. L. Feng, Q. S. Huo, N. Melosh, G. H. Fredrickson, B. F. Chmelka and G. D. Stucky, *Science*, 1998, **279**, 548-552.
10. Block-Copolymer-Templated Ordered Mesoporous Silica: Array of Uniform Mesopores or Mesopore–Micropore Network?, R. Ryoo, C. H. Ko, M. Kruk, V. Antochshuk and M. Jaroniec, *The Journal of Physical Chemistry B*, 2000, **104**, 11465-11471.

11. Cubic Ia3d large mesoporous silica: synthesis and replication to platinum nanowires, carbon nanorods and carbon nanotubes, F. Kleitz, S. H. Choi and R. Ryoo, *Chemical Communications*, 2003, 2136-2137.
12. Template synthesis of asymmetrically mesostructured platinum networks, H. J. Shin, R. Ryoo, Z. Liu and O. Terasaki, *Journal of the American Chemical Society*, 2001, **123**, 1246-1247.
13. Cubic mesoporous silica with large controllable entrance sizes and advanced adsorption properties, J. Fan, C. Z. Yu, T. Gao, J. Lei, B. Z. Tian, L. M. Wang, Q. Luo, B. Tu, W. Z. Zhou and D. Y. Zhao, *Angew Chem Int Edit*, 2003, **42**, 3146-3150.
14. A new family of mesoporous molecular sieves prepared with liquid crystal templates, J. S. Beck, J. C. Vartuli, W. J. Roth, M. E. Leonowicz, C. T. Kresge, K. D. Schmitt, C. T. W. Chu, D. H. Olson and E. W. Sheppard, *Journal of the American Chemical Society*, 1992, **114**, 10834-10843.
15. Fine Control of Pore Size of Highly Ordered MCM-41 by Using Template Mixtures of Dodecyltrimethylammonium Bromide/Hexadecyltrimethylammonium Bromide with Various Molar Ratios, S. Namba, A. Mochizuki and M. Kito, *Chemistry Letters*, 1998, **27**, 569-570.
16. A Neutral Templating Route to Mesoporous Molecular Sieves, P. T. Tanev and T. J. Pinnavaia, *Science*, 1995, **267**, 865-867.
17. Generalized syntheses of large-pore mesoporous metal oxides with semicrystalline frameworks, P. Yang, D. Zhao, D. I. Margolese, B. F. Chmelka and G. D. Stucky, *Nature*, 1998, **396**, 152-155.
18. Nanoparticle Assembly of Ordered Multicomponent Mesostructured Metal Oxides via a Versatile Sol–Gel Process, J. Fan, S. W. Boettcher and G. D. Stucky, *Chemistry of Materials*, 2006, **18**, 6391-6396.
19. Controllable and Repeatable Synthesis of Thermally Stable Anatase Nanocrystal–Silica Composites with Highly Ordered Hexagonal Mesostructures, W. Dong, Y. Sun, C. W. Lee, W. Hua, X. Lu, Y. Shi, S. Zhang, J. Chen and D. Zhao, *Journal of the American Chemical Society*, 2007, **129**, 13894-13904.
20. Ordered Mesoporous Ce_{1-x}Zr_xO₂ Solid Solutions with Crystalline Walls, Q. Yuan, Q. Liu, W. G. Song, W. Feng, W. L. Pu, L. D. Sun, Y. W. Zhang and C. H. Yan, *J. Am. Chem. Soc.*, 2007, **129**, 6698-6699.
21. Synthesis and characterization of highly ordered mesoporous YSZ by tri-block copolymer, I. M. Hung, D. T. Hung, K. Z. Fung and M. H. Hon, *J Porous Mat*, 2006, **13**, 225-230.

22. A Family of Highly Ordered Mesoporous Polymer Resin and Carbon Structures from Organic–Organic Self-Assembly, Y. Meng, D. Gu, F. Zhang, Y. Shi, L. Cheng, D. Feng, Z. Wu, Z. Chen, Y. Wan, A. Stein and D. Zhao, *Chemistry of Materials*, 2006, **18**, 4447-4464.
23. An Aqueous Cooperative Assembly Route To Synthesize Ordered Mesoporous Carbons with Controlled Structures and Morphology, F. Zhang, Y. Meng, D. Gu, Yan, Z. Chen, B. Tu and D. Zhao, *Chemistry of Materials*, 2006, **18**, 5279-5288.
24. A Facile Aqueous Route to Synthesize Highly Ordered Mesoporous Polymers and Carbon Frameworks with Ia $\overline{3}$ d Bicontinuous Cubic Structure, F. Zhang, Y. Meng, D. Gu, Yan, C. Yu, B. Tu and D. Zhao, *Journal of the American Chemical Society*, 2005, **127**, 13508-13509.
25. One-Step Nanocasting Synthesis of Highly Ordered Single Crystalline Indium Oxide Nanowire Arrays from Mesostructured Frameworks, H. Yang, Q. Shi, B. Tian, Q. Lu, F. Gao, S. Xie, J. Fan, C. Yu, B. Tu and D. Zhao, *Journal of the American Chemical Society*, 2003, **125**, 4724-4725.
26. Synthesis of Porous Single Crystals of Metal Oxides via a Solid–Liquid Route, Yue and Zhou, *Chemistry of Materials*, 2007, **19**, 2359-2363.
27. Preparation of three-dimensional chromium oxide porous single crystals templated by SBA-15, K. K. Zhu, B. Yue, W. Z. Zhou and H. Y. He, *Chemical Communications*, 2003, 98-99.
28. Growth of porous single-crystal Cr₂O₃ in a 3-D mesopore system, K. Jiao, B. Zhang, B. Yue, Y. Ren, S. X. Liu, S. R. Yan, C. Dickinson, W. Z. Zhou and H. Y. He, *Chemical Communications*, 2005, 5618-5620.
29. Formation Mechanism of Porous Single-Crystal Cr₂O₃ and Co₃O₄ Templated by Mesoporous Silica, C. Dickinson, W. Zhou, R. P. Hodgkins, Shi, Zhao and He, *Chemistry of Materials*, 2006, **18**, 3088-3095.
30. General synthesis of ordered crystallized metal oxide nanoarrays replicated by microwave-digested mesoporous silica, B. Z. Tian, X. Y. Liu, H. F. Yang, S. H. Xie, C. Z. Yu, B. Tu and D. Y. Zhao, *Advanced Materials*, 2003, **15**, 1370-+.
31. Porous crystals of cubic metal oxides templated by cage-containing mesoporous silica, W. B. Yue and W. Z. Zhou, *Journal of Materials Chemistry*, 2007, **17**, 4947-4952.
32. Hard Templating Pathways for the Synthesis of Nanostructured Porous Co₃O₄, A. Rumplecker, F. Kleitz, E.-L. Salabas and F. Schuth, *Chemistry of Materials*, 2007, **19**, 485-496.

33. Weakly ferromagnetic ordered mesoporous Co_3O_4 synthesized by nanocasting from vinyl-functionalized cubic Ia3d mesoporous silica, Y. Q. Wang, C. M. Yang, W. Schmidt, B. Spliethoff, E. Bill and F. Schuth, *Advanced Materials*, 2005, **17**, 53-+.
34. Facile synthesis and characterization of novel mesoporous and mesorelief oxides with gyroidal structures, B. Z. Tian, X. Y. Liu, L. A. Solovyov, Z. Liu, H. F. Yang, Z. D. Zhang, S. H. Xie, F. Q. Zhang, B. Tu, C. Z. Yu, O. Terasaki and D. Y. Zhao, *Journal of the American Chemical Society*, 2004, **126**, 865-875.
35. Mesoporous crystalline $\beta\text{-MnO}_2$ - a reversible positive electrode for rechargeable lithium batteries, F. Jiao and P. G. Bruce, *Advanced Materials*, 2007, **19**, 657-+.
36. Synthesis and electrochemical properties of semicrystalline gyroidal mesoporous MnO_2 , Q. Zhou, X. Li, Y. G. Li, B. Z. Tian, D. Y. Zhao and Z. Y. Jiang, *Chinese J Chem*, 2006, **24**, 835-839.
37. Highly Electrochemical Reaction of Lithium in the Ordered Mesoporous $\beta\text{-MnO}_2$, J.-Y. Luo, J.-J. Zhang and Y.-Y. Xia, *Chemistry of Materials*, 2006, **18**, 5618-5623.
38. Electrochemical capacitance characterization of NiO with ordered mesoporous structure synthesized by template SBA-15, Y.-g. Wang and Y.-y. Xia, *Electrochimica Acta*, 2006, **51**, 3223-3227.
39. Ordered Mesoporous Fe_2O_3 with Crystalline Walls, F. Jiao, A. Harrison, J.-C. Jumas, A. V. Chadwick, W. Kockelmann and P. G. Bruce, *Journal of the American Chemical Society*, 2006, **128**, 5468-5474.
40. Synthesis of thermally stable mesoporous cerium oxide with nanocrystalline frameworks using mesoporous silica templates, S. C. Laha and R. Ryoo, *Chemical Communications*, 2003, 2138-2139.
41. Nanostructured metal oxides synthesized by hard template method for gas sensing applications, E. Rossinyol, J. Arbiol, F. Peiro, A. Cornet, J. R. Morante, B. Tian, T. Bo and D. Zhao, *Sensors and Actuators B-Chemical*, 2005, **109**, 57-63.
42. Preparation and characterization of three-dimensional mesoporous crystals of tungsten oxide, B. Yue, H. Tang, Z. Kong, K. Zhu, C. Dickinson, W. Zhou and H. He, *Chemical Physics Letters*, 2005, **407**, 83-86.
43. Factors affecting the preparation of ordered mesoporous ZrO_2 using the replica method, B. Liu and R. T. Baker, *Journal of Materials Chemistry*, 2008, **18**, 5200-5207.
44. Reversible replication between ordered mesoporous silica and mesoporous carbon, M. Kang, S. H. Yi, H. I. Lee, J. E. Yie and J. M. Kim, *Chemical Communications*, 2002, 1944-1945.

45. Taking nanocasting one step further: Replicating CMK-3 as a silica material, A. H. Lu, W. Schmidt, A. Taguchi, B. Spliethoff, B. Tesche and F. Schuth, *Angew Chem Int Edit*, 2002, **41**, 3489-+.
46. Mesoporous CeO₂: Synthesis by nanocasting, characterisation and catalytic properties, J. Roggenbuck, H. Schafer, T. Tsoncheva, C. Minchev, J. Hanss and M. Tiemann, *Microporous and Mesoporous Materials*, 2007, **101**, 335-341.
47. Ordered mesoporous ZnO for gas sensing, T. Wagner, T. Waitz, J. Roggenbuck, M. Fröba, C. D. Kohl and M. Tiemann, *Thin Solid Films*, 2007, **515**, 8360-8363.
48. Synthesis of Mesoporous Magnesium Oxide by CMK-3 Carbon Structure Replication, J. Roggenbuck, G. Koch and M. Tiemann, *Chemistry of Materials*, 2006, **18**, 4151-4156.
49. Ordered Mesoporous Magnesium Oxide with High Thermal Stability Synthesized by Exotemplating Using CMK-3 Carbon, J. Roggenbuck and M. Tiemann, *Journal of the American Chemical Society*, 2005, **127**, 1096-1097.
50. e. A. Trovarelli, *Catalysis by Ceria and Related Materials*, Imperial College Press, 2002.
51. in Handbook on the Physics and Chemistry of Rare Earths, eds. J. J.-C. G. B. n. Karl A. Gschneidner and K. P. Vitalij, Elsevier, 2010, pp. ii-ii.
52. Electrolytes for solid oxide fuel cells, J. W. Fergus, *Journal of Power Sources*, 2006, **162**, 30-40.
53. M. Mogensen, D. Lybye, K. H. K. and N. Bonanos, The Electrochemical Society, Ceria revisited: Electrolyte or electrode material?, eds. S. C. Singhal and J. Mizusaki, Quebec City (CA), 2005, pp. 1068-1074.
54. Ceria-based materials for solid oxide fuel cells, V. V. Kharton, F. M. Figueiredo, L. Navarro, E. N. Naumovich, A. V. Kovalevsky, A. A. Yaremchenko, A. P. Viskup, A. Carneiro, F. M. B. Marques and J. R. Frade, *Journal of Materials Science*, 2001, **36**, 1105-1117.
55. Electrical and ionic conductivity of Gd-doped ceria, S. R. Wang, T. Kobayashi, M. Dokiya and T. Hashimoto, *J Electrochem Soc*, 2000, **147**, 3606-3609.
56. Preparation and properties of dense Ce_{0.9}Gd_{0.1}O_{2-δ} ceramics for use as electrolytes in IT-SOFCs, T. S. Zhang, J. Ma, L. H. Luo and S. H. Chan, *Journal of Alloys and Compounds*, 2006, **422**, 46-52.
57. The effect of cobalt oxide addition on the conductivity of Ce_{0.9}Gd_{0.1}O_{1.95}, E. Jud and L. J. Gauckler, *J Electroceram*, 2005, **15**, 159-166.

58. Preparation and sintering of $\text{Ce}_{1-x}\text{Gd}_x\text{O}_{2-x/2}$ nanopowders and their electrochemical and EPR characterization, A. Sin, Y. Dubitsky, A. Zaopo, A. S. Aricò, L. Gullo, D. La Rosa, S. Siracusano, V. Antonucci, C. Oliva and O. Ballabio, *Solid State Ionics*, 2004, **175**, 361-366.
59. Synthesis and properties of $\text{Ce}_{1-x}\text{Gd}_x\text{O}_{2-x/2}$ solid solution prepared by flame spray pyrolysis, D. J. Seo, K. O. Ryu, S. B. Park, K. Y. Kim and R.-H. Song, *Materials Research Bulletin*, 2006, **41**, 359-366.
60. Small polaron electron transport in reduced CeO_2 single crystals, H. L. Tuller and A. S. Nowick, *Journal of Physics and Chemistry of Solids*, 1977, **38**, 859-867.
61. Small-polaron mobility in nonstoichiometric cerium dioxide, I. K. Naik and T. Y. Tien, *Journal of Physics and Chemistry of Solids*, 1978, **39**, 311-315.
62. Unusual oxygen storage/redox behavior of high-surface-area ceria prepared by a surfactant-assisted route, D. Terribile, A. Trovarelli, C. de Leitenburg, G. Dolcetti and J. Llorca, *Chemistry of Materials*, 1997, **9**, 2676-+.
63. The preparation of high surface area $\text{CeO}_2\text{-ZrO}_2$ mixed oxides by a surfactant-assisted approach, D. Terribile, A. Trovarelli, J. Llorca, C. de Leitenburg and G. Dolcetti, *Catalysis Today*, 1998, **43**, 79-88.
64. The synthesis and characterization of mesoporous high-surface area ceria prepared using a hybrid organic/inorganic route, D. Terribile, A. Trovarelli, J. Llorca, C. de Leitenburg and G. Dolcetti, *Journal of Catalysis*, 1998, **178**, 299-308.
65. New insights into the defective structure and catalytic activity of Pd/ceria, J. A. Wang, J. M. Dominguez, A. Montoya, S. Castillo, J. Navarrete, M. Moran-Pineda, J. Reyes-Gasga and X. Bokhimi, *Chemistry of Materials*, 2002, **14**, 4676-4683.
66. Catalytic methanol decomposition over palladium deposited on mesoporous cerium oxide, M. P. Kapoor, Y. Ichihashi, K. Kuraoka, W. J. Shen and Y. Matsumura, *Catalysis Letters*, 2003, **88**, 83-87.
67. Vapor phase hydrogenation of phenol over palladium supported on mesoporous CeO_2 and ZrO_2 , S. Velu, M. P. Kapoor, S. Inagaki and K. Suzuki, *Appl Catal a-Gen*, 2003, **245**, 317-331.
68. Mesostructured CeO_2 and Pd/CeO_2 nanophases: Templated synthesis, crystalline structure and catalytic properties, J. H. Zhang, Y. Q. Yang, J. M. Shen and J. A. Wang, *Journal of Molecular Catalysis a-Chemical*, 2005, **237**, 182-190.
69. Mesoporous ceria preparation by templating agents, L. Pino, A. Vita, M. Cordaro, F. Cipiti, M. Lagana and V. Recupero, *Materials Technology*, 2005, **20**, 18-23.
70. D. M. Lyons, Poster presentation, Dublin Institute of Technology, 1998.

71. Preparation of ordered mesoporous ceria with enhanced thermal stability, D. M. Lyons, K. M. Ryan and M. A. Morris, *Journal of Materials Chemistry*, 2002, **12**, 1207-1212.
72. Surface studies of ceria and mesoporous ceria powders by solid-state H-1 MAS NMR, D. M. Lyons, J. P. McGrath and M. A. Morris, *Journal of Physical Chemistry B*, 2003, **107**, 4607-4617.
73. Mesoporous thin films of high-surface-area crystalline cerium dioxide, M. Lundberg, B. Skarman, F. Cesar and L. R. Wallenberg, *Microporous and Mesoporous Materials*, 2002, **54**, 97-103.
74. Hierarchically mesostructured doped CeO₂ with potential for solar-cell use, A. Corma, P. Atienzar, H. Garcia and J. Y. Chane-Ching, *Nature Materials*, 2004, **3**, 394-397.
75. Preparation of mesoporous cerium oxide templated by tri-block copolymer for solid oxide fuel cell, I. M. Hung, H. P. Wang, W. H. Lai, K. Z. Fung and M. H. Hon, *Electrochimica Acta*, 2004, **50**, 745-748.
76. Crystallography and porosity effects of CO conversion on mesoporous CeO₂, M. Lundberg, B. Skarman and L. R. Wallenberg, *Microporous and Mesoporous Materials*, 2004, **69**, 187-195.
77. The generation of mesostructured crystalline CeO₂, ZrO₂ and CeO₂-ZrO₂ films using evaporation-induced self-assembly, T. Brezesinski, M. Antonietti, M. Groenewolt, N. Pinna and B. Smarsly, *New Journal of Chemistry*, 2005, **29**, 237-242.
78. Mesostructured crystalline ceria with a bimodal pore system using block copolymers and ionic liquids as rational templates, T. Brezesinski, C. Erpen, K. Iimura and B. Smarsly, *Chemistry of Materials*, 2005, **17**, 1683-1690.
79. Controlled assembly of preformed ceria nanocrystals into highly ordered 3D nanostructures, A. S. Deshpande, N. Pinna, B. Smarsly, M. Antonietti and M. Niederberger, *Small*, 2005, **1**, 313-316.
80. Monodisperse, bimodal mesoporous ceria catalysts and adsorbents for air purification, K. Suzuki and A. K. Sinha, *Journal of Materials Chemistry*, 2007, **17**, 2547-2551.
81. Mesoporous CeO₂ and CuO-loaded mesoporous CeO₂: Synthesis, characterization, and CO catalytic oxidation property, W. H. Shen, X. P. Dong, Y. F. Zhu, H. R. Chen and J. L. Shi, *Microporous and Mesoporous Materials*, 2005, **85**, 157-162.
82. W. B. Yue and W. Z. Zhou, Elsevier, Mesoporous metal oxides templated by FDU-12 using a new convenient method, eds. R. Xu, J. Chen, Z. Gao and W. Yan, Beijing, CN, 2007, pp. 1755-1762.

83. Preparation of a large Mesoporous CeO₂ with crystalline walls using PMMA colloidal crystal templates, T. W. Wang, O. Sel, I. Djerdj and B. Smarsly, *Colloid Polym Sci*, 2006, **285**, 1-9.
84. Personal Communication, W. Zhou, 2007.
85. Personal Communication, W. B. Yue, 2007.
86. Gadolinium doped Ceria nanocrystals synthesized from mesoporous silica, E. Rossinyol, E. Pellicer, A. Prim, S. Estrade, J. Arbiol, F. Peiro, A. Cornet and J. R. Morante, *Journal of Nanoparticle Research*, 2008, **10**, 369-375.
87. C₆₀: Buckminsterfullerene, H. W. Kroto, J. R. Heath, S. C. O'Brien, R. F. Curl and R. E. Smalley, *Nature*, 1985, **318**, 162-163.
88. Helical microtubules of graphitic carbon, S. Iijima, *Nature*, 1991, **354**, 56-58.
89. Carbon supports for low-temperature fuel cell catalysts, E. Antolini, *Applied Catalysis B: Environmental*, 2009, **88**, 1-24.
90. Synthesis of new, nanoporous carbon with hexagonally ordered mesostructure, S. Jun, S. H. Joo, R. Ryoo, M. Kruk, M. Jaroniec, Z. Liu, T. Ohsuna and O. Terasaki, *Journal of the American Chemical Society*, 2000, **122**, 10712-10713.
91. Preparation and Characterization of Highly Ordered Graphitic Mesoporous Carbon as a Pt Catalyst Support for Direct Methanol Fuel Cells, F. Su, J. Zeng, X. Bao, Y. Yu, J. Y. Lee and X. S. Zhao, *Chemistry of Materials*, 2005, **17**, 3960-3967.
92. Ordered nanoporous arrays of carbon supporting high dispersions of platinum nanoparticles, S. H. Joo, S. J. Choi, I. Oh, J. Kwak, Z. Liu, O. Terasaki and R. Ryoo, *Nature*, 2001, **412**, 169-172.
93. Graphitic mesoporous carbons synthesised through mesostructured silica templates, A. B. Fuertes and S. Alvarez, *Carbon*, 2004, **42**, 3049-3055.
94. Ionic Conductivity of Cubic Solid Solutions in the System CaO-Y₂O₃-ZrO₂, D. W. Strickler and W. G. Carlson, *Journal of the American Ceramic Society*, 1964, **47**, 122-127.
95. Electrical Resistivity of Stabilized Zirconia at Elevated Temperatures, J. M. Dixon, L. D. LaGrange, U. Merten, C. F. Miller, J. T. Porter and Ii, *J Electrochem Soc*, 1963, **110**, 276-280.
96. Ionic conduction in zirconia films of nanometer thickness, X. Guo, E. Vasco, S. Mi, K. Szot, E. Wachsman and R. Waser, *Acta Materialia*, 2005, **53**, 5161-5166.
97. Study on La and Y co-doped ceria-based electrolyte materials, X. Sha, Z. Lü, X. Huang, J. Miao, Z. Ding, X. Xin and W. Su, *Journal of Alloys and Compounds*, 2007, **428**, 59-64.

98. Degradation of the electrical conductivity in stabilised zirconia systems: Part I: yttria-stabilised zirconia, C. Haering, A. Roosen and H. Schichl, *Solid State Ionics*, 2005, **176**, 253-259.
99. J. H. Joo and G. M. Choi, The Electrochemical Society, Growth and electrical conductivity of thin film YSZ by pulsed laser deposition, ed. S. C. S. a. J. Mizusaki, Quebec (CA), 2005, pp. 1051-1056.
100. T. Ishihara, M. Enoki, Y. J.W and H. Matsumoto, The Electrochemical Society, Power Generating Property of SOFC Using La(Sr)Ga(Mg,Fe)O₃ Electrolyte Coated with LaGaO₃ Film, ed. S. C. S. a. J. Mizusaki, Quebec (CA), 2005, pp. 1117-1126.
101. K.Yamahara, C. P. Jacobson, S.J.Visco and L. C. D. Jonghe, The Electrochemical Society, Influence of Powders on Ionic Conductivity of Polycrystalline Zirconias, ed. S. C. S. a. M. Dokiya, Paris, 2003, pp. 187-195.
102. M. Becker, A.Weber, A.C.Müller and E. Ivers-Tifée, The Electrochemical Society, Characterization of Cathode Supported Thin Film Electrolytes, ed. S. C. S. a. M. Dokiya, Paris, 2003, pp. 222-228.
103. Grain Boundary Blocking Effect in Zirconia: A Schottky Barrier Analysis, X. Guo and J. Maier, *J Electrochem Soc*, 2001, **148**, E121-E126.
104. Mechanical and electrical properties of ZrO₂ (3Y) doped with RENbO₄ (RE = Yb, Er, Y, Dy, YNd, Sm, Nd), T.-H. Yeh, W.-C. Hsu and C.-C. Chou, *J. Phys. IV France*, 2005, **128**, 213-219.
105. Practical solid oxide fuel cells with anodes derived from self-assembled mesoporous-NiO-YSZ, M. Mamak, N. Coombs and G. A. Ozin, *Chemical Communications*, 2002, 2300-2301.
106. Highly-ordered mesoporous nanocrystalline yttria-stabilized zirconia synthesized through evaporation-induced self-assembly method, I. M. Hung, D.-T. Hung, K.-Z. Fung and M.-H. Hon, *Materials Letters*, 2008, **62**, 1147-1150.
107. Controlled Formation of Highly Ordered Cubic and Hexagonal Mesoporous Nanocrystalline Yttria-Zirconia and Ceria-Zirconia Thin Films Exhibiting High Thermal Stability¹³, E. L. Crepaldi, G. J. d. A. A. Soler-Illia, A. Bouchara, D. Grosso, D. Durand and C. Sanchez, *Angewandte Chemie International Edition*, 2003, **42**, 347-351.
108. Zircon stability and the ZrO₂-SiO₂ phase diagram, W. C. Buttermann and W. R. Foster, *American Mineralogist*, 1967, **52**, 880-885.

109. Superior Perovskite Oxide-Ion Conductor; Strontium- and Magnesium-Doped LaGaO₃: I, Phase Relationships and Electrical Properties, K. Huang, R. S. Tichy and J. B. Goodenough, *Journal of the American Ceramic Society*, 1998, **81**, 2565-2575.
110. Electrode Performance Test on Single Ceramic Fuel Cells Using as Electrolyte Sr- and Mg-Doped LaGaO₃, K. Huang, M. Feng, J. B. Goodenough and C. Milliken, *J Electrochem Soc*, 1997, **144**, 3620-3624.
111. Interfacial Reaction between Nickel Oxide and Lanthanum Gallate during Sintering and its Effect on Conductivity, P. Huang, A. Horky and A. Petric, *Journal of the American Ceramic Society*, 1999, **82**, 2402-2406.
112. A review of anode materials development in solid oxide fuel cells, S. P. Jiang and S. H. Chan, *Journal of Materials Science*, 2004, **39**, 4405-4439.
113. Fabrication and characterization of SDC-LSGM composite electrolytes material in IT-SOFCs, D. Xu, X. Liu, D. Wang, G. Yi, Y. Gao, D. Zhang and W. Su, *Journal of Alloys and Compounds*, 2007, **429**, 292-295.
114. Microstructure and ionic conductivity of Sr- and Mg-doped LaGaO₃, N. Liu, M. Shi, C. Wang, Y. Yuan, P. Majewski and F. Aldinger, *Journal of Materials Science*, 2006, **41**, 4205-4213.
115. Electrical conductivity and mechanical properties of alumina-dispersed doped lanthanum gallates, I. Yasuda, Y. Matsuzaki, T. Yamakawa and T. Koyama, *Solid State Ionics*, 2000, **135**, 381-388.
116. Effect of A-site cation nonstoichiometry on the properties of doped lanthanum gallate, J. W. Stevenson, T. R. Armstrong, L. R. Pederson, J. Li, C. A. Lewinsohn and S. Baskaran, *Solid State Ionics*, 1998, **113-115**, 571-583.
117. Influence of Cobalt and Iron Additions on the Electrical and Thermal Properties of (La,Sr)(Ga,Mg)O_{3-δ}, J. W. Stevenson, K. Hasinska, N. L. Canfield and T. R. Armstrong, *J Electrochem Soc*, 2000, **147**, 3213-3218.
118. Processing and Electrical Properties of Alkaline Earth-Doped Lanthanum Gallate, J. W. Stevenson, T. R. Armstrong, D. E. McCready, L. R. Pederson and W. J. Weber, *J Electrochem Soc*, 1997, **144**, 3613-3620.
119. J. Bradley, P. R. Slater, T. Ishihara and J. T. S. Irvine, The Electrochemical Society, Dependence of Activation Energy on Temperature and Structure in Lanthanum Gallates, ed. S. C. S. a. M. Dokiya, Paris, 2003, pp. 315-323.
120. Preparation of high-density La_{0.90}Sr_{0.10}Ga_{1-y}Mg_yO_{3-δ} (y = 0.20 and 0.30) oxide ionic conductors using HIP, M. Ohnuki, K. Fujimoto and S. Ito, *Solid State Ionics*, 2006, **177**, 1729-1732.

121. Fabrication of $\text{La}_{1-x}\text{Sr}_x\text{Ga}_{1-y}\text{Mg}_y\text{O}_{3-(x+y)/2}$ thin films by electrophoretic deposition and its conductivity measurement, T. Mathews, N. Rabu, J. R. Sellar and B. C. Muddle, *Solid State Ionics*, 2000, **128**, 111-115.
122. Synthesis and characterization of $\text{La}_{0.85}\text{Sr}_{0.15}\text{Ga}_{0.85}\text{Mg}_{0.15}\text{O}_{3-\delta}$ electrolyte by steric entrapment synthesis method, Z.-C. Li, H. Zhang, B. Bergman and X. Zou, *Journal of the European Ceramic Society*, 2006, **26**, 2357-2364.
123. Synthesis and characterization of Sr- and Mg-doped LaGaO_3 by using glycine-nitrate combustion method, M. Shi, N. Liu, Y. Xu, Y. Yuan, P. Majewski and F. Aldinger, *Journal of Alloys and Compounds*, 2006, **425**, 348-352.
124. Doped Lanthanum Gallate Film Solid Oxide Fuel Cells Fabricated On a Ni/YSZ Anode Support, T. He, Q. He, L. Pei, Y. Ji and J. Liu, *Journal of the American Ceramic Society*, 2006, **89**, 2664-2667.
125. Relationship between the ionic and electronic partial conductivities of co-doped LSGM ceramics from oxygen partial pressure dependence of the total conductivity, B. Khorkounov, H. Näfe and F. Aldinger, *Journal of Solid State Electrochemistry*, 2006, **10**, 479-487.
126. Innovative processing of dense LSGM electrolytes for IT-SOFC's, B. Rambabu, S. Ghosh, W. Zhao and H. Jena, *Journal of Power Sources*, 2006, **159**, 21-28.
127. Electrochemical performance and degradation of $(\text{La}_{0.6}\text{Sr}_{0.4})_{0.99}\text{CoO}_{3-\delta}$ as porous SOFC-cathode, P. Hjalmarsson, M. Søgaaard and M. Mogensen, *Solid State Ionics*, 2008, **179**, 1422-1426.
128. Oxygen transport properties of dense and porous $(\text{La}_{0.8}\text{Sr}_{0.2})_{0.99}\text{Co}_{0.8}\text{Ni}_{0.2}\text{O}_{3-\delta}$, P. Hjalmarsson, M. Søgaaard and M. Mogensen, *Solid State Ionics*, 2009, **180**, 1290-1297.
129. Performance of planar single cell lanthanum gallate based solid oxide fuel cells, N. Maffei and A. K. Kuriakose, *Journal of Power Sources*, 1998, **75**, 162-166.
130. Cobalt, D. G. Barceloux and D. Barceloux, *Clinical Toxicology*, 1999, **37**, 201-216.
131. Vacuum impregnation, S. M. D'Alfonzo, *Metal Finishing*, 2000, **98**, 510-512.
132. Debunking myths about vacuum impregnation, W. J. Fisher, *Metal Finishing*, 1999, **97**, 62-66.
133. Practical applications of vacuum impregnation in fruit and vegetable processing, Y. Zhao and J. Xie, *Trends in Food Science & Technology*, 2004, **15**, 434-451.
134. Ordered mesoporous materials in catalysis, A. Taguchi and F. Schüth, *Microporous and Mesoporous Materials*, 2005, **77**, 1-45.

135. Size-Controlled Synthesis and Catalytic Performance of Pt Nanoparticles in Micro- and Mesoporous Silica Prepared Using Supercritical Solvents, H. Wakayama, N. Setoyama and Y. Fukushima, *Advanced Materials*, 2003, **15**, 742-745.
136. MRCI potential curve and analytical potential energy function of the ground state of H₂, C.-L. Yang, Y.-J. Huang, X. Zhang and K.-L. Han, *Journal of Molecular Structure: THEOCHEM*, 2003, **625**, 289-293.
137. A Robust Platinum Carbonyl Cluster Anion [Pt₃(CO)₆]₅₂⁻ Encapsulated in an Ordered Mesoporous Channel of FSM-16: FTIR/EXAFS/TEM Characterization and Catalytic Performance in the Hydrogenation of Ethene and 1,3-Butadiene, T. Yamamoto, T. Shido, S. Inagaki, Y. Fukushima and M. Ichikawa, *The Journal of Physical Chemistry B*, 1998, **102**, 3866-3875.
138. MCM-41 mesoporous molecular sieves supported nickel--physico-chemical properties and catalytic activity in hydrogenation of benzene, A. Lewandowska, S. Monteverdi, M. Bettahar and M. Ziolk, *Journal of Molecular Catalysis A: Chemical*, 2002, **188**, 85-95.
139. Preparation, Characterisation and Performance of Encapsulated Copper-Ruthenium Bimetallic Catalysts Derived from Molecular Cluster Carbonyl Precursors, D. S. Shephard, T. Maschmeyer, G. Sankar, J. M. Thomas, D. Ozkaya, B. F. G. Johnson, R. Raja, R. D. Oldroyd and R. G. Bell, *Chemistry - A European Journal*, 1998, **4**, 1214-1224.
140. Single-Step, Highly Active, and Highly Selective Nanoparticle Catalysts for the Hydrogenation of Key Organic Compounds¹³, R. Raja, T. Khimyak, J. M. Thomas, S. Hermans and B. F. G. Johnson, *Angewandte Chemie International Edition*, 2001, **40**, 4638-4642.
141. Palladium-grafted mesoporous MCM-41 material as heterogeneous catalyst for Heck reactions, C. P. Mehnert and J. Y. Ying, *Chemical Communications*, 1997, 2215-2216.
142. Heterogeneous Heck Catalysis with Palladium-Grafted Molecular Sieves, C. P. Mehnert, D. W. Weaver and J. Y. Ying, *Journal of the American Chemical Society*, 1998, **120**, 12289-12296.
143. Ship-in-Bottle Synthesis of [Pt₁₅(CO)₃₀]₂⁻ Encapsulated in Ordered Hexagonal Mesoporous Channels of FSM-16 and Their Effective Catalysis in Water-Gas Shift Reaction, T. Yamamoto, T. Shido, S. Inagaki, Y. Fukushima and M. Ichikawa, *Journal of the American Chemical Society*, 1996, **118**, 5810-5811.
144. Pore Size Effects in Fischer Tropsch Synthesis over Cobalt-Supported Mesoporous Silicas, A. Y. Khodakov, A. Griboval-Constant, R. Bechara and V. L. Zholobenko, *Journal of Catalysis*, 2002, **206**, 230-241.

145. Synthesis and characteristics of MCM-41 supported CoRu catalysts, J. Panpranot, J. G. Goodwin and A. Sayari, *Catalysis Today*, 2002, **77**, 269-284.
146. Oxide anode materials for solid oxide fuel cells, J. W. Fergus, *Solid State Ionics*, 2006, **177**, 1529-1541.
147. M. Green, University of Milano-Bicocca, Lecture Series for PCAM, Milan, 2009.
148. K. E. Brown, A. J. Breeze, G. Rumbles, B. A. Gregg, P. A. Parilla, J. D. Perkins, H. Tillman, H. H. Horhold and D. S. Ginley, Charge carrier generation and exciton quenching at M₃EH-PPV/small-molecule and M₃EH-PPV/oxide interfaces, 2002, pp. 1186-1189.
149. Simultaneous enhancement of charge transport and exciton diffusion in poly(p - phenylene vinylene) derivatives, D. E. Markov, C. Tanase, P. W. M. Blom and J. Wildeman, *Physical Review B*, 2005, **72**, 045217.
150. Singlet exciton diffusion in MEH-PPV films studied by exciton-exciton annihilation, A. J. Lewis, A. Ruseckas, O. P. M. Gaudin, G. R. Webster, P. L. Burn and I. D. W. Samuel, *Organic Electronics*, 2006, **7**, 452-456.
151. Temperature Dependence of Exciton Diffusion in Conjugated Polymers, O. V. Mikhnenko, F. Cordella, A. B. Sieval, J. C. Hummelen, P. W. M. Blom and M. A. Loi, *The Journal of Physical Chemistry B*, 2008, **112**, 11601-11604.
152. Adsorption of Gases in Multimolecular Layers, S. Brunauer, P. H. Emmett and E. Teller, *Journal of the American Chemical Society*, 1938, **60**, 309-319.
153. The Determination of Pore Volume and Area Distributions in Porous Substances. I. Computations from Nitrogen Isotherms, E. P. Barrett, L. G. Joyner and P. P. Halenda, *Journal of the American Chemical Society*, 1951, **73**, 373-380.
154. Pore size determination in modified micro- and mesoporous materials. Pitfalls and limitations in gas adsorption data analysis, J. C. Groen, L. A. A. Peffer and J. Perez-Ramirez, *Microporous and Mesoporous Materials*, 2003, **60**, 1-17.
155. The Constitution and Fundamental Properties of Solids and Liquids. Part I. Solids, I. Langmuir, *Journal of the American Chemical Society*, 1916, **38**, 2221-2295.
156. LX. On the equilibrium of vapour at a curved surface of liquid, W. Thomson, *Philosophical Magazine Series 4*, **42**, 448 - 452.
157. On the Validity of the Kelvin Equation, J. G. Powles, *J Phys a-Math Gen*, 1985, **18**, 1551-1560.
158. KS Analytical Systems, XRD Operational Theory, 2009.

159. Scherrer after sixty years: A survey and some new results in the determination of crystallite size, J. I. Langford and A. J. C. Wilson, *Journal of Applied Crystallography*, 1978, **11**, 102-113.
160. JEOL, 2010 Transmission Electron Microscope Instruction Manual.
161. Application of Flash-desorption Method to Catalyst Studies. I. Ethylene-Alumina System1, Y. Amenomiya and R. J. Cvetanovic, *The Journal of Physical Chemistry*, 2002, **67**, 144-147.
162. Hamamatsu Photonics, Guide to Streak Cameras, 2002.
163. SerialEM A Program for Automated Tilt Series Acquisition on Tecnai Microscopes Using Prediction of Specimen Position, D. Mastronarde, *Microscopy and Microanalysis*, 2003, **9**, 1182-1183.
164. Study of the Activity and Deactivation of Ni-YSZ Cermet in Dry CH₄ Using Temperature-Programmed Techniques, R. T. Baker and I. S. Metcalfe, *Industrial & Engineering Chemistry Research*, 2002, **34**, 1558-1565.
165. Block copolymer-templated mesoporous oxides, G. J. D. A. Soler-Illia, E. L. Crepaldi, D. Grosso and C. Sanchez, *Current Opinion in Colloid & Interface Science*, 2003, **8**, 109-126.
166. Preparation of Gd₂O₃-doped ZrO₂ by polymeric precursor techniques, E. N. S. Muccillo, R. A. Rocha and R. Muccillo, *Materials Letters*, 2002, **53**, 353-358.
167. Modifying the walls of mesoporous silicas prepared by supramolecular-templating, A. Davidson, *Current Opinion in Colloid & Interface Science*, 2002, **7**, 92-106.
168. CRC Press, Handbook of Chemistry and Physics, 2003-2004, p. 84th Edition.
169. Fast oxygen uptake/release over a new CeOx phase, D. Terribile, J. Llorca, M. Boaro, C. de Leitenburg, G. Dolcetti and A. Trovarelli, *Chemical Communications*, 1998, 1897-1898.
170. Crystalline WO₃ nanowires synthesized by templating method, K. Zhu, H. He, S. Xie, X. Zhang, W. Zhou, S. Jin and B. Yue, *Chemical Physics Letters*, 2003, **377**, 317-321.
171. T. Dougherty, see attached CD.
172. Stichting Blender Foundation, Blender 2.49b, 2008.
173. Sintering behaviors of ceria and gadolinia-doped ceria, H. Inaba, T. Nakajima and H. Tagawa, *Solid State Ionics*, 1998, **106**, 263-268.
174. Thermal-Stability of Doped Ceria - Experiment and Modeling, M. Pijolat, M. Prin, M. Soustelle, O. Touret and P. Nortier, *Journal of the Chemical Society-Faraday Transactions*, 1995, **91**, 3941-3948.

175. EXAFS study of nanocrystalline CeO₂ samples prepared by sol-gel and ball-milling routes, A. V. Chadwick and S. L. P. Savin, *Journal of Alloys and Compounds*, 2009, **488**, 1-4.
176. Dioxygen adsorption on well-outgassed and partially reduced cerium oxide studied by FT-IR, C. Li, K. Domen, K. Maruya and T. Onishi, *Journal of the American Chemical Society*, 2002, **111**, 7683-7687.
177. Transport properties of solid oxide electrolyte ceramics: a brief review, V. V. Kharton, F. M. B. Marques and A. Atkinson, *Solid State Ionics*, 2004, **174**, 135-149.
178. S. Yongkui, W. Haiwen, K. Aiguo and L. Jiang, Method for synthesizing metal oxide mesoporous material by one-step vacuum perfusion, ed. P. O. o. China, China, 2007, p. 8.
179. Optimisation of the surface properties of SBA-15 mesoporous silica for in-situ nanoparticle synthesis, R. Benoit, F. Warmont, V. Meynen, K. De Witte, P. Cool, M. Treguer-Delapierre and M. L. Saboungi, *Microporous and Mesoporous Materials*, 2009, **120**, 2-6.
180. Energetically favored formation of MCM-48 from cationic-neutral surfactant mixtures, R. Ryoo, S. H. Joo and J. M. Kim, *Journal of Physical Chemistry B*, 1999, **103**, 7435-7440.
181. Probing the effect of the carbonisation process on the textural properties and morphology of mesoporous carbons, Z. Yang and R. Mokaya, *Microporous and Mesoporous Materials*, 2008, **113**, 378-384.
182. Processing of mesoporous silica materials (MCM-41) from coal fly ash, H. Misran, R. Singh, S. Begum and M. A. Yarmo, *Journal of Materials Processing Technology*, 2007, **186**, 8-13.